The First Direct Measurement of the Deuteron Electric Dipole Moment at the Cooler Synchrotron COSY

Der Fakultät für Mathematik, Informatik und Naturwissenschaften der RWTH Aachen University vorgelegte Dissertation zur Erlangung des akademischen Grades eines Doktors der Naturwissenschaften

von

Achim Andres, M.Sc.

aus

Eupen (Belgien)

Berichter: Universitätsprofessor Dr. rer. nat. Jörg Pretz
Universitätsprofessor Dr. rer. nat. Achim Stahl

Abstract

Currently, we do not understand why there is more matter than antimatter in our universe. The matter-antimatter asymmetry could only occur under specific conditions called the Sakharov conditions, one of which involves the violation of combined $\mathcal{CP}$ symmetry. Our understanding of the universe is based on the preservation of quantities such as energy, momentum, and charge. Advances in elementary particle physics have led to the discovery of new symmetries, including parity $\mathcal{P}$, charge conjugation $\mathcal{C}$, and time-reversal $\mathcal{T}$ symmetries. Traditionally, these symmetries were believed to be universal. However, over the past few decades, small violations of $\mathcal{C}$, $\mathcal{P}$, and combined $\mathcal{CP}$ symmetries have been detected and incorporated into the Standard Model of particle physics and cosmology. Nonetheless, these violations are insufficient to explain the observed domination of matter over antimatter. Hence, the search for additional $\mathcal{CP}$-violating phenomena continues. A possible manifestation of additional $\mathcal{CP}$ violation is the Electric Dipole Moment (EDM) of elementary particles. The Standard Model predicts a highly suppressed EDM, requiring experiments with high statistical and systematic sensitivity for detection. Conversely, models of physics beyond the Standard Model predict significantly larger EDMs, making EDM measurements an important tool for excluding certain beyond Standard Model theories. To date, all measurements of EDMs have been consistent with zero, providing only upper limits on the EDM size of various particles. The EDM must be a vectorial property aligned with a particle's spin, so measurement techniques focus on detecting changes in spin polarization signals caused by the interaction of a potential EDM with electric fields. Because charged particles are accelerated by electric fields, storage rings are ideal for charged particle EDM experiments such as the deuteron, for which no experimental limit is available so far. The goal of this thesis is to perform the first direct measurement of the deuteron Electric Dipole Moment at the Cooler Synchrotron at Forschungszentrum Jülich by observing the influence of the Electric Dipole Moment on the polarization of a stored bunched and polarized deuteron beam. The measured values presented in this thesis are dominated by systematic errors, from which an upper limit of the deuteron Electric Dipole Moment is derived:

$$|d^d| < 2.2 \times 10^{-16}\,\mathrm{e} \cdot \mathrm{cm}\ (95\,\%\ \text{C.L.})$$

Contents

1. Introduction

Presently, we lack an understanding of why there is more matter than antimatter in our universe. This matter-antimatter asymmetry could only arise if certain conditions, known as the Sakharov conditions, are met, one of which involves the violation of the combined $\mathcal{CP}$ symmetry. The preservation of quantities like energy, momentum, and charge forms the foundation of our comprehension of the universe. With the developments in particle physics, new symmetries were discovered, namely the parity $\mathcal{P}$, charge conjugation $\mathcal{C}$ and time-reversal $\mathcal{T}$ symmetries. Traditionally, it was believed that these symmetries held universally. However, over the past decades, small amounts of $\mathcal{C}$, $\mathcal{P}$ and combined $\mathcal{CP}$ violation have been identified and incorporated into the Standard Model of particle physics and cosmology. Nevertheless, these are not sufficient to explain the dominance of matter over antimatter. Hence, the search continues for additional manifestations of $\mathcal{CP}$ violation.

One potential contribution to additional $\mathcal{CP}$ violation is the so-called Electric Dipole Moment (EDM) of elementary particles. The EDM is highly suppressed by the Standard Model of elementary particles. Therefore, experiments with high statistical and systematic sensitivity are required for their determination. However, models incorporating physics beyond the Standard Model predict significantly larger Electric Dipole Moments. Hence, EDM measurements are an important tool to exclude beyond the Standard Model physics parameter space. Discovering a finite EDM would enhance our comprehension and potentially extend the Standard Model. So far, all measurements of EDMs are statistically and systematically consistent with zero. From these measurements, only upper limits have been derived on the size of an EDM.

Electric Dipole Moments have to be aligned with the particle's spin. Therefore, measurement techniques aim to detect a change in the spin polarization signal resulting from the interaction of a potential EDM with electric fields. Since charged particles are accelerated by electric fields, particle storage rings are a natural choice for charged particle EDM experiments. While EDM measurements for muons have been conducted in storage rings, the current experimental limit for protons is derived from theoretical considerations applied to atomic EDM measurements. Additionally, no experimental limit for the deuteron is available so far. Future direct measurements for protons and deuterons are proposed in dedicated storage rings utilizing pure electric fields or a combination of electric and magnetic fields. Feasibility studies are underway within the JEDI (Jülich Electric Dipole moment Investigations) collaboration at the existing storage ring, the Cooler Synchrotron COSY at Forschungszentrum Jülich.

The aim of this thesis is to perform the first direct measurement of the deuteron Electric Dipole Moment at the Cooler Synchrotron facility at Forschungszentrum Jülich by observing the influence of the Electric Dipole Moment on the polarization of a stored bunched and polarized beam in the storage ring. The measured values reported in this thesis are dominated by systematic uncertainties from which a first upper limit of the deuteron Electric Dipole moment is derived:

$$|d^d| < 2.2 \times 10^{-16}\,\mathrm{e}\cdot\mathrm{cm}\ (95\,\%\ \mathrm{C.L.}). \tag{1.1}$$

This thesis is structured as follows:

In chapter 2, the matter-antimatter asymmetry is introduced. After discussing fundamental symmetries, the Electric Dipole Moment of fundamental particles is introduced as an additional manifestation of $\mathcal{CP}$ violation. The chapter is finalized with an overview of existing EDM limits for various particles.

In sections 3 and 4, the motion of particles, including relevant parameters such as tunes and chromaticity, and the evolution of polarized beams in accelerators are described. Most importantly, the basic principle of the measurement is outlined by explaining how an EDM modifies the polarization of a bunched beam in a particle accelerator.

Section 5 illustrates the Cooler Synchrotron COSY at Forschungszentrum Jülich. An overview of the full facility is given, along with all installations which are important for this thesis, including the spin manipulators and polarimeters installed in the ring.

Chapter 6 describes the data analysis methods. The extraction of all important variables, such as the vertical and horizontal polarization from data taken with the internal polarimeters, is relevant for the experiment.

In chapter 7, the methodology of the first direct measurement of the deuteron Electric Dipole Moment is explained. It was found that unknown systematics are dominating the experiment, which are explored in the following section 8.

The results of the first direct measurement of the deuteron Electric Dipole Moment are discussed in section 9.

The thesis ends in section 10 with an outlook of possible future Electric Dipole Moment measurement activities in storage rings and conclusions in section 11.

2. Scientific Motivation

This thesis is written within the JEDI [1] (**J**uelich **E**lectric **D**ipole moment **I**nvestigations) Collaboration at Forschungszentrum Jülich. The aim of the collaboration is contributing to the understanding of the matter-antimatter asymmetry in the universe by exploring possible experiments of measuring permanent and oscillating Electric Dipole Moments of charged particles in storage rings.

2.1. Baryon Asymmetry

The matter-antimatter asymmetry in the visible universe remains unexplainable by the Standard Model of elementary particles and the theory of general relativity. In the early moments of the universe, particularly during the first fractions of a second after the Big Bang, conditions were extremely energetic and hot. At such high temperatures ($\approx 3000\,\mathrm{K}$), particle-antiparticle pairs were continuously created from the available energy and shortly after annihilated, resulting in the conversion of the particles and antiparticles into energy. The processes that created particles and antiparticles were expected to be in balance, resulting in an equal amount of matter and antimatter. However, as the universe expanded and cooled, the conditions changed and the creation and annihilation of particle-antiparticle pairs became less frequent. At some point, the universe underwent a phase called baryogenesis, where a tiny excess of matter over antimatter was generated. This slight imbalance had significant consequences, leading to the predominance of matter in the observable universe today. The matter-antimatter asymmetry can be quantified by the baryon asymmetry parameter η [2]

$$\eta = \frac{N_B - N_{\bar{B}}}{N_B + N_{\bar{B}}} \approx \frac{N_B - N_{\bar{B}}}{N_\gamma}, \tag{2.1}$$

where N_B, $N_{\bar{B}}$ and N_γ denote the baryon, antibaryon and photon densities respectively. The approximation $N_B + N_{\bar{B}} \approx N_\gamma$ is used since the end products of annihilation processes are mostly photons. The ratio was independently determined from the power spectrum of the temperature fluctuations in the Cosmic Microwave Background (CMB) and the abundance of light elements in the intergalactic medium (IGM). The two measurements are consistent within their uncertainties [2]

$$\eta^{\mathrm{IGM}} = (5.80 \pm 0.27) \times 10^{-10} \text{ and } \eta^{\mathrm{CMB}} = 6.160^{+0.153}_{-0.156} \times 10^{-10}. \tag{2.2}$$

The Standard Model of elementary particle physics combined with the Standard Model of cosmology predicts the baryon asymmetry [3]

$$\eta^{\mathrm{SM}} \approx 10^{-18}, \tag{2.3}$$

which is eight orders of magnitude smaller than the measured values. Two possible scenarios could explain the domination of matter

1. Antimatter regions, separated from matter-dominated regions like our Milky Way, are still existing. The Alpha Magnetic Spectrometer (AMS) experiment on the International Space Station (ISS) [4] is actively searching for antimatter-dominated regions in our universe.
2. Symmetry breaking during the annihilation of baryons and antibaryons during the baryogenesis phase of the universe.

Andrei Sakharov postulated three conditions in 1967 to explain baryogenesis [5].

1. **Baryon number violation:** Processes that violate baryon number conservation are required to evolve from a state with no baryons into a state with baryons, considering that the initial system was in a state with baryon number $B = 0$.
2. **$\mathcal{C}$ and $\mathcal{CP}$ symmetry violation:** Conservation of $\mathcal{C}$ and $\mathcal{CP}$ symmetries would result in the same probability of processes creating particles and their respective antiparticles. This is linked to baryon number violation, as otherwise, no baryon asymmetry could have occurred. More information about $\mathcal{C}$ and $\mathcal{CP}$ symmetries is given in section 2.2.
3. **Interactions out of thermal equilibrium:** A system in thermal equilibrium means that all physical quantities are stable, making the transition from $B = 0$ to $B \neq 0$ impossible.

2.2. Symmetries and their Transformations

The formal connection between the conservation of a physical quantity and the invariance of the corresponding system under a transformation, which defines a symmetry, was found in 1918 by the mathematician Emmy Noether [6]. In other words, each conservation law is connected to an underlying symmetry. She found that the invariance of a system to a time transformation leads to the energy conservation law and translation invariance and rotation invariance result in momentum and angular momentum conservation, respectively. These symmetries are also called continuous symmetries.

With further discoveries in elementary particle physics, new, discrete symmetries were found, which can be mathematically described by operators applied to quantum systems. The main discrete symmetries in particle physics are parity transformation ($\mathcal{P}$), charge conjugation ($\mathcal{C}$), and time reversal ($\mathcal{T}$) symmetry [7].

- **Parity Transformation** describes the inversion of the three spatial coordinates while leaving the time coordinate unchanged

$$(\vec{x}, t) \rightarrow (-\vec{x}, t). \tag{2.4}$$

  Polar vectors, such as momentum or position, undergo inversion through parity transformation. However, axial vectors like spin and angular momentum remain unaffected by the transformation. Similarly, electric fields, which are represented by polar vectors, are reversed under parity transformation, while magnetic fields, represented by axial vectors, remain unaffected.

- **Charge Conjugation Transformation** inverts additive quantum numbers like charge, baryon number, lepton number, or strangeness, which leads to the conversion of particles into their respective antiparticles in the underlying physical process. An inversion of charge also leads to a direct change in the direction of electric and magnetic fields. However, spin, momentum, mass, and the lifetime of a particle remain unaffected.
- **Time Reversal Transformation** inverts the sign of the time coordinate

  $$(\vec{x}, t) \rightarrow (\vec{x}, -t). \tag{2.5}$$

  For a time-reversal symmetric process, the reaction rate of a process should be the same as for the reverse reaction.

2.2.1. Symmetry Breaking in the Standard Model

In the early 20th century, it was common sense that the symmetries are conserved in any process. However, the interest in their violations arised starting from 1950 when the first symmetry breaking theories were developed. In 1957, Wu et al. saw the first evidences of parity violation in the weak sector in their famous experiment observing the beta decay of polarized ^{60}Co [8]

$$^{60}\mathrm{Co} \rightarrow ^{60}\mathrm{Ni} + e^- + \bar{\nu}_e. \tag{2.6}$$

It was observed that the direction of electron emission tended to be opposite to the direction of nuclear spin. Applying a parity transformation would reverse the sign of the electrons' velocity, but the polarization direction would remain unchanged. A second important experiment considering symmetry breaking is the decay of charged pions [9]

$$\pi^- \rightarrow \mu^- + \bar{\nu}_\mu, \tag{2.7}$$

$$\pi^+ \rightarrow \mu^+ + \nu_\mu. \tag{2.8}$$

By measuring the spin direction of the emitted muon, it was discovered that neutrinos have negative helicity i.e., the projection of the spin axis on the momentum vector $h = \vec{S} \cdot \vec{p}$, whereas anti-neutrinos only appear with positive helicity. Consequently, neutrinos are named left-handed and anti-neutrinos are referred to as right-handed. Although the existence of right-handed neutrinos is theoretically possible, no empirical evidence supporting their presence has been found so far. As a result, the unique handedness of neutrinos breaks the $\mathcal{P}$ invariance [10].

A $\mathcal{C}$ transformation converts a neutrino into an anti-neutrino while preserving the spin and momentum. Applying a $\mathcal{C}$ transformation on the reaction described in Eq. (2.8) leads to

$$\mathcal{C}(\pi^+ \rightarrow \mu_L^+ + \nu_{\mu,L}) \Rightarrow \pi^- \rightarrow \mu_L^- + \bar{\nu}_{\mu,L}. \tag{2.9}$$

Consequently, a left-handed neutrino would be transformed into a left-handed anti-neutrino. However, as no evidence of such a particle has been discovered, there is experimental evidence that the $\mathcal{C}$ symmetry is also broken.

As a consequence of parity and charge conjugation symmetry breaking, a new combined symmetry can be applied to the pion decay

$$\mathcal{CP}(\pi^+ \rightarrow \mu_L^+ + \nu_{\mu,L}) \Rightarrow \mathcal{C}(\pi^+ \rightarrow \mu_R^+ + \nu_{\mu,R}) \Rightarrow \pi^- \rightarrow \mu_R^- + \bar{\nu}_{\mu,R}, \tag{2.10}$$

which is in fact a conversion from Eq. (2.8) to (2.7), meaning that the process is $\mathcal{CP}$ conserving. The first evidence of $\mathcal{CP}$ violation was found in the Kaon sector. In 1964, James Cronin and Val Fitch conducted an experiment [11], revealing that the Kaon decay violates $\mathcal{CP}$ symmetry, by observing the decay of K_L into pions. The decay into two pions would not be possible if K_L was a pure $\mathcal{CP}$ eigenstate. However, decays into two pions were observed. This implies that $\mathcal{CP}$ symmetry can be broken in weak interactions. It is possible to extend the Standard Model using the so-called CKM (Cabibbo-Kobayashi-Maskawa)[12] matrix to account for the finding of $\mathcal{CP}$ violation. In recent times, $\mathcal{CP}$ violation was also observed in the B meson sector [13].

In strong interactions, the QCD Lagrangian of the Standard Model includes $\mathcal{CP}$-violating term (the so-called $\bar{\theta}_{\mathrm{QCD}}$ term), which can be linked to an Electric Dipole Moment (EDM) of nucleons. More information is given in the following section 2.3.2.

Lastly, a new symmetry, known as the $\mathcal{CPT}$ theorem [14], was introduced by combining all three symmetries. This implies that, through successive applications of the $\mathcal{C}$, $\mathcal{P}$, and $\mathcal{T}$ transformations to a system, it will return to its initial state. To date, the $\mathcal{CPT}$ theorem has remained valid, with no observed violations. The stability of the $\mathcal{CPT}$ theorem has implications for other processes involving symmetry violation: if a reaction violates time reversal symmetry, the $\mathcal{CP}$ symmetry is also violated if the $\mathcal{CPT}$ theorem holds.

2.3. Electric Dipole Moments

The Electric Dipole Moment of an elementary particle is a fundamental property like momentum, charge, or mass and is aligned with the particle's spin axis. The existence of a permanent Electric Dipole Moment above the predictions of the Standard Model would be an additional source of $\mathcal{CP}$ violation and a hint towards physics beyond the Standard Model if the $\mathcal{CPT}$ theorem holds, and it could contribute to our understanding of the matter-dominated universe.

2.3.1. Definition

Classically, the Electric Dipole Moment $\vec{d}$ describes the separation of charges in a system

$$\vec{d} = \int_V \mathrm{d}x^3 \; \vec{x} \cdot \rho(\vec{x}), \tag{2.11}$$

where $\rho(\vec{x})$ denotes the charge density distribution of the system. The Magnetic Dipole Moment (MDM) is defined in an analogous way

$$\vec{\mu} = \frac{1}{2} \int_V \mathrm{d}x^3 \; \left(\vec{x} \times \vec{j}(\vec{x})\right). \tag{2.12}$$

For the Magnetic Dipole Moment, $\vec{j}(\vec{x})$ describes the current density. The dependencies of the Electric Dipole Moment and the Magnetic Dipole Moment with the spin of a particle are given by [15]

$$\vec{d} = d \cdot \vec{S} \quad \text{with} \quad d = \eta_{\mathrm{EDM}} \frac{q\hbar}{2mc} \quad \text{and} \quad \vec{\mu} = \mu \cdot \vec{S} \quad \text{with} \quad \mu = g\frac{q\hbar}{2m}, \tag{2.13}$$

where $\vec{S}$ denotes a unit vector, i.e. $|\vec{S}| = 1$, directed along $\vec{s}$, the true spin vector with

$$|\vec{s}| = \frac{\hbar}{2}, \tag{2.14}$$

for spin-1/2 particles and

$$|\vec{s}| = \hbar, \tag{2.15}$$

for a spin-1 particle. The particle's mass and charge are given by m and q, Planck's constant and the speed of light are denoted by $\hbar$ and c and the dimensionless factors η_{EDM} and g describe the strength of the Electric Dipole Moment and the Magnetic Dipole Moment, respectively.

Using the Magnetic Dipole Moment as defined in Eq. (2.13), the g-factor can be calculated for an elementary particle X using

$$\mu_X = g_X \frac{q\hbar}{2m_X} s_X. \tag{2.16}$$

Rearranging leads to the g-factor which reads for the deuteron

$$g_d = \mu_d \frac{2m_d}{q|\vec{s}|} \approx 1.714\,025\,461. \tag{2.17}$$

However, for neutral particles like the neutron ($q = 0$), Eq. (2.17) cannot be used. Therefore, the magnitudes of the Magnetic Dipole Moment are described using the Bohr magneton for leptons or the nuclear magneton for hadronic systems [16]

$$\mu_B = \frac{q\hbar}{2m_e} = 5.788\,381\,801\,2(26) \times 10^{-5}\,\text{eV/T}, \tag{2.18}$$

$$\mu_N = \frac{q\hbar}{2m_p} = 3.152\,451\,255\,0(15) \times 10^{-8}\,\text{eV/T}. \tag{2.19}$$

In official databases like the NIST database [17], the g-factor of hadrons is defined with respect to the nuclear magneton

$$\mu_X = g_X \frac{e\hbar}{2m_p} s_X = g_X \mu_N s_X \text{ with } X \in \{p, n, d, ..\}, \tag{2.20}$$

which leads to a g-factor of

$$g_d = \frac{\mu_d}{\mu_N} \approx 0.857\,438\,234. \tag{2.21}$$

Thus, for the deuteron, the genuine definition of the g-factor as defined in Eq. (2.17) and the g-factor with respect to the nuclear magneton as defined in Eq. (2.21) can be transformed into each other using

$$g_d = \frac{\mu_d}{\mu_N} \frac{m_d}{m_p}. \tag{2.22}$$

In section 4.2, the so-called Thomas-BMT Equation is discussed which describes the motion of spins in external electric and magnetic fields with a nonzero Electric Dipole Moment component. The differential equations are a central element for the experimental methods described in this thesis. For the derivation of the Thomas-BMT Equation, the definition of the fundamental g-factor as defined in Eq. (2.17) is used [18].

Related to the dimensionless g factor is the anomalous gyromagnetic g-factor G, defined as

$$G = a = \frac{g-2}{2}. \tag{2.23}$$

In the leptonic sector, the letter a is often used for the anomalous gyromagnetic factor, while in the hadronic sector the letter G is used. The g-factor can be related to Dirac's equation which describes fundamental properties of fermions (spin-1/2 particles). The outcome of the g-factor is given by $g = 2$ and $a = 0$. However, higher order correction factors of the fine structure constant lead to deviations of $g = 2$. Unrelated to the Dirac Equation, the factor (g-2)/2 appears also in the derivation of the Thomas-BMT Equation. In this case it is important to use the g-factor as defined in Eq. (2.17). The magnetic properties of the deuteron and the proton are summarized in Table 2.1.

Note the Electric Dipole Moment and the Magnetic Dipole Moment are always aligned (parallel or antiparallel) to the particle's spin direction since the spin axis is the only marked direction in a quantum system [19]. The proof of the alignment of the Electric Dipole Moment with the spin axis in the absence of external electric fields, assuming that $|a\rangle$ is a state of definite parity ($\mathcal{P}\,|a\rangle = \pm\,|a\rangle$), makes use of the so-called Wigner-Eckart theorem and shows that the expectation value of the Electric Dipole Moment is proportional to the spin vector [20]

$$\langle a|\,\vec{d}\,|a\rangle \propto \langle a|\,\vec{S}\,|a\rangle\,. \tag{2.24}$$

Table 2.1.: Magnetic properties of the proton and the deuteron [17]. The g-factor is calculated according to Eq. (2.17).

Particle	$S\ /\ \hbar$	Mass / mc^2 (MeV)	$\mu\ /\ \mu_N$	g	G
proton	1/2	938.272 081 3(58)	2.792 847 344 63(82)	5.585 694 689 3(16)	1.792 847 344 650(8)
deuteron	1	1875.612 928(12)	0.857 438 233 5(22)	1.714 025 45(1)	−0.142 987 270(8)

2.3.2. Electric Dipole Moments and $\mathcal{CP}$-Violation

The $\mathcal{CP}$ violating properties can be revealed by applying a parity $\mathcal{P}$ and time reversal symmetry $\mathcal{T}$ transformation to the non-relativistic Hamiltonian $\hat{\mathcal{H}}$ of a particle at rest in an external magnetic $\vec{B}$ and electric $\vec{E}$ field with Electric Dipole Moment and Magnetic Dipole Moment [21]

$$\hat{\mathcal{H}} = -\mu\,\vec{S}\cdot\vec{B} - d\,\vec{S}\cdot\vec{E}, \tag{2.25}$$

$$\mathcal{P}:\hat{\mathcal{H}} = -\mu\,\vec{S}\cdot\vec{B} + d\,\vec{S}\cdot\vec{E}, \tag{2.26}$$

$$\mathcal{T}:\hat{\mathcal{H}} = -\mu\,\vec{S}\cdot\vec{B} + d\,\vec{S}\cdot\vec{E}. \tag{2.27}$$

By applying the parity operator in Eq. (2.26), the direction of the electric field is inverted, while the magnetic field and the spin remain unchanged. The change of sign in the Electric Dipole Moment contribution of the Hamiltonian means that the Electric Dipole Moment violates $\mathcal{P}$ invariance while the Magnetic Dipole Moment contribution preserves the parity. The time reversal transformation in Eq. (2.27) behaves in an almost identical way. Spin and magnetic field are inverted, while the electric field is preserved, leading to the same conclusions as for the parity transformation. Consequently, also $\mathcal{CP}$ is violated if the $\mathcal{CPT}$ theorem holds. The breach of parity and time reversal symmetry, assuming a nonzero Electric Dipole Moment $d \neq 0$, is shown in Figure 2.1.

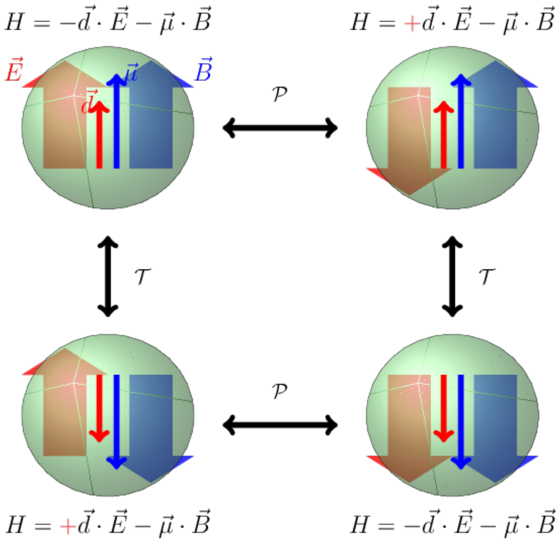

Figure 2.1.: Schematic of a particle with an Electric Dipole Moment and Magnetic Dipole Moment in an external electromagnetic field. Applying time reversal transformation, spin and magnetic field are inverted. Parity transformation leads to an inversion of the electric field. Both transformations lead to a breach of symmetry in the Electric Dipole Moment contribution of the Hamiltonian. Created by Jörg Pretz/ JEDI Collaboration.

Predictions of Electric Dipole Moments within the Standard Model can be calculated from Feynman diagrams. The Electric Dipole Moment of quarks requires at least three-loop diagrams resulting in very small predictions [21, 22]

$$d_q \leq 1 \times 10^{-34}\,\mathrm{e} \cdot \mathrm{cm} - 1 \times 10^{-35}\,\mathrm{e} \cdot \mathrm{cm}. \tag{2.28}$$

Four-loop Feynman diagrams are required for non-vanishing Electric Dipole Moments for leptons, resulting in significantly smaller predictions for electrons [19, 21]

$$d_e \leq 1 \times 10^{-38}\,\mathrm{e} \cdot \mathrm{cm}. \tag{2.29}$$

The Electric Dipole Moment also plays an important role in the strong sector of the Standard Model, where it contributes to the so-called $\bar{\theta}_{\mathrm{QCD}}$ term. The Lagrangian of quantum chromodynamics (QCD) contributing to the $\mathcal{CP}$ violation is given by [23]

$$\mathcal{L}_{\bar{\theta}_{\mathrm{QCD}}} = -\bar{\theta}_{\mathrm{QCD}} \frac{g_s^2}{64\pi^2} \epsilon^{\mu\nu\alpha\beta} G^a_{\mu\nu} G^a_{\alpha\beta}, \tag{2.30}$$

with $G^a_{\mu\nu}$ being the gluon field strength tensor, $\epsilon^{\mu\nu\alpha\beta}$ denoting the total-asymmetric four-tensor and the strong coupling constant represented by g_s. Predictions of the proton and neutron Electric Dipole Moment have been parameterized with respect to $\bar{\theta}_{\mathrm{QCD}}$, leading to [24]

$$d_n^{\bar{\theta}_{\mathrm{QCD}}} = \bar{\theta}_{\mathrm{QCD}} \cdot (-2.9 \pm 0.9) \times 10^{-16}\,\mathrm{e} \cdot \mathrm{cm}, \tag{2.31}$$

$$d_p^{\bar{\theta}_{\mathrm{QCD}}} = \bar{\theta}_{\mathrm{QCD}} \cdot (-1.1 \pm 1.1) \times 10^{-16}\,\mathrm{e} \cdot \mathrm{cm}. \tag{2.32}$$

Measurements of the Electric Dipole Moment of the neutron constrain the $\bar{\theta}_{\mathrm{QCD}}$ parameter to [23]

$$\bar{\theta}_{\mathrm{QCD}} \leq 10^{-10}. \tag{2.33}$$

While the order of magnitude of $\bar{\theta}_{\mathrm{QCD}}$ is expected to be $\mathcal{O}(1)$, the smallness of this parameter remains theoretically not understood. This problem is also called the strong $\mathcal{CP}$ problem. The postulation of hypothetical new particles, like axions, could solve the strong $\mathcal{CP}$ problem. However, no experimental observations have been made up to date. Also, the JEDI collaboration conducted a measurement for the search of axions or axion-like particles. More information about this measurement is given in section 4.2.3 [25, 26].

2.3.3. Existing Electric Dipole Moment Limits

Due to its $\mathcal{CP}$-violating properties, the Electric Dipole Moment is an interesting measurable quantity. All experiments rely on the fact that the Electric Dipole Moment is either parallel or antiparallel to the spin of a particle, making the polarization of an ensemble of particles the most important observable.

The first measurement of the neutron Electric Dipole Moment was published in 1957 by Smith, Ramsey, and Purcell. Starting from a neutron sample created by a reactor, the neutron beam is polarized using total reflection from a polished, magnetized iron mirror. Afterwards, the polarized neutrons traversed the main magnetic field. When applying an additional radio-frequency (RF) magnetic field whose frequency is adjusted to the Larmor frequency of the neutrons, the polarization rotates into the plane perpendicular to the main magnetic field. After this, a homogeneous electric field is superimposed either parallel or antiparallel to the quantization axis leading to a precession of the perpendicular polarization with the angular frequency

$$\omega = \frac{2|\mu B \pm dE|}{\hbar}. \tag{2.34}$$

The sign change indicates the flip of the electric field. By subtracting the two frequencies, the Electric Dipole Moment can be determined using

$$d = \frac{\Delta\omega\hbar}{4E}. \tag{2.35}$$

The experiment led to the first measurement of the neutron Electric Dipole consistent with zero [27]

$$d_n = (-0.1 \pm 2.4) \times 10^{-20}\,\mathrm{e} \cdot \mathrm{cm}. \tag{2.36}$$

Over the past years, the experiments became more and more sensitive leading to more stringent neutron Electric Dipole Moment limits using ultracool neutrons in modernized experimental setups [28]. The history of neutron Electric Dipole Moment limits is depicted in Figure 2.2.

In the early days of Electric Dipole Moment measurements, neutrons were a natural choice as they are not accelerated by electric fields. However, it was not possible to measure Electric Dipole Moments of charged particles. Trapping charged particles in particle accelerators where they are stored with long beam lifetimes offers the possibility to measure their electric dipole moments in future experiments.

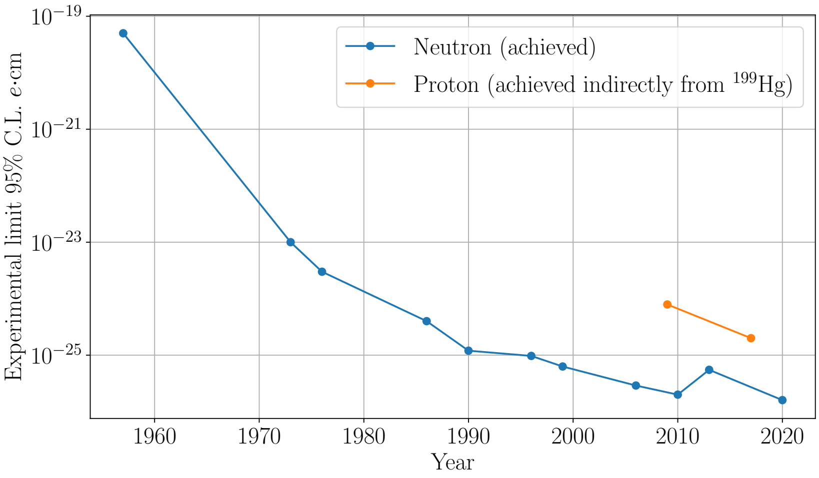

Figure 2.2.: Proton and neutron Electric Dipole Moment limits determined from direct and indirect measurements are sorted by publication year. The limits are taken from [27, 28, 29, 30, 31, 32, 33, 34, 35, 36, 37] and [38, 39] and adapted to 95 % C.L. if necessary. In dedicated storage rings, the sensitivity of the measurement of Electric Dipole Moments of charged particles is expected to drastically increase. More information about future Electric Dipole Moment storage ring experiments is given in section 10.2.

The proton Electric Dipole Moment can be measured in diamagnetic atoms. The finite size of the nucleus and magnetic interactions between nucleons and electrons results in an atomic Electric Dipole Moment. The best limit was achieved using mercury-199 (^{199}Hg). The atoms are polarized by a 254 nm laser system and the precession of polarization is measured in two cells with aligned and anti-aligned static magnetic and electric fields. The obtained Electric Dipole Moment limit for ^{199}Hg and the deduced proton Electric Dipole Moment limit are given in Table 2.2 [38]. There is no direct measurement of the proton Electric Dipole Moment available.

The Λ-hyperon and the μ Electric Dipole Moment limit were parasitically measured while measuring the Magnetic Dipole Moment of the particles. The direct Electric Dipole Moment measurement of the muon at the $g-2$ experiment [15, 40] is similar to the experiment reported in this thesis.

The Electric Dipole Moment of the τ lepton was measured by the BELLE collaboration at the KEKB e^+e^- collider analyzing the $e^+e^- \to \tau^+\tau^-$ reaction [41].

The Electric Dipole Moment of the electron was measured using trapped molecular ions $^{180}\mathrm{Hf}^{19}\mathrm{F}^+$ using spin resonance spectroscopy on metastable electronic states [42].

An overview of recent Electric Dipole Moment measurements, including the confidence limits is shown for a few particle species in Figure 2.3. The values are summarized in Table 2.2. The goal of the JEDI collaboration is to extend Figure 2.3 with a first direct measurement of the proton and deuteron Electric Dipole Moment.

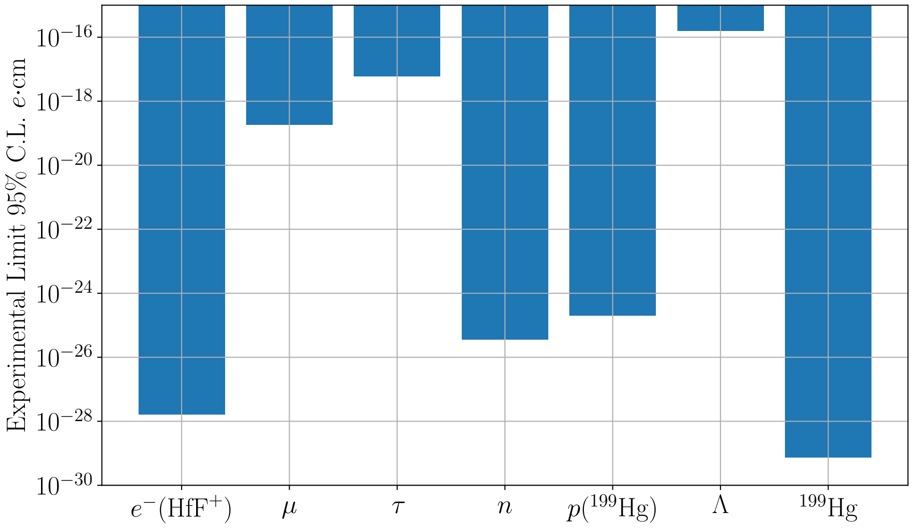

Figure 2.3.: Experimental 95 % confidence limits for various particles. For the electron and proton, no direct measurement is available. The confidence limits are calculated from measurements with $^{199}\mathrm{Hg}$ and $^{180}\mathrm{Hf}^{19}\mathrm{F}^+$. The values are taken from Table 2.2 and adapted to 95 % C.L. if necessary.

Table 2.2.: Most recent Electric Dipole Moment results of various particles. Each result is consistent with 0. In case statistical and systematic errors are reported, they are combined in quadrature. There is no direct measurement of the proton Electric Dipole Moment limit available. The confidence limit is calculated from the measurement of the mercury Electric Dipole Moment limit.

Particle	Experimental Result / (e · cm)	Limit / (e · cm)	C.L. / %	Year	Ref.
μ	$(-0.1 \pm 0.9) \times 10^{-19}$	1.9×10^{-19}	95	2018	[15]
τ	$(-0.62 \pm 0.63) \times 10^{-17}$	6.1×10^{-18}	95	2022	[41]
$p\left(^{199}\mathrm{Hg}\right)$		2.0×10^{-25}	95	2017	[39]
$e^-\left(\mathrm{HfF}^+\right)$	$(0.9 \pm 7.9) \times 10^{-29}$	1.6×10^{-28}	90	2017	[42]
$^{199}\mathrm{Hg}$	$(2.2 \pm 3.1) \times 10^{-30}$	7.4×10^{-30}	95	2009	[38]
n	$(-0.21 \pm 1.82) \times 10^{-26}$	3.6×10^{-26}	90	2020	[28]
Λ	$(-3.0 \pm 7.4) \times 10^{-17}$	1.5×10^{-16}	95	1981	[40]

3. Beam Dynamics in Storage Rings

To understand how the Electric Dipole Moment is measured, it is crucial to understand particle behaviour in an accelerator. In an accelerator, electric and magnetic fields affect the particles, keeping them on course. This path evolution is known as beam dynamics. This chapter explains the coordinate system used in accelerators and discusses the interaction of different accelerator components through the Lorentz force. The mathematical descriptions in the following sections are taken from [43].

3.1. Coordinate System

The equation of motion for particles in an ensemble is parameterized by their spatial coordinates ($\vec{r}$) and momenta ($\vec{p}$). This results in trajectories described in a six-dimensional phase space. In a storage ring composed of deflectors with static electromagnetic fields, particle motion is time-independent, and the arc length s is chosen as the independent variable. For convenience, it is better to use a Cartesian coordinate system based on curvilinear coordinates. The origin of this system moves precisely along the reference orbit $\vec{r}_{\mathrm{ref}}$ with the reference momentum $\vec{p}_{\mathrm{ref}}$. In a planar ring, the basis vectors ($\vec{e}_s$ and $\vec{e}_x$) define a plane, and their orthogonal vector is $\vec{e}_y = \vec{e}_s \times \vec{e}_x$. It is worth noting that $\vec{e}_s$ is parallel to the momentum vector of the reference orbit $\vec{p}_{\mathrm{ref}}$. The coordinate transformation from s_i to s_f, illustrated in Figure 3.1, involves a rotation

$$\vec{e}_{x,f} = \cos(\theta)\vec{e}_{x,i} + \sin(\theta)\vec{e}_{s,i}, \tag{3.1}$$

$$\vec{e}_{y,f} = \vec{e}_{y,i}, \tag{3.2}$$

$$\vec{e}_{s,f} = -\sin(\theta)\vec{e}_{x,i} + \cos(\theta)\vec{e}_{s,i}, \tag{3.3}$$

with

$$\theta = \int_{s_i}^{s_f} \frac{\mathrm{d}s}{\rho(s)} = \int_{s_i}^{s_f} h(s)\mathrm{d}s. \tag{3.4}$$

The bending radius is given by $\rho(s)$ and for convenience purposes the inverse $h(s) = {}^{1}/_{\rho(s)}$ is also introduced. Consequently, also the change of the unit vectors over time can be derived

$$\dot{\vec{e}}_x = \frac{\mathrm{d}\vec{e}_x}{\mathrm{d}\theta}\frac{\mathrm{d}\theta}{\mathrm{d}t} = \frac{1}{\rho}s\vec{e}_s, \tag{3.5}$$

$$\dot{\vec{e}}_y = 0, \tag{3.6}$$

$$\dot{\vec{e}}_s = \frac{\mathrm{d}\vec{e}_s}{\mathrm{d}\theta}\frac{\mathrm{d}\theta}{\mathrm{d}t} = -\frac{1}{\rho}\dot{e}_x. \tag{3.7}$$

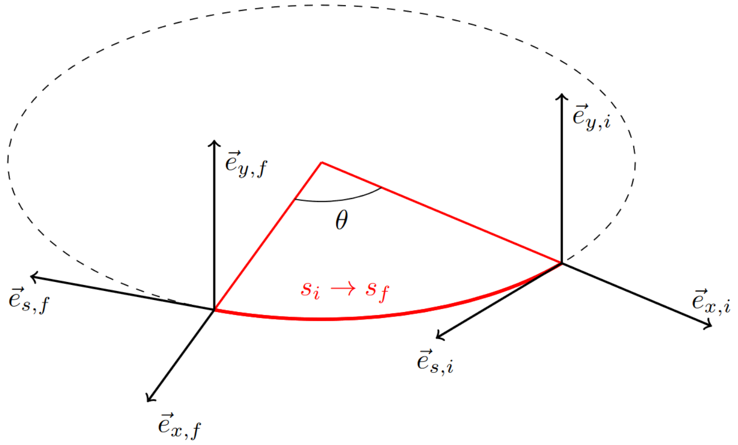

Figure 3.1.: Co-moving curvilinear cartesian coordinate system. The black dotted line denotes the reference particle's trajectory. The vertical direction is given by $\vec{e}_y$, the unit vector $\vec{e}_x$ always points in the radial direction, and the tangential component $\vec{s}$ always points in the direction of the momentum of the reference particle. Taken from [44].

A particle's trajectory ($\vec{r}(s)$) can be described with respect to the trajectory of the reference particle

$$\vec{r}(s) = \vec{r}_{\text{ref.}}(s) + x(s)\vec{e}_x(s) + y(s)\vec{e}_y(s), \tag{3.8}$$

where $x(s)$ and $y(s)$ describe the transverse deviations of the particle in horizontal and vertical directions with respect to the reference particle's trajectory.

3.2. Lorentz Force

The Lorentz force describes the change of momentum $\vec{p}$ of a particle with mass m and charge q in the presence of electric $\vec{E}$ and magnetic fields $\vec{B}$

$$\vec{F}_L = \frac{\mathrm{d}\vec{p}}{\mathrm{d}t} = q\left(\vec{E} + c\vec{\beta} \times \vec{B}\right), \tag{3.9}$$

where $c\vec{\beta}$ denotes the particle's velocity. A typical particle accelerator comprises magnets with static fields that do not change over time if the beam is not accelerated, guiding and focusing the particle beam. The subsequent description will concentrate on planar storage rings using purely magnetic elements. In principle, electric fields can also bend the particle's trajectory. However, reaching sufficient magnetic fields is technically easier than constructing pure electric deflectors. Nonetheless, in conventional particle accelerators, the particles are accelerated using electric fields because an acceleration using only magnetic fields is not possible ($F \propto \vec{\beta} \times \vec{B}$).

3.3. Transverse Motion

Magnets like dipole, quadrupole, and sextupole magnets define the transverse motion of a particle beam in an accelerator. An equilibrium of centrifugal force and Lorentz force is used for deflection

$$m\gamma|\vec{\beta}c|^2\vec{h} + qc\left(\vec{\beta} \times \vec{B}\right) = 0, \tag{3.10}$$

where $\vec{h} = (h_x, h_y, 0) = (1/\rho_x, 1/\rho_y, 0)$ is already introduced in Eq. (3.4) as the inverse of the bending radius.

3.3.1. Bending Magnets (Dipoles)

Vertical magnetic fields leading to momentum changes in the accelerator plane (bending the beam) are present in dipole magnets. The bending radius of a particle with a momentum of $p_x = \gamma m v$ can be expressed by

$$\frac{1}{\rho_x} = \frac{q}{p_x} B_y. \tag{3.11}$$

Note that a vertical magnetic field leads to a change of direction in the accelerator plane (or vice versa). The total reflection angle θ_{bend} can be calculated by integrating over the length of the dipole magnet

$$\theta_{\text{bend}} = \int \frac{\mathrm{d}s}{\rho} = \int B\frac{q}{p}\mathrm{d}s = \frac{q}{p}BL, \tag{3.12}$$

where L denotes the length of the magnet. Dipole magnets appear in particle accelerators in arcs to bend the beam on a circular path. In addition, smaller dipole magnets, also called steerer magnets, are used to correct the trajectory from the deviation of the ideal path.

3.3.2. Focusing Magnets (Quadropoles)

The next important family of magnets are quadrupole magnets, which have two north and two south poles. Due to the natural inherent divergence of a charged particle beam, focusing magnets like quadrupoles are necessary. In a quadrupole, the magnetic field increases with increasing radius from the magnetic center. The magnetic field lines of a quadrupole magnet are shown in Figure 3.2b. The deflection angle can be calculated via

$$\alpha = -\frac{L}{\rho} = \frac{qc}{\beta E} B(r) L = -\frac{qc}{\beta E} g r L, \tag{3.13}$$

where L denotes the path length of the particle through the magnetic field $B(r)$. The energy of the particle is given by E and the magnetic field is given by

$$B(r) = \frac{\mathrm{d}B(r)}{\mathrm{d}r} r = g r, \tag{3.14}$$

where r denotes the radial distance from the magnetic center of the quadrupole magnet. The dependency of the deflection angle α with respect to the increasing magnetic field in the outer regions of the quadrupole is shown in Figure 3.2a.

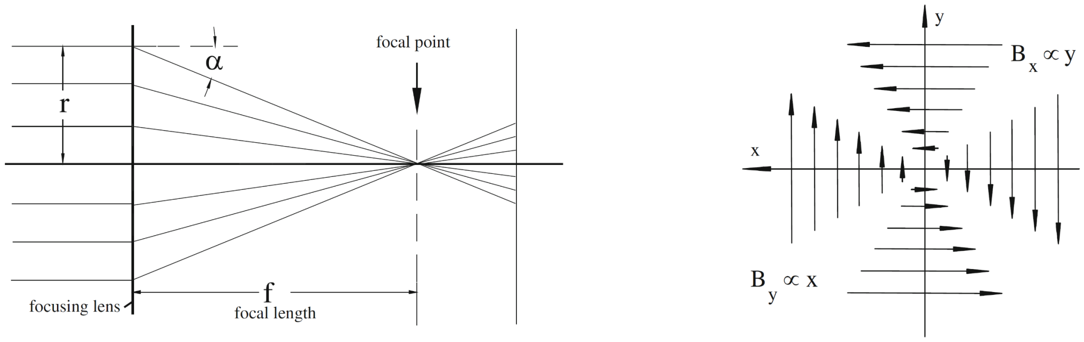

(a) Focusing properties of a quadrupole. (b) Magnetic field patterns of a quadrupole.

Figure 3.2.: The left panel depicts the focusing properties of a quadrupole magnet with increasing deflection angle for outer particles. The right panel shows the magnetic field lines of a quadrupole. Taken from [45].

The linear dependence of the magnetic field with increasing distance from the magnetic center is obtained from the scalar potential $V = -gxy$. The derived fields are given by

$$-\frac{\partial V}{\partial x} = B_x = gy, \tag{3.15}$$

$$-\frac{\partial V}{\partial y} = B_y = gx. \tag{3.16}$$

As a consequence, the focusing strength of a quadrupole is given by

$$k = \frac{q}{p}g = \frac{qc}{\beta E}g, \tag{3.17}$$

which leads to the definition of the focal length

$$f = \frac{1}{kL}. \tag{3.18}$$

In this manner, the quadrupole magnet deflects particles that are not horizontally aligned in the magnet towards the center, creating a focusing effect. Simultaneously, any particle not vertically centered will be diverted away from the magnet's center. Therefore, a combination of focusing and defocusing magnets is required to achieve a net focusing effect in both horizontal and vertical planes.

3.3.3. Equations of Motion

There are several ways to derive the equations of motion of particles using the Lorentz force or the Lagrangian or Hamiltonian in curvilinear coordinates. In this section, the derivation is only outlined. The full derivations can be looked up in [43].

The Lorentz force can be used as an ansatz to derive the equations of motion. As only a pure magnetic accelerator is assumed, the Lorentz force is reduced to

$$m\ddot{\vec{r}}(s) = q\left(\dot{\vec{r}}(s) \times \vec{B}\right). \tag{3.19}$$

The derivatives of $\vec{r}$ as defined in Eq. (3.8) are given by

$$\dot{\vec{r}}(s) = \dot{x}\vec{e}_x + \dot{y}\vec{e}_y + \left(1 + \frac{x}{\rho}\right)\dot{s}\vec{e}_s, \tag{3.20}$$

$$\ddot{\vec{r}}(s) = \left[\ddot{x} - \left(1 + \frac{x}{\rho}\right)\frac{\dot{s}^2}{\rho}\right]\vec{e}_x + \ddot{y}\vec{e}_y + \left[\frac{2}{\rho}\dot{x}\dot{s} + \left(1 + \frac{x}{\rho}\right)\ddot{s}\right]\vec{e}_s. \tag{3.21}$$

Since the arc length s, rather than the time t is the independent variable, the time derivatives get replaced by derivatives with respect to the arc length s

$$\frac{\mathrm{d}x}{\mathrm{d}t} = \dot{x} \rightarrow \frac{\mathrm{d}x}{\mathrm{d}s} = x', \tag{3.22}$$

transforming the derivatives of $\vec{r}$ into

$$\dot{\vec{r}}(s) = x'\dot{s}\vec{e}_x + y'\dot{s}\vec{e}_y + \left(1 + \frac{x}{\rho}\right)\dot{s}\vec{e}_s, \tag{3.23}$$

$$\begin{aligned}\ddot{\vec{r}}(s) = &\left[x''\dot{s}^2 + x'\ddot{s} - \left(1 + \frac{x}{\rho}\right)\frac{\dot{s}^2}{\rho}\right]\vec{e}_x + \left(y''\dot{s}^2 + y'\ddot{s}\right)\vec{e}_y \\ &+ \left[\frac{2}{\rho}x'\dot{s}^2 + \left(1 + \frac{x}{\rho}\right)\ddot{s}\right]\vec{e}_s.\end{aligned} \tag{3.24}$$

Using Eq. (3.19) and (3.24) the famous Hill equations can be derived

$$x''(s) + \left(\frac{1}{\rho^2(s)} - k(s)\right)x(s) = \frac{1}{\rho(s)}\frac{\Delta p}{p_0}, \tag{3.25}$$

$$y''(s) + k(s)y(s) = 0, \tag{3.26}$$

where $x(s)$ and $y(s)$ describe the transverse deviations of the particle in horizontal and vertical directions with respect to the reference particle's trajectory. The bending radius $\rho(s)$ and the focusing strength $k(s)$ were introduced in previous sections. Lastly, a final term taking the dispersive effects (off-momentum particles with respect to the reference momentum $p_{\text{off}} = \Delta p + p_0$) are also taken into account. In a horizontal focusing lattice ($k > 0$), the beam gets simultaneously defocused in the vertical direction. Therefore, horizontal focusing and defocusing magnets are necessary to achieve net focusing effects.

Neglecting dispersive effects ($\Delta p = 0$) reduces Hill's equations to second-order homogeneous differential equations of the form

$$x''(s) + K(s)x(s) = 0 \text{ with } K(s) = \frac{1}{\rho^2(s)} - k(s), \tag{3.27}$$

$$y''(s) + k(s)y(s) = 0. \tag{3.28}$$

The general solutions, being similar to the solution of a harmonic oscillator, of both equations are identical since they both have the same structure. Using the following ansatz

$$x(s) = \sqrt{\epsilon\beta(s)}\cos\left(\Psi(s) + \Psi_0\right), \tag{3.29}$$

where $\beta(s)$ and $\Psi(s)$ denote the so-called betatron function and the betatron phase, respectively. The amplitude of the oscillation is given by $\sqrt{\epsilon\beta(s)}$. The emittance ϵ and the betatron

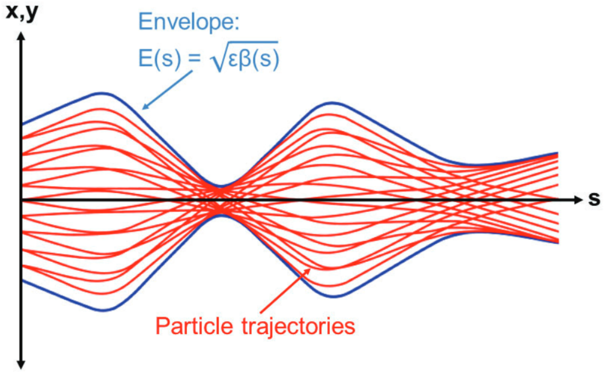

Figure 3.3.: Transverse motion (in x and y) of a particle beam limited be the envelope $E(s) = \sqrt{\epsilon_{\max}\beta(s)}$. Taken from [46].

function $\beta(s)$ will be discussed in further detail in the following section. Since the coefficient $K(s)$ describes the magnetic layout of the circular accelerator, it is periodic with respect to C, where C describes a periodic length

$$K(s + C) = K(s). \tag{3.30}$$

The emittance is a unique quantity for a particle in an ensemble of particles. The envelope $E(s)$ of a particle beam is defined by the particle with the largest emittance. Figure 3.3 shows the transverse motion of a particle beam with a maximum oscillation amplitude being the envelope.

3.3.4. Beam Emittance and Betatron Tune

Using the solution of Hill's Equation (3.29), its first derivative, and considering only conservative forces, the betatron phase Ψ_0 drops out, leading to the following equation defining an ellipse

$$\gamma(s) = x^2(s) + 2\alpha(s)x(s)x'(s) + \beta(s)x'(s) = \epsilon = \text{const.} \tag{3.31}$$

The area of this ellipse, $F = \pi\epsilon$, remains constant, but the orientation of the ellipse varies at each position of the accelerator. The parameter ϵ exemplifies Liouville's theorem [47], which states that the six-dimensional phase space is conserved. The optical functions $\alpha(s)$ and $\gamma(s)$ are given by

$$\alpha(s) = -\frac{\beta'(s)}{2}, \tag{3.32}$$

$$\gamma(s) = \frac{1 + \alpha^2(s)}{\beta(s)}, \tag{3.33}$$

and are also called Twiss parameters. The Twiss parameters describe the emittance of a particle at position x and angle x' at each position s in the ring.

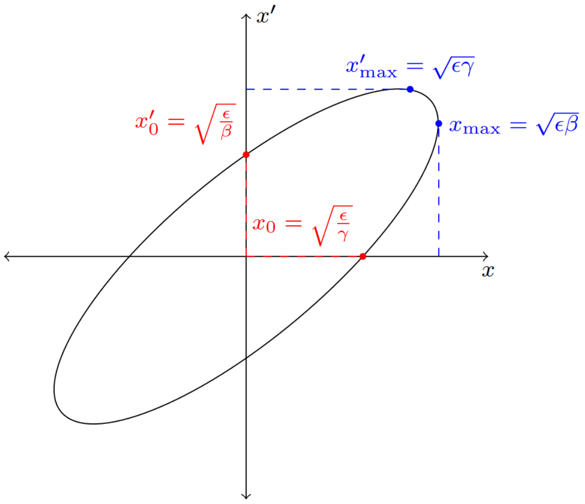

Figure 3.4.: Phase Space Ellipse of transverse deviation x and momentum deviation x'. According to Liouville's theorem, the area $F = \pi\epsilon$ stays constant while the orientation of the ellipse varies along the ring position s. Taken from [44].

Related to the betatron function $\beta(s)$ is the so-called betatron tune. The betatron tune is defined as the number of betatron oscillations per turn in the ring and can be calculated as

$$Q = \frac{1}{2\pi}\int_s^{s+C} \psi' \mathrm{d}s = \frac{1}{2\pi}\int_s^{s+C} \frac{\mathrm{d}s}{\beta(s)}, \tag{3.34}$$

where C denotes the periodicity of the ring. Note that the oscillation amplitude is an intrinsic property of each particle, as depicted in Figure 3.3. Errors in the quadrupole field distribution can distort the motion of the beam. These errors are closely linked to the betatron motion, resulting in alterations to the β-functions and tunes. Small adjustments in the tune can be reasonably estimated by [48]

$$\Delta Q = \frac{1}{4\pi}\oint \beta(s)\Delta K(s)\mathrm{d}s, \tag{3.35}$$

where ΔK describes the variation in the quadrupole strength function $K(s)$ due to field errors.

3.3.5. Chromaticity

Particles deviating in momentum from the reference momentum p_0 experience a slightly varied quadrupole strength compared to the reference particle, resulting in different focusing. The phenomenon of chromatic aberration, familiar from optics, manifests this error. Figure 3.5 displays this effect, with the focusing quadrupole.

Starting from quadrupole strength with a particle off-momentum $p = p_0 + \Delta p$

$$k(p) = -\frac{q}{p}g = -\frac{q}{p_0 + \Delta p}g \approx -\frac{q}{p_0}\left(1 - \frac{\Delta p}{p_0}\right)g = k_0 - \Delta k. \tag{3.36}$$

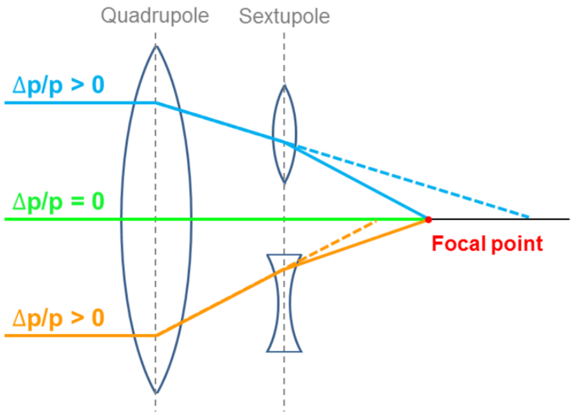

Figure 3.5.: The influence of the momentum-dependent variation in the focusing strength of a quadrupole is called chromaticity. Sextupoles generate quadrupole components depending on the radial position of particles. When placed in dispersive regions, these sextupoles can correct the chromaticity effect. Taken from [49].

A momentum deviation is equivalent to a quadrupole field error

$$\Delta k = \frac{\Delta p}{p_0} k_0. \tag{3.37}$$

As the particle maintains its momentum deviation across numerous turns, every quadrupole adds the same error to the particle's trajectory. Consequently, the overall tune shift is calculated by integrating across all quadrupoles within the accelerator and using Eq. (3.35). This dimensionless quantity,

$$\zeta = \frac{\Delta Q}{\Delta p/p_0} = \frac{1}{4\pi} \oint k(s)\beta(s)\mathrm{d}s, \tag{3.38}$$

is called natural chromaticity and increases with increasing focusing strength $k(s)$. The primary influences originate from quadrupoles characterized by significant focusing strengths, particularly in regions where the betatron function is substantial, such as dispersive regions. Given that a tune shift might result in an operational point coinciding with optical resonances [45], leading to particle losses, compensation for chromaticity becomes imperative. To address this, corrections are implemented at locations where particles diverge based on their momenta—specifically, positions featuring non-zero dispersion. Sextupole magnets are strategically placed at these positions, possessing a focusing strength chosen to counteract chromatic effects.

3.4. Longitudinal Motion

The longitudinal motion of the particle beam phase space is mainly driven by dispersive effects and synchrotron motion.

3.4.1. Dispersion

The longitudinal motion of the beam is primarily influenced by the longitudinally oscillating accelerating electric field of the cavity. Particles in the circulating beam must arrive with a fixed phase in relation to the accelerating frequency for successful acceleration and bunching. Therefore, the cavity frequency needs to be an integer multiple of the revolution frequency. This poses a challenge as the cavity frequency (and the magnetic field in the dipoles) needs to be adjusted while accelerating the particle beam, hence the name synchrotron. Orbit lengthening due to dispersive effects leads to momentum deviations, which affect the revolution frequency according to the following relation

$$\frac{\Delta f}{f_0} = \frac{\Delta L}{L_0} - \frac{\Delta v}{v_0}. \tag{3.39}$$

The change in revolution frequency when changing the momentum of a particle can be rewritten as

$$\frac{\Delta f}{f_0} = \left(\alpha_p - \frac{1}{\gamma_0^2}\right)\frac{\Delta p}{p} = \eta_{\mathrm{slip}}\frac{\Delta p}{p}, \tag{3.40}$$

where η_{slip} is called the slip factor. The momentum-dependent path-length change of the particle with respect to the reference orbit L_0 can be described by the momentum compaction factor α_p

$$\alpha_p = \frac{1}{L_0}\int_0^{L_0} \frac{D(s)}{\rho(s)}\mathrm{d}s. \tag{3.41}$$

The dispersion is contingent upon the particle's curvature $K(s)$ Eq. (3.30), relying on the bending powers of the main dipoles designed for particles possessing different momenta.

3.4.2. Synchrotron Oscillations

Synchrotron oscillations occur when particles arrive too late or too early at the accelerating cavity. The energy gain per revolution in the cavity is given by

$$\Delta E_s = qU_0 \sin\left(\phi_s\right), \tag{3.42}$$

where ϕ_s denotes the phase at which the reference particle is supposed to arrive at the cavity. Deviations from this phase, $\Delta\phi = \phi_{\mathrm{particle}} - \phi_s$, lead to oscillations in the longitudinal phase space. The differential equation describing these oscillations is given by [48]

$$\frac{\mathrm{d}^2}{\mathrm{d}t}\Delta\phi + \frac{h\eta\omega_s^2}{2\pi p_s v_s} qU_0 \cos\left(\phi_s\right)\Delta\phi = \frac{\mathrm{d}^2}{\mathrm{d}t}\Delta\phi + \omega_{\mathrm{syn}}^2\Delta\phi = 0. \tag{3.43}$$

The oscillation frequency of the longitudinal oscillation is given by $f_{\mathrm{sym}} = \omega_{\mathrm{syn}}/2\pi$. The number of oscillations per turn can be written as

$$Q_{\mathrm{syn}} = \frac{\omega_{\mathrm{syn}}}{2\pi f_{\mathrm{COSY}}}, \tag{3.44}$$

where f_{COSY} denotes the revolution frequency of the beam.

3.5. Orbit Correction

Building an accelerator without any imperfections is impossible, inevitably leading to alignment and field errors. To mitigate these effects, accelerator designers install steerer correction magnets. These magnets are used for both horizontal and vertical correction. The corrective influence of these magnets can be mathematically expressed by the following equation [45]

$$\Delta u_i = \frac{\beta_i}{2\sin(\pi Q)} \sum_{k=1}^{n} \theta_k \sqrt{\beta_k} \cos(\Psi_i - \Psi_k - \pi Q). \tag{3.45}$$

Here, Δu_i denotes the alteration in orbit observed at the ith Beam Position Monitor (BPM), influenced by the beta functions (β) and betatron phases (Ψ) at both the BPM location and the steerer magnets. The steerer magnets introduce a correction with a kick of θ_k. The summation encompasses all steerer magnets indexed by n. Furthermore, the equation incorporates the betatron tune Q. It is important to note that this equation assumes no coupling between planes and no dispersion. The steerer magnets' kick angles θ can be calculated by measuring the change in orbit at each beam position monitor u_i. For m beam position monitors and n steerer magnets, the relation between orbit deviation at the ith beam position and steerer kick angle θ_k can be expressed as a matrix equation of the form

$$\begin{pmatrix} \Delta u_1 \\ \Delta u_2 \\ \vdots \\ \Delta u_m \end{pmatrix} = \begin{pmatrix} M_{11} & M_{12} & \dots & M_{1n} \\ M_{21} & M_{22} & \dots & M_{2n} \\ \vdots & \vdots & \ddots & \vdots \\ M_{m1} & M_{m2} & \dots & M_{mn} \end{pmatrix} \begin{pmatrix} \theta_1 \\ \theta_2 \\ \vdots \\ \theta_n \end{pmatrix}. \tag{3.46}$$

The matrix $\mathbf{M}$ is also called the Orbit Response Matrix. The Orbit Response Matrix entries can be calculated via

$$M_{ik} = \frac{\sqrt{\beta_i}\sqrt{\beta_k}}{2\sin(\pi Q)} \cos\left(\Psi_i - \Psi_k - \pi Q\right). \tag{3.47}$$

By inverting the Orbit Response Matrix, the steerer magnet corrector kicks can be calculated as

$$\vec{\theta} = -\mathbf{M}^{-1}\vec{u}. \tag{3.48}$$

However, in most accelerators, the number of beam position monitors is not equal to the number of steerer magnets, making the inversion of the Orbit Response Matrix with classical tools impossible. In this case, methods like Singular Value Decomposition solve the issue approximately.

The importance of Orbit Correction becomes evident when studying its effects in spin tracking simulations. In short, the Electric Dipole Moment leads to a buildup of the vertical polarization component on a longitudinally polarized beam. However, stray fields and other imperfections can mimic this effect. These imperfections lead to a deviation of the transverse orbit, which can be quantified with the root mean square value measured at the beam position monitors. The buildup $|S_y|$ as a function of the distorted vertical orbit is shown in Figure 3.6. In the case of a vertical orbit RMS of $\Delta y_{\mathrm{RMS}} = 1.6\,\mathrm{mm}$, the buildup to an Electric Dipole Moment

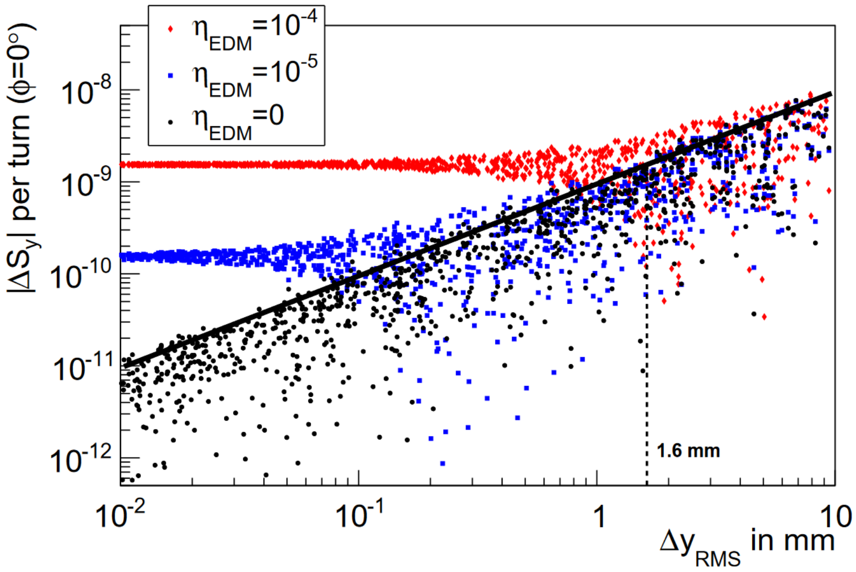

Figure 3.6.: The simulation studies the absolute average change in the vertical spin component, denoted as $|\Delta S_y|$, per turn. This analysis is conducted in relation to varying Δy_{RMS} values within a simulation setting. These different Δy_{RMS} values are generated through randomized Gaussian shifts in vertical quadrupoles. The simulation also considers different magnitudes of the Electric Dipole Moment. The solid line represents the 90 % upper confidence limit for purely misaligned conditions. The dashed line corresponds to the point where the signal induced by misalignments matches an Electric Dipole Moment signal with an associated Electric Dipole Moment value $\eta_{\mathrm{EDM}} = 10^{-4}$ while maintaining an initial Wien filter phase with respect to the spin precession frequency of $\phi_{\mathrm{rel.}} = 0°$. More information about the phase feedback is provided in section 6.7. Taken from [50].

of $\eta_{\mathrm{EDM}} = 10^{-4}$ cannot be distinguished from a buildup due to accelerator imperfections [50]. The orbit RMS for the horizontal and vertical plane is given by

$$\Delta x_{\mathrm{RMS}} = \sqrt{\frac{1}{n_x}\sum_{i\in\mathrm{BPMs}} x_i^2} \text{ and } \Delta y_{\mathrm{RMS}} = \sqrt{\frac{1}{n_y}\sum_{i\in\mathrm{BPMs}} y_i^2}, \tag{3.49}$$

where x_i and y_i denote the beam position in the horizontal and vertical plane, measured using the ith beam position monitor. The total number of horizontal and vertical orbit measurements is given by n_x and n_y.

4. Spin Dynamics in Storage Rings

The so-called EDM Precursor experiments in COSY are conducted using polarized deuteron beams. In the following section, the theoretical background of polarized beams inside a storage ring is described. As COSY is a fully magnetic machine, the discussion focuses on the equation of motions for the spin in magnetic machines.

4.1. Polarization

For a collection of particles with spins, the polarization of the ensemble is defined as the average orientation of those spins along a particular axis. In quantum systems, the spin defines the unique quantization axis. Consequently, other vectorial attributes of the system, such as the magnetic moment or the Electric Dipole Moment, must align with this axis. The spin of a single particle can have different configurations relative to its quantization axis which is by convention the z-axis in a Cartesian coordinate system. The projection of the spin along the z-axis can be described by the operator $S_z = m\hbar$, where $\hbar$ denotes the reduced Planck's constant and m is the associated spin quantum number. For a particle with the spin quantum number s, $(2s+1)$ different configurations for m can be found taking the following values: $m \in \{-s, -s+1, \dots, s-1, s\}$. A schematic configuration for spin-1/2-particles ($m \in \{-1/2, 1/2\}$) and spin-1-particles ($m \in \{-1, 0, 1\}$) is shown in Figure 4.1. In this section, a mathematical description of the beam polarization based on the spin formalism is given for spin-1/2 particles (Fermions) as well as spin-1 particles (Bosons). The definitions of the polarization used in sections 4.1.1 and 4.1.2 are taken from [51].

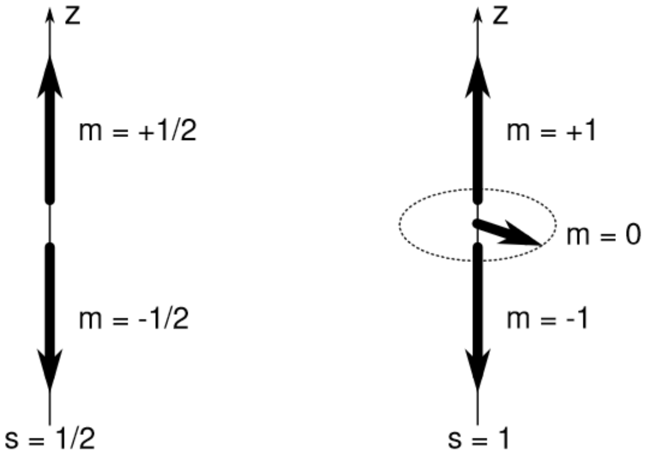

Figure 4.1.: Configurations of the spin quantum number m for spin-1/2 particles (left) and spin-1 particles (right). Taken from [52].

4.1.1. Spin-1/2-Particles

Particles with half-integer spin ($s = 1/2$) like electrons and protons are also called fermions and can only be in the states $m = \pm 1/2$. They can be characterized by two-component normalized Pauli spinor ψ

$$\psi = \begin{pmatrix} u \\ d \end{pmatrix}. \tag{4.1}$$

The two compex amplitudes u and d satisfy the normalization condition $|u|^2 + |d|^2 = 1$. In quantum mechanics, a measurement of an observable is given by the expectation value of a hermitian operator $\hat{A}$

$$\langle \hat{A} \rangle = \langle \psi | \hat{A} | \psi \rangle = \psi^\dagger \hat{A} \psi. \tag{4.2}$$

For simplification, the matrix ρ can be defined for spin-1/2 particles as

$$\rho = |\psi\rangle\langle\psi| = \begin{pmatrix} |u|^2 & ud^* \\ u^*d & |d|^2 \end{pmatrix}, \tag{4.3}$$

where the star denotes the complex conjugate of the variable. The expectation value of an observable can then be rewritten as

$$\langle \hat{A} \rangle = \mathrm{Tr}(\rho \hat{A}). \tag{4.4}$$

In a cartesian coordinate system $(\vec{e_x}, \vec{e_y}, \vec{e_z})$, the two components of the spinor correspond to the two different spin states along the quantization axis, which can be arbitrarily chosen as $\vec{e_z}$. A spin measurement corresponds to the hermitian operator

$$\hat{\vec{S}} = \frac{\hbar}{2}\vec{\sigma}, \tag{4.5}$$

where $\vec{\sigma} = (\sigma_1, \sigma_2, \sigma_3)$ denotes the vector of the Pauli matrices

$$\sigma_1 = \begin{pmatrix} 0 & 1 \\ 1 & 0 \end{pmatrix}, \quad \sigma_2 = \begin{pmatrix} 0 & -i \\ i & 0 \end{pmatrix}, \text{ and } \sigma_3 = \begin{pmatrix} 1 & 0 \\ 0 & -1 \end{pmatrix}. \tag{4.6}$$

For completion, the *0*th Pauli matrix is also referred to as the identity matrix

$$\sigma_0 = \begin{pmatrix} 1 & 0 \\ 0 & 1 \end{pmatrix}. \tag{4.7}$$

The spin vector $\vec{S} = (S_x, S_y, S_z)$ is defined as the expectation value of the hermitian spin operator $\hat{\vec{S}}$

$$\vec{S} = \left\langle \hat{\vec{S}} \right\rangle = \mathrm{Tr}\left(\rho \hat{\vec{S}}\right) = \frac{\hbar}{2}\mathrm{Tr}\left(\rho\vec{\sigma}\right) = \frac{\hbar}{2}\begin{pmatrix} 2\mathrm{Re}(ud^*) \\ 2\mathrm{Im}(ud^*) \\ |u|^2 - |d|^2 \end{pmatrix}. \tag{4.8}$$

The spin $\vec{S}$ is a property of a single particle. Since billions of particles are injected and stored into the ring, it makes more sense to change to the expectation value of spin observables of an ensemble with a total amount of particles N. The density matrix ρ reads for an ensemble of particles

$$\rho = \frac{1}{N}\begin{pmatrix} \sum\limits_{i=1}^{N} |u^{(i)}|^2 & \sum\limits_{i=1}^{N} u^{(i)} d^{(i)*} \\ \sum\limits_{i=1}^{N} u^{(i)*} d^{(i)} & \sum\limits_{i=1}^{N} |d^{(i)}|^2 \end{pmatrix} = \frac{1}{2}\left(\sigma_0 + \vec{P}\vec{\sigma}\right). \tag{4.9}$$

The polarization vector $\vec{P}$ contains the expectation values of the spin operators in the ensemble of particles

$$\vec{P} = \frac{1}{N}\sum_{i=1}^{N} \vec{S}_i. \tag{4.10}$$

Having an ensemble of N^+ particles in the quantization state $m = +1/2$ and N^- particles in the quantization state $m = -1/2$, the polarization vector along the quantization axis P_V can be written as

$$P_V = \frac{N^+ - N^-}{N^+ + N^-}. \tag{4.11}$$

The polarization vector along the quantization axis of a beam of several spin-1/2-particles can take the following values

$$-1 \leq P_V \leq 1, \tag{4.12}$$

where $P_V = 0$ denotes an unpolarized beam.

4.1.2. Spin-1-Particles

As the quantum number m of a spin-1-particle can take three configurations ($m \in \{-1, 0, 1\}$), a three-dimensional spinor is needed to describe the spin state of an individual particle

$$\psi = \begin{pmatrix} a_1 \\ a_2 \\ a_3 \end{pmatrix}. \tag{4.13}$$

The Pauli matrices get replaced by the following spin operators

$$\hat{S}_1 = \frac{\hbar}{\sqrt{2}}\begin{pmatrix} 0 & 1 & 0 \\ 1 & 0 & 1 \\ 0 & 1 & 0 \end{pmatrix}, \quad \hat{S}_2 = \frac{\hbar}{\sqrt{2}}\begin{pmatrix} 0 & -i & 0 \\ i & 0 & -i \\ 0 & i & 0 \end{pmatrix}, \text{ and } \hat{S}_3 = \hbar\begin{pmatrix} 1 & 0 & 0 \\ 0 & 0 & 0 \\ 0 & 0 & -1 \end{pmatrix}. \tag{4.14}$$

The consequence of the spin-1 operator having three eigenvalues is that the density operator, which was introduced in Eq. (4.3), turns into a 3×3 matrix meaning that nine independent hermitian matrices are required. In addition to the identity matrix $\mathbf{I}$, five further matrices can be defined in Cartesian notation as

$$\hat{S}_{ij} = \frac{3}{2}\left(\hat{S}_i\hat{S}_j + \hat{S}_j\hat{S}_i\right) - 2\mathbf{I}\delta_{ij} \text{ with } i, j \in \{1, 2, 3\}, \tag{4.15}$$

where δ_{ij} denotes the Kronecker delta

$$\delta_{ij} = \begin{cases} 1 & \text{for } i = j \\ 0 & \text{for } i \neq j \end{cases}. \tag{4.16}$$

The results for the operators yield the following density matrix for an ensemble of spin-1 particles

$$\rho = \frac{1}{3}\left[\mathbf{I} + \frac{3}{2}\sum_{i=1}^{3} P_i S_i + \frac{1}{3}\sum_{i=1}^{3}\sum_{j=1}^{3} P_{ij} S_{ij}\right] \text{ with } P_{ij} = P_{ji}. \tag{4.17}$$

The polarization states of the spin-1 particle are given by the parameters P_i and P_{ij}. In an ensemble of spin-1 particles with N^+ particles in the quantization state, $m = +1$, N^0 particles with $m = 0$ and N^- particles in $m = -1$, the vector polarization P_V along the quantization axis is defined in a similar way as for spin-1/2 particles

$$P_V = \frac{N^+ - N^-}{N^+ + N^- + N^0}, \tag{4.18}$$

while the tensor polarization is given by

$$P_T = \frac{N^+ + N^- - 2N^0}{N^+ + N^- + N^0}. \tag{4.19}$$

The connection of the formulas of vector and tensor polarization for spin-1 particles leads to the following boundary of the vector polarization for nontensor components of the beam polarization

$$P_T = 0 \Rightarrow -\frac{2}{3} \leq P_V \leq \frac{2}{3}, \tag{4.20}$$

which means that for spin-1 particles only a maximum vector polarization of $|P_V| \leq 66.6\,\%$ can be measured. However, if tensor components are present in the beam polarization, a vector polarization of $|P_V| = 1$ can be achieved as well.

4.2. The Generalized Thomas-Bargmann-Michel-Telegdi (T-BMT) Equation

In Eq. (2.25), the non-relativistic Hamiltonian for a particle in external electromagnetic fields in its rest frame is introduced, leading to the non-relativistic spin equation of motion

$$\frac{\mathrm{d}\vec{S}}{\mathrm{d}t} = \vec{\Omega} \times \vec{S} = \vec{\mu} \times \vec{B} + \vec{d} \times \vec{E}. \tag{4.21}$$

The Electric Dipole Moment $\vec{d}$ and Magnetic Dipole Moment $\vec{\mu}$ are defined in Eq. (2.13). This differential equation describes the spin precession, perpendicular to $\vec{\Omega}$ with an angular frequency of $|\vec{\Omega}|$. Since external electromagnetic fields are usually described in the laboratory reference frame, Eq. (4.21) needs to be transformed from the particle's rest frame to the laboratory frame, resulting in the so-called Thomas-BMT equation. The generalized form of the Thomas-BMT equation describes the spin motion of relativistic particles in homogeneous electromagnetic fields, including contributions from the Electric Dipole Moment [53]

$$\frac{\mathrm{d}\vec{S}}{\mathrm{d}t} = \vec{\Omega}_{\mathrm{MDM}} \times \vec{S} + \vec{\Omega}_{\mathrm{EDM}} \times \vec{S}, \tag{4.22}$$

$$\vec{\Omega}_{\mathrm{MDM}} = -\frac{q}{m}\left[\left(G+\frac{1}{\gamma}\right)\vec{B} - \frac{G\gamma}{\gamma+1}\left(\vec{\beta}\cdot\vec{B}\right)\vec{\beta} - \left(G+\frac{1}{\gamma+1}\right)\vec{\beta}\times\frac{\vec{E}}{c}\right], \tag{4.23}$$

$$\vec{\Omega}_{\mathrm{EDM}} = -\frac{q}{mc}\frac{\eta_{\mathrm{EDM}}}{2}\left[\vec{E} - \frac{\gamma}{\gamma+1}\left(\vec{\beta}\cdot\vec{E}\right)\vec{\beta} + c\vec{\beta}\times\vec{B}\right]. \tag{4.24}$$

The electric field $\vec{E}$ and magnetic field $\vec{B}$ are evaluated in the curvilinear laboratory reference frame while the spin vector $\vec{S}$ is defined within its rest frame.

4.2.1. Spin Tune and Invariant Spin Axis in a Magnetic Storage Ring

Assuming a beam motion perpendicular to the electromagnetic fields ($\vec{\beta}\cdot\vec{B} = \vec{\beta}\cdot\vec{E} = 0$), subtracting the rotation of the momentum vector in a storage ring and ignoring electric fields (full magnetic ring), the T-BMT equation can be reduced to

$$\vec{\Omega} = \vec{\Omega}_{\mathrm{MDM}} + \vec{\Omega}_{\mathrm{EDM}} = -\frac{q}{m}\left[G\vec{B} + \frac{\eta_{\mathrm{EDM}}}{2}\vec{\beta}\times\vec{B}\right]. \tag{4.25}$$

By applying the following transformations

$$\mathrm{d}l = c\beta\mathrm{d}t, \tag{4.26}$$

$$\vec{S} = S\vec{e}_s, \tag{4.27}$$

the rotation angle is given by

$$\frac{d\vec{S}}{S} = \frac{1}{c\beta}\vec{\Omega}\times\vec{e}_s = \vec{\Omega}'\times\vec{e}_s. \tag{4.28}$$

In the following, $B_\perp$ denotes the vertical magnetic field component (in $\vec{e}_y$), and consequently $\int B\perp \mathrm{d}l$ describes the integral of the magnetic field a particle experiences in one turn around the accelerator. Ignoring the EDM contribution for the moment ($\eta_{\mathrm{EDM}} = 0$), the modified rotation axis can be written as

$$\vec{\Omega}'_{\mathrm{MDM}} = -\frac{1}{c\beta}\frac{q}{m}GB_\perp\mathrm{d}l\cdot\vec{e}_y. \tag{4.29}$$

For a full turn, this can be written as

$$\vec{\Omega}'_{\mathrm{MDM}} = -\frac{1}{c\beta}\frac{q}{m}G\int B_\perp\mathrm{d}l\cdot\vec{e}_y. \tag{4.30}$$

The field integral $\int B_\perp \mathrm{d}l$ can be evaluated by comparing the Lorentz force with the centrifugal force

$$\frac{m\gamma v^2}{r} = qvB_\perp \tag{4.31}$$

$$\frac{m\gamma c\beta}{q} = B_\perp r \tag{4.32}$$

$$\frac{2\pi m\gamma c\beta}{q} = B_\perp 2\pi r. \tag{4.33}$$

The last term describes the ring integral of the vertical magnetic field around the storage ring which can also be written as the integral of the vertical magnetic field along the storage ring

$$\frac{2\pi m\gamma c\beta}{q} = \int B_\perp \mathrm{d}l. \tag{4.34}$$

Using Eq. (4.30) and (4.34) finally leads to

$$\vec{\Omega}'_{\mathrm{MDM}} = -\frac{1}{c\beta}\frac{q}{m}G\frac{2\pi m\gamma c\beta}{q} \cdot \vec{e}_y \tag{4.35}$$

$$= -2\pi\gamma G \cdot \vec{e}_y. \tag{4.36}$$

In an ideal pure magnetic ring with vertical magnetic fields, the spins rotate around the vertical axis ($\vec{e}_y$) by an angle $|\gamma G|$ per turn. This rotation angle of the spin per turn of the beam in the storage ring is also called the spin tune

$$\nu_s = \gamma G. \tag{4.37}$$

The rotation frequency of the spins can be calculated by multiplying the spin tune with the revolution frequency of the beam circulating in the ring

$$f_s = |\nu_s| f_{\mathrm{COSY}} \approx 121\,\mathrm{kHz}, \tag{4.38}$$

using $\gamma \approx 1.126$ and $f_{\mathrm{COSY}} \approx 751\,\mathrm{kHz}$ at $p_d \approx 970\,\mathrm{MeV/c}$, and the gyromagnetic anomaly for deuterons $G \approx -0.142$. Note that the spin tune is a negative quantity, meaning that for a clockwise rotating beam, the spin precesses counterclockwise (and vice versa). The axis around which the spins precess is also called the Invariant Spin Axis. In the case of a pure magnetic ring without an Electric Dipole Moment, the Invariant Spin Axis always points in the vertical direction along the dipole magnet field axis ($\vec{e}_y$) in an ideal storage ring.

4.2.2. Influence of the Electric Dipole Moment on the Spin Motion in a Magnetic Storage Ring

Allowing for a non-zero Electric Dipole Moment, an additional rotation out of the plane needs to be added for the full one-turn rotation

$$\vec{\Omega}'_{\mathrm{EDM}} = -\frac{1}{c\beta}\frac{q}{m}\eta\frac{\beta}{2}\int B_\perp \mathrm{d}l \cdot (\vec{e}_z \times \vec{e}_y) \tag{4.39}$$

$$= \pi\gamma\eta\beta \cdot \vec{e}_x, \tag{4.40}$$

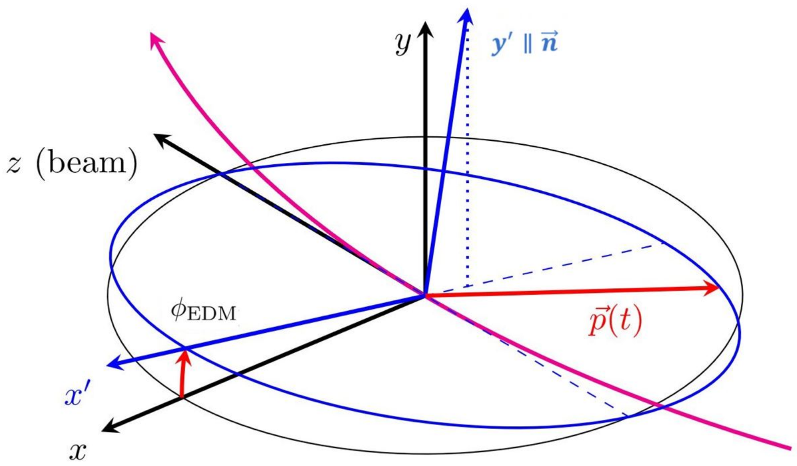

Figure 4.2.: Effects of a non-zero EDM on the spin motion: In an ideal magnetic ring without taking EDM effects of the circulating beam into account, the spin precesses in the $x-z$ plane around the vertical axis. The beam moves along the z axis. A non-zero EDM leads to a rotation of the precession plane by an angle ϕ_{EDM} perpendicular to the beam momentum direction. Figure is adapted from FIG. 1 in [54].

which describes the rotation of the Invariant Spin Axis in radial ($\vec{e}_x$) direction. The tilt angle of the rotation plane with respect to the spin precession plane without EDM ($x-z$) plane, can be calculated using

$$\tan\left(\frac{|\vec{\Omega}'_{\text{EDM}}|}{|\vec{\Omega}'_{\text{MDM}}|}\right) = \tan(\phi_{\text{EDM}}) = -\eta\frac{\beta}{2G} \overset{\phi_{\text{EDM}} \ll 1}{\approx} \phi_{\text{EDM}}. \tag{4.41}$$

To determine the Electric Dipole Moment of the deuteron, the radial component (x) of the so-called Invariant Spin Axis needs to be measured. Note that no longitudinal tilt of the Invariant Spin Axis is expected. The effect of the Electric Dipole Moment is also depicted in Figure 4.2. The black dotted circle shows the spin precession plane without an Electric Dipole Moment. In this case, the vertical y axis coincides with the Invariant Spin Axis $\vec{n}$. A non-zero Electric Dipole Moment rotates the spin precession plane (and the Invariant Spin Axis) by an angle ϕ_{EDM} in the radial direction with respect to the beam momentum vector. In an ideal ring, the Invariant Spin Axis would be constant along the ring. However, field imperfections and orbit distortions add tilts to the Invariant Spin Axis along the ring. In spin tracking simulation studies, these systematic tilts need to be separated from the actual signal of the Electric Dipole Moment.

A non-zero Electric Dipole Moment changes the spin tune

$$2\pi\nu_s^{\text{EDM}} = |\vec{\Omega}'_{\text{EDM}} + \vec{\Omega}'_{\text{MDM}}| = 2\pi\gamma G\sqrt{1+\left(\frac{\eta\beta}{2G}\right)^2}. \tag{4.42}$$

However, this correction term is tiny and can be safely ignored.

4.2.3. Axion or Axion Like Particles Search using Oscillating Electric Dipole Moments

The following section is based on *First Search for Axionlike Particles in a Storage Ring Using a Polarized Deuteron Beam* [26]. The presented limits on the axion-like particle's mass and, conclusively, on the oscillating Electric Dipole Moment are derived by the JEDI collaboration, from data taken during a six-week-long beam time in spring 2019 at the Cooler Synchrotron COSY.

Axions, or axion-like particles (ALPs), are hypothetical particles first proposed in 1977 by Weinberg [55] and Wilczek [56]. Axions were initially postulated to resolve the strong $\mathcal{CP}$ problem in quantum chromodynamics, possessing a strict correlation between their mass m_a and the decay constant f_a. ALPs, on the other hand, do not address the strong $\mathcal{CP}$ problem and lack a strict correlation between their mass and decay constant. However, both types of particles are considered candidates for dark matter. According to the pre-inflationary PQ symmetry breaking, axions were created during the inflation period of the Big Bang, coherently oscillating in a classical scalar field [57]

$$a(t) = a_0 \cos\big(\omega_a(t - t_0) + \phi_a(t_0)\big), \tag{4.43}$$

where a_0 denotes the amplitude of the scalar field and ω_a the angular frequency. The angular frequency of the field can be directly related to the axion mass via

$$\hbar\omega_a = m_a c^2. \tag{4.44}$$

The local phase of the axion or ALP field is given by $\phi_a(t_0)$ and is an unknown quantity which can even change depending on the starting point of the measurement t_0. As a consequence of the axion coupling to the nucleon or the nucleon spin, the Electric Dipole Moment gets an additional oscillating contribution [58, 59]

$$d(t) = d_{\mathrm{dc}} + d_{\mathrm{ac}} \cos\big(\omega_a(t - t_0) + \phi_a(t_0)\big), \tag{4.45}$$

where d_{dc} describes the permanent Electric Dipole Moment which is discussed in the previous section. The spin motion can be calculated using the Thomas-BMT Eq. (4.22) relative to the momentum vector. For simplicity, the terms including $\vec{\beta} \cdot \vec{B}$ and $\vec{\beta} \cdot \vec{E}$ are omitted. The axion enters the spin motion through the time-dependent Electric Dipole Moment contribution $d(t)$ and the so-called axion wind effect [18, 53]

$$\begin{aligned}
\frac{\mathrm{d}\vec{S}}{\mathrm{d}t} &= \vec{\Omega} \times \vec{S} = (\vec{\Omega}_{\mathrm{MDM}} - \vec{\Omega}_{\mathrm{rev}} + \vec{\Omega}_{\mathrm{EDM}} + \vec{\Omega}_{\mathrm{wind}}) \times \vec{S} \text{ with} && (4.46)\\
\vec{\Omega}_{\mathrm{MDM}} &= -\frac{q}{m}\left(G + \frac{1}{\gamma}\right)\vec{B}, && (4.47)\\
\vec{\Omega}_{\mathrm{rev}} &= -\frac{q}{\gamma m}\vec{B}, && (4.48)\\
\vec{\Omega}_{\mathrm{EDM}} &= -\frac{1}{S\hbar} d(t) c\vec{\beta} \times \vec{B}, && (4.49)\\
\vec{\Omega}_{\mathrm{wind}} &= -\frac{1}{S\hbar}\frac{C_N}{2f_a}[\hbar\partial_0 a(t)]\vec{\beta}. && (4.50)
\end{aligned}$$

Through the time derivative $\partial_0 a(t)$, a second oscillating contribution is present called axion-wind, which depends on the coupling strength C_N and the generic axion or ALP decay constant f_a, also called the PQ order parameter. This parameter is crucial for describing the interaction between gluons and nucleons. The torque from axion-wind causes the particles' spins to rotate around an axis parallel to the beam's direction, while the torque from oscillating EDM results in spin rotation about an axis perpendicular to the beam's direction, away from the ring plane, at an oscillation frequency of f_{osc} in both cases, if the resonance condition

$$\frac{c^2 m_a}{\pi} = \gamma G f_{\text{COSY}}, \tag{4.51}$$

is met. By changing the beam momentum γ, it is possible to scan for the axion mass m_a. As soon as the resonance condition is met, a jump is expected from the in-plane polarization into the vertical component. By changing the beam momentum, the dipole magnetic fields also need to be adjusted to keep the particle orbit stable.

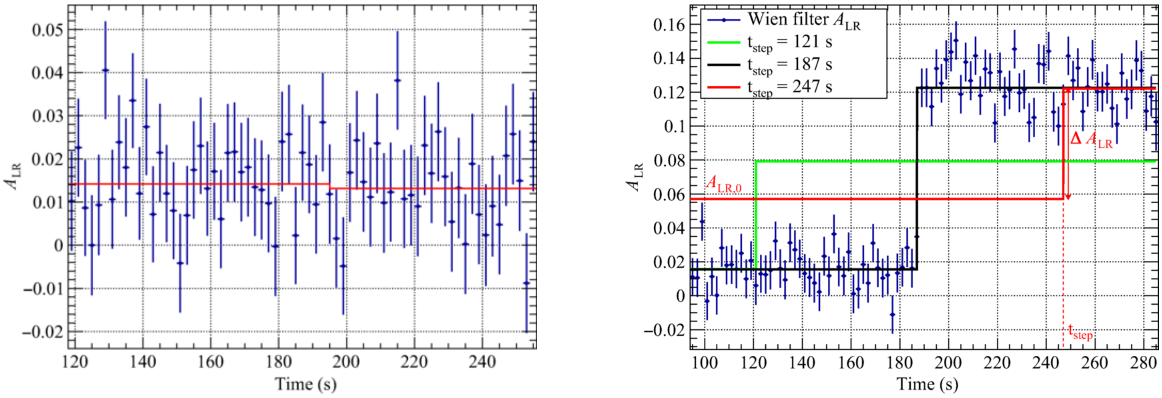

(a) Axion Scan

(b) Artificial Axion Scan using the RF Wien filter

Figure 4.3.: The left-right asymmetry, which is proportional to the vertical polarization (cf. section 6.4), varies as a function of time. **Left:** During the measurement of the left-right asymmetry, the beam momentum is changed, scanning for the axion mass. As soon as the resonance condition is met, a sudden jump of the vertical polarization is expected, as shown in the right panel. **Right:** Here the RF Wien filter is used as an artificial axion signal. Step functions are fitted to search for this jump. Taken from [26].

Such a scan is shown in Figure 4.3a. The left-right asymmetry measured using an internal polarimeter in COSY, which is proportional to the vertical polarization (cf. section 6.4), is plotted as a function of time. The polarization is rotating in the horizontal plane with the spin precession frequency f_s. By changing the cavity frequency, the particles are slightly accelerated, which increases the gamma factor. As soon as the resonance condition is met, a sudden jump appears, as shown in Figure 4.3b. Here, the RF Wien filter is used as an additional spin rotator. Because of the unknown phase of the axion fields, four bunches are co-rotating in the accelerator, each with a different direction.

The left-right asymmetry is fitted using a step function with a step at a fixed time in the cycle. The time is varied through all bins. The change of polarization shown in Figure 4.3a yields results consistent with zero. In total, 103 ramps were measured, covering a spin precession range from 119 997 to 121 457 Hz, and hence an axion mass of 4.95 to 5.02 neV/c^2. No signal was observed.

The construction of the 90 % confidence limit is based on the sensitivity of the measured jumps of vertical polarization and Feldman-Cousin intervals. The limits as a function of spin precession frequency (or scanned axion mass) are shown in Figure 4.4. The green data points are taken with a slower ramp speed than the blue data points. The sensitivity depends mostly on the luminosity of the particle beam. If more deuterons are injected into COSY and scattered into the polarimeter, the statistical uncertainty is lower for the step fits.

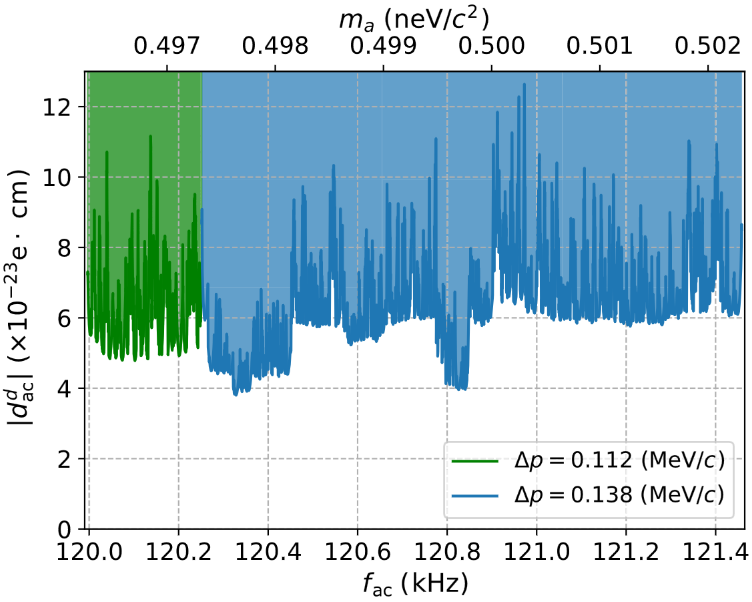

Figure 4.4.: Exclusion plot of the ALP-induced oscillating EDM for the 90 % confidence level sensitivity in an axion mass range from 4.95 to 5.02 neV/c^2 for two different momentum ramp speeds Δp. Taken from [26].

The averaged upper limit on the oscillating amplitude of the Electric Dipole Moment is given by

$$|d^d_{\text{ac}}| < 6.4 \times 10^{-23}\,\text{e} \cdot \text{cm}\ (90\,\%\ \text{C.L.}). \tag{4.52}$$

This experimental value can be used to derive limits on various coupling constants of axion-like particles. A limit of the axion coupling to the deuteron EDM operator $g_{ad\gamma}$ can be set to

$$|g_{ad\gamma}| < 1.7 \times 10^{-7}\,\text{GeV}^2. \tag{4.53}$$

Also, the coupling of axion-like particles to gluons can be constrained to

$$\left|\frac{C^d_G}{f_a}\right| < 0.46 \times 10^{-4}\,\text{GeV}^{-1}. \tag{4.54}$$

4.3. Polarimetry

The notation and coordinate system conventions described in the upcoming section are taken from [60, 61].

To describe the cross-section of a spin-1 beam hitting an unpolarized target, two distinct coordinate systems are needed. The first coordinate system describes the orientation of the incoming spin component, which is also illustrated in Figure 4.5a. When considering the momentum vectors of the incident particle ($\vec{p}_{\text{in}}$) and the outgoing particle ($\vec{p}_{\text{out}}$), the z-axis aligns with $\vec{p}_{\text{in}}$, while the y-axis aligns with the cross product of $\vec{p}_{\text{in}}$ and $\vec{p}_{\text{out}}$. The x-axis completes a right-handed coordinate system with the other two axes. The target is located at $(0, 0, 0)$. In this context, Φ represents the angle between the spin axis projected into the x-y-plane, and Θ represents the angle between the spin axis and the z-axis.

The differential cross-section for the elastic scattering process of polarized spin-1 particles onto an unpolarized (carbon) target, in units of the unpolarized differential cross-section σ_0, can be written as

$$\frac{\sigma}{\sigma_0} = 1 + \frac{3}{2} p_y A_y(\theta) + \frac{2}{3} p_{xz} A_{xz}(\theta) + \frac{1}{3}\big(p_{xx} A_{xx}(\theta) + p_{yy} A_{yy}(\theta) + p_{zz} A_{zz}(\theta)\big), \tag{4.55}$$

where p_i denotes the components of the deuteron vector polarization and p_{ik} the Cartesian components of the deuteron tensor polarization, with $i, k \in \{x, y, z\}$. In addition, the vector and tensor analyzing powers of the spin-1 particles are given by A_i and A_{ik}, respectively. Relative to the fixed Cartesian coordinate system, the scattering angles of the outgoing particles are defined in spherical coordinates $\vartheta(\theta, \phi)$.

Notably, the left side of the detector corresponds to $\phi = 0°$, the right side to $\phi = 180°$, the upward direction to $\phi = 270°$, and the downward direction to $\phi = 90°$. The scattering angle θ is located in the x-z plane (cf. Figure 4.5b).

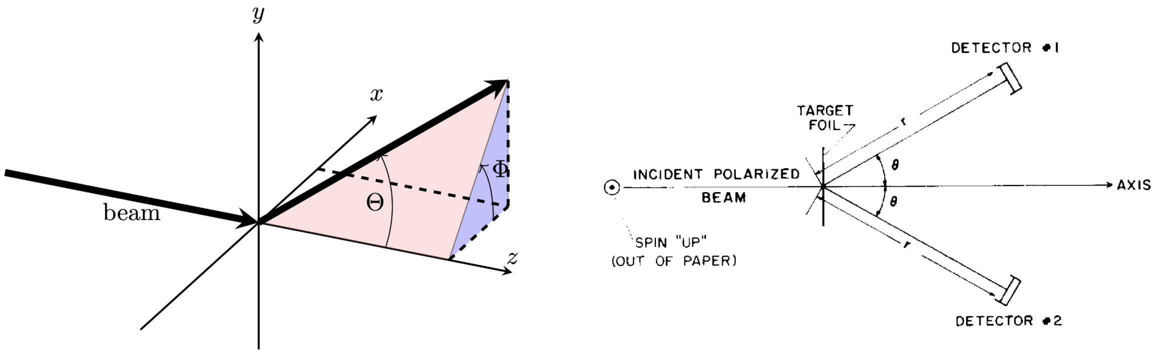

(a) Spin angles $S = (\Theta, \Phi)$.

(b) Scattering Angle θ

Figure 4.5.: Cartesian coordinate system for polarimetry. The left panel shows the spin configuration angle at the target $S = (\Theta, \Phi)$. The right panel shows the experimental setup with the scattering angle θ. The polar angle ϕ describes the angle out or in the plane. Taken from [60, 62].

The atomic beam source provides first p_Z and second-rank p_{ZZ} polarizations relative to the quantization axis S. The vector polarization p_Z of a spin-1/2 of a spin-1 beam can take values between -1 and 1. The tensor polarization is between -2 and 1 for a spin-1 particles. A spin-1/2 can not have a tensor component. Throughout this experiment, deuterons (spin-1 particles) only having vector polarization are used, which reduces Eq. (4.55) to

$$\frac{\sigma}{\sigma_0} = 1 + \frac{3}{2} p_y A_y(\theta). \tag{4.56}$$

In the given coordinate system, the vertical component can be written as

$$p_y = p_Z \sin(\Theta) \sin(\Phi - \phi). \tag{4.57}$$

Using Eq. (4.55) and (4.57) yields

$$\frac{\sigma}{\sigma_0} = 1 + \frac{3}{2} p_Z A_y \sin(\Theta) \sin(\Phi - \phi). \tag{4.58}$$

- **Vertical Polarization:** The beam is vertically polarized when the spin vector points in $S = (\Theta, \Phi) = (\pi/2, 0)$. The cross-section becomes

$$\frac{\sigma}{\sigma_0} = 1 + \frac{3}{2} p_Z A_y \cos(\phi). \tag{4.59}$$

- **Horizontal Polarization:** In section 4.2.1, the spin tune was introduced, denoting the angular frequency of the horizontal spin precession $\Omega_s = 2\pi f_{\mathrm{COSY}} \nu_s$. In the case of a horizontally polarized beam rotating in the accelerator plane, the spin vector S can be written as $S = (\Theta, \Phi) = (\Omega_s t, 0)$. The cross-section is given by

$$\frac{\sigma}{\sigma_0} = 1 - \frac{3}{2} p_Z A_y \sin(\Omega_s t) \sin(\phi). \tag{4.60}$$

5. Experimental Setup

The experiments described in this thesis were conducted at the Cooler Synchrotron (COSY) at Forschungszentrum Jülich. In this section, an overview of the accelerator facility is given, along with all the devices that are relevant to this thesis.

5.1. The Cooler Synchrotron COSY - Overview

The facility encompasses more than just the COSY ring. It consists of various sections, each serving a distinct purpose. Initially, the H^- and D^- negative ions are extracted from the sources and directed to the cyclotron through the Source beamline (SBL). The particle sources differ for polarized and unpolarized particles due to the need for a small collider in the production of polarized beams. Within the cyclotron, the beams undergo acceleration to reach their designated injection kinetic energy of 45 MeV (momentum $p = 295\,\mathrm{MeV}$) for H^- ions and 76 MeV($p = 540\,\mathrm{MeV}$) for D^- ions. Subsequently, they traverse the Injection beamline (IBL) and are injected into COSY utilizing a charge-exchange injection system. In the main ring, with a circumference of 184 m, the particles can be accelerated up to a momentum of 3.7 GeV. In addition, two Stochastic Coolers (for vertical and horizontal phase space cooling each) and two Electron Coolers provide excellent beam conditions for experiments. To manipulate the polarization of the bunched, polarized beams, an RF Solenoid, a Siberian Snake, and an RF Wien filter are available. The polarization can be measured at two different polarimeters in the ring, namely WASA (Wide Angle Shower Apparatus) and JePo (JEDI Polarimeter). Three additional extraction beamlines are available for experiments in external areas [63]. For the experiment reported in this thesis, only the two internal experiments are relevant. An overview of the facility is shown in Figure 5.1

5.2. Beam Sources and Pre-Accelerator

In this section, a short overview of the beam sources providing polarized and unpolarized protons and deuterons for the experiments, and the pre-accelerator JULIC of the facility is given.

5.2.1. Beam Sources

The initial phase of particle travel starts in the beam source, where three specialized ion sources are utilized — two for unpolarized beams and one for polarized beams (cf. Figure 5.2). To function as an injector in COSY, the beam needs pulsing with a maximum repetition rate of 0.5 Hz and a macro-pulse duration ranging from 10 to 20 ms. While most cyclotron systems operate continuously, macro-pulsing is achieved by modulating the extraction voltage in the

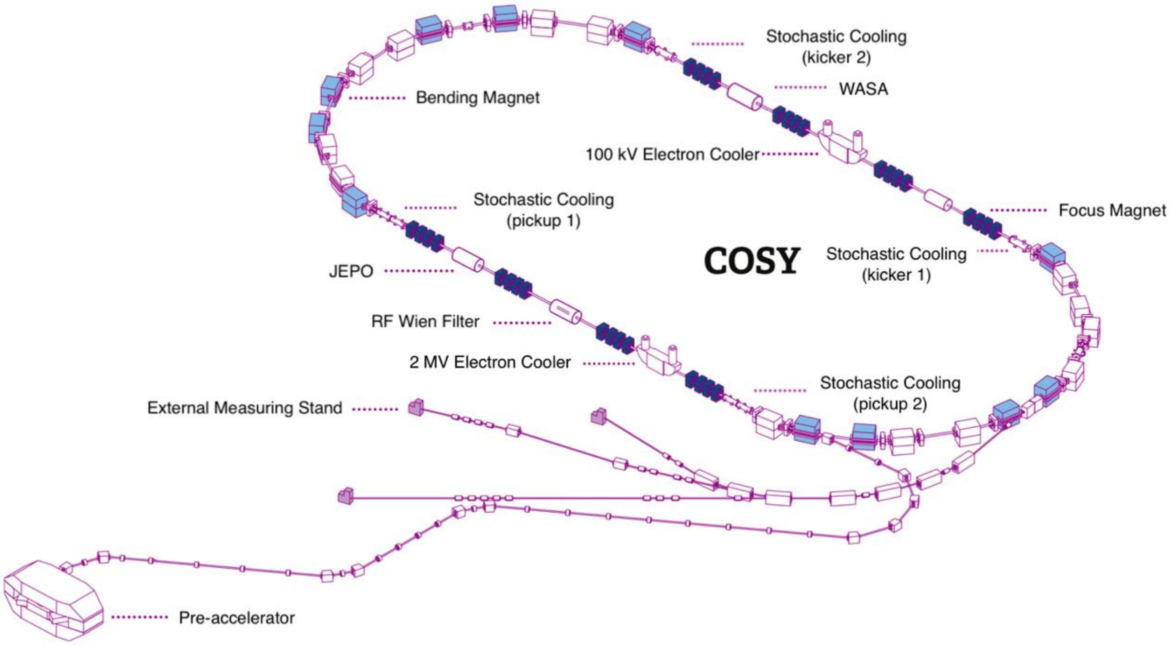

Figure 5.1.: Overview of the accelerator facility: The beam sources are located below the pre-accelerator COSY, from where they are injected into the injection beamline after initial acceleration in the cyclotron. The main ring is equipped with an accelerating cavity, two electron coolers, and two stochastic coolers to reduce the beam's phase space, as well as several polarization manipulators and polarization measurement devices. Created by Jamal Slim/ JEDI Collaboration and adapted by this author.

ion sources. Optionally, a beam chopper in the beamline can be employed for micro-pulsing, reducing beam intensity before entering the cyclotron. The particle energy from the source is around 4.5 keV for H^- ions and 7.6 keV for D^- ions [64].

The IBA and AEA sources provide unpolarized H^- and D^- ions. These industrial-grade sources, named after the companies IBA in Louvain-la-Neuve (Belgium) and AEA in Culham (England), can operate independently. They deliver over 300 μA beams in pulsed operation. The polarized beam source was built by a collaboration of three groups from Bonn, Erlangen, and Cologne [65] and is based on a colliding process of polarized uncharged hydrogen or deuterium atoms, initially proposed by Haeberli in 1967 [66]. A sketch of the polarized source is shown in Figure 5.3. The source consists of three parts, namely the pulsed atomic beam source, the cesium beam source, and the charge exchange and extraction region.

Within the atomic beam source, hydrogen or deuterium molecules undergo initial dissociation into individual atoms through an electric discharge. To avoid recombination, small quantities of oxygen and nitrogen are introduced. The atoms then traverse a nozzle, undergoing cooling to reach temperatures of approximately 30 K. By cooling the beam, it is optimized to be focused by hexapole magnets after the dissociator. The focusing is necessary for the charge exchange with cesium later on. The polarization of the uncharged hydrogen or deuterium atoms is achieved by three radio frequency transfers. These consist of adjustable magnetic fields, which can be switched on or off individually to achieve transitions into different hyperfine states. Different combinations of magnetic fields lead to different states of vector and tensor polarization. The

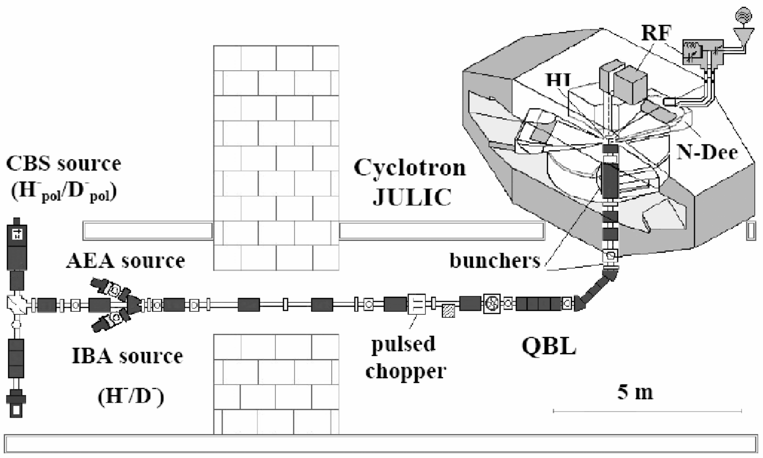

Figure 5.2.: Overview of the particle sources in COSY: The AEA and IBA sources provide unpolarized charged hydrogen or deuterium ions, which are guided through the source beamline (SBL or QBL) to the cyclotron. In the left part, the source for polarized charged hydrogen or deuterium ions is shown. A detailed schematic is shown in Figure 5.3. Taken from [64].

collision between the neutral cesium beam (Cs^0) coming from a cesium ionizer and the polarized atomic beam ($\vec{\mathrm{H}}^0$ and $\vec{\mathrm{D}}^0$) occurs in a central charge exchange region. The charge exchange reaction

$$\vec{\mathrm{H}}^0 + \mathrm{Cs}^0 \rightarrow \vec{\mathrm{H}}^- + \mathrm{Cs}^+, \tag{5.1}$$

$$\vec{\mathrm{D}}^0 + \mathrm{Cs}^0 \rightarrow \vec{\mathrm{D}}^- + \mathrm{Cs}^+, \tag{5.2}$$

generates negatively charged ions that can be extracted. Subsequently, the polarized beam undergoes passage through a Wien filter, which adjusts the spin orientation to align with the vertical magnetic field direction in the cyclotron to preserve the polarization during the preacceleration process [67].

5.2.2. Jülich Light Ion Cyclotron (JULIC)

The Jülich light ion cyclotron (JULIC) accelerates ions up to their injection energies into COSY, reaching 45 MeV for H^- beams and 76 MeV for D^- beams. Functioning as an isochronous cyclotron, it has been utilized for nuclear physics experiments since 1968. While initially designed for this purpose, it underwent refurbishment between 1990 and 1992 to function as a pre-accelerator for COSY.

Cyclotrons accelerate charged particles outward along a spiral path. The acceleration is achieved through an RF electric field between magnetic regions, with magnetic fields maintaining the particles' trajectory. The changing electric field polarity in this region ensures a continuous accelerating force for the particles.

In an isochronous cyclotron like JULIC, particles consistently complete one loop in the same amount of time, meaning that the acceleration frequency can be constant, ensuring they always

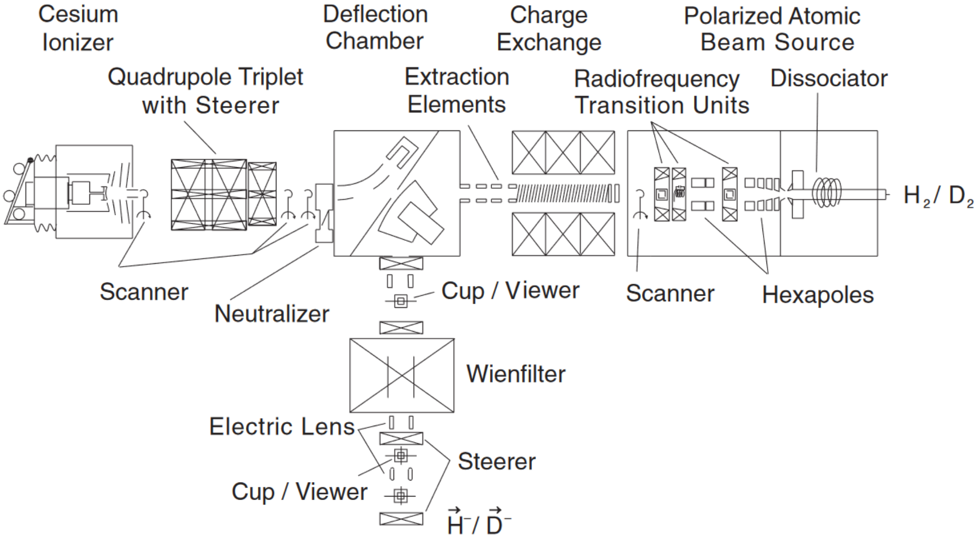

Figure 5.3.: Source providing polarized beams in COSY: Hydrogen or deuterium atoms are dissociated and focused at the polarized atomic beam source. By switching on or off the three radio frequency units, the atoms get polarized. After polarizing, the atoms collide with a cesium beam coming from the cesium ionizer, where they pick up an extra charge to be deflected by the dipole. They are then sent through the source beamline to the injection cyclotron. Figure is taken from [67].

reach the same RF phase in the accelerating gap. For continuous beams, the magnetic field increases by the Lorentz factor γ in the radial direction. Additionally, JULIC operates as a separated sector cyclotron, utilizing the shape of its poles to vertically focus the beam due to edge focusing and compensate for the relativistic mass increase. The RF electric field employed for charged particle acceleration is referred to as the cyclotron frequency [68]. For the return yoke of the magnet, approximately 700 t of iron is necessary.

5.2.3. Injection beamline (IBL) and Injection

When the particles are accelerated in the cyclotron, they get extracted into the injection beamline (IBL) to COSY. The IBL is a transfer line, being 94 m long, containing quadrupole magnets to focus, dipole magnets to bend, and steerer magnets to steer the beam. In addition, several devices like Faraday Cups to measure the beam intensity at the exit of the cyclotron and at the injection at COSY, and slit systems to measure the beam emittance, are installed. Also, a polarimeter called LEP (Low Energy Polarimeter) is installed in the injection beamline, which is used to measure the polarization of the incoming ions. The injection into COSY is a so-called stripping injection. While injecting into the main ring, two electrons at a thin carbon foil are ”stripped” away, turning the H^- or D^- ions into protons or deuterons.

5.3. COSY

In the main COSY ring, polarized and unpolarized deuteron and proton beams are accelerated up to a momentum of $p = 3.7\,\mathrm{GeV/c}$, equivalent to approximately $E_{\mathrm{kin},d} = 2.2\,\mathrm{GeV}$ for deuterons and $E_{\mathrm{kin},p} = 2.8\,\mathrm{GeV}$ for protons.

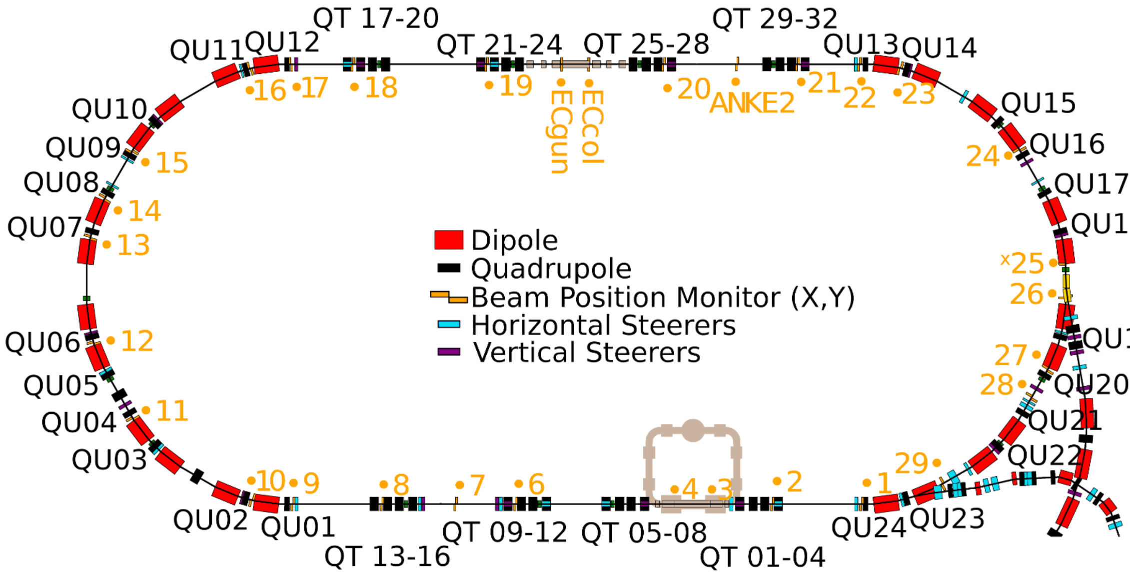

Figure 5.4.: Floorplan of COSY showing dipole magnets (red), quadrupole magnets and their names (black), beam position monitors and their names (orange), and horizontal (blue) and vertical (purple) steerer magnets. Figure is taken from [69].

COSY is built as a racetrack-shaped synchrotron and consists of two 40-meter-long straight sections. Each straight segment contains 16 quadrupole magnets, arranged in four groups of four quadrupoles each. In the straight sections, the RF cavity for acceleration, the two electron and stochastic coolers, spin manipulators like the Siberian Snake and the RF Wien filter, and the two internal polarimeters, WASA and JePo are installed. The arc sections, with a length of 52 meters each, consist of three replicated cells (magnet combinations). In total, 24 water-cooled dipole magnets with a maximum magnetic field of 1.58 T bend the beam around the ring. Each half-cell section follows a quadrupole-dipole-quadrupole-dipole structure, with adjustable quadrupole polarities, resulting in a six-fold symmetric arc. The total length of the synchrotron is 184 m.

Additionally, COSY incorporates 18 sextupoles for chromaticity correction, influencing the Spin Coherence Time – a critical parameter for experiments requiring a long in-plane polarization of the beam, such as those conducted within the JEDI collaboration for Electric Dipole Moment measurement [70].

Throughout the accelerator complex, all components operate under vacuum conditions. For the successful operation of COSY, a vacuum pressure of approximately $10^{-10} - 10^{-11}$ mbar is needed. The vacuum chamber exhibits a rectangular shape in the arcs to fit into the geometrical design of the dipoles and a circular configuration in the straight sections.

Additionally, the beam position is measured with 29 Beam Position Monitors (BPMs) distributed along the ring. Schottky pickups for revolution frequency, tune, and chromaticity measurements are incorporated, along with an Ionization Profile Monitor (IPM) for observing the beam profile. The beam position can be corrected with 25 horizontal and 21 vertical steerer magnets [63, 71]. A floor plan of COSY is shown in Figure 5.4.

Since the commissioning of COSY in 1992, many successful hadron physics experiments like ANKE[1] [72], WASA[2] [73], EDDA[3] [74], and PAX[4] [75] have been conducted.

5.3.1. Beam Cooling

The electron cooler, operating at a maximum voltage of 100 kV, is positioned in the middle of the Cooler Telescope, as illustrated in Figure 5.1. Electrons are electrostatically accelerated in the electron gun to match the velocity of the stored ion beam in COSY. Guided and focused by a longitudinal magnetic field generated by the gun solenoid, these electrons are subsequently deflected 90° into the 2 m-long drift solenoid region using a dipole.

Within this region, the paths of the electron and the ion beam overlap on an effective cooling length of approximately 1.5 m. Afterwards, a second dipole separates the electron beam from the ion beam, directing it towards the collector solenoid. Before being discharged, the electron beam undergoes electrostatic deceleration to the potential of the electron gun. A schematic of the 100 kV Cooler is shown in Figure 5.5. To counteract the Coulomb repulsion, it is necessary to apply a magnetic field along the trajectory of the electron beam. A more dense electron beam requires an increased guiding field to prevent overheating. Typically, solenoid and toroid magnets around the electron cooler drift section generate the guiding field [76].

The primary objective of the electron cooler is to reduce the beam emittances and momentum spread of the ion beam in longitudinal and transverse directions, which is crucial in polarization experiments to increase the so-called Spin Coherence Time. More information about the interplay of Spin Coherence Time and beam width is given in section 7.2 [77]. In 2015, a second electron cooler, namely the 2 MV cooler, was installed in the opposite straight after the injection in the ring, which allows cooling ion beams up to the full momentum range of COSY. The electron cooler itself was not used in the experiment reported in this thesis, as a 970 MeV deuteron beam can be cooled with the 100 kV cooler. However, the solenoidal field of the 2 MV solenoid was used as an additional spin manipulator. More information including a schematic can be found in section 5.4.4.

5.3.2. Stochastic Cooling

COSY is equipped with two stochastic coolers (horizontal and vertical), a system comprising a pickup detector and a kicker. The pickup detector measures the deviation of the particle beam from the designated orbit. Subsequently, the information is transmitted diagonally to the kicker. Upon the beam's entry into the kicker, a corrective bump is applied, effectively correct-

---

[1] **A**pparatus for Studies of **N**ucleon and **K**aon **E**jectiles

[2] **W**ide-**A**ngle **S**hower **A**pparatus

[3] **E**xcitation function **D**ata acquisition **D**esigned for **A**nalysis of phase shifts

[4] **P**olarized **A**ntiproton e**X**periments

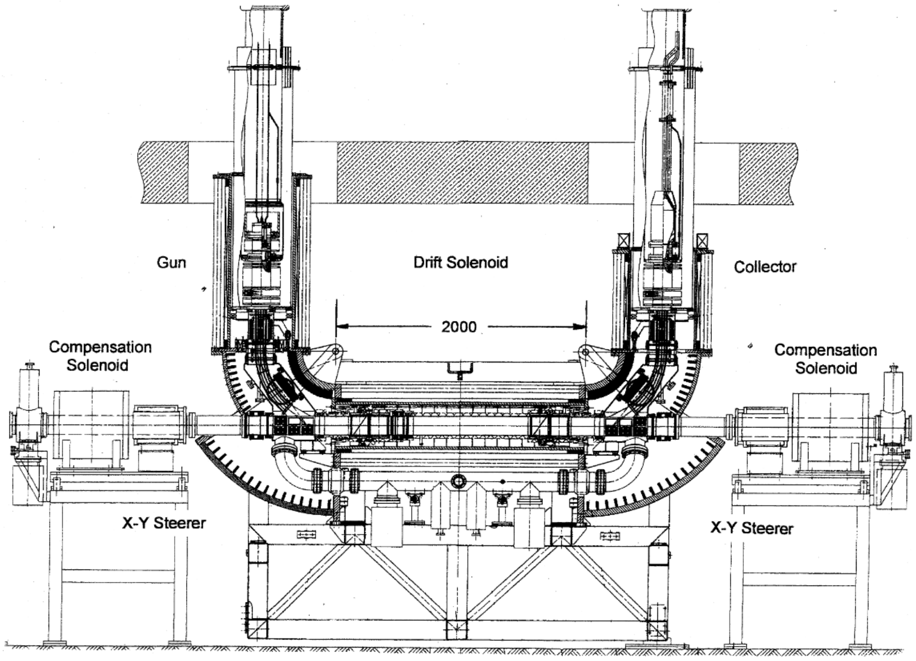

Figure 5.5.: Schematic view of the 100 kV cooler: The electrons are electrostatically accelerated in the electron gun and guided via a 90° deflector into the beamline where they mix with the ion beam. After cooling the ion beam, the electrons are bent again by 90° with a second deflector and collected with the electron collector. The x and y steerer before and after the electron cooler are used to match the ion beam with the electron beam. Taken from [78].

ing the deviation observed earlier. This process enables phase space reduction in both planes. During the experiments reported in this thesis, no stochastic beam cooling is used [79].

5.3.3. Beam Diagnostics

In this section, a few diagnostic components installed in the COSY ring, which are important for the experiments reported in this thesis, are presented.

- **Beam Cooling:** The quality of the beam cooling can be quantified by analyzing beam profiles of recombined particles at the exit of the first dipole after the Cooler telescope, approximately 24 m downstream of the electron cooler. The recombined particle beam profiles are detected using a multi-wire proportional chamber (MWPC). More information about this analysis is given in section 7.3.1.
- **Beam Position Monitors (BPMs):** The measurement of horizontal and vertical beam positions is conducted through a set of 31 (horizontal) and 30 (vertical) beam position monitors (BPMs) in the respective planes. To accommodate the varying shapes of the beam pipe, a design featuring rectangular (150 mm × 60 mm [80]) tubes in the arcs and cylindrical tubes in the straight sections has been developed. Each BPM typically comprises electrode pairs placed around the beam pipe.

During each revolution, the bunched ion beam induces signals on these electrodes. The signals from opposing electrodes are combined into a difference and a sum signal. The sum signal is directly proportional to the beam intensity, while the ratio of the difference and sum signals allows for the determination of the beam position concerning the BPM center [81]. The position of the beam in horizontal and vertical direction can be calculated by using the following formulas

$$X = K_x \left(\frac{V_L - V_R}{V_L + V_R} \right) + X_{\text{off}}, \tag{5.3}$$

$$Y = K_y \left(\frac{V_U - V_D}{V_U + V_D} \right) + Y_{\text{off}}. \tag{5.4}$$

The measured voltage values in the four electrodes of the beam position monitor are V_L, V_R, V_U, and V_D. The geometry factors K_x and K_y are related to the sensitivity of the sensors and X_{off} and Y_{off} are correction factors taking physical offsets of the beam position monitors into account. In 2019, these offsets were measured using the so-called beam-based alignment technique [69]. The offsets which that found for all beam position monitors are listed in Table A.1. More information about the orbits during the experiments reported in this thesis is given in section 7.7.2.1.

The JEDI collaboration developed a new generation of beam position monitors based on Rogowski coils. The main advantage is the reduced size of 13 cm, saving space in the accelerator ring. The disadvantage is that they can only be operated on a designated revolution frequency [82].

- **Ionization Profile Monitor (IPM):** Measuring beam profiles allows determining the transverse widths of the ion beam in the horizontal and vertical directions. By considering the optical function values at the measurement location, it becomes possible to calculate the beam emittances. In synchrotrons, the most common non-destructive measurement of beam profiles is the ionization profile monitors (IPM) [83]. In COSY, the IPM is positioned in the middle of the second arc after injection.

  Within the IPM setup, ions and electrons are generated through collisions involving the circulating ion beam and residual gas atoms. The electrodes of the IPM create an electric field, accelerating ions and electrons towards a micro-channel plate (MCP)[84]. The accelerated electrons collide with a phosphor screen located behind the MCPs, generating light spots that are captured by CCD cameras. This method provides a spatial resolution of approximately 100 μm.

- **Betatron Tune and Chromaticity:** Betatron tunes are crucial parameters for comparing simulation models of COSY with the real machine. At COSY, tune measurements are carried out by exciting coherent betatron oscillations using a so-called stripline unit [80]. Resonant oscillations occur when the excitation frequency aligns with a betatron sideband frequency. From these measurements, the fractional part of the betatron tunes can be determined. Obtaining the beam chromaticities involves repetitive tune measurements for different ion beam velocities.

5.4. Spin Manipulators in COSY

Throughout the ring, a few devices are installed which are and can be used as spin manipulators. The RF solenoid is used to rotate the initial vertical polarization provided by the source into the accelerator plane. The Siberian snake, the RF Wien filter, and the 2MV solenoid are used to determine the Invariant Spin Axis.

5.4.1. Radio Frequency Solenoid

The RF solenoid serves as one of the spin manipulation devices at COSY. This 57.5 cm-long solenoid comprises a 25-turn air-core water-cooled copper coil with an average diameter of 21 cm [85]. The solenoid produces a sinusoidal magnetic field (maximum 1.17 mT) parallel to the beam momentum vector and is used to rotate the vertical polarization provided by the beam source into the accelerator plane. The solenoid operates as part of an RLC resonant circuit at an RF voltage of 5.7 kV, producing a longitudinal RF field integral of 0.67 Tmm [86].

According to the Thomas-BMT equation (4.22), particle spins experience kicks as soon as they possess a component perpendicular to the magnetic field, resulting in a rotation around the solenoidal magnetic field. To rotate the polarization into the horizontal plane, the frequency of the solenoid needs to be set to one of the harmonics of the spin precession frequency

$$f_{\text{sol}} = |K + G\gamma| f_{\text{COSY}} \text{ with } K \in \mathbb{Z}. \tag{5.5}$$

The magnetic anomaly, the revolution frequency, and the Lorentz factor are denoted by G, f_{COSY}, and γ. For technical reasons, the $K = 1$ harmonic is used. Even though the resonance frequency can be calculated using Eq. (5.5), the resonance frequency needs to be determined experimentally as it can change due to imperfections in the experimental conditions. The resonance frequency is found by performing a so-called variable-frequency Froissart-Stora scan sweeping through a frequency range around the expected resonance frequency. By changing the solenoid frequency and finally hitting the resonance, the vertical polarization starts to flip according to the Froissart-Stora formula [87]

$$P_{V,f} = P_{V,i} \left(2 \exp \left(-\frac{\pi \epsilon_{\text{sol}}^2}{2|\alpha|} \right) - 1 \right). \tag{5.6}$$

The initial and final vertical polarization before and after crossing the resonance are given by $P_{V,i}$ and $P_{V,f}$. The resonance strength and the rate at which the resonance is crossed are denoted by ϵ_{sol} and α. Once the resonant frequency is found, it is fixed throughout the experiment, and the duration of the RF solenoid is varied until half a flip of the polarization, i.e., the polarization is rotated into the horizontal plane, is done. During the experiment, the RF solenoid was sometimes adjusted when the flip was not completely successful. However, a polarization which is not completely rotated into the horizontal plane is not crucial for the experiment as it is shown in sections 7.6.2 and 7.6.3. The frequencies used for the experimental periods described in this thesis are given in Table 7.2. In Figure 5.6, the rotation of the left-right asymmetry (proportional to the vertical polarization, section 6.4) is shown. At 175 s for a period of ten seconds in the cycle, the RF solenoid is switched on at the resonant frequency resulting in the full rotation such that $P_{V,f}/P_{V,i} = -1$. By adjusting the timing of the RF solenoid, the polarization is rotated into the accelerator plane, i.e., $P_{V,f} = 0$. The absolute value of the asymmetry reduces during the spin flip due to a loss of spin coherence. This process is further discussed in section 7.2.

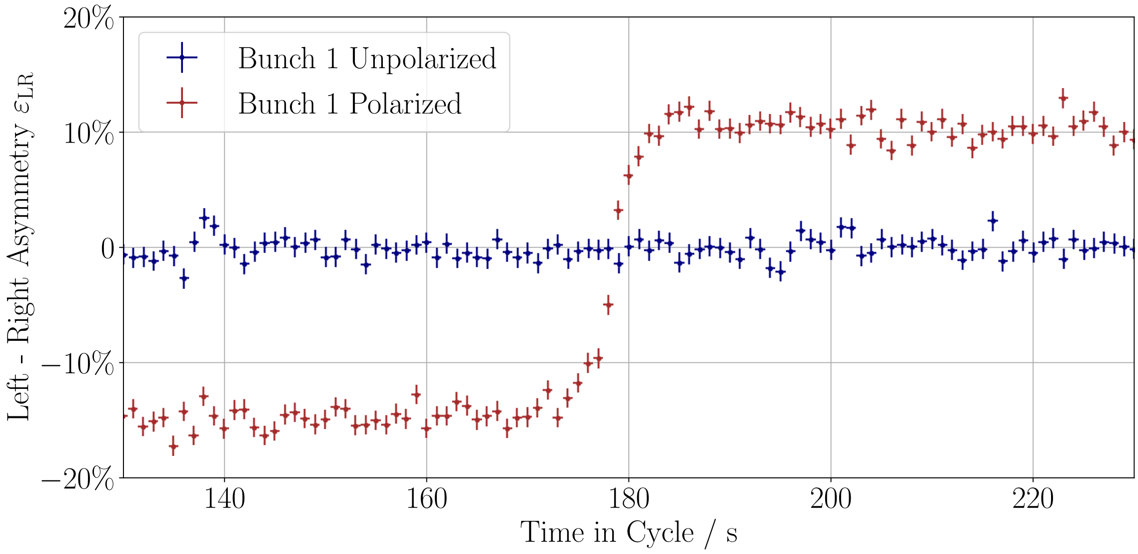

Figure 5.6.: The left-right asymmetry, which is proportional to the vertical polarization of the beam as a function of time for a cycle using unpolarized and polarized beam. At 175 s, the RF Solenoid is switched on for a period of 10 s at the resonant frequency resulting in a full rotation of the polarization, such that $P_{V,f}/P_{V,i} = -1$. During the measurement, two polarized bunches were circulating in the machine. For illustration purposes, only the rotation of the first bunch is shown. The absolute value of the asymmetry reduces during the spin flip due to a loss of spin coherence.

5.4.2. Radio Frequency Wien Filter

A conventional Wien filter provides an electric and a magnetic field which are orthogonal to each other and the beam momentum direction. By adjusting the electromagnetic field inside the device to the design momentum of the particle beam, the force acting on the beam becomes zero

$$F_C = F_L \tag{5.7}$$
$$qE = q\beta cB \tag{5.8}$$
$$E = \beta cB. \tag{5.9}$$

The particle's velocity for no deflection in the device is given by

$$\beta c = \frac{|\vec{E}|}{|\vec{B}|}. \tag{5.10}$$

A simulation of the Lorentz force inside the real device, installed in the first straight section after injection, at a power of 1 kW is shown in Figure 5.7. When entering and exiting the device, the beam experiences a Lorentz force with opposite signs, which means that the integrated Lorentz force is zero. Inside the device, the Lorentz force is the same as outside the device.

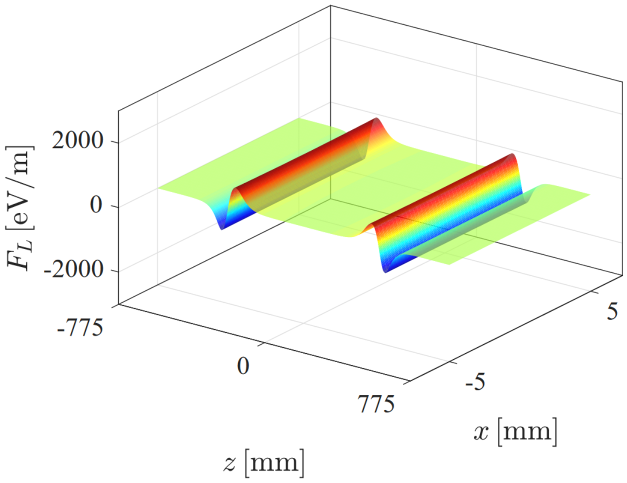

Figure 5.7.: Simulation of the Lorentz force inside the RF Wien filter. The z axis points in the direction of the beam momentum vector. When entering the RF Wien filter, the beam experiences non-zero Lorentz forces which have the same amplitude in opposite directions and cancel out. In the device, the main field is zero. Taken from [88].

If a particle does not fulfill the Lorentz force condition (cf. Eq. (5.10)), it is either deflected by the electric or magnetic field, meaning that the Wien filter selects only particles at the correct momentum, hence the name filter. For the experiment reported in this thesis, the filtering purpose of the device is not relevant as COSY provides fantastic beam conditions. However, for the determination of the Invariant Spin Axis, a vertical magnetic field is necessary for spin manipulation, which has to be compensated by an electric field to avoid impact on the beam's trajectory. While the magnetic field allows a rotation of the polarization, the beam itself stays unaffected. In order to observe an effect on the beam polarization, the magnetic field needs to run on one of the harmonics of the spin precession frequencies. This is where the radio frequency enters the field, which allows for a periodic switching of the magnetic field, similar to the radio frequency of the RF solenoid. The electromagnetic field is produced using parabolically-shaped parallel plates through which the electromagnetic wave travels in the device. The RF Wien filter is designed to operate at frequencies ranging from 120 kHz to 1621 kHz. To ensure, that the RF Wien filter runs on the right frequency, an online phase feedback system was developed which is further discussed in section 6.7.

In addition, the entire Wien filter can be rotated around the beam pipe. When the magnetic RF Wien filter is pointing vertically to the accelerator plane, the RF Wien filter is in the so-called Electric Dipole Moment mode. When the magnetic field of the RF Wien filter is in the accelerator plane, the RF Wien filter is in the Magnetic Dipole Moment mode. By rotating the RF Wien filter around the beam pipe, the radial component of the Invariant Spin Axis can be probed. More information about the determination of the radial component of the Invariant Spin Axis is given in section 7.6. The RF Wien filter is typically operated at a power of 1 kW. The RF Wien filter after it was installed in COSY can be seen in Figure 5.8.

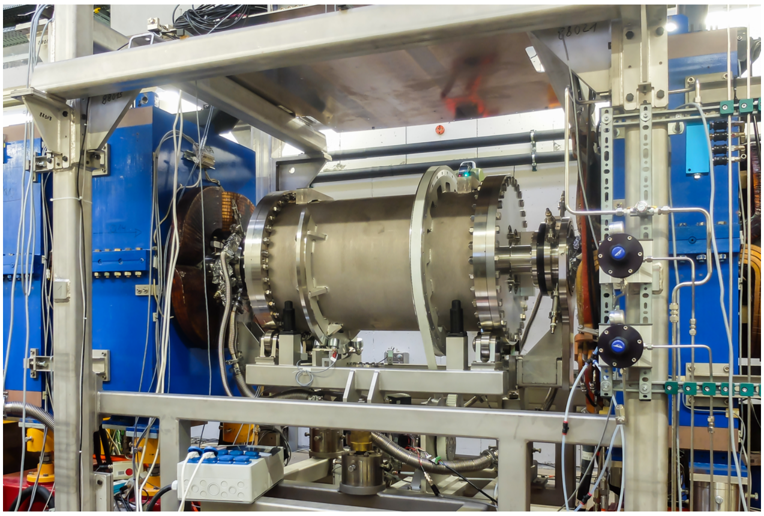

Figure 5.8.: RF Wien filter installed in COSY. The beam enters the device from left to right. The white belt is used to rotate the device around the beam pipe. The picture was taken by Volker Hejny/ JEDI Collaboration.

After the first experimental period using the RF Wien filter for the determination of the Invariant Spin Axis in 2018, fast RF switches were installed into the driving circuit of the device, which produced the electromagnetic wave. The RF switches can be triggered at the revolution frequency, allowing for bunch selection. By preparing two (or four) bunches with the RF cavity, the Wien filter can be used to only influence the polarization of the so-called signal bunch, while the so-called Pilot bunch is unaffected by the RF Wien filter fields and acts as a co-magnetometer [89]. This gating of the Pilot bunch allows for the measurement of the Invariant Spin Axis using the so-called Pilot bunch method, which will be further explained in section 7.6.3. The switches can only be operated at a reduced RF Wien filter power of 500 W. The plates inside the RF Wien filter creating the RF electromagnetic wave are shown in Figure 5.9.

Initially, the RF Wien filter was planned with a ferrite cage around the device. Simulations have shown that the parallelism of the electrodes has the largest influence on the homogeneity of the electric field, while the alignment of the ferrite blocks significantly impacts the homogeneity of the magnetic field in the RF Wien filter. However, these ferrite blocks have never been installed [88]. There is a simulation of the magnetic field axis available in which the effects of the geometrical misalignments (within a reasonable range) of the electrodes and the ferrite cage are studied. The simulations conclude that the variance of possible relative field errors of the vertical magnetic field with respect to the full field integrated over the length of the RF Wien filter is given by

$$\mathrm{Var}\left(\frac{\int_{\frac{-l}{2}}^{\frac{l}{2}} |\vec{H}_{\perp}|\mathrm{d}l}{\int_{\frac{-l}{2}}^{\frac{l}{2}} |\vec{H}|\mathrm{d}l}\right) \approx 1 \times 10^{-3}. \tag{5.11}$$

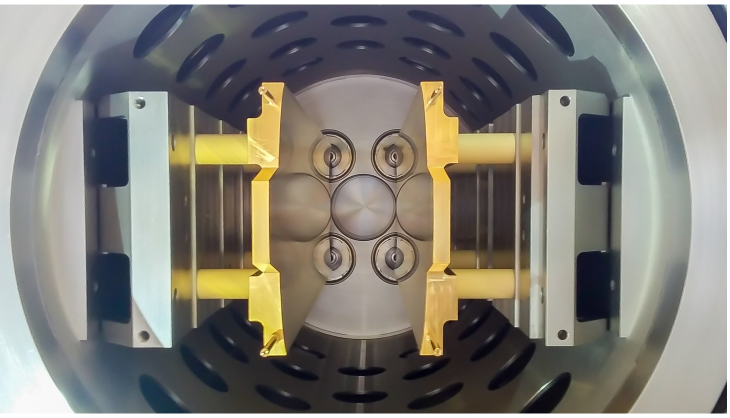

Figure 5.9.: A view along the beam axis in the RF Wien filter. The parabolic parallel electrodes produce the RF electromagnetic wave used to rotate the polarization. The picture was taken by Irakli Keshelashvili/ JEDI Collaboration.

Using small angle approximation, this relative field error corresponds to a systematic error of 1 mrad for the vertical magnetic field axis in the longitudinal direction. However, these simulations correspond to the case with the installed ferrites, which were never used in the real experiment [90].

5.4.3. Siberian Snake

The superconducting Siberian snake installed in COSY was delivered in 2017 for the PAX (Polarized Antiprotons Experiment) experiment to provide longitudinal polarization at the PAX installation. It was installed in the second straight section of COSY at the former ANKE magnet position. The superconducting magnet is cooled using liquid helium and provides a maximum longitudinal field of 6 T at a current of 258.83 A. The Siberian snake in COSY is of the first kind, meaning that the rotation axis of the spin is longitudinal with respect to the beam momentum direction.

In circular accelerators providing polarized particles, Siberian snakes are used to avoid crossing of depolarizing resonances by forcing the spin tune to half-integers. The great advantage is that this procedure is independent of beam energy. When setting up COSY for the Precursor experiments, no depolarizing resonances occur when accelerating to 970 MeV/c. However, the Siberian snake is used to rotate the Invariant Spin Axis after acceleration. More information about the effect of the Siberian snake on the Invariant Spin Axis is given in section 7.4. The Siberian snake installed in COSY is shown in Figure 5.10.

5.4.4. 2 MV Solenoid

Although the 2MV electron cooler is not used during the experiment reported in this thesis to cool down the deuteron beam, as the 100 kV cooler is sufficient, the solenoidal field of the straight cooling section can be used as an additional spin rotator. The principle is the same as already described in the previous section for the Siberian snake, as it only adds an additional solenoidal field in the beam momentum direction in the first straight section after injection.

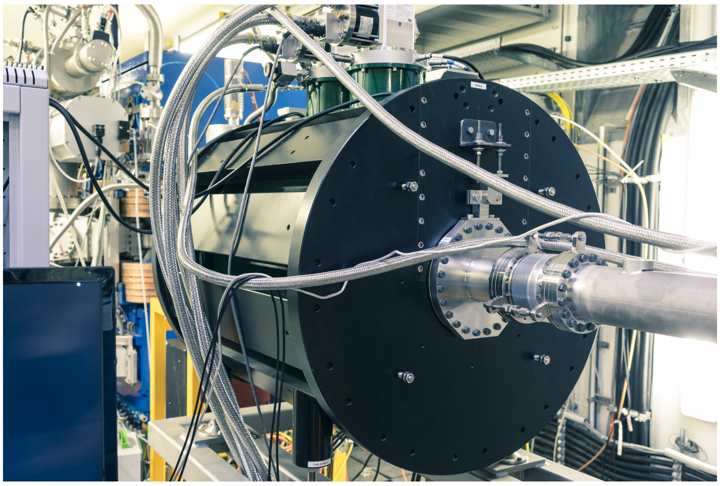

Figure 5.10.: The superconducting Siberian snake in COSY during the commissioning experiment in 2017. The picture was taken by Irakli Keshelashvili/ JEDI Collaboration.

However, by adding an extra field, the spin physics developed in section 7.4 and 7.6 can be further probed.

The maximum solenoidal field is much weaker than the field of the Siberian snake, being 0.2 T. To ensure the magnetic field in the cooling section meets the required straightness, a solenoid made up of many short coils is used. Each coil can be adjusted horizontally and vertically. The desired straightness is gven by ($\Delta\theta < 1 \times 10^{-5}$ rad). After assembling the cooling solenoid, the magnetic field's straightness is checked. This system incorporates a moving mirror inside the solenoid that reflects a laser beam. The mirror is connected to a magnetic rod that aligns with the magnetic field. The mirror support, using jewel bearings, helps to precisely track the magnetic field's sideways components. A detector captures the reflected laser beam to measure the straightness of the field [91].

5.5. Polarimeters in COSY

Polarimeters are instruments installed in COSY to measure the vertical polarization component and the amount of in-plane polarization of the particle bunch circulating in the accelerator. Two polarimeters are installed in the ring. Until late 2019, the forward detectors of the Wide Angle Shower Apparatus (WASA) served as a polarimeter. In 2019, the JEDI collaboration built a new dedicated polarimeter for proton and deuteron Electric Dipole Moment measurements, known as the Jedi Polarimeter (JEPO).

Both polarimeters operate on a common principle: a scattering process on a thick carbon target scratches the halo of the bunched beam. Depending on the beam's polarization orientation, the beam scatters into four detector segments: up, down, left, and right as seen from the beam direction. An asymmetry in the left-right direction indicates the vertical polarization component, while an asymmetry in the up-down direction is used to determine the amount of in-plane polarization. For detailed determination methods, refer to sections 6.4 and 6.5.

The process of extracting particles from the target involves applying a white noise electric field, comprising overlaid sinusoidal signals. This electric field's influence on the target's extraction rate is continuously controlled by a feedback system called the Schneider Box. The Schneider Box regulates the voltage applied to the beam to maintain a consistent extraction rate over time. Figure 5.11 illustrates the loss of particles over time due to extraction from the carbon target. Beam loss occurs linearly as soon as extraction begins, at a rate in the order of 2.5×10^7 particles/s. Earlier loss in the cycle is due to acceleration and orbit correction.

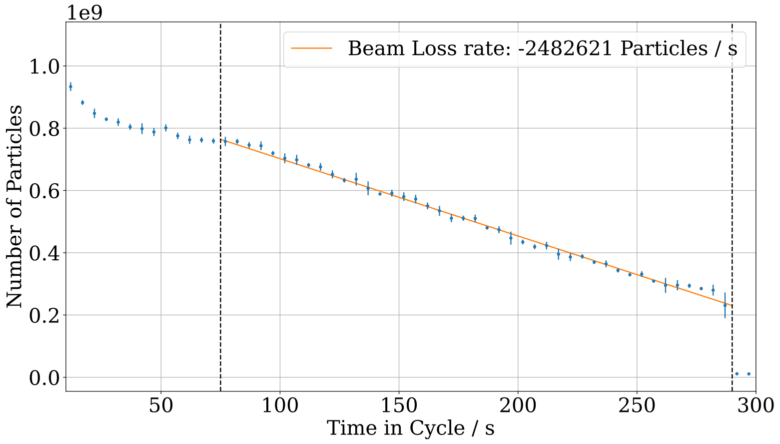

Figure 5.11.: Beam loss due to the beam extraction on the carbon target occurs at a rate in the order of 2.5×10^7 particles/s. The dashed lines in the figure mark the extraction period. The initial loss occurs when running the orbit correction.

5.5.1. Wide Angle Shower Apparatus (WASA)

The Wide Angle Shower Apparatus (WASA) initial development and construction took place in 1996 at the Department of Radiation Sciences of the University of Uppsala in Sweden, and it was subsequently installed at the CELSIUS accelerator and storage ring. The primary objective of WASA was to detect light mesons like π_0 and η. It comprised two main components: a central detector, often referred to as the calorimeter, made up of CsI crystal scintillators capable of covering nearly 4π solid angles, and a forward detector located downstream of the beam.

In 2006, the entire WASA detector, along with its microsphere hydrogen pellet target, was relocated to the COSY accelerator facility at Forschungszentrum Jülich for the WASA-at-COSY [92] campaign. Some upgrades were introduced to accommodate higher energies and count rates. This updated configuration allowed the WASA detector to conduct experiments until 2014.

Between 2014 and the end of 2016, the entire detector, including the pellet target, was removed from COSY. The central detector was moved to the Fragment Separator at GSI in Darmstadt to search for hypernuclei [93]. The forward detector part was reinstalled to function as a polarimeter for the JEDI collaboration. Additionally, a new FPGA-based trigger system was developed for this revised configuration.

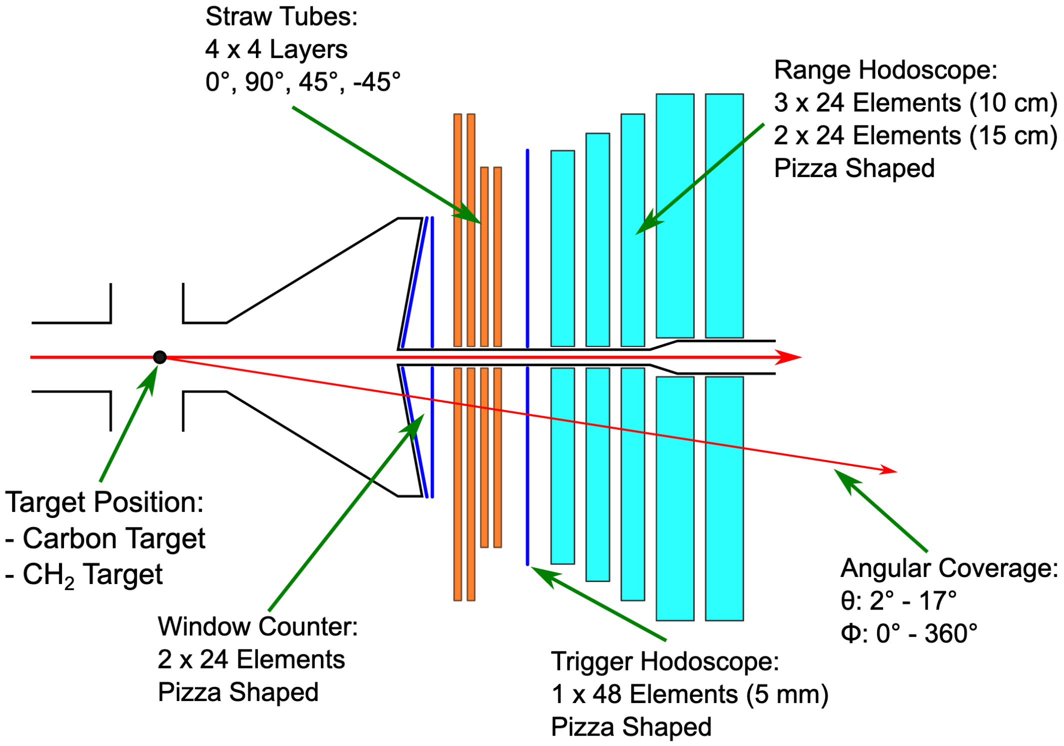

Figure 5.12.: Schematic of the WASA forward detector. The beam travels horizontally from left to right, passing a 2-cm-thick carbon block target. The beam is heated in the vertical direction to bring the particles to the target's front face. Forward-scattered particles exit the vacuum through a stainless steel window at angles between 2° and 17°. They then pass through two pie-shaped plastic scintillator window counters, an array of straw tubes for position and angle tracking, a segmented trigger hodoscope, and five layers of plastic scintillator calorimeter detectors (depicted in light blue). All scintillator counters are read out using photomultiplier tubes mounted at the outer edges of each segment. Taken from [26].

The final detector setup for the first experimental period in 2018 to measure the orientation of the Invariant Spin Axis consisted of an unpolarized carbon target from which the deuterons scatter into two layers of forward window counters (FWC1 and FWC2) with 24 elements each. These were followed by four layers of straw tubes, which were rotated by 45°. Next, a single layer of the forward trigger hodoscope (FTH) was mounted, featuring 48 elements rotated by 3.75° relative to the other detector modules. The last part of the detector consisted of five layers of the forward range hodoscope, with 24 elements in each layer. The first three layers (FRH1, FRH2, and FRH3) were constructed from 11 cm thick plastic scintillators, while the latter two (FRH4 and FRH5) were made from 15 cm thick scintillators. A schematic of the WASA forward detector is shown in Figure 5.12.

For polarimetry, the detector is partitioned into four distinct segments, each responsible for monitoring a specific azimuthal angle approximately spanning $\Delta\phi \approx 90°$. These four segments are referred to as "up," "down", "left," and "right" when viewed from the perspective of the incoming beam direction. The angular geometrical area encompasses $\theta = 2$ to 17° and $\phi = 0$ to 360°.

5.5.2. Jedi Polarimeter (JePo)

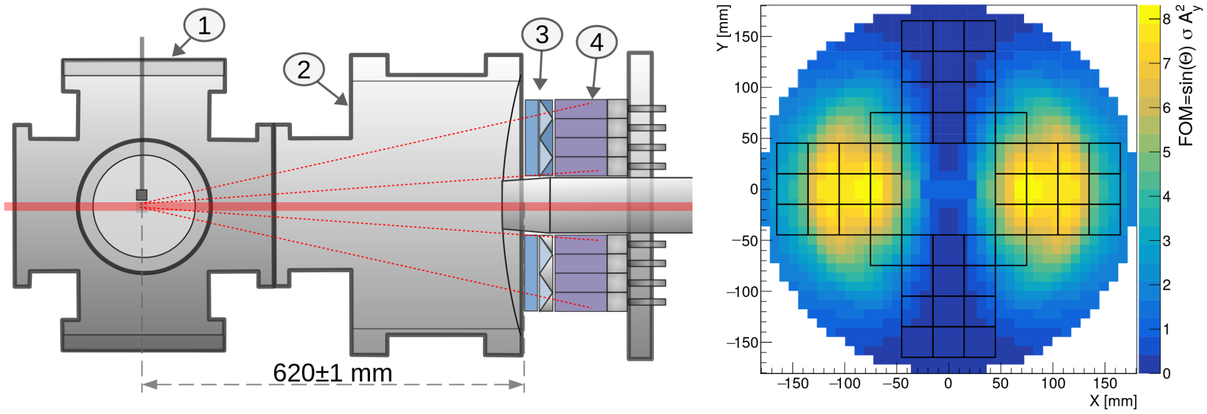

(a) Conceptual Design

(b) LYSO crystal locations and FOM.

Figure 5.13.: **Left:** Schematic of the polarimeter with (1) a target chamber containing horizontal and vertical 2 cm thick carbon blocks which are movable, (2) a vacuum flight chamber equipped with an 800 μm stainless steel exit window, (3) ΔE counter and 2+2 cm plastic scintillators for tracking, and (4) the scattered projectiles are stopped in the LYSO modules. **Right:** The black boxes show the coordinates of the LYSO crystals. Figures are taken from [94].

In 2019, a new dedicated polarimeter for proton and deuteron Electric Dipole Moment research was installed in the ring. A schematic of the polarimeter is shown in Figure 5.13a. A horizontal and a vertical target are deployed in the polarimeter. For the experiments reported in this thesis, only the vertical target is used. When the beam is accelerated and cooled, the target is moved using a rod close to the halo of the beam. By applying a local beam bump, the beam is moved to its final position close to the target. After scattering and passing through an 800 μm thick stainless steel window, the projectiles encounter a plastic scintillator energy-loss detector. Finally, the projectiles are stopped using heavy inorganic LYSO (cerium-doped lutetium yttrium oxyorthosilicate) crystal scintillators. Each crystal measures $3 \times 3 \times 8\,\mathrm{cm}^3$. The signals are read out using SiPM chips directly mounted on the scintillators.

In COSY, the operating deuteron momentum of $p = 970\,\mathrm{MeV/c}$ ($T_d = 270\,\mathrm{MeV}$) is chosen as the so-called Figure of Merit defined by FOM $= \sigma(\theta)A_y^2(\theta)\sin(\theta)$ is maxing out for the chosen design of the polarimeter when analyzing d+C scattering events. It can be shown that the statistical uncertainty squared on an Electric Dipole Moment measurement is proportional to the inverse of the Figure of Merit. Therefore, a detector design is crucial for maxing out the integral of the FOM over the polar angle θ. The placement of the scintillators measuring the polar angle, along with the Figure of Merit for a deuteron beam scattering elastically on a carbon block, is shown in Figure 5.13b [94].

5.6. The Fiber-Optics-based Reference Frequency Distribution System

The Fiber-Optics-based Reference Frequency Distribution System was installed during the summer shutdown in 2020 and is used to synchronize all frequency-related devices in COSY. For the Electric Dipole Moment experiment, the essential systems are the frequency generators for the COSY RF cavity, the RF solenoid, and the RF Wien filter. For reference synchronization, a GPS-driven 10 MHz signal is used. Without the reference signal, the individual oscillators for each device had to be retuned once per day in the range of 10 mHz, which is up to two orders of magnitude larger than the typical cycle-by-cycle variation of the spin tune. Without corrections of the frequencies, off-resonance behavior is observed. This adds new sources of uncertainties when running the RF solenoid to rotate the initial vertical polarization into the horizontal plane, which is described in section 5.4.1. Off-resonance behavior leads to incomplete or too large rotations of the polarization and therefore different starting conditions for the experiment in each cycle. Off-resonance behavior also leads to a more complex buildup of vertical polarization when running the RF Wien filter. This behavior is further described in section 7.6.3.1.

The signals are distributed using fiber-optic cables to the relevant systems of the Electric Dipole Moment experiment, providing clean frequency signals with low phase noise and a high signal-to-noise ratio. The advantage of fiber-optic cables is that signals and data are transported over short and long distances without distortions, as fiber-optic cables are electromagnetically non-radiating and immune to interference and grounding issues on low and high bandwidths. Using the fiber-optic system, the source generators of TTL (transistor-transistor logic) and sine-wave signals are decoupled from their origin and destination systems.

6. Data Analysis

To determine the Invariant Spin Axis and consequently the first direct result of the Electric Dipole Moment of the deuteron, the polarization of the bunched deuteron beam needs to be studied using data from the internal polarimeters in COSY. In the following sections, an overview of the analysis of the extraction of the polarization and other relevant parameters is given.

6.1. Software

To start this chapter about the data analysis, a short introduction to the software is given. As the main tool for data collected in COSY, Python is used for calculations and simulations as well as for connecting to the EPICS servers. All data recorded with the polarimeters is analyzed using the analysis tool ROOT.

6.1.1. ROOT

ROOT is an object-oriented, open-source software framework developed at CERN for analyzing data. It started in 1994 when René Brun and Fons Rademakers created it to replace the older Fortran-based PAW software. The need for something stronger arose because of the expected challenges in handling data from the Large Hadron Collider (LHC). While initially designed for particle physics, ROOT is now used in different areas like data mining. Written in C++, ROOT has many functionalities, including console or graphical user interface operation, advanced statistical analysis (multidimensional histogramming), making histograms and graphs, fitting functions, statistical data analysis, various math functions, 3D visualizations, and supporting distributed computing. ROOT has become a vital tool for researchers in various scientific fields [95].

6.1.2. EPICS

The Experimental Physics and Industrial Control System (EPICS) is an open-source software framework designed for creating distributed control systems for large-scale experiments, including applications in particle accelerators, telescopes, and fusion reactors [96]. These experiments require the collection and transmission of data from multiple sources for operational and analytical purposes. Originally built for a collaboration between the Los Alamos National Laboratory and the Argonne National Laboratory, EPICS has evolved into a widely adopted platform, with numerous institutions worldwide contributing to its ongoing development.

EPICS relies on Client/Server and Publish/Subscribe communication methods to allow for data exchange between various computing components. Servers, known as Input/Output Controllers

(IOCs), handle real-world input/output operations and local control functions. Data transfer within EPICS utilizes a unique data structure known as the Process Variable (PV). A PV can be envisioned as a comprehensive data entity, encompassing essential information such as the name and value of a measured variable, along with additional details like units and timestamp information. Moreover, a PV is versatile enough to support more complex data types, including waveforms and machine states, as well as facilitating the processing of other PVs.

6.2. Event Rates

The following sections about the determination of polarization quantities are valid for both polarimeters (WASA and JePo). After scattering on the carbon target, the projectiles are measured by all four quadrants of the polarimeter. The event rate in each quadrant R_X is given by

$$R_X = \dot{N}_X = \frac{\mathrm{d}N_X}{\mathrm{d}t} \text{ with } X \in \{\text{L,U,R,D}\}, \tag{6.1}$$

where N denotes the number of detected events. The letters L, U, R, and D represent the detector in which the particle scatters. The detectors are placed at azimuthal angles of $\phi_L = 0°$, $\phi_U = 90°$, $\phi_R = 180°$ and $\phi_D = 270°$, each covering a range of $\Delta\phi_X \approx 90°$. The detector rates in each quadrant can be calculated by integrating over the solid angle

$$R_X = I d_t \int_X a_X(\vartheta, \phi)\sigma(\vartheta, \phi)\mathrm{d}\Omega. \tag{6.2}$$

The variable I denotes the beam current intensity, d_t the target density, $a_X(\theta, \phi)$ the combined detector efficiency and acceptance, and $\sigma(\theta, \phi)$ the spin dependent elastic cross-section on an unpolarized carbon target, introduced in section 4.3. In each time bin $(T_i, T_i + \Delta T)$, where $\Delta T = 2\,\mathrm{s}$, the total number of detected events is given by

$$N_X = \int_{T_i}^{T_i+\Delta T} R_X \mathrm{d}t. \tag{6.3}$$

The quadrants are illustrated for the Jedi Polarimeter JePo in Figure 6.1. The marked red regions denote a single quadrant that encompasses 13 LYSO crystals. The colour denotes the number of measured particles in each crystal. During an extraction time of 220 s, approximately 1.13×10^7 scattered particles are detected. In this example, a typical cycle for the determination of the Invariant Spin Axis is used. Using the quadrants, the left-right asymmetry (vertical polarization), as well as the up-down asymmetry (horizontal polarization) can be computed. The directions are noted as seen from the beam.

An example of the events measured by the four quadrants of the polarimeter is shown in Figure 6.2. The example is taken from a so-called Spin Coherence Time (cf. section 7.2) measurement with the Jedi Polarimeter JePo during the Precursor Run II. Events occur in the polarimeter when the noise extraction of the beam starts at 75 s. The event rates change in the left and right detector at 90 s when the RF solenoid rotates the vertical polarization into the accelerator plane. A feedback loop, called Schneiderbox, measures the total amount of rates in the polarimeter and controls the voltage on the stripline to keep the extraction rate constant. The counting rates of each detector differ in absolute value due to variations in the acceptances

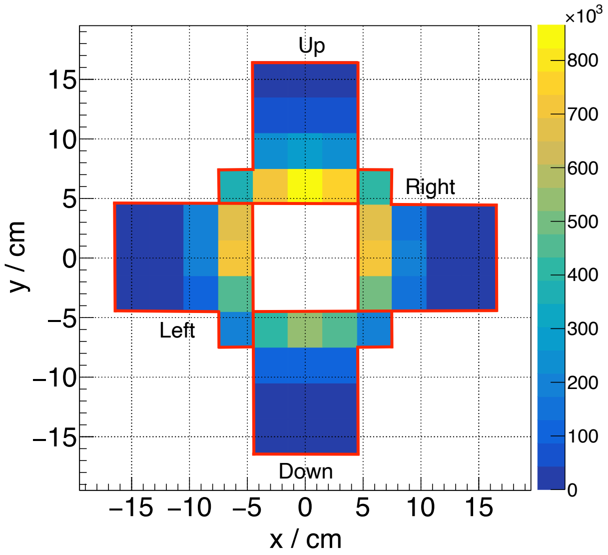

Figure 6.1.: Illustration of the four distinct quadrants of the Jedi polarimeter JePo. The quadrants are marked with a red colour. The z axis denotes the number of measured scattered particles during a 220 s extraction interval in each crystal. In total 1.13×10^7 particles are measured. The directions are noted as seen from the beam.

of individual detectors. Furthermore, the beam does not precisely pass through the geometric center of the detector, contributing to asymmetrical counting rates.

6.3. Event and Bunch Selection

At the polarimeter, the particles with the largest vertical betatron amplitudes scatter on the carbon target. The scattered particles are detected by the four quadrants inside the polarimeter. The selection of events and bunches is based on the COSY phase, which is defined as

$$\phi_{\text{COSY}} = \frac{t_{\text{event}} - t_{\text{turn}}}{f_{\text{COSY}}} \bmod 2\pi, \tag{6.4}$$

where t_{event} denotes the time of an event hitting the detector, t_{turn} denotes the time of the turn, and f_{COSY} denotes the revolution frequency. The COSY phase is shown as a function of time in the cycle in Figure 6.3a for single-bunch operation (Precursor I) and two-bunch operation (Precursor II) in Figure 6.3b. The colour denotes the number of entries within a time and COSY phase bin. As the COSY phase is calculated from the time of arrival in the polarimeter, the width of the peak for a constant time reflects the longitudinal beam profile of the particles with the largest betatron amplitudes at the polarimeter.

In Figure 6.4a and 6.4b, the time-integrated over the entire cycle COSY phase is shown for single-bunch and two-bunch operation. Assuming a Gaussian distribution, the individual peaks are fitted using a least squares fit. In the upcoming sections, only events within a two-standard-

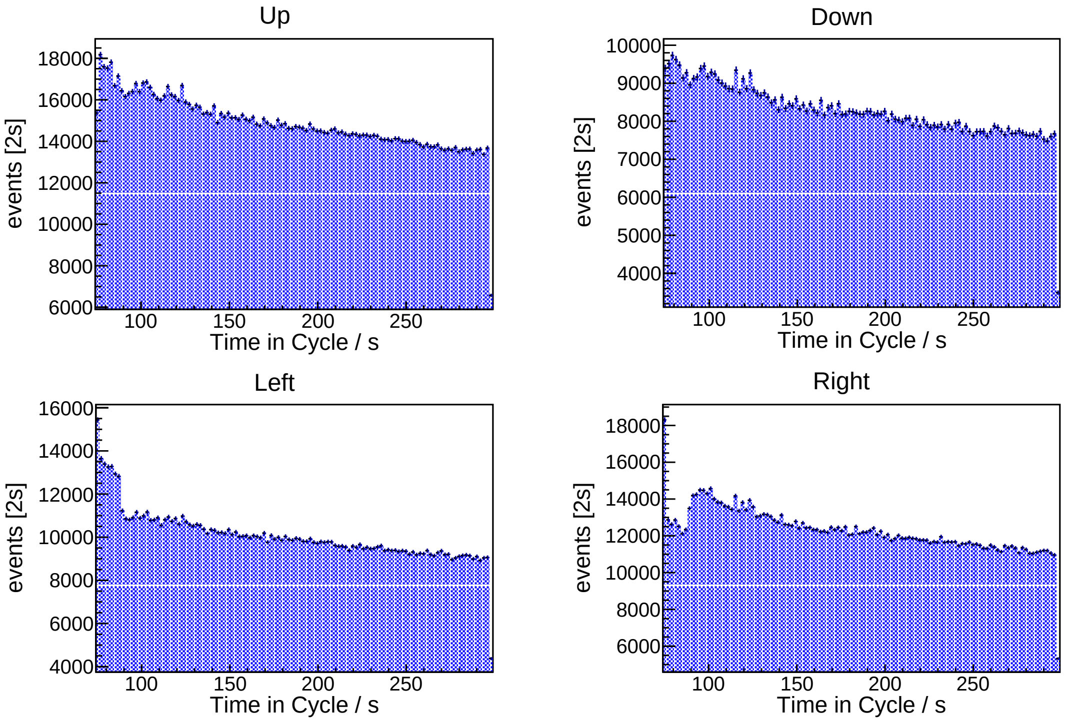

Figure 6.2.: Example of the number of events measured using the four quadrants of the WASA polarimeter throughout a cycle. The change of number of events in the left and right detector occurs due to the rotation of the vertical polarization using the RF solenoid at 90 s. More information about the detection of the vertical polarization is given in section 6.4.

deviation range around the mean value are taken into account for the determination of the Invariant Spin Axis, ignoring the other tails of the bunches. Systematic studies of event selections are further discussed in section 7.4.4 and 7.8.1. In addition, a good separation of the bunches is important for successful gating of the RF Wien filter when applying the Pilot bunch method (cf. section 7.6.3).

6.3.1. Event Selection Studies

In section 6.3, the event selection based on the COSY phase is discussed. The COSY phase scales with the longitudinal bunch shape. Note that no exact values of the bunch length can be determined from this analysis as, at the target in the polarimeter, particles of the bunches scatter with the largest betatron amplitude. However, by selecting only events in the head and tails of the Gaussian distribution, particles with larger synchrotron oscillation amplitudes can be compared with events with smaller synchrotron oscillation amplitudes in the center of the bunch distribution.

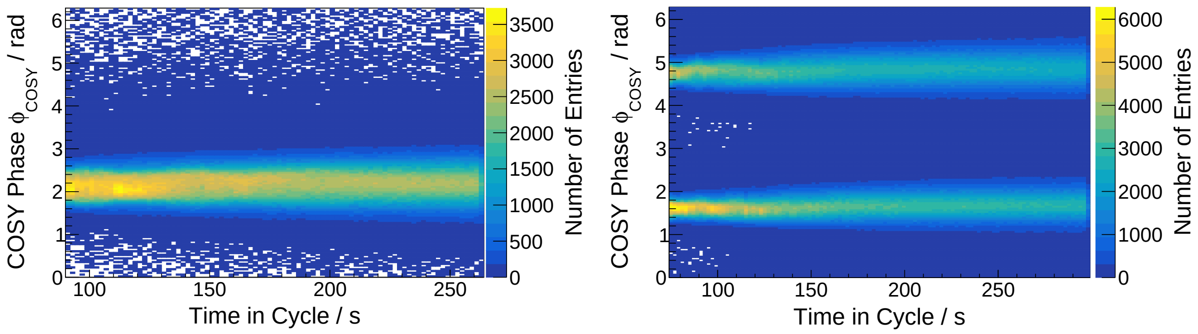

(a) Single Bunch

(b) Two Bunches

Figure 6.3.: COSY Phase ϕ_{COSY} for a single bunch and two bunches stored in COSY as a function of time in the cycle.

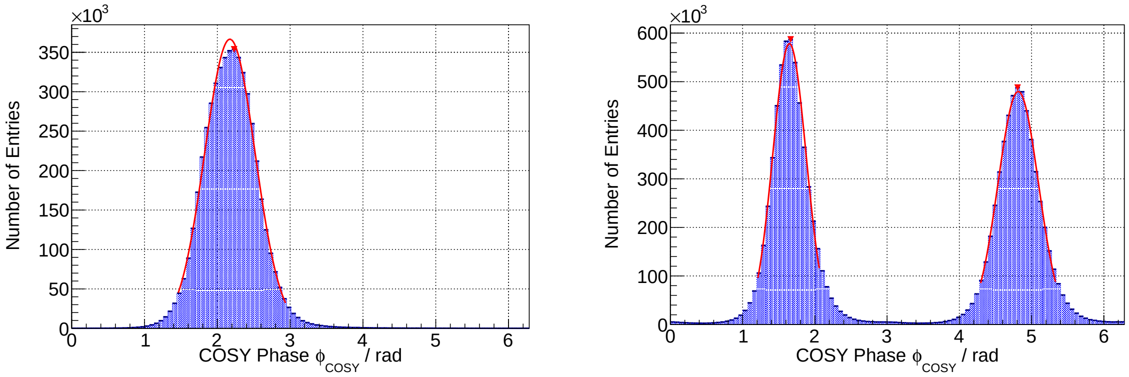

(a) Single Bunch

(b) Two Bunches

Figure 6.4.: COSY Phase ϕ_{COSY} for a single bunch and two bunches stored in COSY integrated over the cycle time. A two-standard-deviation range around the mean is used for further calculation of the Invariant Spin Axis.

To have enough statistics in both cases, the event distribution is split in such a way that the number of events remains constant. Due to the symmetry of the Gaussian distribution, it is sufficient to find the solution for x of the following equation

$$\int_{-\infty}^{x} G(x';\mu,\sigma)dx' \overset{!}{=} \int_{x}^{\mu} G(x';\mu,\sigma)dx'. \tag{6.5}$$

This can be numerically solved, which leads to $x \approx 0.67\sigma$, where σ denotes the standard deviation of the distribution. The following events in the center of the distribution

$$\phi_{\text{COSY}} \in [-0.67, 0.67]\sigma_{\phi_{\text{COSY}}}, \tag{6.6}$$

and the events in the head and tail of the distribution

$$\phi_{\text{COSY}} \in [-5\sigma_{\phi_{\text{COSY}}}, -0.67\sigma_{\phi_{\text{COSY}}}] \vee [0.67\sigma_{\phi_{\text{COSY}}}, 5\sigma_{\phi_{\text{COSY}}}], \tag{6.7}$$

are studied when calculating the orientation of the Invariant Spin Axis at the solenoids and the RF Wien filter. The results are presented in section 7.4.4 and 7.8.1.

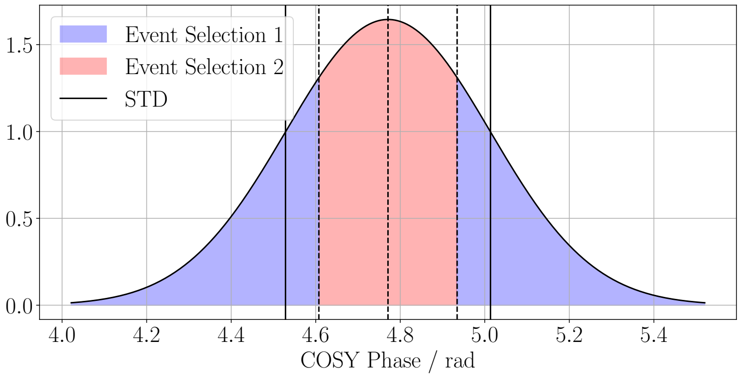

Figure 6.5.: Schematic of the optimal split for event selection studies of the COSY phase. For the event selection studies, all events inside the range of $[-0.67, 0.67]$ standard deviations of the COSY phase event distribution are compared with all events outside this range.

The event selection of real data is shown in Figure 6.6 for the case of two bunches in COSY. In Figure 6.6a, the center events are shown, and in Figure 6.6b, the head and tail event selection is shown. Note that the number of events in both cases for the individual bunches is approximately the same, which simplifies the remaining fitting procedure as the fit to the spin tune phase and the buildup of the polarization is prone to errors when the number of events is too small.

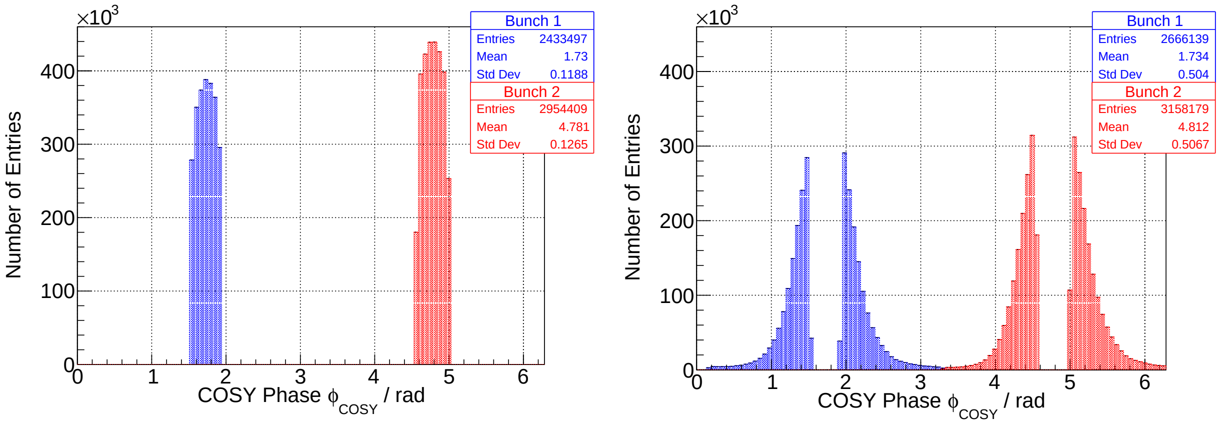

(a) Central Events.

(b) Head and Tail events.

Figure 6.6.: Example of the event selections based on the COSY phase ϕ_{COSY}, as defined in Eq. (6.4), for two bunches stored in COSY. The left panel illustrates the event selection of the central events, and the right panel depicts the selected events in the head and tail of the two bunches.

6.4. Left - Right Asymmetry (Vertical Polarization)

To compute the left-right asymmetry, two point-like detectors at azimuthal angles of $\phi_L = 0°$ and $\phi_R = 180°$ are assumed. The left-right asymmetry is directly proportional to the vertical polarization component of the bunched beam. The averaged unpolarized differential cross-section is given by

$$\bar{\sigma}_{0X} = \int_{\text{Detector}} \sigma_0 \mathrm{d}\Omega \text{ with } X \in \{L, R\}. \tag{6.8}$$

Using the differential cross-section derived in Eq. (4.59), the event rates in a time interval Δt in both detectors are given by

$$N_R = I d_t \bar{\sigma}_{0R} \Delta t \left(1 - \frac{3}{2} p_Z A_z\right), \tag{6.9}$$

$$N_L = I d_t \bar{\sigma}_{0L} \Delta t \left(1 + \frac{3}{2} p_Z A_z\right), \tag{6.10}$$

assuming that the vector analyzing component A_z is the same for all four quadrants. To determine the vector polarization, the following left-right-asymmetry is calculated

$$\epsilon_{\text{LR}} = \frac{N_R - N_L}{N_R + N_L} \tag{6.11}$$

$$= \frac{3}{2} p_Z A_Z, \tag{6.12}$$

assuming $\bar{\sigma}_{0L} = \bar{\sigma}_{0R}$. Note that the constructed asymmetry is independent of beam parameters such as the beam intensity I and the target density d_t. The statistical uncertainty of the left-right asymmetry can be calculated using Gaussian error propagation as

$$\sigma_{\epsilon_{\text{LR}}} = \sqrt{\frac{4N_R^2 N_L + 4N_R N_L^2}{(N_R + N_L)^4}} = \sqrt{\frac{4N_L N_R}{(N_R + N_L)^3}}, \tag{6.13}$$

assuming Poisson statistics for the number of events in the individual detectors for a distinct time bin

$$\sigma_{N_X} = \sqrt{N_X} \text{ for } X \in \{R, L\}. \tag{6.14}$$

An example of the left-right asymmetry as a function of time in the cycle is shown in Figure 6.7 for a measurement of the Spin Coherence Time (cf. section 7.2). The left-right asymmetry changes at 90 s when rotating the vertically polarized beam into the horizontal plane. Afterwards, the Siberian snake is switched on at 100 s, which leads to a small change in the left-right asymmetry. These fake effects are a result of imperfections in the Siberian snake. Towards the end of the cycle, the left-right asymmetry saturates at $-10\,\%$. In principle, the left-right asymmetry should read zero after rotating the vertical polarization into the horizontal plane. However, fake asymmetries occur when the beam hits the carbon target at an angle or due to acceptance differences of the quadrant. Therefore, unpolarized cycles are used as a baseline to correct the left-right asymmetry of polarized cycles. More information about this calibration is given in the following section 6.4.1.

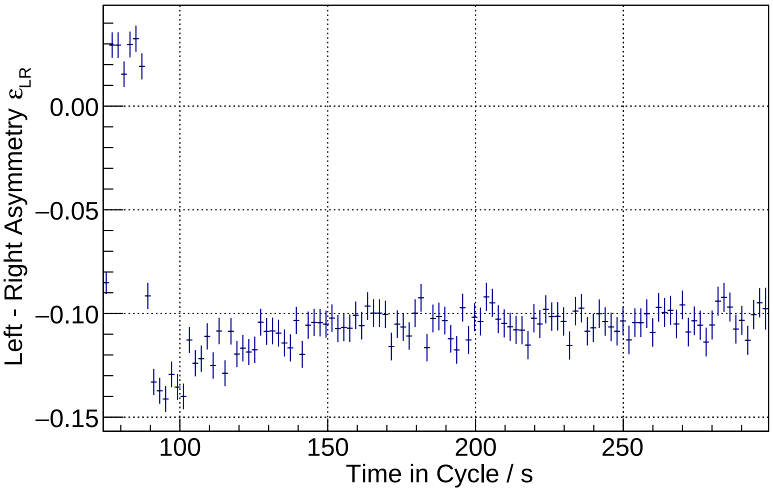

Figure 6.7.: Left-right asymmetry as a function of time in the cycle during a measurement of the Spin Coherence Time.

6.4.1. Left - Right Asymmetry Correction using Unpolarized Cycles

The calibration of the left-right asymmetry is performed using the left-right asymmetry from unpolarized cycles. As no vertical or tensor polarization is present in the beam, the left-right asymmetry should be zero throughout the cycle, which can be used as a baseline for cycles with a polarized beam. Each setting for the determination of the Invariant Spin Axis was measured five times. In total, four cycles are taken with a polarized beam, and one cycle is measured using an unpolarized beam. The five cycles for the same setting, including the unpolarized one, are collectively referred to as a "Run" in this thesis. The cycles in which polarized beams are used are corrected using the cycles with an unpolarized beam. Subsequently, the settings for measuring the Invariant Spin Axis are altered, and the same procedure is repeated.

An example of the uncorrected left-right asymmetry from a cycle using an unpolarized beam is shown in Figure 6.8 (red data points). Assuming a linear model for the fake buildup of the left-right asymmetry, a least squares fit is performed according to

$$f_{\text{buildup}}(t; t_{\text{WF}}, A, B) = A \cdot (t - t_{\text{WF}}) + B, \tag{6.15}$$

where t_{WF} denotes the fixed time switching on the RF Wien filter. The time-dependent correction is empirical. It is probably caused by small movements of the beam during the cycle and cannot be related to polarization rotations as no polarization is present in the beam. Only the time range after switching on the RF Wien filter is used, as this is the main measurement time for the determination of the Invariant Spin Axis. The left-right asymmetry is corrected using the fit parameter values

$$\epsilon_{\text{LR}}^{\text{corr.}}(t \geq t_{\text{WF}}) = \epsilon_{\text{LR}}^{\text{uncorr.}}(t \geq t_{\text{WF}}) - f_{\text{buildup}}(t; t_{\text{WF}}, A, B). \tag{6.16}$$

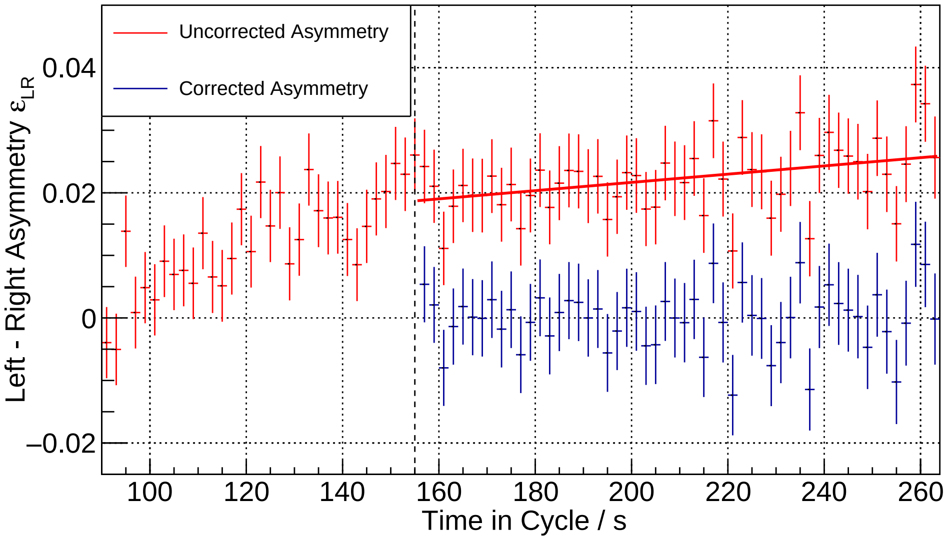

Figure 6.8.: Correction of the left-right asymmetry of an unpolarized cycle during the main measurement period after switching on the RF Wien filter at $t_{\mathrm{WF}} = 155\,\mathrm{s}$ (dashed black line) assuming a fake asymmetry according to Eq. (6.15). The fit parameters read $A = 0.66(25) \times 10^{-4}\,{}^{1}\!/\mathrm{s}$, $B = 0.0190(16)$ and the fit quality is given by $\chi^2/\mathrm{ndf} = {}^{54.17}\!/_{53} = 1.02$. The left-right asymmetry is corrected according to Eq. (6.16), leading to the zero line polarization, which is expected for an unpolarized beam.

For simplicity, the corrected left-right asymmetry is written as ϵ_{LR} in the following. The corrected left-right asymmetry of a cycle using an unpolarized beam is shown in Figure 6.8 (blue data points). The corrected left-right asymmetry is a zero line. The fit results are used to correct the left-right asymmetry for the remaining cycles for each Run with the same settings with a polarized beam. An example of such a cycle is illustrated in Figure 6.9. Note that the shown time range is restricted to the main measurement period when running the RF Wien filter to determine the orientation of the Invariant Spin Axis at the location of the RF Wien filter. The change of left-right asymmetry before switching on the RF Wien filter is related to orbit and beam profile changes when ramping the Siberian snake.

The corrected left-right asymmetry is proportional to the true vertical polarization component. In principle, the asymmetry should be at zero before switching on the RF Wien filter at 155 s in the cycle. However, sometimes the RF solenoid has inconsistencies in rotating the polarization into the horizontal plane. This is not an issue, as the experimental observable which is used to determine the orientation of the Invariant Spin Axis is based on the polarization change after switching on the RF Wien filter.[1] The change in polarization is also corrected by the slope A in Eq. (6.15). More information about the change of polarization and its relation to the measurement of the Invariant Spin Axis is explained in sections 7.6.2 and 7.6.3.

---

[1] Linear change of ϵ_{LR} between 155 s and 180 s.

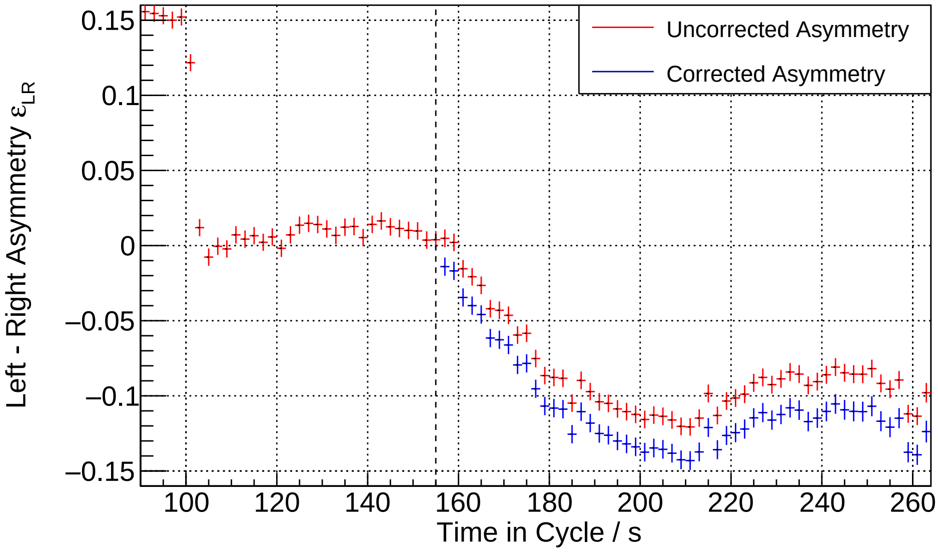

Figure 6.9.: Correction of the left-right asymmetry of a cycle using a polarized beam which was taken during the same Run as the unpolarized cycle in Figure 6.8. Note that the time range of correction is limited to the measurement period when the RF Wien filter ($t_{\mathrm{WF}} = 155\,\mathrm{s}$, dashed black line) is rotating the polarization. At 90 s, the RF solenoid rotates the initial vertical polarization into the accelerator plane.

6.5. Up - Down Asymmetry (In-Plane Polarization)

The analytical work from Eq. (6.20) to (6.31) is taken from former IKP student Dennis Eversmann's PhD Thesis *High Precision Spin Tune Determination at the Cooler Synchrotron in Jülich* [44, p.41-46].

The difficulty of analyzing the in-plane polarization is related to the fast in-plane rotation of the polarization, i.e., the spin tune which is introduced in section 4.2.1. The angular precession of the in-plane polarization can be written as

$$P_H(t) = P_Z \sin(2\pi\nu_s f_{\mathrm{COSY}} t). \tag{6.17}$$

The magnitude of the in-plane polarization is given by

$$P_Z = \sqrt{p_x^2 + p_z^2}, \tag{6.18}$$

with z pointing in the longitudinal beam direction and x pointing in the radial direction. Note that with a polarimeter, the in-plane polarization can only be measured in quadrature. A determination of the individual longitudinal and radial polarization is not possible. The angular frequency of the polarized deuteron beam is approximately

$$f_s = |\nu_s| f_{\mathrm{COSY}} \approx 0.16 \cdot 751\,\mathrm{kHz} = 121\,\mathrm{kHz}. \tag{6.19}$$

On the other hand, the data acquisition (DAQ) of the polarimeter can only handle event rates up to 5000 Hz. A simple least squares fit of the event rates with the spin tune and in-plane magnitude as parameters is not possible, as only one event is detected per 24 spin revolutions. In the following chapter, a method based on mapping the event rates into two periods (4π) oscillation period is given. First, the event rates of the upper and lower detectors are subdivided into $\Delta T = 2\,\mathrm{s}(\approx 10^6$ turns) bins. By generating specialized count rate asymmetries, the in-plane polarization can be calculated. One significant benefit of the mapping method is its freedom from dependence on beam properties, except for polarization. Factors such as beam luminosity and detector acceptance do not influence the results.

For each event recorded in the up and down detector, a turn number n is assigned. The spin phase advance ϕ_s is defined as

$$\phi_s(n) = 2\pi n|\nu_s^0|, \tag{6.20}$$

where ν_s^0 denotes the assumed spin tune for each recorded event. In theory, it is known that the spin tune is negative (counter-clockwise rotation of the polarization for a clockwise rotating beam). For practical and historical reasons, only the absolute value is used in this thesis. Using the modulo operator, the spin phase advance is mapped into a 4π interval

$$\phi_s(n) = \phi_s(n) \bmod 4\pi. \tag{6.21}$$

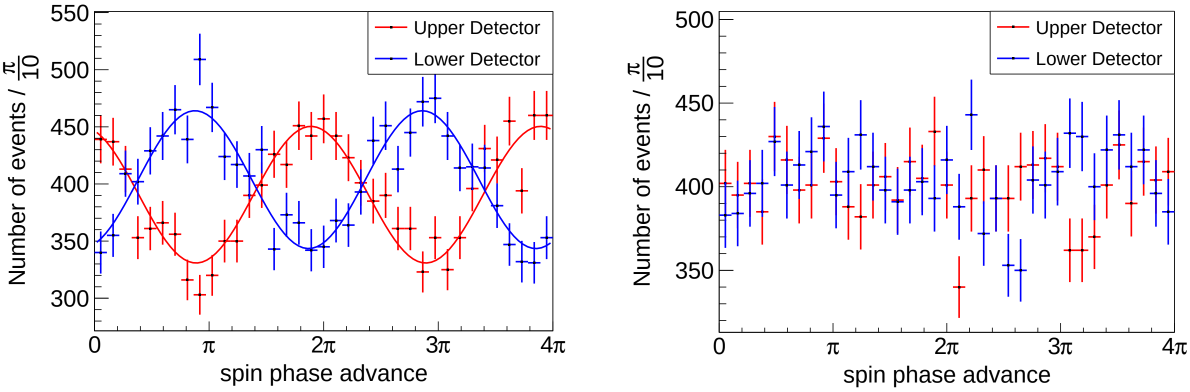

(a) $\nu_s^0 = 0.1609706675$ (b) $\nu_s^0 = 0.1609702$

Figure 6.10.: The spin phase advance, as per Eq. (6.21), is computed separately for the up and down detectors, each under the assumption of two distinct spin tunes ν_s over a macroscopic time range. The left panel shows a distinct oscillation pattern, indicating that the assumed spin tune is close to the real spin tune, while the right panel shows no effect.

This process is iterated for each microscopic time interval, separately for the up and down detectors. In Figure 6.10, two examples of the mapped spin phase advance, following Eq. (6.21), are presented for two distinct assumed spin tunes. The statistical error for each bin is determined by $\sigma_{\text{bin}} = \sqrt{N}$ assuming Poisson statistics. Figure 6.10a shows a distinct oscillation pattern for both detectors with opposite signs, suggesting that the assumed spin tune approximately matches the actual spin tune. The phase shift of π is a result of the polar angle dependence ϕ in the cross-section of a polarized deuteron beam scattering on a carbon target (cf. Eq. (4.60)). Conversely, in Figure 6.10b, no oscillation pattern is evident, indicating that the assumed spin tune is inconsistent with the true spin tune. The events depicted in Figure 6.10 depend on the

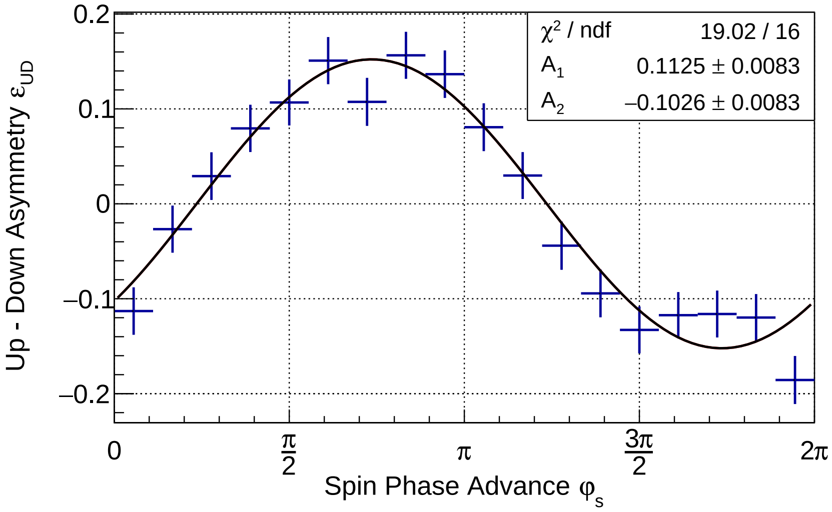

Figure 6.11.: Vertical up-down asymmetry ϵ_{UD} as a function of the Spin Phase Advance along with a least square fit according to Eq. (6.26). The data is collected during a two-second interval. The amplitude of the oscillation corresponds to the amount of the up-down asymmetry which is proportional to the in-plane polarization.

acceptance of the upper and lower detectors, the beam luminosity, and the target density. In the following, new count rates are computed which cancel out these dependencies.

Based on the spin phase advance in Eq. (6.21), the following new count rates are defined

$$N_X^{\pm}(\phi_s) = \begin{cases} N_X(\phi_s) \pm N_X(\phi_s + 3\pi) & \text{for } 0 \le \phi_s < \pi \\ N_X(\phi_s) \pm N_X(\phi_s + \pi) & \text{for } \pi \le \phi_s < 2\pi \end{cases}, \tag{6.22}$$

where X denotes either the upper or lower detector. Based on these count rates, an up-down asymmetry, similar to the asymmetry for the vertical polarization in Eq. (6.12) can be computed

$$\epsilon_{\mathrm{UD}}(\phi_{\mathrm{s}}) = \frac{N_{\mathrm{U}}^{-}(\phi_{\mathrm{s}}) - N_{\mathrm{D}}^{-}(\phi_{\mathrm{s}})}{N_{\mathrm{U}}^{+}(\phi_{\mathrm{s}}) + N_{\mathrm{D}}^{+}(\phi_{\mathrm{s}})} \tag{6.23}$$

$$= \frac{3}{2} p_Z \frac{\overline{\sigma_{0\mathrm{U}}}\overline{A_y} - \overline{\sigma_{0\mathrm{D}}}\overline{A_y}}{\overline{\sigma_{0\mathrm{U}}} + \overline{\sigma_{0\mathrm{D}}}} \sin\left(\phi_{\mathrm{s}} + \tilde{\phi}_s\right) \tag{6.24}$$

$$= \tilde{\epsilon}_{\mathrm{UD}} \sin\left(\phi_{\mathrm{s}} + \tilde{\phi}_s\right), \tag{6.25}$$

where $\sigma_{\bar{0}\mathrm{U}}$ and $\sigma_{\bar{0}\mathrm{D}}$ denote the unpolarized scattering cross-section averaged over the detector acceptance for the upper and lower detector. The averaged analyzing power is given by $\bar{A}_y$ and the amount of in-plane polarization is given by P_Z. An example of the up-down asymmetry is shown in Figure 6.11. The resulting sine curve is fitted by the least squares method according to

$$\epsilon_{\mathrm{UD}}(\phi_s) = A_1 \sin(\phi_s) + A_2 \cos(\phi_s). \tag{6.26}$$

Note that this formula corresponds to a normal sine fit with

$$A_1 \sin\left(\tilde{\phi}_s\right) + A_2 \cos\left(\tilde{\phi}_s\right) = \tilde{\epsilon}_{\mathrm{UD}} \sin\left(\phi_{\mathrm{s}} + \tilde{\phi}_s\right) \text{ with } A_1 = \tilde{\epsilon}_{\mathrm{UD}} \cos(\phi_{\mathrm{s}}) \text{ and } A_2 = \tilde{\epsilon}_{\mathrm{UD}} \sin(\phi_{\mathrm{s}}). \tag{6.27}$$

From the resulting fit parameters, the initial spin precession phase $\tilde{\phi}_s$ and the in-plane polarization can be calculated via

$$\tilde{\epsilon}_{\mathrm{UD}} = \sqrt{A_1^2 + A_2^2}, \tag{6.28}$$

$$\tilde{\phi}_s = \operatorname{atan2}(A_2, A_1), \tag{6.29}$$

where atan2 denotes the two-dimensional arctangent [97]. For simplification, the amplitude and phase are from here on written as ϵ_{UD} and ϕ_s. The statistical uncertainty can be calculated using Gaussian error propagation

$$\sigma^2_{\epsilon_{\mathrm{UD}}} = \frac{A_1^2\sigma^2_{A_1} + A_2^2\sigma^2_{A_2} + 2A_1A_2\sigma_{A_1}\sigma_{A_2}\rho(A_1, A_2)}{A_1^2 + A_2^2}, \tag{6.30}$$

$$\sigma^2_{\phi_s} = \frac{A_2^2\sigma^2_{A_1} + A_1^2\sigma^2_{A_2} - 2A_1A_2\sigma_{A_1}\sigma_{A_2}\rho(A_1, A_2)}{\left(A_1^2 + A_2^2\right)^2}, \tag{6.31}$$

where $\rho(A_1, A_2)$ denotes the correlation coefficient between the fit parameters A_1 and A_2. An example of the vertical up-down asymmetry as a function of time is shown in Figure 6.15.

When fitting an oscillation, a bias of the amplitude parameters occurs if the amplitude relative to the uncertainties is small, i.e., if the in-plane polarization is small. A new method, based on Feldman - Cousin confidence intervals and Bayes' theorem was developed in reference [98].

6.5.1. Determination of the Spin Tune

For the determination of the time-dependent spin tune, a fixed, constant spin tune ν_s^0 is chosen, which acts as a baseline for the change of the spin tune $\Delta\nu_s$. The turn-dependent spin tune can be split into a constant term and the turn-dependent deviations

$$\frac{\nu_s(n)}{\nu_s^0} = 1 + \frac{\Delta\nu_s(n)}{\Delta\nu_s^0} \tag{6.32}$$

$$= 1 + \frac{\Delta f_s(n)}{f_s} - \frac{\Delta f_{\mathrm{COSY}}(n)}{f_{\mathrm{COSY}}} \tag{6.33}$$

$$= 1 + \frac{1}{2\pi\nu_s^0}\frac{\partial\phi_s(n)}{\partial n}. \tag{6.34}$$

The definition of the spin tune $\nu_s = {}^{f_s}\!/\!{}_{f_{\mathrm{COSY}}}$ transfroms Eq. (6.33) into Eq. (6.34) and the phase $\phi_s(n)$ corresponds to the phase defined in Eq. (6.29). The determination of the turn-dependent phase difference allows for the calculation of the spin tune

$$\nu_s(n) = \nu_s^0 + \frac{1}{2\pi}\frac{\partial\phi_s(n)}{\partial n}, \text{ or} \tag{6.35}$$

$$\nu_s(t) = \nu_s^0 + \frac{1}{2\pi f_{\mathrm{COSY}}}\frac{\partial\phi_s(t)}{\partial t}. \tag{6.36}$$

In Eq. (6.36), the conversion from the turn number to the time frame is used,

$$t = \frac{n}{f_{\mathrm{COSY}}}. \tag{6.37}$$

The effect of sampling a spin tune ν_s^0 which does not correspond to the true oscillation frequency is depicted in Figure 6.12. The orange curve illustrates the sampling frequency while the blue curve represents the true oscillation frequency. The phase difference between the curves is depicted by the arrows which increase over time. As soon as the sampling frequency hits the true oscillation frequency, the phase difference remains constant. In other words, the spin tune phase ϕ_s denotes the phase difference between the assumed spin tune ν_s^0 and the true spin tune frequency ν_s.

In Figure 6.13, this effect is shown for real spin tune data. The left panel shows the spin tune phase for different assumed spin tunes ν_s^0. To determine the derivative of the spin tune phase, the spin tune phase is fitted with a polynomial of 8th order. The instability of the phase (and consequently of the spin tune) is a consequence of imperfections in the ring, like small orbit changes, etc. The change of phase according to the fit is given by

$$\phi_s = \sum_{i=0}^{8} a_i t^i. \tag{6.38}$$

The derivation is given by

$$\frac{\partial \phi_s}{\partial t} = \sum_{i=0}^{8} a_i t^{i-1} i, \tag{6.39}$$

where a_i denotes the ith fit parameter. The statistical uncertainty including the correlation coefficient $\rho(a_j, a_k)$ between the fit parameters a_j and a_k of $\frac{\partial \phi_s}{\partial t}$ is given by

$$\sigma_{\left(\frac{\partial \phi_s}{\partial t}\right)}(t)^2 = \sum_{i=0}^{8} \left(t^{i-1} i \sigma_{a_i}\right)^2 + 2 \sum_{j=1}^{8} \sum_{\substack{k=1 \\ j \neq k}}^{8} t^{j-1} j \cdot t^{k-1} k \cdot \sigma_{a_j} \sigma_{a_k} \rho\left(a_j, a_k\right). \tag{6.40}$$

The statistical uncertainty of the time-dependent spin tune is given by

$$\sigma_{\nu_s}(t) = \frac{1}{2\pi} \sigma_{\left(\frac{\partial \phi_s}{\partial t}\right)}(t). \tag{6.41}$$

The time-dependent spin tune is shown in Figure 6.13 (right panel). The results are independent of the initial choice of the baseline spin tune ν_s^0. Small deviations can occur due to inconsistencies in the fitting procedure. The statistical sensitivity is in the order of $\mathcal{O}(10^{-10})$ which corresponds to a sensitivity for the oscillation frequency of the polarization of $\mathcal{O}(1\,\mathrm{mHz})$.

The online determination of the spin tune is crucial for the experiment, as an online feedback system constantly measures the oscillating polarization frequency and adjusts the RF Wien filter frequency to one of the harmonics of the spin tune. More information about the phase feedback is given in section 6.7. During the experiment, the spin tune is determined based on the resonance frequency of the RF solenoid to rotate the vertical polarization into the accelerator plane. If the spin tune is changed due to additional solenoidal fields of the Siberian

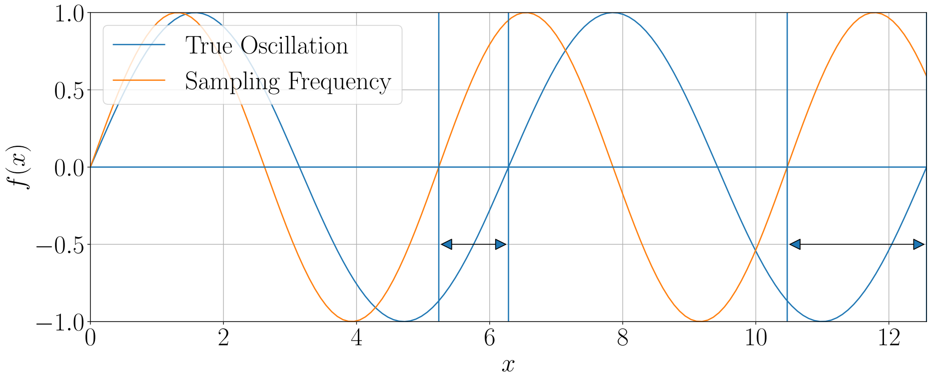

Figure 6.12.: Schematic showing the phase difference when the assumed spin tune (orange curve) is faster than the real spin tune (blue curve). The arrows indicate the phase shift. If the assumed spin tune matches the real one, the phase shift stays constant over time.

snake or the 2 MV solenoid, a Fourier spectrum of the data rates in the polarimeter in a certain range around the expected spin tune is computed. The spin tune which leads to the largest amplitude is used as a new spin tune for the next cycle.

6.5.2. Correction of the Up - Down Asymmetry

In principle, the procedure in the last section can be used to calculate the amount of in-plane polarization throughout a cycle. However, for most runs, a polynomial fit of the spin tune phase is not possible. The RF Wien filter rotates the polarization several times in a cycle, resulting in spin tune phases that cannot be fitted directly. Therefore, an easier approach is chosen, assuming a constant spin tune throughout a cycle. An initial guess for the spin tune can be calculated using the following formula

$$
\begin{aligned}
\nu^{0}_{s,\text{guess}} &= \nu_s^{\text{Init}} + \Delta\nu_s^{\text{Solenoids}} && (6.42)\\
&= \gamma G + \Delta\nu_s^{\text{Solenoids}} && (6.43)\\
&= \frac{G}{\sqrt{1-\frac{v^2}{c^2}}} + \Delta\nu_s^{\text{Solenoids}} && (6.44)\\
&= \frac{G}{\sqrt{1-\frac{f^2_{\text{COSY}}L^2_{\text{COSY}}}{c^2}}} + \Delta\nu_s^{\text{Solenoids}}, && (6.45)
\end{aligned}
$$

where G, f_{COSY}, and L_{COSY} denote the anomalous g factor, the revolution frequency, and the length of COSY, respectively. In addition, ramping solenoidal fields, such as the 2MV Cooler solenoid or the Siberian snake, manipulate the spin tune. The change of spin tune due to solenoidal fields is discussed and derived in section 7.4. In this section, the final result of the

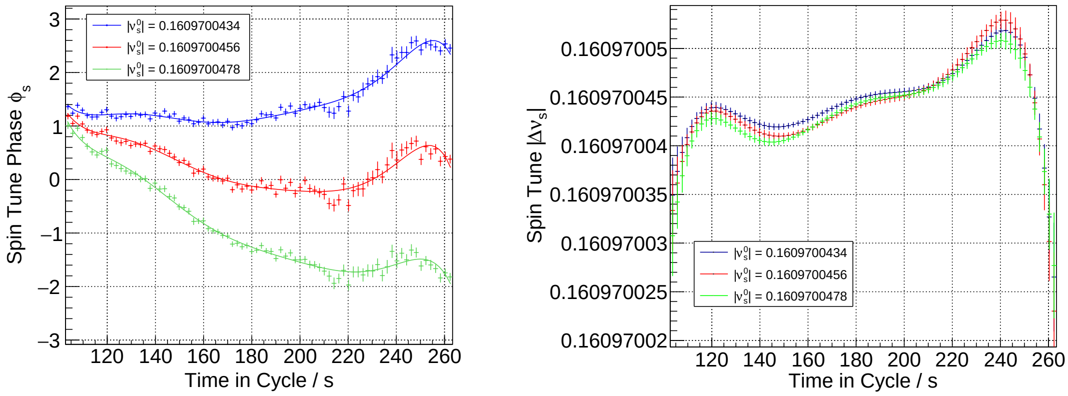

Figure 6.13.: The change of spin tune phase for different baseline spin tunes which is used to determine the time-dependent spin tune change by fitting a polynomial is shown in the left panel. The resulting time-dependent spin tune is shown in the right panel.

change of the spin tune with respect to the initial spin tune without extra solenoidal fields is given by

$$\begin{aligned}\Delta\nu_s^{\text{Solenoids}} =& \frac{1}{-\pi\sin(\pi\nu_s^0)} \times \\ & \Bigg[\cos(\pi\nu_s^0)\left(\cos\left(\frac{k_{\text{Snake}} I_{\text{Snake}}}{2}\right)\cos\left(\frac{k_{\text{2MV Sol.}} I_{\text{2MV Sol.}}}{2}\right) - 1\right) \\ & - \sin\left(\frac{k_{\text{Snake}} I_{\text{Snake}}}{2}\right)\sin\left(\frac{k_{\text{2MV Sol.}} I_{\text{2MV Sol.}}}{2}\right) \\ & - n_z^{\text{2MV Sol.}}\sin(\pi\nu_s^0)\sin\left(\frac{k_{\text{Snake}} I_{\text{Snake}}}{2}\right)\cos\left(\frac{k_{\text{2MV Sol.}} I_{\text{2MV Sol.}}}{2}\right) \\ & - n_z^{\text{Sib. Snake}}\sin(\pi\nu_s^0)\sin\left(\frac{k_{\text{Snake}} I_{\text{Snake}}}{2}\right)\cos\left(\frac{k_{\text{2MV Sol.}} I_{\text{2MV Sol.}}}{2}\right)\Bigg] \\ & + \Delta\nu_{s,0}.\end{aligned} \tag{6.46}$$

The parameters I_{Snake} and $I_{\text{2MV Sol.}}$ denote the currents in amperes applied to the power supplies of the solenoids. The calibration factors k_{Snake} and $k_{\text{2MV Sol.}}$ describe the conversion from applied current to effective spin rotation angle inside the solenoidal field. Additionally, $n_z^{\text{2MV Sol.}}$ and n_z^{Snake} represent the longitudinal projection of the Invariant Spin Axis at the location of the 2MV solenoid and the Siberian snake magnet. The offset $\Delta\nu_{s,0}$ takes spin tune changes during the cycle into account. The final results for the individual measurements are given in section 7.4. The combination of Eqs. (6.45) and (6.46) allows for a calculation of an initial guess of the spin tune to determine the final up-down asymmetry. In most cases, the first guess of the spin tune does not precisely match the correct spin tune of the cycle. Therefore, the phase calculated from the initial guess is fitted with a linear function

$$\phi_s = at + b \Rightarrow \frac{\partial\phi_s}{\partial t} = a. \tag{6.47}$$

Using Eq. (6.36), the final guess for the spin tune can be calculated via

$$\nu_s^{\text{Final}} = \nu_s^{\text{Init.}} + \frac{a}{2\pi f_{\text{COSY}}}. \tag{6.48}$$

This procedure is illustrated in Figure 6.14. The red data points represent the spin tune phase, which is calculated using the initial guess of the spin tune $\nu_s^{\text{Init.}}$. The spin tune phase is fitted with a linear function (black curve). The fit parameters are used to calculate the final guess for the spin tune ν_s^{Final}. As it can be clearly seen, the final spin tune phase remains more constant throughout the cycle than the spin tune phase calculated from the initial guess of the spin tune.

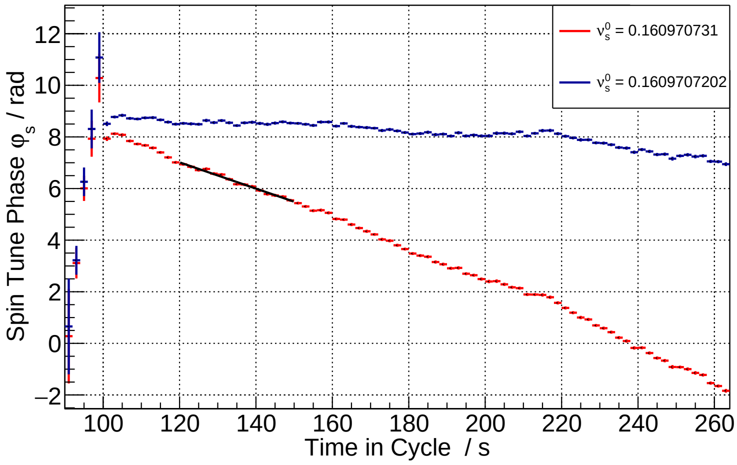

Figure 6.14.: The red data points represent the spin tune phase calculated using the initial guess calculated via Eq. (6.45). The phase is fitted with Eq. (6.47) from 120 to 150 s. The fit quality is given by $\chi^2/\text{ndf} = {}^{10.52}/_{13} = 0.81$, and the slope reads $-0.051\ {}^1/_s$. Using Eq. (6.48), the final spin tune guess can be calculated resulting in more stable phases and a more precise determination of the up-down asymmetry.

The gain of this optimization method is illustrated in Figure 6.15. The uncorrected asymmetry corresponds to the asymmetry calculated using the initial guess of the spin tune, while the corrected asymmetry shows the up-down asymmetry for the final guess of the spin tune. The lower panel shows the ratio of the two asymmetries. Depending on how close the initial guess is to the true initial spin tune, the ratio changes. In the case of Figure 6.15, the correction is in the order of magnitude of 1 %.

To summarize this chapter, the up-down asymmetry is calculated using the following steps:

1. Calculate an initial guess for the spin tune taking the extra solenoidal fields of the Siberian snake and the 2MV solenoid into account, i.e., Eq. (6.45).
2. Calculate the spin tune phase using the initial guess for the spin tune and fit the phase using a linear function. From the fit parameters, the offset to the true spin tune can be calculated, which leads to the final guess of the spin tune.
3. Using the final guess of the spin tune, the up-down asymmetry can be calculated while the spin tune phase should stay more or less constant during the cycle.

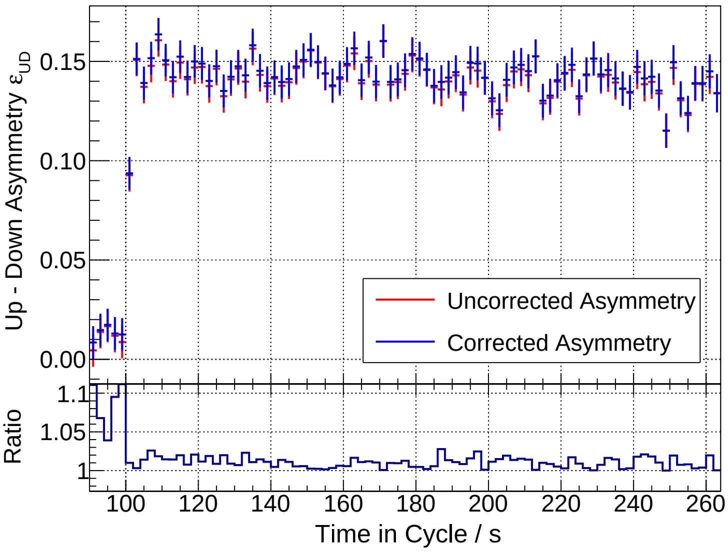

Figure 6.15.: Comparison of the up-down asymmetry using the initial guess of the spin tune $\nu_s^{\text{Init.}}$ and using the final guess of the spin tune ν_s^{Final}. The lower panel shows the ratio of the two ratios. In this case, the correction of up-down asymmetry is in the order of 1 %.

6.6. Angle between Vertical and Horizontal Polarization & Total Polarization

As it will be further described in sections 7.6.2 and 7.6.3, the determination of the Invariant Spin Axis can be calculated by observing a buildup rate of the vertical polarization initialized by the RF Wien filter. In section 7.6.2, a model for the buildup is developed describing the angle between the vertical and in-plane polarization components and the total polarization. The angle is defined as

$$\alpha = \arctan\left(\frac{P_V}{P_H}\right) = \arctan\left(\frac{\epsilon_{\text{LR}}}{\epsilon_{\text{UD}}}\right), \tag{6.49}$$

$$\sigma_\alpha^2 = \frac{\epsilon_{\text{UD}}^2 \sigma_{\epsilon_{\text{LR}}}^2 + \epsilon_{\text{LR}}^2 \sigma_{\epsilon_{\text{UD}}}^2}{\epsilon_{\text{UD}}^2 + \epsilon_{\text{LR}}^2}, \tag{6.50}$$

and is independent of the magnitude of the polarization and of analyzing powers.

The total amount of polarization of the circulating deuteron beam can be determined from the in-plane and vertical polarization components

$$P = \sqrt{P_V^2 + P_H^2}. \tag{6.51}$$

From the left-right and up-down asymmetries measured using the polarimeters, a new variable $\epsilon_{\text{tot.}}$ can be computed, which scales with the total amount of polarization as both asymmetries share the analyzing power as a common scaling factor

$$\epsilon_{\text{tot}} = \sqrt{\epsilon_{\text{LR}}^2 + \epsilon_{\text{UD}}^2}, \tag{6.52}$$

$$\sigma_{\epsilon_{\text{tot}}} = \frac{1}{\epsilon_{\text{tot}}} \sqrt{\epsilon_{\text{LR}}^2 \sigma_{\epsilon_{\text{LR}}}^2 + \epsilon_{\text{UD}}^2 \sigma_{\epsilon_{\text{UD}}}^2}. \tag{6.53}$$

For simplicity, $\epsilon_{\text{tot.}}$ is called from here on also total polarization. An example of both, the angle between vertical and horizontal polarization and the total polarization, is given in the final section of this chapter in Figure 6.22.

6.7. The Phase Feedback

The spin tune phase feedback serves two purposes:

- By continuously monitoring the deuteron-carbon scattering events at the polarimeter, the spin precession frequency is measured throughout the measuring period. The feedback ensures that the RF Wien filter is operating on resonance with a sideband of the spin precession frequency.
- In addition, the phase feedback ensures a constant phase relation (or relative phase) between the spin direction and oscillating frequency of the RF Wien filter.

The effects of the Phase Feedback are shown in Figure 6.16. The bunched beam crossing an RF device (for example, the RF Wien filter) is depicted by the Gaussian bunch distribution at the integer values. On top of the bunched beam, the spin precession in the horizontal accelerator plane is shown. Lastly, also the oscillating radio frequency of the device (RF Wien filter) is shown. If the device is on resonance, the phase of the radio frequency has a fixed relation with respect to the phase of the spin precession at each crossing. In the context of the experiment, the precession frequency in the horizontal plane is given by

$$f_{\text{s}} = \gamma G f_{\text{COSY}}. \tag{6.54}$$

The RF Wien filter needs to run on resonance with the precessing spin. The resonance condition is fulfilled when

$$f_{\text{WF}} = f_{\text{COSY}} |k + \gamma G| \quad \text{with} \quad k \in \mathbb{Z}. \tag{6.55}$$

For technical reasons, the factor $k = -1$ is chosen for the RF Wien filter which corresponds to a Wien filter frequency of approximately $f_{\text{WF}} = 871\,\text{kHz}$.

In an ideal machine, the phase feedback is only necessary to adjust the relative phase between the spin precession frequency and the RF Wien filter frequency and thus, the spin direction at each turn inside the RF Wien filter. However, during the past years, the spin tune was the main subject of many measuring campaigns. It was found that the spin precession frequency changes from cycle to cycle and even during the cycle, the spin tune changes slightly. In Figure 6.17, the change of spin tune over the experimental period of two days is shown. The initial spin tune is defined as the spin tune which is measured during the period of 100 s and 110 s in the cycle before the solenoids are switched on. The typical change of the spin precession frequency

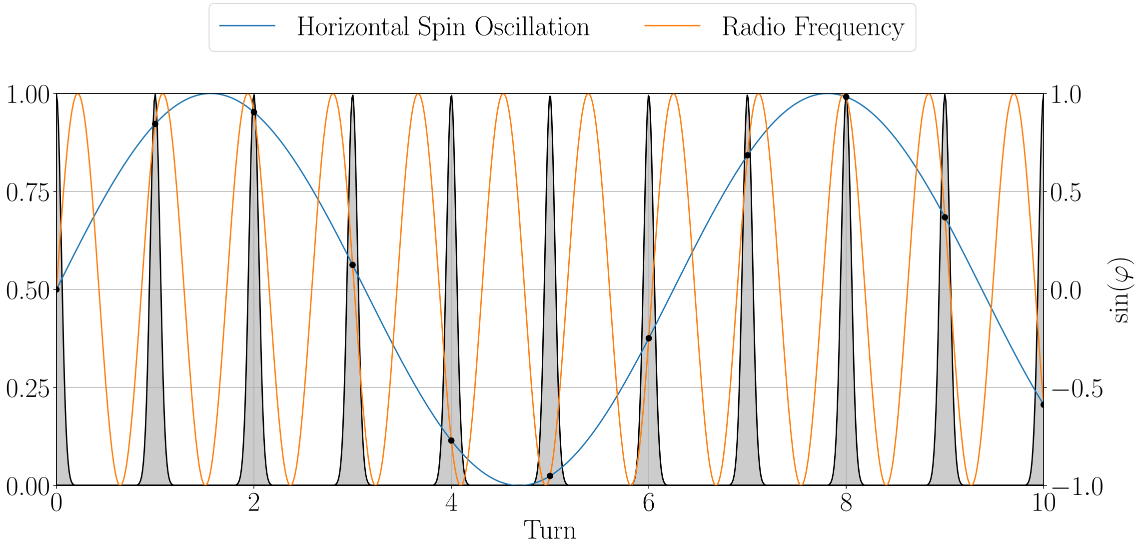

Figure 6.16.: Schematic of the functionality of the phase feedback. The bunched beam, which is represented by the black Gaussian-shaped curves, enters the RF Wien filter each turn. While the horizontal polarization vector component is precessing in the accelerator plane, the RF Wien filter needs to run on a harmonic of the precession frequency for the measurement of the orientation of the Invariant Spin Axis. At each distinct turn number, the phase relation between spin precession and Wien filter remains constant which is represented by the black data points. This is achieved and corrected by an active online phase feedback controlling the RF Wien filter frequency and absolute phase of the oscillation while measuring the oscillation frequency and phase of the precessing polarization on the horizontal plane.

is in the order of 10 mHz. The change of spin tune is very sensitive to temperature changes, magnet settings, and other systematic sources. However, the phase feedback is indispensable, not just because of the day-to-day change in spin tune, but also because of the change in spin tune during a cycle. The change of spin tune during a cycle is shown in Figure 6.13.

In previous experiments at the Cooler Synchrotron COSY, the absolute phase of the spin tune was varied leading to a different buildup when using the RF solenoid [99, 100]. For these experiments, the frequency of the cavity of COSY is changed, slightly changing the Lorentz factor and consequently also the spin precession oscillation frequency. For the experiments reported in this thesis, the frequency of the cavity in COSY f_{COSY} is kept constant, and the RF Wien filter frequency f_{WF} or phase ϕ_{WF} is changed to keep the phase relation constant. The phase relation is given by

$$\phi_{\mathrm{rel.}}(t) = 2\pi(t - t_0)(f_{\mathrm{WF}} - \nu_s f_{\mathrm{COSY}}) + \phi_0, \tag{6.56}$$

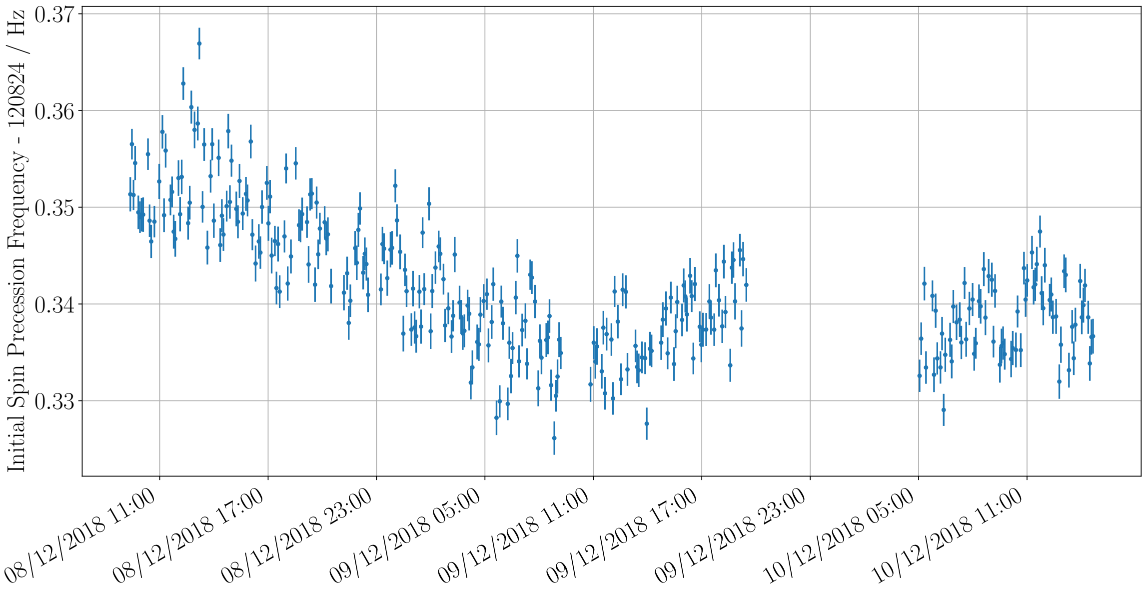

Figure 6.17.: An example of the change of the initial spin tune over the experimental period of two days. The change of spin tune, which is in the order of 10 mHz, is the reason why the phase feedback is necessary to match the phase between the radio frequency of the RF Wien filter and the spin tune oscillation.

where t denotes the time in the cycle, t_0 the start of the measurement and ϕ_0 the phase at $t = t_0$. The time can be sampled as the RF Wien filter is located at a fixed position in the ring to $t - t_0 = {}^{n}/f_{\text{COSY}}$, where n denotes the turn number

$$\phi_{\text{rel.}}(n) = 2\pi n \left(\frac{f_{\text{WF}}}{f_{\text{COSY}}} - \nu_s \right) + \phi_0. \tag{6.57}$$

If the resonance condition as defined in Eq. (6.55) is fulfilled, the fraction of Wien filter frequency and revolution frequency can be written as

$$\frac{f_{\text{WF}}}{f_{\text{COSY}}} = k + \gamma G, \tag{6.58}$$

leading to a stable and fixed phase relation between Wien filter frequency and spin precession frequency

$$\phi_{\text{rel.}}(n) = 2\pi n k + \phi_0. \tag{6.59}$$

Figure 6.18 shows the basic signal flow of the phase feedback. Using the polarimeter, the horizontal spin precession frequency (the spin tune ν_s) and the phase of the spin precession is constantly measured

$$P_H(t) = P_Z \sin(\omega_s t + \phi_s) \text{ with } \omega_s = 2\pi f_{\text{COSY}} \nu_s. \tag{6.60}$$

The RF Wien filter frequency f_{WF} is set by a frequency generator. The absolute phase of the frequency generator is controlled $\phi_{\text{WF}}^{\text{abs.}}$. In addition, also the timestamps of the zero crossings of the Wien filter radio frequency signal are recorded. Since this signal is periodic, Fourier analysis is not necessary. Instead, the average duration of the periods (denoted as T_i) between the signals is calculated. This approach achieved highly precise frequency measurements, with uncertainties in the millihertz range

$$A_{\mathrm{WF}}(t) = A_0 \sin\left(\omega_{\mathrm{WF}} t + \phi_{\mathrm{WF}}^{\mathrm{abs.}}\right) \text{ with } \omega_{\mathrm{WF}} = 2\pi f_{\mathrm{WF}}. \tag{6.61}$$

For the resonant case, the spin tune frequency matches the RF Wien filter frequency, $\omega_s = \omega_{\mathrm{WF}}$. Then, the relative phase is determined by calculating the difference between the RF Wien filter phase and the spin precession phase

$$\phi_{\mathrm{rel.}}^{\mathrm{meas}} = \phi_{\mathrm{rel.}} + \phi_{\mathrm{offset}} = \phi_{\mathrm{WF}}^{\mathrm{abs.}} - \phi_{\mathrm{s}} \overset{!}{=} \phi_{\mathrm{rel}}^{\mathrm{set}}, \tag{6.62}$$

where $\phi_{\mathrm{rel}}^{\mathrm{set}}$ denotes the desired phase relation between Wien filter frequency and spin precession frequency. The desired phase relation is tuned by adjusting the Wien filter phase $\phi_{\mathrm{WF}}^{\mathrm{abs.}}$. The constant offset ϕ_{offset} originates from the relative position of the RF Wien filter and the polarimeter and from cable delays. For each cycle, the phase offset is constant.

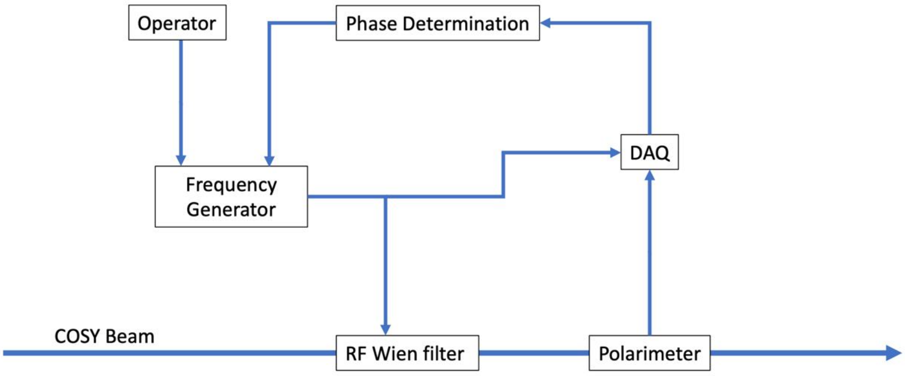

Figure 6.18.: Signal workflow for the phase feedback. Using the polarimeter, the spin tune is constantly measured. By adapting the Wien filter frequency and the absolute Wien filter phase to be the spin tune frequency, the phase relation between spin precession and Wien filter frequency remains constant. The desired phase relation is controlled by the operator. Adapted from FIG. 2 in [99].

In Figure 6.19, the purpose and method of the phase feedback are illustrated. Three measurement periods of 2 s each are schematically shown. The top panel depicts the oscillation of the Wien filter. Without losing generality, the Wien filter phase is set to zero ($\phi_{\mathrm{WF}}^{\mathrm{abs.}} = 0$) for each of the periods. The black dot at each zero crossing represents the signal measured at the discriminator to determine the Wien filter frequency. The panels in the middle represent the horizontal precession of the spins. As the spin precession is too fast for the detector to resolve, only one drawn period in solid lines corresponds to the determination of the up-down asymmetry amplitude and the spin tune phase, as shown in Figure 6.11.

The lower panel depicts the measured relative phase between the Wien filter frequency and spin tune frequency. Two scenarios that can be corrected by the phase feedback are illustrated.

The blue curve corresponds to the case where the frequency of the RF Wien filter is matched to the spin precession frequency but with a constant offset. In this case, a phase shift in the Wien filter frequency generator needs to be introduced, as shown in Figure 6.20 (left panel).

The second scenario is illustrated by the orange curve. If the spin precession frequency does not match the Wien filter frequency, the relative phase between the Wien filter frequency and spin precession changes linearly over time. In this case, the frequency of the RF Wien filter needs to be changed. To calculate the correction factors, the relative phase is fitted in real-time with an analytical fit using a linear model. An offset of the fit with respect to the desired phase relation is fed into the frequency generator. A slope indicates a a frequency shift which can be corrected using

$$\Delta f_{\mathrm{WF}} = \frac{a}{2\pi f_{\mathrm{COSY}}}. \tag{6.63}$$

The Wien filter frequency and the absolute phase changes at the frequency generator of the RF Wien filter are shown schematically in Figure 6.20. If the spin tune or the spin tune phase of the polarized deuteron beam changes, either the Wien filter frequency or the absolute phase (or both) can be changed.

In Figure 6.21, the action of the phase feedback is shown for a real cycle. The top panel depicts the relative phase between the Wien filter frequency and the spin tune, i.e., Eq. (6.57). The panel in the middle shows the correction the phase feedback is doing on the Wien filter frequency which is in the order of milli Hertz and the lower panel shows the set values for the absolute Wien filter phase to correct the relative phase between Wien filter frequency and spin precession for arbitrary changes of the spin tune phase.

6.8. Summary

To summarize this chapter, each measured cycle contains relevant information for the determination of the direction of the Invariant Spin Axis. For each cycle, the following parameters need to be computed:

- **Vertical Polarization:** Computed from an asymmetry of scattered particles in the left and right quadrant of the polarimeter. The asymmetry scales directly with the vertical polarization. The asymmetry of detected events needs to be corrected using cycles without polarization.
- **Horizontal Polarization:** Computed from an asymmetry of scattered particles in the upper and lower quadrant of the polarimeter. Since the in-plane polarization is rotating with the spin precession frequency (or spin tune), the amount of in-plane polarization cannot be determined directly. The algorithm to compute the asymmetry is based on a mapping method in which events are mapped into a single oscillation period. An oscillation is revealed as soon as the right spin precession frequency is chosen. Therefore, this algorithm is also used to determine the spin precession frequency. The amplitude of the oscillation is also called up-down asymmetry and scales directly with the amount of in-plane polarization.
- **Angle between Vertical and Horizontal Polarization:** Determined by calculating the angle between vertical left-right and up-down asymmetry.

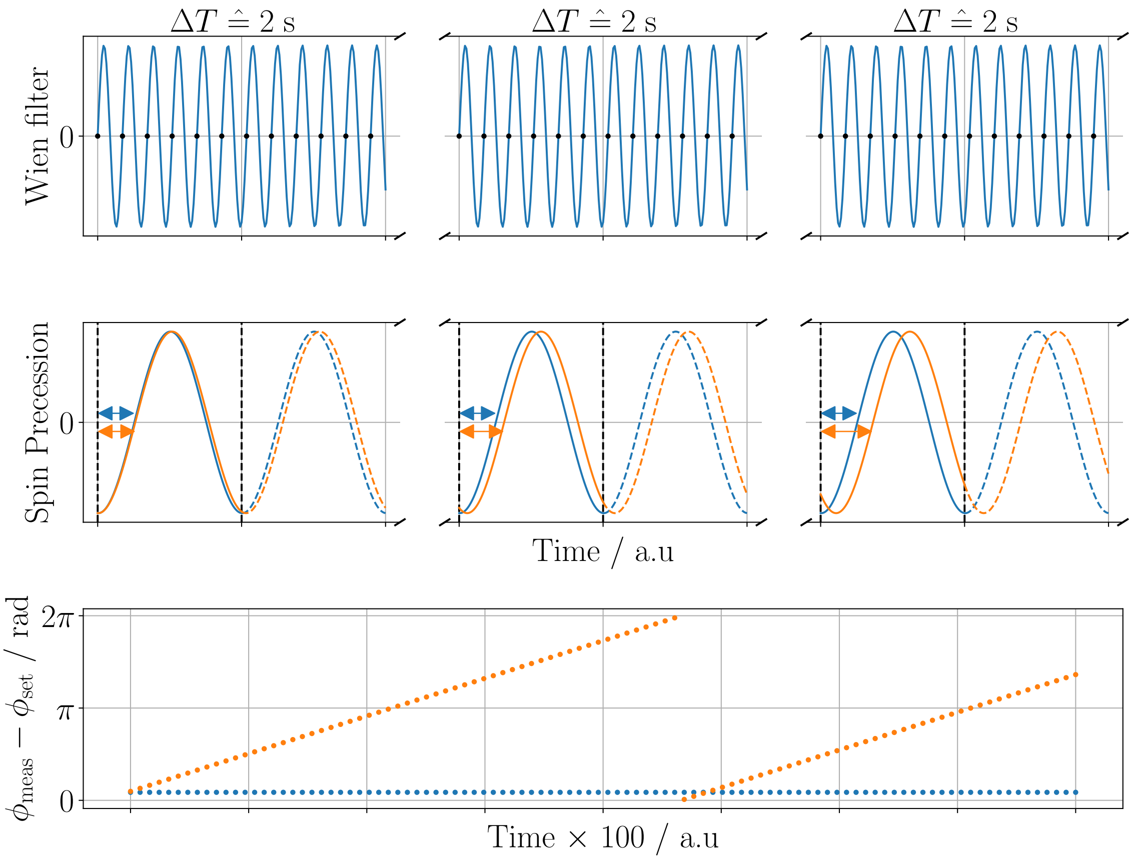

Figure 6.19.: The top panel shows the Wien filter oscillation for three consecutive measurement periods, each set to 2 s. Without loss of generality, the Wien filter phase is set to 0 rad. The black dots represent the measurements of the discriminator to measure the Wien filter frequency. The panels in the middle show the precession of the spin for the same periods. The spin tune phase is determined from a mapping method, which is further described in section 6.5, and illustrated by the arrows. Two scenarios are shown: **Off-resonance (orange):** The Wien filter frequency is not a harmonic of the spin precession frequency, which leads to an increase in the relative phase. This is adjusted by changing the Wien filter frequency correspondingly (cf. Figure 6.20, right panel). **Off-phase (blue):** A constant offset of the relative phase leads to an offset of the relative phase with respect to the desired phase ϕ_{set}. This is corrected by changing the phase of the Wien filter frequency generator (cf. Figure 6.20, left panel).

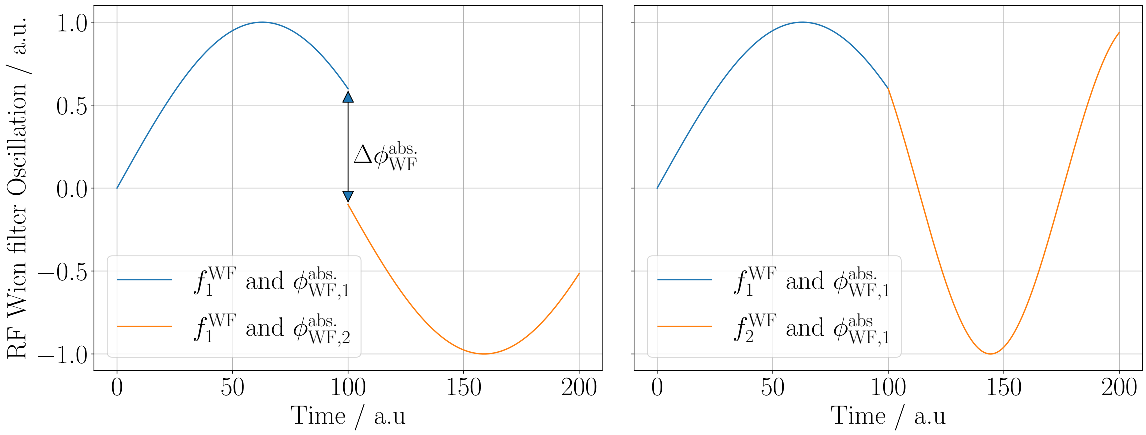

Figure 6.20.: Schematic of the operation of the RF Wien filter frequency generator. When the spin tune frequency changes, either the absolute phase or the frequency of the RF Wien filter wave can be adjusted to match the horizontal spin precession frequency and phase.

- **Total Polarization:** Calculated from the sum of squared left-right asymmetry and up-down asymmetry and describes the amount of polarization of the particle bunch.
- **Relative Phase:** Describes the phase relation between Wien filter frequency and spin precession frequency and is used to correct the frequency and absolute phase of the RF Wien filter frequency generator.

An example of all relevant variables for the Electric Dipole Moment Precursor experiment for a typical cycle in COSY is shown in Figure 6.22. A vertically polarized beam is injected into the ring, accelerated, and cooled. After 90 s, the target is moved into the beam, and the extraction into the polarimeter starts. At 100 s, the RF solenoid rotates the polarization into the accelerator plane. Afterwards, the phase feedback measures the phase relation between the spin precession frequency and the RF Wien filter (which is not switched on) and adjusts the frequency generator to the desired frequency and phase. At 155 s, the RF Wien filter is switched on, and a vertical polarization buildup appears. The buildup can be used to determine the orientation of the Invariant Spin Axis and hence the Electric Dipole Moment. More information about the buildup is given in the following section 7.

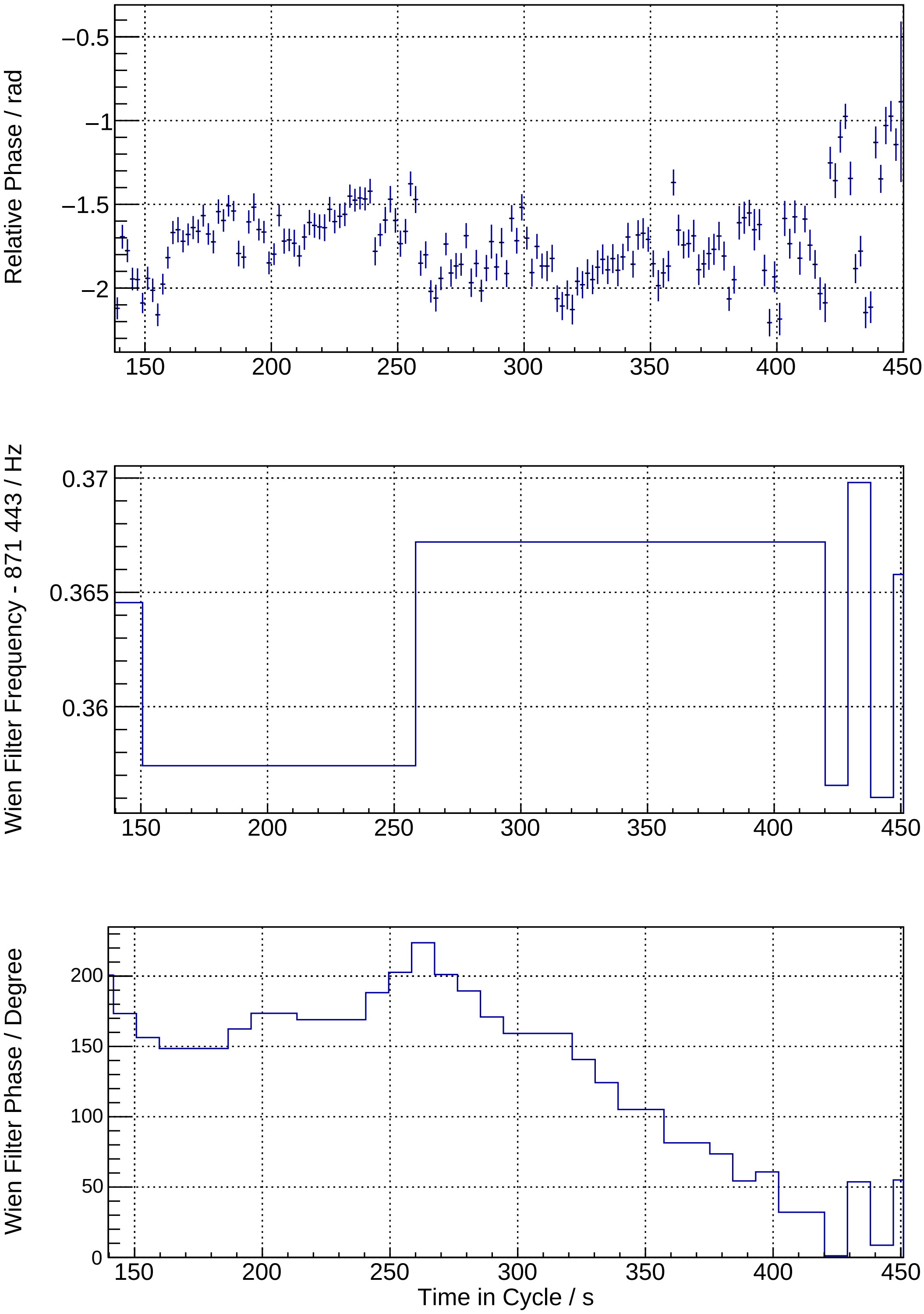

Figure 6.21.: Top: Relative Phase between the measured spin precession frequency and the Wien filter frequency. The other panels show the corrections of the Wien filter frequency f_{WF} and the absolute phase of the RF Wien filter $\phi_{\mathrm{abs}}^{\mathrm{WF}}$.

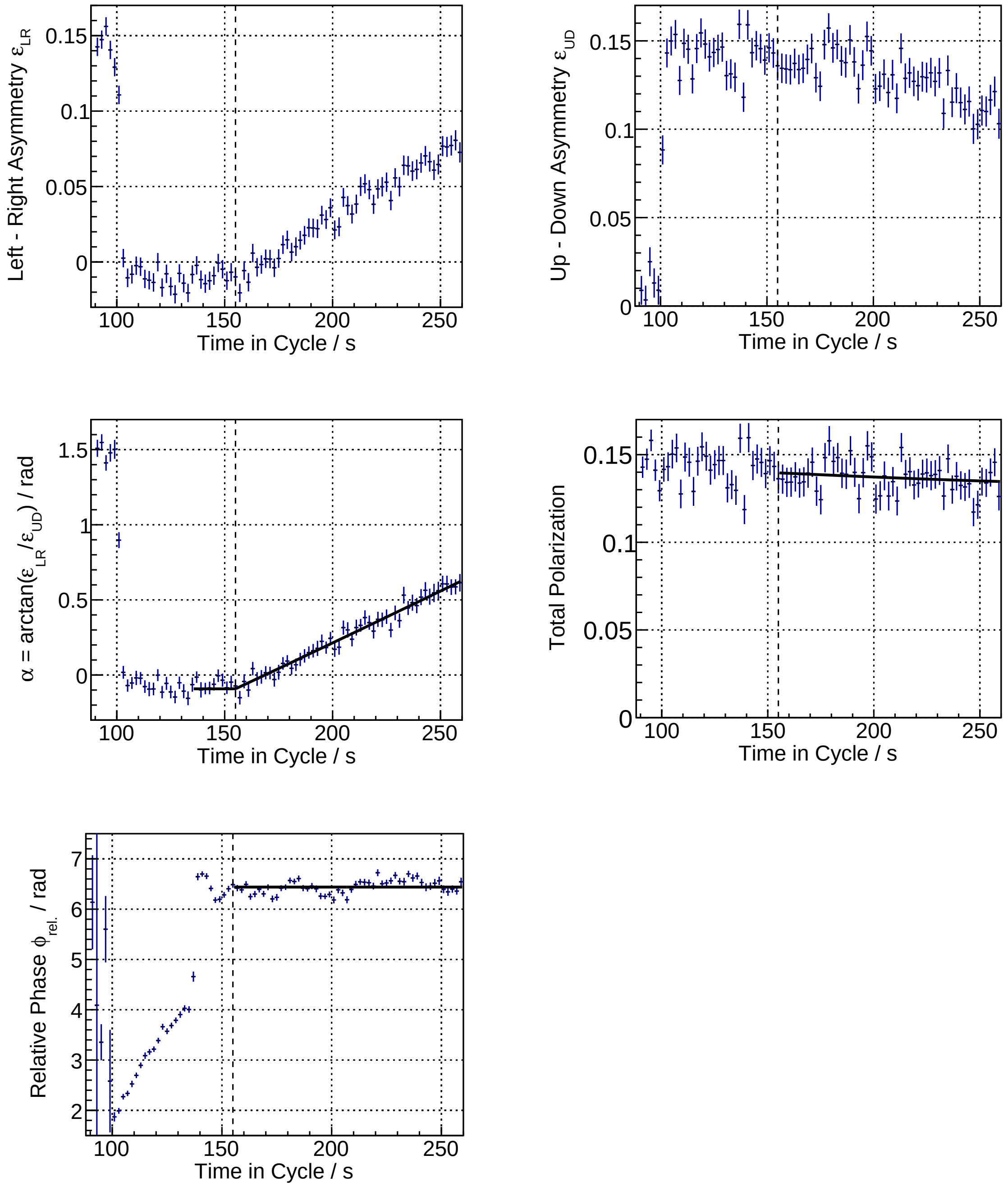

Figure 6.22.: Summary of all relevant observables, namely the left-right asymmetry, the up-down asymmetry, the angle between vertical and horizontal polarization, the total polarization and the relative phase between Wien filter and spin precession frequency, which are used to determine the orientation of the Invariant Spin Axis. The dashed line marks the timestamp when the RF Wien filter is switched on. The resulting change of polarization can be used to determine the orientation of the Invariant Spin Axis as further described in section 7.6.2 and 7.6.3.

7. The Deuteron EDM Precursor Experiment

In the following sections, the experimental periods, which lead to the first direct determination of the deuteron Electric Dipole Moment are described. In the first half of the chapter, the prerequisites are discussed, followed by a description of the experimental method and an overview of both measurement periods. Afterwards the final results are summarized.

The measurement of the deuteron Electric Dipole Moment was done during two experimental periods, also referred to as Precursor 1 (2018) and Precursor 2 (2021). The experimental periods along with an overview of all data taken are further described in section 7.7. The first experimental period gave valuable input for the second measurement time. Upgrades in between both experimental periods are described are discussed in section 7.7.2. The most important beam parameters are summarized in Table 7.1. As they only serve as estimates, no statistical and systematic uncertainties are given.

Table 7.1.: Beam parameters used during both experiments Precursor 1 (2018) & 2 (2021). No uncertainties are given, as they only serve as estimators. During the second Precursor Run, the number of particles is shared between two bunches circulating in the machine.

Parameter	Symbol	Value
Beam Revolution Frequency	f_{COSY}	750 602.6 Hz
RF Wien filter resonant frequency	f_{WF}	871 422 Hz
RF solenoid resonant frequency	f_{sol}	871 422 Hz
Spin tune frequency	f_{spin}	120 847.3 Hz
Lorentz Factor	γ	1.126
Beam Velocity	β	0.460 c
Momentum	p	970 MeV/c
COSY Circumference	L_{COSY}	183.57 m
Number of polarized (unpolarized) deuterons	N_d	$\approx 10^9 (10^{10})$

7.1. Measuring Scheme

This section outlines a standard configuration of a typical experimental cycle. The period, spanning from the particle injection to the conclusion of the measurement period and the subsequent ramp-down of COSY magnets, is referred to as a cycle. At the end of each cycle, the magnets ramp down for the next injection. Successive cycles, maintaining accelerator and beam conditions, constitute a run. An exception arises in the selection of polarized and unpolarized beams for various cycles within the same run. While maintaining beam conditions and experimental settings the same as in cycles with polarized beam, an unpolarized beam is injected into the ring, which is used to calibrate the rates inside the polarimeter. More information about this calibration is outlined in section 6.4.1. The order of polarization states for the experiment is in Precursor I and II: Up Polarized, Up Polarized, Up Polarized, Up Polarized, Unpolarized. A typical cycle encompasses the following steps:

1. A vector-polarized deuteron beam is injected into COSY. The initial polarization of the beam aligns with the Invariant Spin Axis of COSY, nearly vertical and parallel to the guiding fields of the dipole.
2. The up-polarized or unpolarized deuteron beam gets bunched and accelerated up to the final momentum of 970 MeV/c. The RF cavity remains switched on after acceleration for continuous bunching of the beam.
3. Electron cooling of the bunched beam to reduce beam emittances and momentum spread in horizontal and vertical directions. An orbit bump is applied at the cooler sections to align the deuteron beam with the electron beam. After cooling, the bump is removed, and the cooler dipole magnets are switched off to reduce systematic effects on the orbit.
4. Orbit correction with steerer magnets takes place as depicted in section 3.5.
5. Application of a local bump at the polarimeter to bring the beam close to the carbon target.
6. White noise is introduced to the stripline unit to induce vertical heating of the beam and initiate scattering processes involving the outermost deuterons onto the internal carbon target. The scattered particles are detected using the internal polarimeters installed in COSY.
7. The initial vertical polarization is rotated into the accelerator plane using the RF solenoid. If a polarized beam is injected into COSY, the polarization starts to precess with the angular frequency $\Omega_s = 2\pi f_{\mathrm{COSY}} \nu_s$ after rotation of the polarization. The RF solenoid is also ramped for unpolarized cycles but has no impact on the beam. The frequency and the amplitude of the RF solenoid for both experimental periods are given in Table 7.2.

Table 7.2.: Frequencies of the RF solenoid to rotate the vertical polarization of the particle beam into the horizontal accelerator plane.

	Precursor 1 (2018)	Precursor 2 (2021)
f_{sol} / Hz	871 430.6	871 429.66

8. Ramping of the Siberian snake to rotate the Invariant Spin Axis accordingly. The ramping of the Siberian snake changes the spin precession frequency.
9. Using the rates measured with the polarimeter, the (modified) spin precession frequency is measured for the phase frequency loop to adjust the Wien filter frequency and the relative phase between the Wien filter frequency and spin tune.
10. The actual measurement period starts. The polarization of the beam is manipulated using the RF Wien filter. Polarization behavior changes as a function of time and is measured using the counting rates in the polarimeter. The measuring period typically lasts for a hundred seconds until most deuterons are removed from the beam.
11. Lastly, a measurement of the horizontal and vertical betatron tunes is performed before the COSY magnets ramp down at the end of each cycle.

The timings for the individual steps are summarized in Table 7.3 for the two measurement campaigns Precursor I & II. During the second Precursor Run, the measurement period was extended during the experiment to switch from the initial slope method to the Pilot bunch method. The timing from the extended measurement period is given inside the brackets. For the optimization of the Spin Coherence Time and the determination of the Invariant Spin Axis at the solenoids, steps 9 and 10 are not relevant.

Table 7.3.: Timings of the individual measurement steps. During the second Precursor experiment, the cycle length was extended. The numbers inside the brackets stand for the extended measurement period.

	Precursor I	Precursor II
Acceleration Off	0.674 s	0.674 s
E-Cooling	3 – 43 s	5 – 50 s
Orbit Correction	87 s	55 s
Carbon Target In	85 s	75 s
White Noise Extraction & Schneiderbox	85 s	75 s
DAQ On	91 s	75 s
RF solenoid	100 – 102.6 s	87.4 – 89.2 s
Siberian Snake / 2MV solenoid On	110 s	100 s
Phase Feedback On	124 s	130 s
RF Wien filter On	155 s	155 s
Tune/ Chromaticity Measurement	-	299.2 s (440 s)
RF Wien filter & Siberian Snake / 2MV solenoid Off	285 s	300 s (442 s)
DAQ Off	288 s	300 s (448 s)

7.2. Spin Coherence Time

The Spin Coherence Time is a crucial parameter for the experiments reported in this thesis. During the cycle length of 300 s to 500 s, the polarization in the horizontal (also called in-plane polarization) plane needs to be preserved. The in-plane polarization represents the alignment of particle spins along a single direction within the horizontal plane. Any depolarizing effects of the in-plane polarization need to be taken into account on the buildup of the vertical polarization when the RF Wien filter is switched on, which is further discussed in sections 7.6.2.1 and 7.6.3.1. The duration for which the beam maintains its polarization is termed the Spin Coherence Time (SCT). It is essential to ensure that the Spin Coherence Time is at least as long as the measurement duration. Typically, the Spin Coherence Time is defined as the time taking for the polarization to decrease to $^1\!/_e$ with respect to its initial value.

The source of depolarization is related to the fast precession of the in-plane polarization at the spin tune $\nu_s = G\gamma$. Consequently, a spread of the beam energy distribution $\Delta\gamma$ leads to a spread of the spin tune distribution, meaning that some particles oscillate slower or faster than the design particle

$$\frac{\Delta\nu_s}{\nu_s} = \frac{\Delta\gamma}{\gamma} \propto \frac{\Delta p}{p} \propto \frac{\Delta l_{\text{orbit}}}{l_{\text{orbit}}}, \tag{7.1}$$

where l_{orbit} denotes the orbit circumference. In an ideal accelerator, the length of the orbit corresponds to the length of the storage ring. The momentum distribution leads to the depolarization of the in-plane polarization. Optimizing Spin Coherence Time means reducing the momentum spread of the beam. Various methods are applied at COSY to reduce the momentum spread:

- **Bunching using the RF Cavity:** The basic principle of a radio-frequency cavity is bunching the coasting beam into bunches by applying oscillating fields. Particles that arrive with their design momentum encounter zero potential. However, particles arriving either earlier or later will encounter fields that either slow down or speed up their motion, respectively. Consequently, the beam momentum spread is reduced.
- **Phase space reduction using electron cooling:** Recent studies of beam cooling, reducing the velocity distribution of the deuterons, showed a significant effect on the Spin Coherence Time [101]. However, constant beam cooling is not desirable during the experiment, as usually, a local bump has to be applied to align the deuteron beam with the electron beam, which leads to further rotations of the Invariant Spin Axis due to a disturbed orbit. Therefore, the deuterons are only pre-cooled at the beginning of the cycle.
- **Sextupole field correction:** Enhanced Spin Coherence Times are obtained through the optimization of three sextupole magnet families within the arcs of the ring to counteract secondary effects. Particles undergo transverse betatron oscillations around the typical orbit, elongating the path length and subsequently the momentum as the beam is grouped. Sextupoles counterbalance this effect by guiding oscillating particles towards an orbit with a reduced radius within the arcs. Furthermore, sextupoles offer the flexibility to regulate the chromaticity of the ring. Minimal or absent chromaticity is linked with the longest Spin Coherence Time [70].

In Dennis Eversmann's PhD thesis, a mathematical description of the loss of polarization is given [44, p.60-62]. Here, the model description is only outlined. The model tracks the probability of a particle at turn number n to have a polarization along the longitudinal axis while rotating in the horizontal plane with the spin tune ν_s. The up-down asymmetry (= in-plane polarization) for the decay of spin polarization can be described using

$$\varepsilon_{\mathrm{UD}}\big(\gamma_{\mathrm{s}}(t)\big) = \varepsilon_0 \left(\left[1 - \sqrt{\pi}\gamma_s(t)\mathrm{e}^{-\gamma_s^2(t)}\mathrm{erfi}\big(\gamma_s(t)\big)\right]^2 + \pi\gamma_s^2(t)\mathrm{e}^{-2\gamma_s^2(t)} \right)^{\frac{1}{2}}, \tag{7.2}$$

$$\text{with } \gamma_s(t) = \sqrt{2}\pi\Delta\nu_s t \cdot f_{\mathrm{COSY}}. \tag{7.3}$$

The attenuation parameter $\gamma_s(t)$ includes the spread of the spin tune distribution $\Delta\nu_s$ and is the only fit parameter apart from the up-down asymmetry ε_0 after the spin flip when ramping the RF solenoid. The Spin Coherence Time can be calculated using

$$\varepsilon_{\mathrm{UD}}\big(\gamma_s(\tau_{\mathrm{SCT}})\big) = \frac{1}{e}. \tag{7.4}$$

This equation can only be numerically solved, yielding

$$\gamma_s(\tau_{\mathrm{SCT}}) = \sqrt{2}\pi\Delta\nu_s\tau_{\mathrm{SCT}}f_{\mathrm{COSY}} \overset{!}{\approx} 1.571, \tag{7.5}$$

$$\tau_{\mathrm{SCT}} \approx \frac{0.3536}{\Delta\nu_s f_{\mathrm{COSY}}} \quad \text{and} \quad \sigma_{\tau_{\mathrm{SCT}}} \approx \frac{0.3536}{\Delta\nu_s^2 f_{\mathrm{COSY}}}\sigma_{\Delta\nu_s}. \tag{7.6}$$

Two examples of a measurement of the Spin Coherence Time during a sextupole scan are shown in Figure 7.1a and 7.1b. At 90 s in the cycle, the vertical polarization is rotated into the horizontal plane using the RF solenoid. In the left panel, the up-down asymmetry drops after a few seconds, which leads to a short Spin Coherence Time of

$$\tau_{\mathrm{SCT}} = (47.53 \pm 1.23)\,\mathrm{s}. \tag{7.7}$$

The right panel shows a measurement of the Spin Coherence Time, in which a value of

$$\tau_{\mathrm{SCT}} = (689.63 \pm 77.50)\,\mathrm{s} \tag{7.8}$$

is reached. In Figure 7.1a, the up-down asymmetry is larger than zero after 150 s due to the fitting bias of sine functions with small amplitudes and large uncertainties.

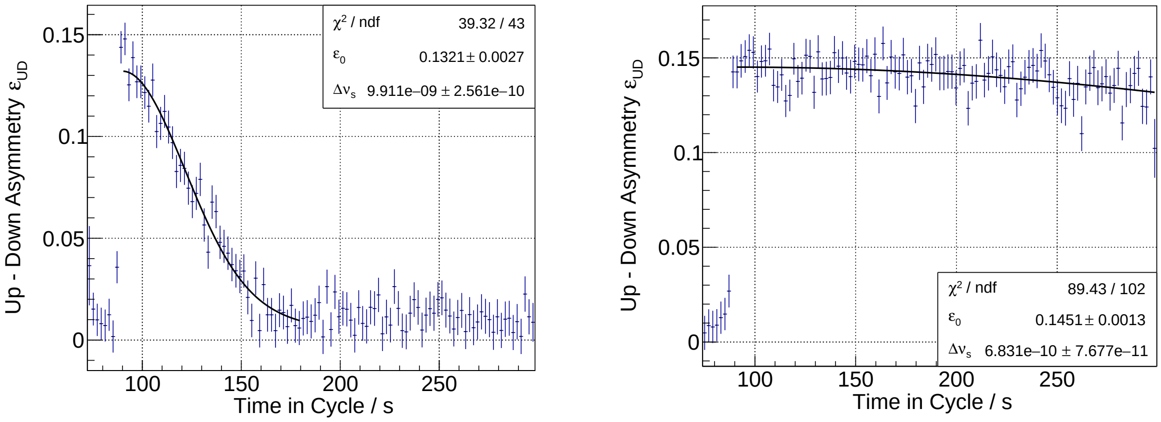

(a) Short SCT.

(b) Long SCT.

Figure 7.1.: Two examples of measuring the Spin Coherence Time while changing the sextupole currents. The left measurement yields a short Spin Coherence Time of (47.53 ± 1.23) s. The right panel shows a measurement of the Spin Coherence Time of (689.63 ± 77.50) s.

The optimization of the Spin Coherence Time by finding the correct currents of the sextupole families is a lengthy process, carefully measuring a grid of different combinations of applied currents. In Figure 7.2, a typical scan of the Spin Coherence Time is shown. After the optimal settings of the sextupole families MXG and MXS are found, the last sextupole family is optimized. The currents are given in % with respect to the maximum current the power supply of the magnet can handle. A long Spin Coherence Time along the entire measurement period is crucial for the success of the experiment.

7.2.1. Influence of the Siberian Snake on the Spin Coherence Time

During the experiment, the dependence of the Spin Coherence Time as a function of the applied current to the Siberian snake is measured. The dependence is shown in Figure 7.3 for both experimental periods in 2018 before aligning the Siberian snake with the beam-based alignment method and in 2021 after the alignment. More information about the alignment of the Siberian

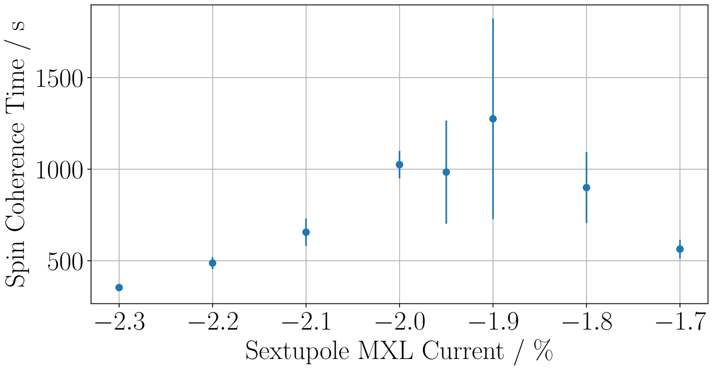

Figure 7.2.: Sextupole scan of the MXL sextupole family to correct second order effects and optimize the Spin Coherence Time. A Spin Coherence Time of $> 1000\,\mathrm{s}$ is necessary for the experiment. The sextupole currents are in % with respect to the maximum current the power supply of the magnet can handle.

snake is given in section 7.7.2.2. In both cases, the Spin Coherence Time drastically decreases for non-zero currents.

The orientation of the Invariant Spin Axis is measured by a buildup of the vertical polarization. However, spin-decoherence effects can mimic this effect of a buildup and need to be included in the fits. The buildup models of the vertical polarization are further described in sections 7.6.2.1 and 7.6.3.1.

The reason for the change in Spin Coherence Time for non-zero currents applied to the Siberian snake is most certainly due to a change in the longitudinal bunch shape structure when ramping the Siberian snake.

7.3. Cycle Selection

The full determination of the Invariant Spin Axis using the RF Wien filter takes approximately a day. It's important that during the measurement period, the experimental conditions are as stable as possible. Therefore, it's important to carefully select cycles which enter the final fit for the determination of the orientation of the Invariant Spin Axis. For each cycle, the following conditions are checked:

- **Fit Quality:** For the final fit of the determination of the Invariant Spin Axis, each cycle needs to be individually fitted to determine the buildup rate of the vertical polarization. Only fits for which the reduced χ^2 is within a three standard deviation region $\sigma_{\chi^2} = \sqrt{2/\mathrm{ndf}}$ around 1 are accepted. More information about the buildup of the vertical polarization along with examples of the fits is given in section 7.6.2 and 7.6.3.
- **Sextupole Magnets:** A failure of power supplies connected to the sextupole families would drastically change the Spin Coherence Time. To exclude failures, the read-back of the power supply currents is checked for each cycle, as well as the Spin Coherence Time, which can even be measured for cycles using the RF Wien filter.

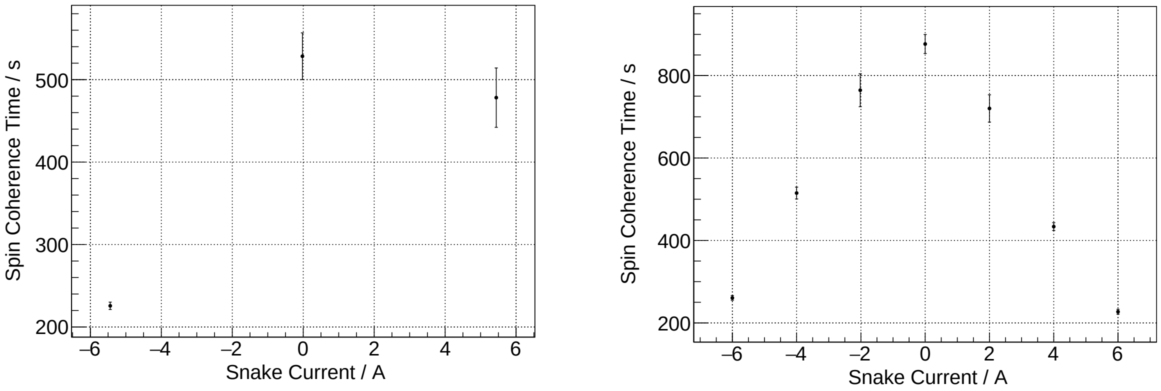

(a) Precursor 1 (2018)

(b) Precursor 2 (2021)

Figure 7.3.: Dependence of the Spin Coherence Time as a function of the Siberian snake current. The data points show an average of the Spin Coherence Time for multiple consecutive cycles. The left panel depicts the results for the first Precursor run before the Siberian snake was aligned using the beam-based alignment technique. The right panel depicts data taken during the second Precursor run. In both cases, the Spin Coherence Time drastically decreases when ramping the Siberian snake.

In addition to the fit quality and the sextupole magnets, the reduction of beam emittance using beam cooling and the orbit needs to be stable. These two topics need some sophisticated explanation, which are given in the following section.

7.3.1. Beam Cooling

Successful electron cooling is crucial for optimizing the operation of the RF Wien filter and achieving a long Spin Coherence Time. When running the electron cooler, recombination of the electrons and the circulating protons/deuterons can occur. The neutral hydrogen or deuterium beam is not affected by magnets. In the first dipole in the arc, at a distance of 24.3 m after the 100 kV electron cooler, an extraction line is installed to decouple the neutral recombined particle beam from the circulating protons/deuterons. The extraction line has a length of 75 cm and a width of 5 cm. At the end of the extraction line, the beam passes through a 50 μm thin extraction window, stripping electrons from the neutral beam. The charged particles are detected via two multi-wire proportional chambers (MWPC) rotated with respect to each other by 90° to measure horizontal and vertical beam profiles. The extraction beam line in the dipole is illustrated in Figure 7.4.

The MWPC functions similarly to a proportional counter found in a Geiger-Müller counter. It comprises a chamber filled with gas, housing a set of parallel wires. These wires connect to a high voltage (anode), while the conductive walls of the MWPC are grounded. At COSY, the MWPCs employ 64 thin wires spaced 1 mm apart, and the ionization gas used is a mixture of argon and isobutane.

As a particle traverses the chamber, it ionizes the gas along its path. The resulting ions and electrons undergo acceleration due to the electric field across the chamber, triggering a localized cascade of ionization known as the Townsend avalanche. This cascade generates a current that

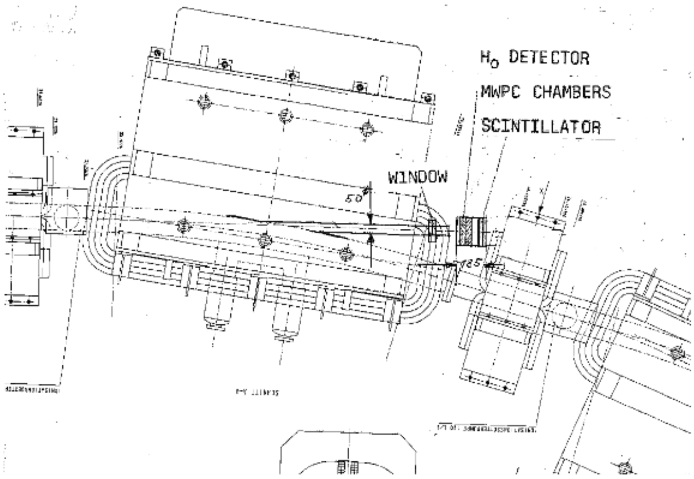

Figure 7.4.: Extraction line for the recombined and neutral particles in the electron cooler, located in the first dipole of the arc after the 100 kV cooler. After the extraction line, the particles are detected in the multi-wire proportional chamber (MWPC). Taken from [102].

flows from the wire closest to the particle's trajectory to the walls of the wire chambers. Current pulses can be individually detected at each wire, allowing for the creation of the beam profiles. An example of the measured profiles as a function of time is shown in Figure 7.5a (horizontal) and Figure 7.5b (vertical). The y axis represents the 64 wires spaced 1 mm apart. The colour denotes the number of particles measured at a specific wire. A time binning of 1 s is chosen for the analysis. The cooling process starts at 10 s and ends at 49 s in the cycle.

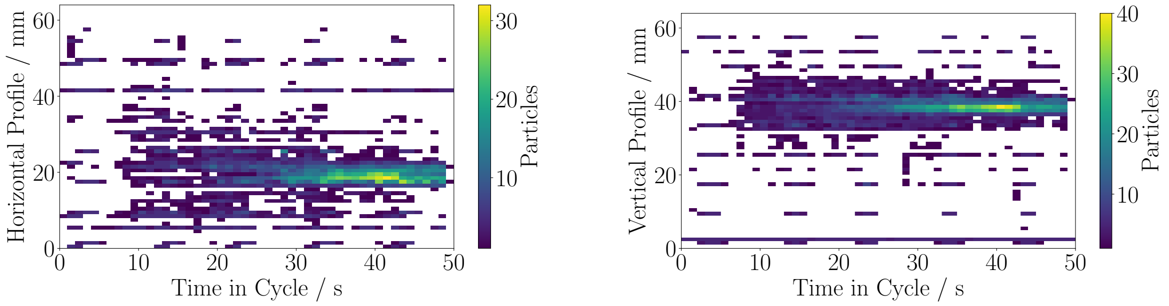

(a) Horizontal Profile.

(b) Vertical Profile.

Figure 7.5.: Horizontal (left) and vertical (right) neutral, recombined beam profiles measured at the MWPC as a function of time. In both planes, 64 wires spaced 1 mm apart measure the incident neutral particles.

The profiles for a time bin of $t \in [40, 41]$ s are shown in Figure 7.6a (horizontal) and Figure 7.6b (vertical). The detected particles are shown as a function of the MWPC wire. Poisson statistics are assumed for the hits in each wire, $\sigma_N = \sqrt{N}$. The profiles are fitted with a least-square fit assuming a Gaussian profile distribution

$$f_{\text{Profile}}(w; A, \mu, \sigma) = A \exp\left(-\frac{1}{2}\left(\frac{w-\mu}{\sigma}\right)^2\right), \tag{7.9}$$

where A, μ, and σ denote the height, mean, and standard deviation of the profile, respectively. The position of the wire is given by w. As a measure for the beam profile width, the standard deviation of the least-square fit is taken.

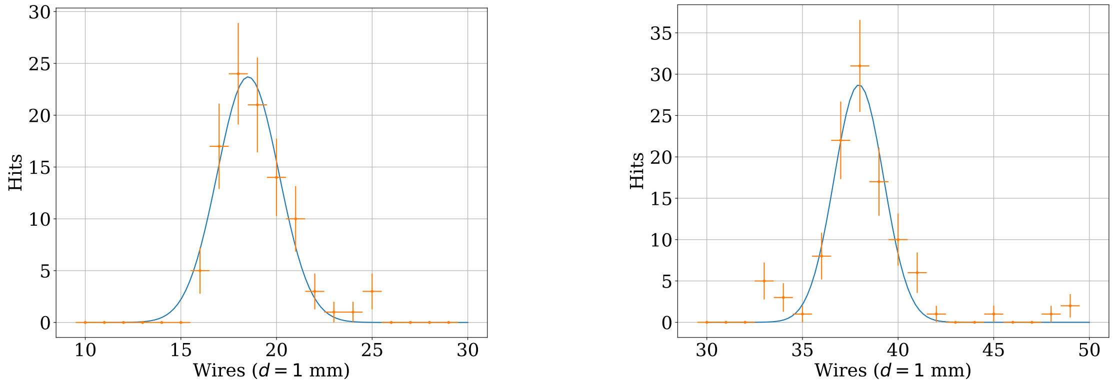

(a) Horizontal Profile

(b) Vertical Profile.

Figure 7.6.: Recombined beam profiles in the time bin $T = (40, 41)$ s along with a fit to determine the beam width.

The width of the neutral beam profiles is shown in Figure 7.7 as a function of time in the cycle. The shadow illustrates the statistical uncertainty on the profile width σ_σ, determined by the least-square fit according to Eq. (7.9). The beam profile width decreases from the beginning of the cooling process from roughly 6 mm to below 2 mm both in vertical and horizontal polarization which is a prerequisite for a successful experiment. For further data processing, only cycles in which the vertical beam width is in the range from 1.3 mm to 2.2 mm and horizontal beam width at the end of the cooling process is in the range from 1.8 mm to 2.8 mm are used. These areas are marked with the dashed lines in Figure 7.7.

For a couple of cycles, the beam cooling was not successful, and no profiles were successfully measured. These cycles are discarded for any other analysis. Unfortunately, the data of the recombined particles was only collected during the Precursor II run in 2021.

7.3.2. Steerer & Orbit

Stable conditions throughout the experiment are crucial for the stability of the determination of the Invariant Spin Axis. The steerers used to correct the orbit as close to the design orbit are connected to power supplies which fail to ramp the steerer magnets from time to time. The readback of the applied currents at the power supplies is stored in the COSY archiver. This data can be used to select cycles in which the steerer magnets ramp to the wrong magnetic fields. For both experiments, for each steerer magnet power supply, a range of the readback is determined by analyzing the distribution of steerer currents of each cycle. The ranges are listed

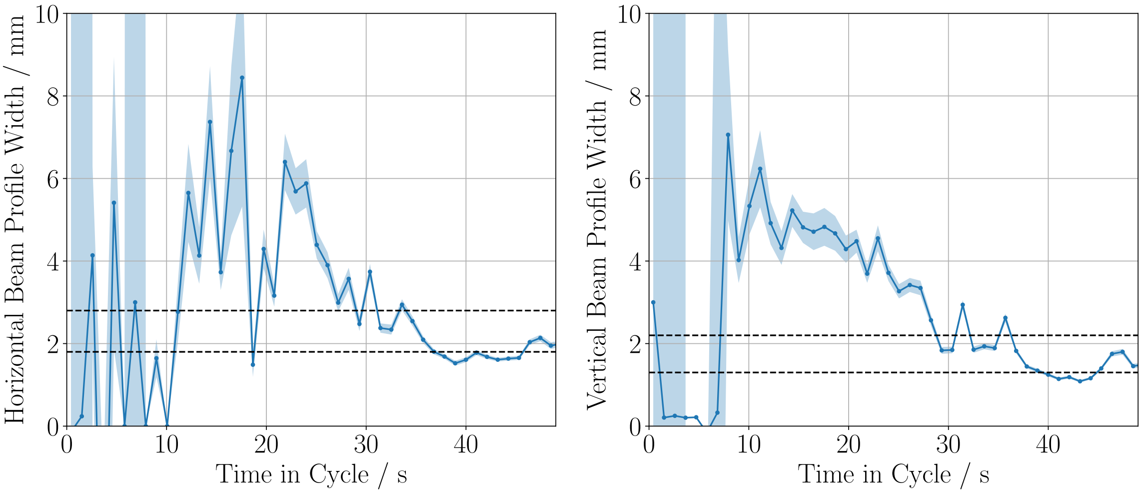

Figure 7.7.: Horizontal and Vertical Profile width as a function of time measured at the MWPC. The width of the beam decreases throughout the cooling process. The shadow illustrates the uncertainty of the least-square fit on the width parameter σ as defined in Eq. (7.9). The dashed lines mark the range in which the width is accepted for further analysis.

in Table B.1 and B.2. In addition, the orbit is also constantly measured as the readings of the BPMs are stored. If a BPM reading is not within a predefined margin, the cycle is discarded as well. The accepted range for each beam position monitor is listed in Table B.3 and B.4.

7.4. Determination of the Invariant Spin Axis using Static Solenoids

The longitudinal component of the Invariant Spin Axis can be determined using solenoids in the ring, which provide static solenoidal magnetic fields parallel to the beam direction, thus not influencing the beam but the beam polarization. For the experiment, the Siberian snake in the second straight section of COSY, as well as the 2 MV solenoid of the 2 MV electron cooler, are used. By ramping the solenoids, the spin precession frequency of the beam changes. This change can be used to calculate the longitudinal component of the Invariant Spin Axis at the location of the solenoid (either the Siberian snake, the 2 MV solenoid, or both).

Using extra solenoids, the Invariant Spin Axis can be rotated in the longitudinal (beam) direction. This will be important in section 7.8 when the RF Wien filter is used to determine the orientation of the Invariant Spin Axis as the Siberian snake is used to align the Invariant Spin axis longitudinally with the magnetic field axis of the RF Wien filter. For the alignment, calibration measurements of the Siberian snake have to be performed which will be further explained in the upcoming section.

7.4.1. Theory

The analytical work from Eq. (7.10) to (7.20) is based on *Spin tune mapping as a novel tool to probe the spin dynamics in storage rings* [103]. The full derivations are given in section C.1.

The standard spinor formalism describes the motion of the spin with one-turn spin rotation matrices. By forcing a closed solution, the change of spin tune $\Delta\nu_s$ with respect to the initial spin tune without extra solenoids ν_s^0, can be calculated as

$$\Delta\nu_s = -\frac{1}{\pi}\left[\cot\left(\pi\nu_s^0\right)\left(\cos\left(\frac{\chi_X}{2}\right)-1\right)-\left(\vec{n}\cdot\vec{k}_X\right)\sin\left(\frac{\chi_X}{2}\right)\right], \tag{7.10}$$

where ν_s^0 denotes the unperturbed spin tune without extra solenoids and $\vec{n}$ denotes the Invariant Spin Axis. The subscript X denotes either the Siberian snake or the 2 MV solenoid. The spin rotation angle χ_X around the $\vec{k}$ axis for one pass through a solenoid can be calculated by evaluating the Thomas-BMT equation (4.22)

$$\chi_X\vec{k} = \vec{\Omega}_{\mathrm{MDM}} = -\frac{q}{m_d}\left[\left(G+\frac{1}{\gamma}\right)\vec{B}-\frac{G\gamma}{\gamma+1}\left(\vec{\beta}\cdot\vec{B}\right)\cdot\vec{B}\right]. \tag{7.11}$$

For a magnetic solenoid, the electric field contribution can be set to zero. The magnetic field direction of the solenoid and the beam momentum vector both point in z direction

$$\vec{B} = B\vec{e}_z \text{ and } \vec{\beta} = \beta\vec{e}_z. \tag{7.12}$$

Using $\gamma^2 = {}^1/_{(1-\beta^2)}$, the spin rotation axis can be further simplified to

$$\chi_X\vec{k} = \vec{\Omega}_{\mathrm{MDM}} = -\frac{qB}{\gamma m_d}\left(1+G\right)\vec{e}_z. \tag{7.13}$$

The magnetic field is given by the field integral which is directly related to the current I_X in the coil

$$B = \int B_z \mathrm{d}z = k'_X I_X. \tag{7.14}$$

The calibration factor k'_X is unique for a solenoid and can be in principle calculated by Ampere's law in terms of coil windings. In the following, the spin rotation angle because of the magnetic field of a solenoid is written as

$$\chi_X = k_X I_X \text{ with } k_X = -\frac{qk'_X}{\gamma m_d}\left(1+G\right). \tag{7.15}$$

The Invariant Spin Axis can be defined in a co-rotating frame where y points perpendicular to the accelerator plane, z points in beam direction, and x points perpendicular to x and y. The Invariant Spin Axis is defined as

$$\vec{n} \approx n_x\vec{e}_x + 1\vec{e}_y + n_z\vec{e}_z, \tag{7.16}$$

assuming that the tilts in radial (x) and longitudinal direction (z) of the Invariant Spin Axis are small. For a solenoid, the magnetic field points in the longitudinal direction

$$\vec{k} = \vec{e}_z, \tag{7.17}$$

which means that the scalar product leads to the projection of the Invariant Spin Axis in the longitudinal direction at the solenoid

$$\vec{n} \cdot \vec{k}_X = n_z^X. \tag{7.18}$$

Note that a determination of the radial component of the Invariant Spin Axis using a static solenoid is in principle also possible by providing a horizontal field. However, horizontal magnetic fields lead to orbit distortions. To compensate for the horizontal magnetic field, an additional vertical electric field could be used, i.e., a static Wien filter.

The final formula for the change of spin tune using a single solenoid is given by

$$\Delta\nu_s^X = -\frac{1}{\pi}\left[\cot(\pi\nu_s^0)\left(\cos\left(\frac{k_X I_X}{2}\right) - 1\right) - n_z^X \sin\left(\frac{k_X I_X}{2}\right)\right] + \Delta\nu_{s,0}, \tag{7.19}$$

where X denotes either the Siberian snake or the 2MV solenoid. An additional offset parameter $\Delta\nu_{s,0}$ is introduced. This offset takes the drift of the spin tune in the cycle into account. This parameter is further discussed in section 7.4.2 and 7.4.3.

During the second Precursor run, experiments were done using two solenoids at the same time. The derivation of the spin tune change as a function of two solenoids ramping at the same time is very similar to the case using only a single solenoid. By following the same steps as in the case for a single solenoid, the change of spin tune as a function of two solenoids is given by

$$\begin{aligned}\Delta\nu_s^{\text{Solenoids}} =& \frac{1}{-\pi\sin(\pi\nu_s^0)} \times \\ & \Bigg[\cos(\pi\nu_s^0)\left(\cos\left(\frac{k_{\text{Snake}} I_{\text{Snake}}}{2}\right)\cos\left(\frac{k_{\text{2MV Sol.}} I_{\text{2MV Sol.}}}{2}\right) - 1\right) \\ & - \sin\left(\frac{k_{\text{Snake}} I_{\text{Snake}}}{2}\right)\sin\left(\frac{k_{\text{2MV Sol.}} I_{\text{2MV Sol.}}}{2}\right) \\ & - n_z^{\text{2MV Sol.}}\sin(\pi\nu_s^0)\sin\left(\frac{k_{\text{Snake}} I_{\text{Snake}}}{2}\right)\cos\left(\frac{k_{\text{2MV Sol.}} I_{\text{2MV Sol.}}}{2}\right) \\ & - n_z^{\text{Snake}}\sin(\pi\nu_s^0)\cos\left(\frac{k_{\text{Snake}} I_{\text{Snake}}}{2}\right)\sin\left(\frac{k_{\text{2MV Sol.}} I_{\text{2MV Sol.}}}{2}\right)\Bigg] \\ & + \Delta\nu_{s,0}.\end{aligned} \tag{7.20}$$

A summary of all relevant parameters of the change in spin tune formula is given in Table 7.4. For a single solenoid (either $I_{\text{snake}} = 0$ or $I_{\text{2MV Sol.}} = 0$), Eq. (7.20) can be reduced to Eq. (7.19).

7.4.2. Methodology

The measuring scheme for the determination of the Invariant Spin Axis using the solenoids is very similar to the measuring scheme described in section 7.1. However, the phase feedback and the RF Wien filter are not needed, i.e., skipping steps 9 and 10.

In Figure 7.8, the change in spin tune when ramping the solenoids is visualized. In this example, the current set to the power supply of the Siberian snake is −6 A, and the current set to the

Table 7.4.: Description of the variables and fit parameters in Eq. (7.20).

Symbol	Description	Type	Unit
ν_s^0	Initial spin tune without solenoids	Fixed Parameter	
k_{Snake}	Snake conversion factor: Snake current → spin flip angle	Parameter	$^{\text{rad}}/_{\text{A}}$
$k_{\text{2MV Sol.}}$	2MV Sol. conversion factor: Solenoid current → spin flip angle	Parameter	$^{\text{rad}}/_{\text{A}}$
n_z^{Snake}	Longitudinal component of the Invariant Spin Axis at the Siberian snake	Parameter	rad
$n_z^{\text{2MV Sol.}}$	Longitudinal component of the Invariant Spin Axis at the 2 MV solenoid	Parameter	rad
I_{Snake}	Set current to the Siberian snake	Variable	A
$I_{\text{2MV Sol.}}$	Set current to the 2 MV solenoid	Variable	A
$\nu_{s,0}$	Offset taking spin tune drifts into account	Parameter	

power supply of the 2 MV solenoid is -20 A.[1] The colour denotes the magnitude of the up-down asymmetry, which is introduced in section 6.5, as a function of the scanned frequency. The scanned frequency is scaled by the revolution frequency f_{COSY} to the spin tune domain. At 100 s in the cycle, the two solenoids are switched on. Ramping the magnets to their full magnetic field takes about 5 s, resulting in a new spin tune depending on the 2 MV solenoid setting, the Siberian snake setting, and the initial orientation of the longitudinal component of the Invariant Spin Axis.

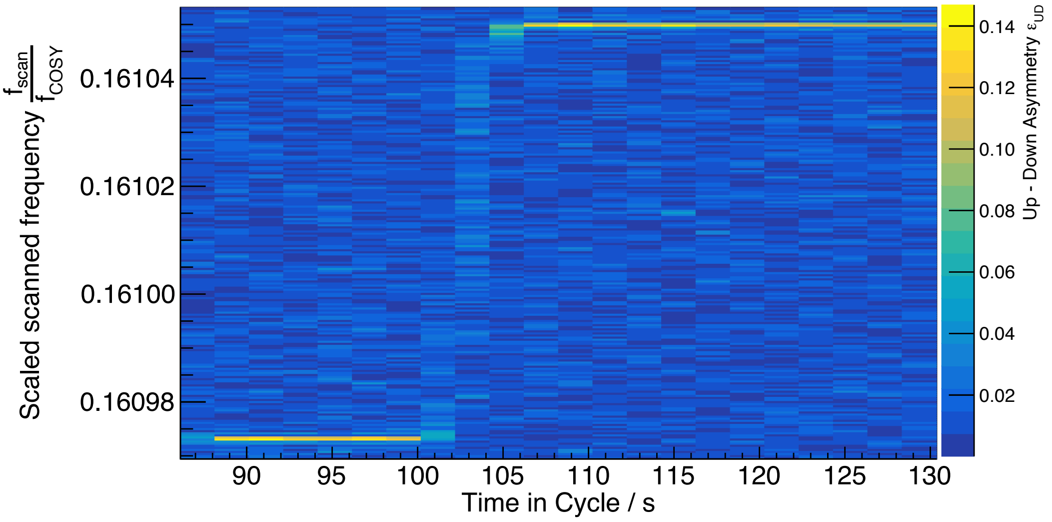

Figure 7.8.: The change of spin tune as a function of time in the cycle: The power supplies of the 2 MV solenoid and the Siberian snake are set to -20 A and -6 A at 100 s in the cycle. After 5 s, the ramping is finished, which leads to a change in spin tune, observable in the spectrum using the up-down asymmetry as a function of the scanned frequency.

To precisely measure the change of spin tune, a frequency scan is done for each cycle contributing to the determination of the longitudinal Invariant Spin Axis components at the solenoids. A first estimate for the initial spin tune and the modified spin tune is taken from the spin tune scan for a time interval before and after ramping the Siberian snake and the 2 MV solenoid.

---

[1] Note that the currents set to the solenoids are not directly comparable, as the final magnetic field depends mainly on the number of loops in the coil of the magnet.

An example of the spectra is shown in Figure 7.9a (before solenoids) and 7.9b (after solenoids). In both examples, the scanned frequency resulting in the peak is taken as an initial guess for the initial and modified spin tune ($\nu_{s,0}^{\text{Init.}}, \nu_{s,0}^{\text{Mod.}}$).

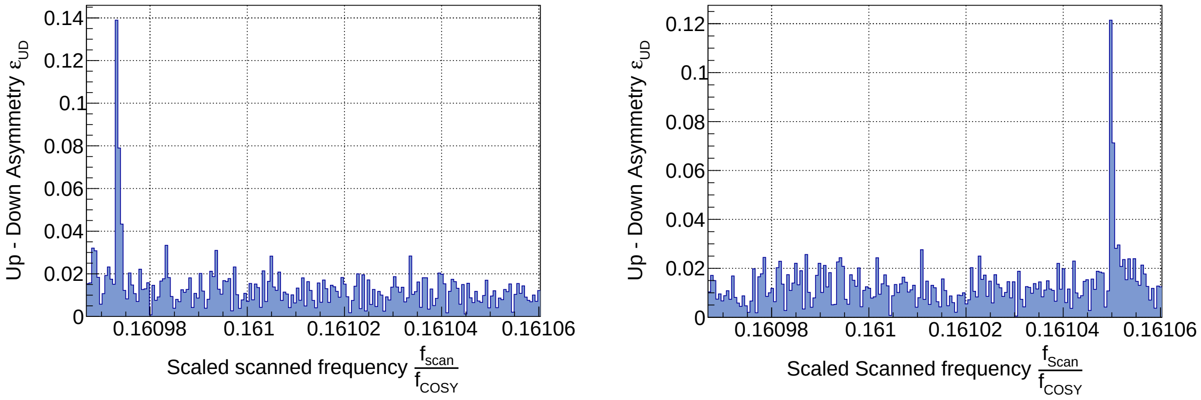

(a) $t_{\text{ev}} \in [96.2, 98.2]s$

(b) $t_{\text{ev}} \in [106.2, 108.2]s$

Figure 7.9.: Histograms of the up-down asymmetry as a function of the scaled scanned frequency for events in a two-second period before and after ramping both solenoids. A peak arises at the true spin tune, which is used as an initial guess for $\nu_{s,0}^{\text{Init.}}$ and $\nu_{s,0}^{\text{Mod.}}$. These spectra essentially correspond to a Fourier Spectrum.

The initial guesses for the initial and modified spin tunes are used to calculate the spin tune phase as already discussed in section 6.5.1. The spin tune phase for the initial and modified spin tune guesses are shown in Figures 7.10a and 7.10b. Assuming that the spin tune does not change over the period of 10 s, the spin tune phase is fitted during the period of 89 to 99 s and 107 to 117 s with a linear function

$$\phi_s = at + b \Rightarrow \frac{\partial \phi_s}{\partial t} = a, \tag{7.21}$$

i.e., the initial spin tune is defined as the averaged spin tune between 89 and 99 s in the cycle, and the modified spin tune is defined as the averaged spin tune between 107 and 117 s in the cycle when the solenoids are switched on. The exact initial and modified spin tunes can be calculated using Eq. (6.36)

$$\nu_s^X = \nu_{s,0}^X + \frac{1}{2\pi f_{\text{COSY}}} \frac{\partial \phi_s}{\partial t} = \nu_{s,0}^X + \frac{a}{2\pi f_{\text{COSY}}}, \tag{7.22}$$

where X denotes either the initial or the modified spin tune, and a is the slope of the fitted linear function. The statistical uncertainties are calculated using Gaussian error propagation

$$\sigma_{\nu_s^X} = \frac{\sigma_a}{2\pi f_{\text{COSY}}}. \tag{7.23}$$

In the example shown in Figure 7.10, the exact spin tunes are given by

$$\nu_s^{\text{Init.}} = 0.160\,973\,242\,6(21), \tag{7.24}$$

$$\nu_s^{\text{Mod.}} = 0.161\,049\,969\,8(22). \tag{7.25}$$

The spin tune jump is defined as

$$\Delta\nu_s^{\text{Solenoids}} = \nu_s^{\text{Mod.}} - \nu_s^{\text{Init.}} = 7.6726(3) \times 10^{-5}. \tag{7.26}$$

Note that the difference in spin tunes can not be defined with absolute values, as negative changes of the modulated spin tunes are also allowed.

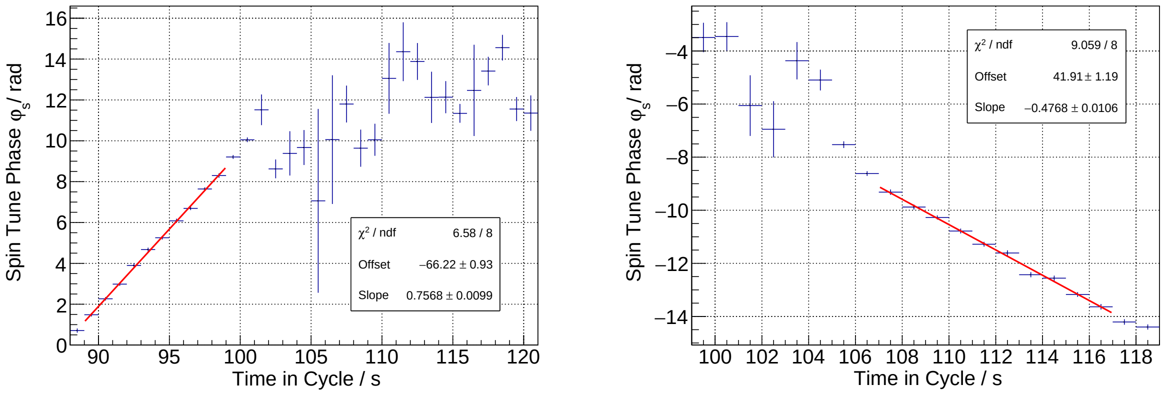

(a) $\nu_{s,0}^{\text{Init.}} = 0.160\,973\,082\,1$

(b) $\nu_{s,0}^{\text{Mod.}} = 0.161\,050\,070\,9$

Figure 7.10.: Spin tune phase determined from the initial guesses of the initial and modified spin tune determined from Figure 7.9a and 7.9b. The spin tune phase is fitted using a linear function to determine the initial and modified spin tune precisely.

7.4.3. Results

During both experimental periods in 2018 and 2021, dedicated cycles are used to calibrate the solenoidal spin rotation angles and to measure the orientation of the Invariant Spin Axis in the longitudinal direction at the Siberian snake and the 2 MV solenoid. The maps are marked as Map 10 in Table 7.13. However, it is also possible to measure the orientation of the longitudinal component of the Invariant Spin Axis parasitically during the measurement using the RF Wien filter. First, the results of the dedicated cycles are presented. The results taken parasitically are discussed in section 7.4.3.1.

A non-zero measurement of the longitudinal orientation of the Invariant Spin Axis is a direct hint to systematics in the ring which need to be taken into account for the final measurement using the RF Wien filter, as in a perfect ring without magnet misalignments, the tilt angle in longitudinal direction is expected to be zero, even for a non-zero Electric Dipole Moment.

First, the averaged initial spin tune ν_s^0 among all cycles which contributes to the determination of the longitudinal component of the Invariant Spin Axis at the solenoids needs to be determined as they enter the fit (cf. Eq. (7.19) and (7.20)) as a fixed parameter. A histogram of the initial spin tunes for both experimental periods is shown in Figure 7.11. The averaged initial spin tunes for both Precursor runs are given by

$$|\nu_s^0| = 0.160\,970\,485(1) \text{ (Precursor 1) and } |\nu_s^0| = 0.160\,973\,254(1) \text{ (Precursor 2)}. \tag{7.27}$$

These numbers can slightly differ from experiment to experiment due to different experimental settings of COSY, which is not an issue, as only the relative changes to the modified spin tunes are relevant for the experiment. Note that the spin tune is a negative quantity as shown in Eq. (4.37). The uncertainty on the averaged initial spin tune is neglected for further data processing.

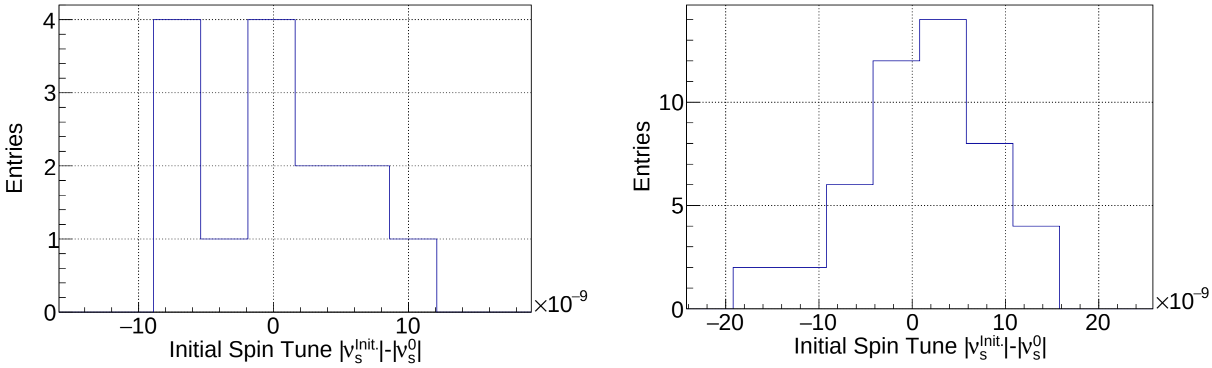

(a) Precursor 1: $|\nu_s^0| = 0.160\,970\,485(1)$

(b) Precursor 2: $|\nu_s^0| = 0.160\,973\,254(1)$

Figure 7.11.: Distribution of the initial spin tune before ramping both solenoids. The initial spin tune is measured for each cycle which contributes to the measurement of the solenoid calibration parameter and the determination of the longitudinal Invariant Spin Axis component at the respective solenoids. The average values are fed into the spin tune jump formula (7.20). Note that the spin tune is a negative quantity as shown in Eq. (4.37).

The calibration measurement of the Siberian snake for the first Precursor Run is shown in Figure 7.12. The change of spin tune is shown as a function of the applied current to the power supply of the Siberian snake. The data is extrapolated using Eq. (7.19). During the second Precursor Run, both the Siberian snake and the 2 MV solenoid are used which requires a calibration of both solenoids. The spin tune change as a function of Siberian snake current and 2 MV solenoid current is shown in Figure 7.13 along with a fit according to Eq. (7.20). The uncertainty of the power supply attached to the Siberian snake is given by $\sigma_{I_{\text{Snake}}} = 1 \times 10^{-3}\,$A. The same uncertainty for the 2 MV solenoid yields $\sigma_{I_{\text{2MV Sol.}}} = 5 \times 10^{-4}\,$A. Both values correspond to the standard deviation of the power supply distribution measured over a couple of minutes.

The fit results are summarized in Table 7.5. Note that during the second Precursor Run, two bunches are co-rotating in COSY in preparation to use the so-called Pilot bunch technique, aiming at the measurement of the orientation of the Invariant Spin Axis at the location of the RF Wien filter. More information about the Pilot bunch technique is given in section 7.6.3. The spin tunes of these bunches are analyzed and fitted independently since both bunches are affected by the solenoidal fields.

The most striking result is the decrease of the orientation of the Invariant Spin Axis in the longitudinal direction by one order of magnitude from Precursor Run I to Precursor Run 2. The measurement of a tilt angle of $1 \times 10^{-4}\,$rad and $1 \times 10^{-5}\,$rad is an important result to estimate the systematic contribution from ring imperfections to the final measurement using the RF Wien filter, where the orientation of the Invariant Spin Axis can be measured in both

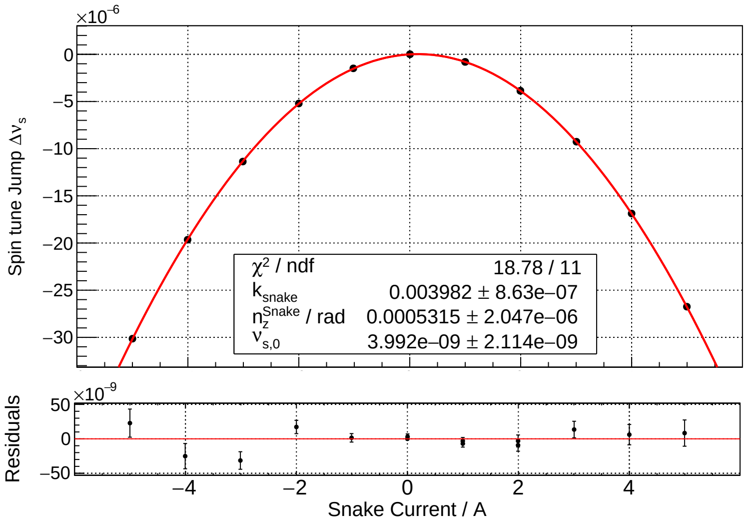

Figure 7.12.: Siberian snake calibration measurement for the first Precursor run by measuring the change in spin tune as a function of the set current to the power supply of the Siberian snake. The data is extrapolated using Eq. (7.19).

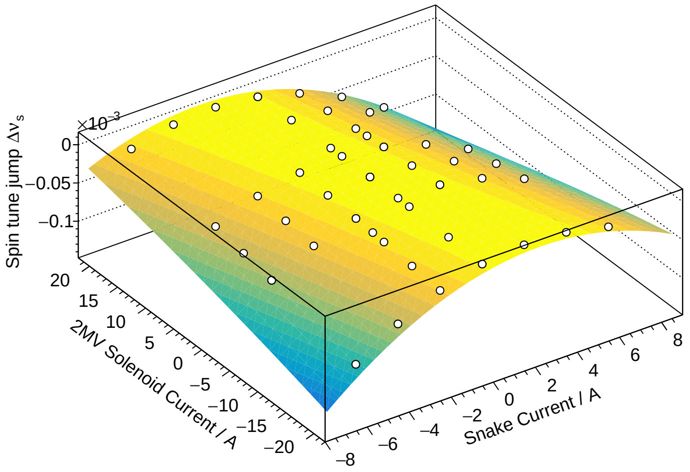

Figure 7.13.: Siberian snake and 2 MV solenoid calibration measurement for the second Precursor run by measuring the change in spin tune as a function of the set current to the power supply of the Siberian snake and the 2 MV solenoid. The data is extrapolated using Eq. (7.20). The plot depicts data taken from the first bunch.

radial and longitudinal directions. The decrease in order of magnitude is most certainly related to the beam-based alignment campaign and the alignment by Stollenwerk, which are discussed in further detail in section 7.7.2.1. This improvement is also predicted by simulations from Maximillian Vitz [104].

Table 7.5.: Summary of the results from the measurements of the longitudinal component of the Invariant Spin Axis at the Siberian snake and the 2 MV solenoid.

		Precursor 1	Precursor 2	
	Parameter	Bunch 1	Bunch 1	Bunch 2
Siberian Snake	k_{Snake} / $^{\text{rad}}/_{\text{A}}$	3.9824(9)	$3.9794(2) \times 10^{-3}$	$3.9794(2) \times 10^{-3}$
	n_z^{Snake} / rad	$5.3(2) \times 10^{-4}$	$-5.7(1) \times 10^{-5}$	$-5.6(1) \times 10^{-5}$
2 MV solenoid	$k_{2\text{ MV Sol.}}$ / $^{\text{rad}}/_{\text{A}}$		$3.9906(3) \times 10^{-4}$	$3.9904(7) \times 10^{-4}$
	$n_z^{2\text{ MV Sol.}}$ / rad		$-7.05(9) \times 10^{-5}$	$-7.07(9) \times 10^{-5}$
	$\Delta\nu_{s,0}$	$3.9(21) \times 10^{-9}$	$5.7(10) \times 10^{-9}$	$5.3(9) \times 10^{-9}$
	χ^2/ndf	$^{18.78}/_{11} = 1.71$	$^{162.82}/_{52} = 3.13$	$^{185.69}/_{52} = 3.57$

The offset parameter $\Delta\nu_{s,0}$, which is artificially introduced in Eq. (7.19) and (7.20), is related to the spin tune drift during the cycle. For both measurement periods, the offset parameter is in the order of 1×10^{-9}, which is comparable to the drift of the spin tune in a 30 s interval.

7.4.3.1. Studying the Influence of the RF Wien Filter on the Spin Tune

In addition to the dedicated cycles for measuring the longitudinal component of the Invariant Spin Axis at the solenoids, the cycles using the RF Wien filter can be used to parasitically determine the orientation of the Invariant Spin Axis in the longitudinal direction at the Siberian snake. The reason for this analysis is twofold. On one side, the influence of the RF Wien filter on the longitudinal component of the Invariant Spin Axis at the Siberian snake can be studied. If the RF Wien filter would change the orientation of the Invariant Spin Axis, the averaged spin tune in COSY would also change. In addition, for each measurement of the Invariant Spin Axis at the RF Wien filter, a measurement of the longitudinal component of the Invariant Spin Axis at the Siberian snake is available, which allows probing the stability of the orientation of the Invariant Spin Axis at the solenoids during the experimental periods.

To probe the influence of the RF Wien filter on the Invariant Spin Axis, the spin tune difference between 89 and 99 s and 155 and 165 s in the cycle is compared, which corresponds to a time interval in which the RF Wien filter is switched on. Multiple spin tune measurements are available for each Wien filter rotation angle and Siberian snake current. These results are averaged for each combined setting. The change in spin tune as a function of the Siberian current and the RF Wien filter rotation angle is shown in Figure 7.14. The data points are selected by the corresponding RF Wien filter rotation angle to rule out dependencies due to different rotation angles. The data points are fitted using a two-dimensional extension of Eq. (7.19), which has no dependencies for the rotation angle of the RF Wien filter. The results are comparable with the results determined using the dedicated cycles which are summarized in Table 7.5. If the RF Wien filter changes the spin tune, the Pilot bunch method, which is used to determine the orientation of the Invariant Spin Axis at the location of the RF Wien filter in the radial and the longitudinal direction, wouldn't work.

Upon conducting a consistency check of the Invariant Spin Axis's longitudinal component at the Siberian snake, denoted as n_z^{Snake}, using data obtained through the RF Wien filter, it is observed that the longitudinal component remains relatively stable across the experimental

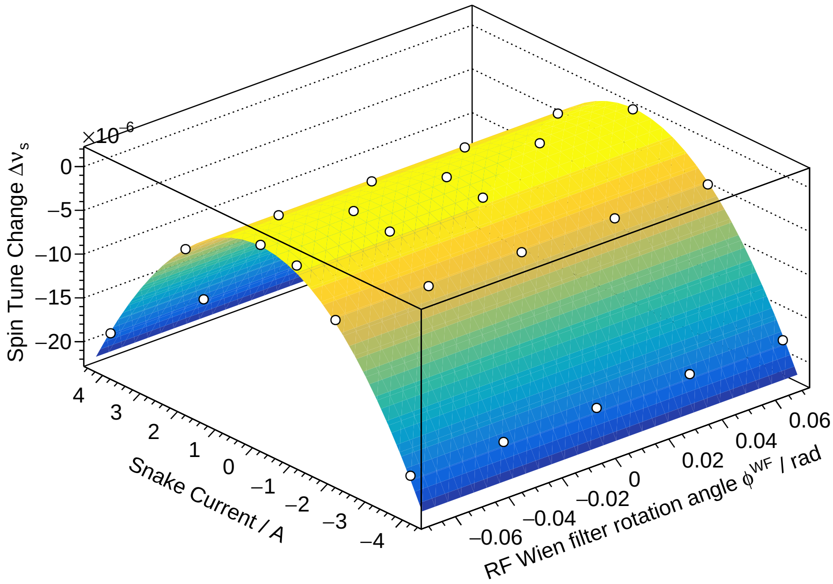

Figure 7.14.: The change of spin tune as a function of the current set to the power supply of the Siberian snake and the RF Wien filter rotation angle. The data is fitted using a two-dimensional extension of Eq. (7.19).

datasets (cf. Figure 7.15: Precursor 1 on the left and Precursor 2 on the right). This stability is notable, particularly given that the data-taking period spans multiple weeks.

7.4.4. Event Selection Studies

The explanations of the Event Selection Studies are given in section 6.3.1. After the selection, the same spin tune determination procedure as described in section 7.4.2 is repeated for both the events in the heads and tails as well as the center events. The results of the event selection studies for the second Precursor Run where both solenoids are calibrated are shown in Figure 7.16. In both cases, the results of the calibration model are consistent with each other. However, this is not a surprising result. If the solenoidal magnetic fields would lead to a larger spin tune spread inside the bunch, then the Spin Coherence Time would vanish after a short period. The results for the first Precursor calibration are shown in Figure C.1. These results are consistent as well.

7.5. Calibration of the RF Wien Filter Levels

In preparation for all experiments, the orientation of the RF Wien filter with respect to the COSY accelerator plane needs to be calibrated. It is well known that the COSY plane is tilted. The orientation of the RF Wien filter with respect to the tilted COSY accelerator plane is calibrated using a laser tracker installed at the inner wall of the COSY tunnel at the location of the RF Wien filter. The laser tracker measures the location of mirrors attached to the

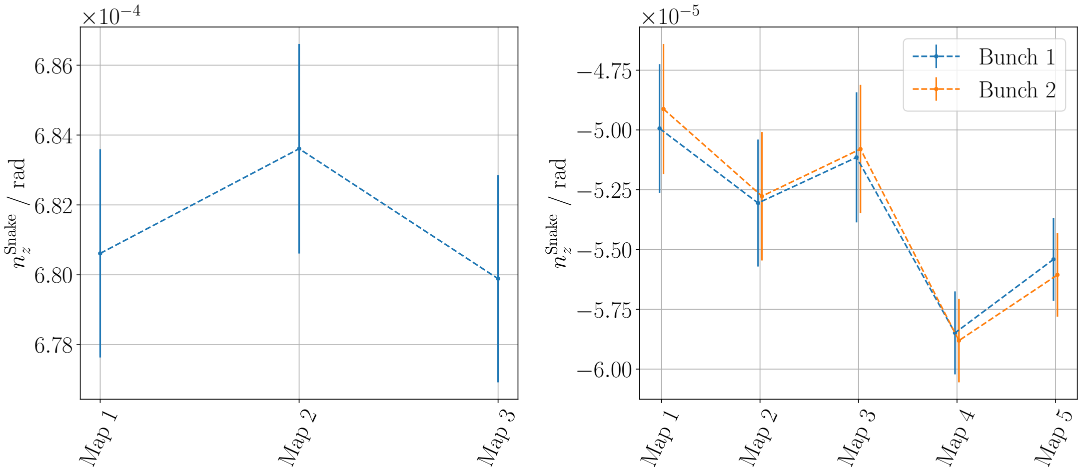

Figure 7.15.: Consistency check of the longitudinal component of the Invariant Spin Axis at the Siberian snake n_z^{Snake} for the data using the RF Wien filter at different rotation angles (cf. Figure 7.14). Among the experimental data (left Precursor 1 and right Precursor 2), the longitudinal component of the Invariant Spin Axis at the Siberian snake stays reasonably constant, especially considering the data is taken over multiple weeks.

fiducials at the RF Wien filter. By aligning the z components of the location of the mirrors, the angle of the RF Wien filter with respect to the COSY plane can be calculated. These measurements were performed by Markus Schmühl. The results of the angles are summarized in Table 7.6. The uncertainty corresponds to the uncertainty of the rotation angle of the RF Wien filter. The value corresponding to the systematic studies is used for the results presented in section 8.3.

Table 7.6.: Alignment angles of the RF Wien filter with respect to the COSY plane for Precursor 1 & 2.

	Precursor 1 (2018)	Precursor 2 (2021)	Systematic Studies (2023)
$\phi_{\text{WF}}^{\text{off}}$ / rad	0.000 95(17)	0.000 55(17)	0.000 67(17)

For the correct alignment of the RF Wien filter rotation angle, this offset needs to be subtracted from the readout of the Wien filter rotation angle, assuming that the magnetic field direction is directly related to the alignment of the RF Wien filter with respect to the COSY plane. The rotation angle of the RF Wien filter, and hence, of the magnetic field direction is given by

$$\phi_{\text{WF}} = \phi_{\text{WF}}^{\text{meas.}} - \phi_{\text{WF}}^{\text{off}}. \tag{7.28}$$

The uncertainty of the measured rotation angle is also given by $\sigma_{\phi_{\text{WF}}^{\text{meas.}}} = 0.17\,\text{mrad}$. Therefore, the final uncertainty of the Wien filter rotation angle is given by

$$\sigma_{\phi_{\text{WF}}} = \sqrt{2}\phi_{\text{WF}}^{\text{meas.}} = \sqrt{2}\phi_{\text{WF}}^{\text{off.}} = 0.000\,24\,\text{rad}. \tag{7.29}$$

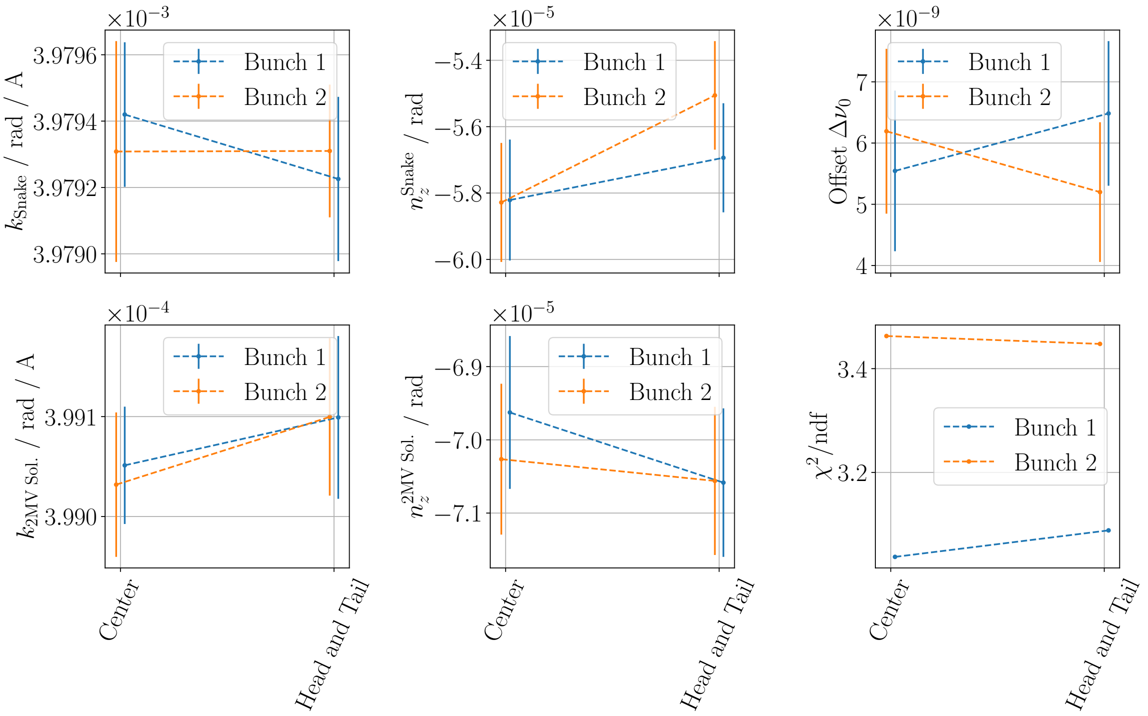

Figure 7.16.: Results of the Event Selection Studies for solenoid calibration data taken during the second Precursor Run. Using both datasets, the fit parameters are determined, which are consistent within their uncertainties.

7.6. Determination of the Invariant Spin Axis using the RF Wien filter

The following derivations of the spin dynamics in an RF Wien filter are based on the internal note *Spin motion in an rf Wien filter* by Volker Hejny [105].

As discussed in section 4.2, the Electric Dipole Moment of the deuteron causes a small rotation of the Invariant Spin Axis in the radial direction by an angle

$$\phi_{\text{EDM}} = \frac{\eta\beta}{2G}, \tag{7.30}$$

where η denotes the dimensionless Electric Dipole Moment strength parameter introduced in Eq. (2.13), and β and G are the beam velocity and the anomalous magnetic moment, respectively. This means that a measurement of the radial direction of the Invariant Spin Axis (ϕ_{EDM}) can be directly translated into an Electric Dipole Moment.

In general, the Invariant Spin Axis can be written as

$$\vec{n} = n_x\vec{e}_x + n_y\vec{e}_y + n_z\vec{e}_z \tag{7.31}$$

$$\approx n_x\vec{e}_x + 1\vec{e}_y + n_z\vec{e}_z, \tag{7.32}$$

assuming that the radial (n_x) and longitudinal (n_z) components of the Invariant Spin Axis are small. In an ideal accelerator, the radial component of the Invariant Spin Axis corresponds directly to the tilt angle of the Invariant Spin Axis due to the effects of the Electric Dipole Moment. However, systematic contributions of the ring can lead to additional tilts of the Invariant Spin Axis in the radial direction. Therefore, the radial component of the Invariant Spin Axis can be written as

$$n_x = \phi_{\mathrm{EDM}} + n_x^{\mathrm{sys.}}, \tag{7.33}$$

where $n_x^{\mathrm{sys.}}$ denotes the systematic contribution of the ring on the radial direction of the Invariant Spin Axis. In addition, in an ideal case, no longitudinal component of the Invariant Spin Axis is expected. Therefore, any non-zero measurement of the longitudinal component of the Invariant Spin Axis is purely systematic

$$n_z = n_z^{\mathrm{sys.}}. \tag{7.34}$$

To probe the radial component of the Invariant Spin Axis, an RF Wien filter is installed in the ring, which can be rotated around the longitudinal axis (beam pipe) by an angle (ϕ^{WF}). The RF Wien filter is operated in the so-called EDM mode, in which the magnetic field points perpendicular to the accelerator plane. By rotating the device, the magnetic field direction changes with respect to the Invariant Spin Axis.

The longitudinal component of the Invariant Spin Axis can be probed by using the Siberian snake in the opposite straight in COSY. By ramping the solenoid, the longitudinal component of the Invariant Spin Axis changes along the ring.

By mapping the so-called resonance strength

$$\epsilon = \frac{\psi_0}{4\pi}|\vec{n} \times \vec{m}|, \tag{7.35}$$

where $\vec{m}$ denotes the magnetic field axis direction of the RF Wien filter with $|\vec{m}| = 1$ and $\vec{n}$ denotes the Invariant Spin Axis, as a function of the Wien filter rotation angle and flip angle of the Invariant Spin Axis due to the solenoid, the Invariant Spin Axis and the magnetic field of the RF Wien filter can be aligned. The settings of Wien filter rotation angle and spin flip in the opposite straight section in the Siberian snake ($\phi^{\mathrm{WF}}, \chi_{\mathrm{Snake}}$) for which the resonance strength is zero ($\vec{n} \parallel \vec{m}$) denote the orientation of the Invariant Spin Axis. The spin kick angle inside the RF Wien filter is given by ψ_0.

The coordinate system is chosen to be in a reference frame with respect to the Invariant Spin Axis $\vec{n}$ at the location of the RF Wien filter

$$\vec{e}_y = \vec{n},\ \vec{e}_x = \vec{n} \times \vec{\beta},\ \text{and}\ \vec{e}_z = \vec{e}_x \times \vec{e}_y. \tag{7.36}$$

The coordinate system is illustrated in Figure 7.17 together with the orientation of the magnetic field of the RF Wien filter.

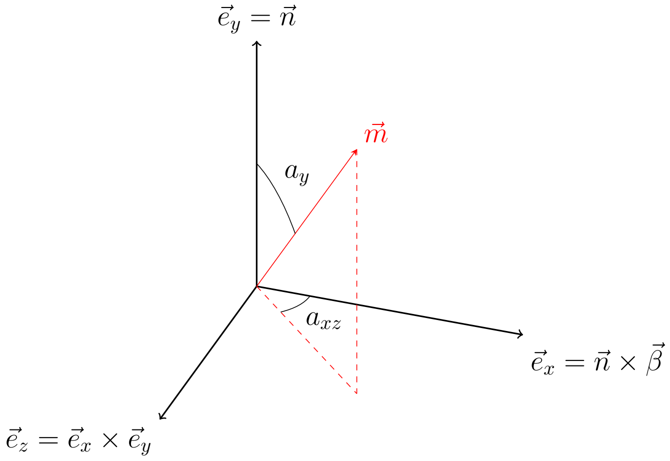

Figure 7.17.: Coordinate system for the description of the magnetic field axis of the Wien filter $\vec{m}$ with respect to the coordinate system defined in Eq. (7.36).

The spin vector at the location of the RF Wien filter is defined with respect to the out-of-plane angle α (the angle between vertical and horizontal polarization plane) and the spin precession angle $\omega_s = 2\pi\nu_s f_{\text{COSY}}$ in the accelerator plane $(x - z)$

$$\vec{S} = \begin{pmatrix} \cos(\alpha)\sin(\omega_s t) \\ \sin(\alpha) \\ \cos(\alpha)\cos(\omega_s t) \end{pmatrix}. \tag{7.37}$$

When the measurement time begins, $t = t_{\text{WF}}$, the spin points along $\vec{e}_z$ without loss of generality. In addition, the spin might have a vertical component when the rotation of the initial vertically polarized beam is not fully rotated into the accelerator plane using the RF solenoid.

In this coordinate system, the magnetic field axis of the RF Wien filter is given by

$$\vec{m} = \begin{pmatrix} -\sin(a_y)\cos(a_{xz}) \\ \cos(a_y) \\ \sin(a_y)\sin(a_{xz}) \end{pmatrix}. \tag{7.38}$$

The parameter a_y describes the angle between the magnetic field of the RF Wien filter and the Invariant Spin Axis (cf. Figure 7.17)

$$\sin(a_y) = |\vec{n} \times \vec{m}|. \tag{7.39}$$

The parameter a_{xz} describes the orientation of the magnetic field of the RF Wien filter in the $x - z$ plane with respect to $\vec{e}_x$.

Using the Thomas-BMT equation (4.22), it is possible to derive coupled differential equations which describe the relative phase between the Wien filter frequency and spin tune $\phi_{\text{rel.}}$ and the opening angle between the vertical polarization and the in-plane polarization plane α with respect to the turn number n. The differential equations depend on the relative phase $\phi_{\text{rel.}}$, the opening angle α, the orientation of the magnetic field of the RF Wien filter with respect to the radial vector $\vec{e}_x$. Most importantly, they depend on the resonance strength ϵ, and hence the opening angle between the magnetic field axis of the RF Wien filter and the Invariant spin axis. A full derivation is given in section D.1. The differential equations are given by

$$\frac{\mathrm{d}\phi_{\text{rel.}}}{\mathrm{d}n} = 2\pi\epsilon \sin(a_{xz} - \phi_{\text{rel.}}) \tan(\alpha), \tag{7.40}$$

$$\frac{\mathrm{d}\alpha}{\mathrm{d}n} = -2\pi\epsilon \cos(a_{xz} - \phi_{\text{rel.}}). \tag{7.41}$$

Using the following identity between turn number n, beam revolution frequency f_{COSY} and time t

$$n = f_{\text{COSY}} t, \tag{7.42}$$

the differential equations can be transformed into

$$\boxed{\begin{aligned}\frac{\mathrm{d}\phi_{\text{rel.}}}{\mathrm{d}t} &= 2\pi\epsilon f_{\text{COSY}} \sin(a_{xz} - \phi_{\text{rel.}}) \tan(\alpha), &(7.43)\\ \frac{\mathrm{d}\alpha}{\mathrm{d}t} &= -2\pi\epsilon f_{\text{COSY}} \cos(a_{xz} - \phi_{\text{rel.}}). &(7.44)\end{aligned}}$$

In the following sections, the meaning of the resonance strength ϵ in the context of the measurement goal of determining the orientation of the Invariant Spin Axis is explained. In addition, the solution of the differential equations depends on the way the phase feedback is used.

Using the phase feedback, the relative phase remains constant

$$\frac{\mathrm{d}\phi_{\text{rel.}}}{\mathrm{d}t} = 0, \tag{7.45}$$

which simplifies the coupled differential equations (7.43) and (7.44). This method is used in the so-called Initial slope method which is further explained in section 7.6.2.

Using the so-called Pilot bunch method, two bunches are co-rotating in COSY. One of the bunches is gated from the RF Wien filter fields and used by the phase feedback to adjust the Wien filter frequency and phase. The other bunch is used as a signal bunch and is affected by the RF Wien filter fields. As it is not phase-locked, the phase behaves according to Eq. 7.43. More information about the Pilot bunch method is given in section 7.6.3.

7.6.1. The Resonance Strength

The resonance strength ϵ is introduced in Eq. (7.35) as the angle between the Invariant Spin Axis and the magnetic field direction of the RF Wien filter scaled with the spin kick of the RF Wien filter

$$\epsilon = \frac{\psi_0}{4\pi} |\vec{n} \times \vec{m}|. \tag{7.46}$$

The parameter is reintroduced in Eq. (7.38) when the orientation of the RF Wien filter field is described with respect to the orientation of the Invariant Spin Axis. In the experiment, the lab frame (i.e. Cartesian coordinates) at the RF Wien filer is used instead of the parameters a_z and a_{xz}. The y axis points perpendicular to the accelerator plane $x - z$. The z axis (or longitudinal component) points into the beam direction and the x axis points perpendicular to y and z into the radial direction.

The orientation of the magnetic field of the RF Wien filter is given by

$$\vec{m} = \begin{pmatrix} \sin\left(\phi^{\mathrm{WF}}\right) \\ \cos\left(\phi^{\mathrm{WF}}\right) \\ 0 \end{pmatrix} \overset{\phi^{\mathrm{WF}} \ll 1}{\approx} \begin{pmatrix} \phi^{\mathrm{WF}} \\ 1 \\ 0 \end{pmatrix}, \tag{7.47}$$

where ϕ^{WF} denotes the rotation angle of the RF Wien filter around the beam pipe which is typically in the order of a few milli radians.

The Invariant Spin Axis without additional contributions from static solenoids is defined as

$$\vec{n} \approx \begin{pmatrix} n_x \\ 1 \\ n_z \end{pmatrix}, \tag{7.48}$$

assuming that the longitudinal n_z and radial components n_x of the Invariant Spin Axis are small.

The radial component, as already defined in Eq. (7.33), is given by

$$n_x = \phi_{\mathrm{EDM}} + n_x^{\mathrm{sys.}}, \tag{7.49}$$

where the first term describes the contribution of the Electric Dipole Moment ϕ_{EDM} as defined in Eq. (7.30). In addition, ring imperfections like magnet misalignments and higher-order multipoles in the magnets lead to orbit distortions and additional systematic tilts of the Invariant Spin Axis in radial ($n_x^{\mathrm{sys.}}$) and longitudinal direction (n_z). Tilts in the longitudinal direction are purely systematic, which is already explained in Eq. (7.34)

$$n_z = n_z^{\mathrm{sys.}}. \tag{7.50}$$

Using the 2 MV solenoid and the Siberian snake, the Invariant Spin Axis at the location of the RF Wien filter is modified. The modified Invariant Spin Axis at the location of the RF Wien filter is given by

$$\vec{n} = \begin{pmatrix} n_x + \frac{\chi_{\mathrm{2MV\ Sol.}}}{2} \\ 1 \\ n_z + \frac{\chi_{\mathrm{Snake}} + \chi_{\mathrm{2MV\ Sol.}} \cos\left(\pi\nu_s^0\right)}{2\sin\left(\pi\nu_s^0\right)} \end{pmatrix}, \tag{7.51}$$

where χ_{Snake} and $\chi_{\text{2MV Sol.}}$ denote the spin flip in the Siberian snake and the 2MV solenoid as defined in Eq. (7.15) and ν_s^0 denotes the unperturbed spin tune. Finally, the resonance strength can be written as

$$\epsilon^2 = \frac{\psi_0^2}{16\pi^2}|\vec{m}\times\vec{n}|^2 \tag{7.52}$$

$$\approx \frac{\psi_0^2}{16\pi^2}\left|\begin{pmatrix}\phi^{\text{WF}}\\ 1\\ 0\end{pmatrix}\times\begin{pmatrix} n_x+\frac{1}{2}\chi_{\text{2MV Sol.}}\\ 1\\ n_z+\frac{\chi_{\text{Snake}}+\chi_{\text{2MV Sol.}}\cos\left(\pi\nu_s^0\right)}{2\sin\left(\pi\nu_s^0\right)}\end{pmatrix}\right|^2 \tag{7.53}$$

$$= \frac{\psi_0^2}{16\pi^2}\left[\left(n_x+\frac{1}{2}\chi_{\text{2MV Sol.}}-\phi^{\text{WF}}\right)^2\right. \tag{7.54}$$

$$\left. + \left(\frac{\chi_{\text{Snake}}+\chi_{\text{2MV Sol.}}\cos\left(\pi\nu_s^0\right)}{2\sin\left(\pi\nu_s^0\right)}+n_z\right)^2\cdot\left(1+\phi^{\text{WF}^2}\right)\right] \tag{7.55}$$

$$\overset{\phi^{\text{WF}}\ll 1}{\approx} \frac{\psi_0^2}{16\pi^2}\left[\left(n_x+\frac{1}{2}\chi_{\text{2MV Sol.}}-\phi^{\text{WF}}\right)^2+\left(\frac{\chi_{\text{Snake}}+\chi_{\text{2MV Sol.}}\cos\left(\pi\nu_s^0\right)}{2\sin\left(\pi\nu_s^0\right)}+n_z\right)^2\right]. \tag{7.56}$$

The 2MV solenoid is only used for a few data points during the second Precursor run. For the measurements using the 2 MV solenoid, the current of the solenoid was not changed but kept constant. Therefore, the spin flip angle in the 2 MV solenoid is used as a fixed parameter and not as a variable in Eq. (7.56). The fit formula for the resonance strength using only the Siberian snake ($\chi_{\text{2MV Sol.}}=0$) is given by

$$\epsilon^2 \approx \frac{\psi_0^2}{16\pi^2}\left[\left(n_x-\phi^{\text{WF}}\right)^2+\left(\frac{\chi_{\text{Snake}}}{2\sin\left(\pi\nu_s^0\right)}+n_z\right)^2\right]. \tag{7.57}$$

For a single solenoid, the fit formula for the resonance strength is a two-dimensional paraboloid. By varying the Wien filter rotation angle ϕ^{WF}, the magnetic field axis of the RF Wien filter can be aligned with the radial component of the Invariant Spin Axis (n_x) setting the first contribution to zero ($n_x-\phi^{\text{WF}}=0$). The Siberian snake acts as a compensation solenoid. By changing the spin flip rotation angle χ_{Snake}, the systematic longitudinal contribution of the Invariant Spin Axis (n_z) can be compensated $\chi_{\text{Snake}}/2\sin(\pi\nu_s)+n_z=0$. By finding the settings of ($\phi^{\text{WF}},\chi_{\text{Snake}}$) which lead to a vanishing resonance strength, the orientation of the Invariant Spin Axis can be found. In Table 7.7, an overview of all parameters and variables used in Eq. (7.56) is given.

For the final fit of the resonance strengths, the unperturbed spin tune (i.e. without solenoids) enters the fit as a fixed parameter. The initial spin tune is averaged among all cycles which contribute to the determination of the Invariant Spin Axis.

7.6.2. The Initial Slope Method

In this section, a first method to extract the resonance strength ϵ from data is presented. The method is based on the way the phase feedback is used. The differential equations for the angle

Table 7.7.: Description of the variables and fit parameters in Eq. (7.56).

Symbol	Description	Type	Unit
ψ_0	Spin kick in the RF Wien filter	Parameter	rad
n_x	Radial component of $\vec{n}$: $n_x = \phi_{\text{EDM}} + n_x^{\text{sys.}}$	Parameter	rad
ϕ_{EDM}	EDM contribution to the radial component of $\vec{n}$		rad
$n_x^{\text{sys.}}$	Systematic contribution to the radial component of $\vec{n}$		rad
ϕ^{WF}	Rotation angle of the RF Wien filter	Variable	rad
$\chi_{\text{2MV Sol.}}$	Spin flip angle in the 2 MV solenoid	Fixed Parameter	rad
χ_{Snake}	Spin flip angle in the Siberian snake	Variable	rad
n_z	Systematic longitudinal component of $\vec{n}$: $n_z = n_z^{\text{sys.}}$	Parameter	rad
ν_s^0	Unperturbed spin tune	Fixed Parameter	

between vertical and horizontal polarization and the relative phase between the Wien filter frequency and spin tune are derived in section 7.6

$$\frac{\mathrm{d}\phi_{\text{rel.}}}{\mathrm{d}n} = 2\pi\epsilon \sin(a_{xz} - \phi_{\text{rel.}}) \tan(\alpha), \tag{7.58}$$

$$\frac{\mathrm{d}\alpha}{\mathrm{d}n} = -2\pi\epsilon \cos(a_{xz} - \phi_{\text{rel.}}). \tag{7.59}$$

During the so-called initial slope method, the phase feedback acts on the measurement bunch, which means that the bunch is affected by the RF Wien filter fields. In section 7.6.3, the phase feedback does not act on the measurement bunch, meaning that two bunches are co-rotating in COSY, while only one bunch is affected by the Wien filter fields, and the other is not.

The effect of the phase feedback is rather easy to explain. It keeps the phase relation between the RF Wien filter frequency and the spin precession frequency constant, reducing the differential equations to

$$\frac{\mathrm{d}\phi_{\text{rel.}}}{\mathrm{d}n} = 0, \tag{7.60}$$

$$\frac{\mathrm{d}\alpha}{\mathrm{d}n} = -2\pi\epsilon \cos(a_{xz} - \phi_{\text{rel.}}). \tag{7.61}$$

This describes a linear increase of α as a function of time. The slope depends on the chosen value for the phase relation between the Wien filter frequency and spin tune

$$\phi_{\text{rel.}} = \phi_{\text{rel.},0}, \tag{7.62}$$

$$\frac{\mathrm{d}\alpha}{\mathrm{d}n} = -2\pi\epsilon \cos(a_{xz} - \phi_{\text{rel.},0}). \tag{7.63}$$

In reality, the relative phase has an arbitrary but constant offset $\phi_{\text{rel.}}^{\text{off}}$ due to latencies in the signal processing and the distance between the RF Wien filter and the polarimeter. Therefore, the relative phase can be written as

$$\phi_{\text{rel.}} = \phi_{\text{rel.},0} = \phi_{\text{rel.}}^{\text{set}} + \phi_{\text{rel.}}^{\text{off}}, \tag{7.64}$$

where $\phi_{\text{rel.}}^{\text{set}}$ denotes the relative phase set by the operators. The linear increase of the angle between vertical and horizontal polarization is shown in Figure 7.18. The angle is fitted using a polynomial of first order. The slope is given by

$$\dot{\alpha} = -2\pi\epsilon f_{\text{COSY}} \cos(a_{xz} - \phi_{\text{rel.,0}}). \tag{7.65}$$

As the resonance strength is determined by fitting the linear increase of the angle between vertical and horizontal polarization, the method is also called the *initial slope* method.

The fit range is determined by the up-down asymmetry (horizontal polarization). If the horizontal polarization is too small, the spin tune is not detectable, which means that the phase feedback stops working. If the up-down asymmetry (horizontal polarization) is below a threshold of 6 %, the fit range is stopped. This is shown in the upper right panel in Figure 7.18. The first vertical dashed line marks the timestamp when the RF Wien filter is switched on ($t_{\text{WF}} = 155\,\text{s}$), the second vertical dashed line marks the timestamp when the up-down asymmetry is below 6 %. This range is used for the determination of the relative phase between the Wien filter frequency and spin tune (upper left panel) and the initial buildup of the angle between vertical and horizontal polarization. The relative phase is still stable after the fit range, which means that the fit range could be extended by lowering the threshold. However, a threshold of 6 % for the horizontal polarization turned out to be the most stable for the fitting process.

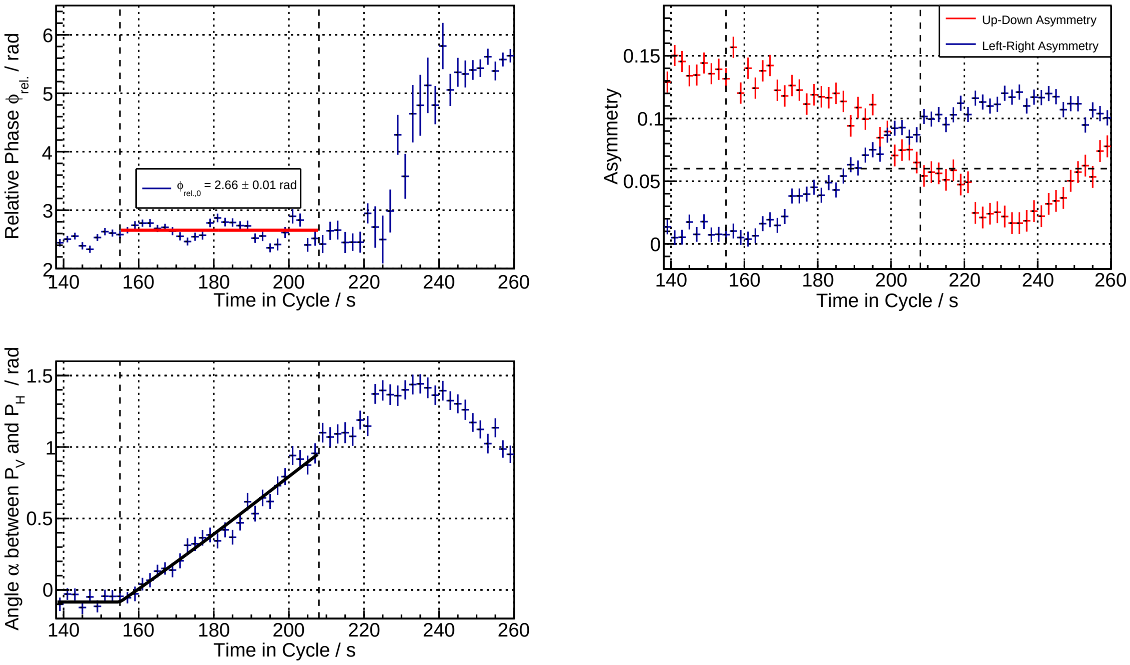

Figure 7.18.: Determination of the fit range for the initial slope method. If the up-down asymmetry (upper right panel) is below a threshold of 6 %, the fit range is stopped. This fit range is used to determine the relative phase (upper left panel) and the slope of the linear increase of the angle between the vertical and horizontal polarization (lower left panel).

The dependence of the slope of the buildup of α as a function of the relative phase $\phi_{\text{rel.}}^{\text{set}}$ is shown in Figure 7.19 for four exemplary cycles. The left panel shows the measured relative phase as a function of time for four cycles. The right panel shows the angle between vertical and horizontal polarization for the same four cycles. For better visibility, data points after the fit range are not shown in both panels.

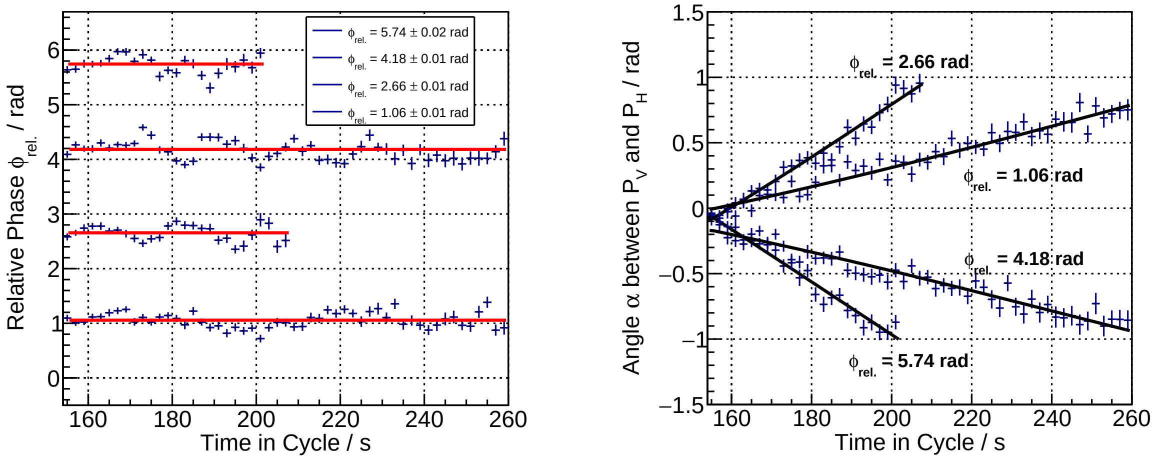

Figure 7.19.: Four distinct cycles to determine the resonance strength using the Initial slope method. **Left:** Measured relative phases as a function of time in the cycle. **Right:** Buildup of the angle between vertical and horizontal polarization plane for the choices of the relative phase between RF Wien filter frequency and spin tune.

For the determination of the resonance strength ϵ, the buildup of α needs to be measured for different values of the relative phase. The dependence of the slope of the buildup of the angle between vertical and horizontal polarization is depicted in Figure 7.20 for an RF Wien filter rotation angle $\phi^{\text{WF}} = 0\,\text{rad}$ and $\chi_{\text{Snake}} = -0.022\,\text{rad}$. The slope determined from data shown in Figure 7.19 is scaled by the revolution frequency

$$\dot{\alpha} = \frac{\mathrm{d}\alpha}{\mathrm{d}t} \to \frac{1}{2\pi f_{\text{COSY}}}\frac{\mathrm{d}\alpha}{\mathrm{d}t} = \frac{1}{2\pi}\frac{\mathrm{d}\alpha}{\mathrm{d}n} \overset{!}{=} -\epsilon\cos(a_{xz} - \phi_{\text{rel.},0}). \tag{7.66}$$

In the following section 7.6.2.1, it is shown that a linear model is not the true dependence of the buildup of the vertical polarization as Spin Coherence Time effects are not negligible.

The scaled slope is fitted using the following model

$$\frac{1}{2\pi}\frac{\mathrm{d}\alpha}{\mathrm{d}n} = A\sin(\phi_{\text{rel.}}) + B\cos(\phi_{\text{rel.}}) + C. \tag{7.67}$$

The offset parameter C is introduced as an additional validation for a systematic buildup. A non-zero offset parameter would be an additional buildup of the vertical polarization consistent for all measured cycles. For the data points given in Figure 7.20, the offset parameter is consistent with zero. Note that Eq. (7.67) can be written as

$$A\sin(x) + B\cos(x) + C = -\epsilon\cos(x-\varphi) + C \text{ with } A = \epsilon\cos(\varphi) \text{ and } B = \epsilon\sin(\varphi). \quad (7.68)$$

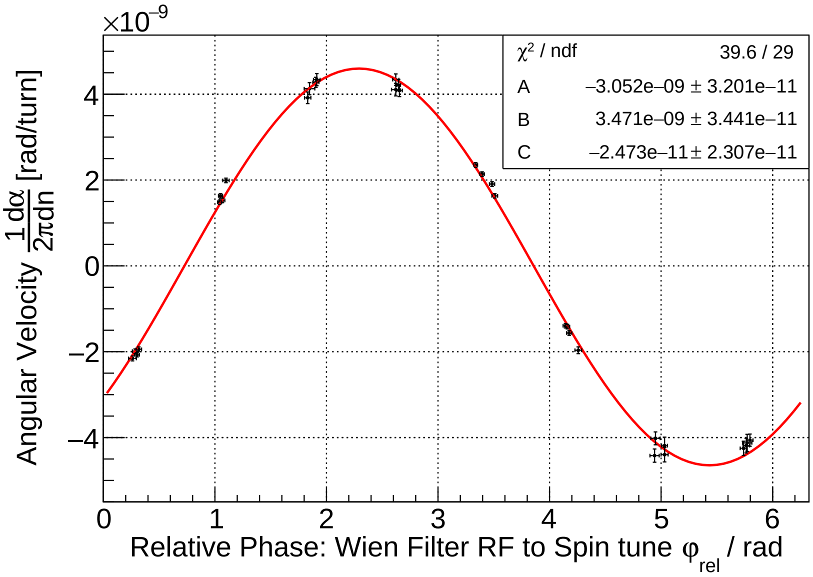

Figure 7.20.: Determination of the resonance strength using the initial slope method for a Wien filter rotation angle $\phi^{\mathrm{WF}} = 0\,\mathrm{rad}$ and $\chi_{\mathrm{Snake}} = -0.022\,\mathrm{rad}$ and for various settings of the relative phase between the Wien filter frequency and spin precession frequency $\phi_{\mathrm{rel.}}$. The resonance strength corresponds to the amplitude of the oscillation.

Using the fit parameters, the resonance strength can be calculated using

$$\epsilon = \sqrt{A^2 + B^2} \rightarrow \epsilon^2 = A^2 + B^2, \quad (7.69)$$

$$\sigma_{\epsilon^2} = 2\sqrt{A^2\sigma_A^2 + B^2\sigma_B^2 + 2\sigma_A\sigma_B AB\rho(A,B)}, \quad (7.70)$$

where $\rho(A,B)$ denotes the correlation coefficient between the fit parameters A and B. Note that the resonance strength squared is directly determined from the fit parameters, as the dependency of the resonance strength squared as a function of the RF Wien filter rotation angle and spin flip in the Siberian snake is derived for the resonance strength squared in Eq. (7.56) and (7.57).

7.6.2.1. Spin Coherence Time Correction

The analytical work from Eq. (7.71) to (7.83) is taken from former IKP student Nils Hempelmanns's PhD Thesis *Polarization Measurement and Manipulation for Electric Dipole Moment Measurements in Storage Rings* [106, p.77-83].

In section 7.2, the decay of polarization in the horizontal plane is discussed. For the buildup of the vertical polarization, decoherence plays an important role, as decay leads to a measurable fake buildup which needs to be distinguished from the buildup due to the RF Wien filter. The effect is illustrated in Figure 7.21. While the vertical component remains constant, the in-plane polarization reduces over time by Δp_H. This leads to a systematic offset of the angle α between vertical and in-plane polarization.

Distinguishing between the effects of spin decoherence and the RF Wien filter can be achieved by examining the magnitude of polarization $\varepsilon_{\text{tot}}^2 = \varepsilon_{\text{LR}}^2 + \varepsilon_{\text{UD}}^2$ and the angle $\alpha = \arctan\left({}^{\varepsilon_{\text{LR}}}/{}_{\varepsilon_{\text{UD}}}\right)$ at the same time. The RF Wien filter maintains the magnitude of the polarization by solely rotating the vector, while spin decoherence leads to a reduction in the magnitude of polarization.

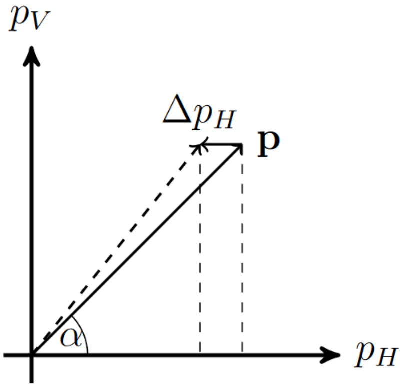

Figure 7.21.: While the vertical polarization component remains constant over time, the in-plane polarization reduces by Δp_H due to loss of polarization. This leads to an apparent buildup of the vertical component of the polarization vector, unrelated to the opening angle of the Invariant Spin Axis and the magnetic field direction of the RF Wien filter and consequently purely systematic. These effects are corrected using Eq. (7.82) and (7.83). Taken from [106].

The evolution of α and $\varepsilon_{\text{tot.}}$ can be described by two coupled differential equations. The differential equation describing α is given by

$$\frac{d\alpha}{dt} = \frac{\partial\alpha}{\partial t} + \frac{\partial\alpha}{\partial\varepsilon_{\text{UD}}}\frac{\partial\varepsilon_{\text{UD}}}{\partial\alpha}, \tag{7.71}$$

where the first term describes the explicit time dependence of the buildup rate due to the RF Wien filter which is already introduced in Eq. 7.65 and given by

$$\frac{\partial\alpha}{\partial t} = -2\pi\epsilon\cos(a_{xz} - \phi_{\text{rel.},0}) = A. \tag{7.72}$$

The angular velocity of the rotation of the polarization depends on the resonance strength and the relative phase between the Wien filter frequency and spin precession. Consequently, the differential equation of the magnitude of polarization is given by

$$\frac{\mathrm{d}\varepsilon_{\text{tot.}}}{\mathrm{d}t} = \frac{\mathrm{d}}{\mathrm{d}t}\sqrt{\varepsilon_{\text{LR}}^2 + \varepsilon_{\text{UD}}^2} \tag{7.73}$$

$$= \frac{1}{\sqrt{\varepsilon_{\text{LR}}^2 + \varepsilon_{\text{UD}}^2}}\left(\varepsilon_{\text{LR}}\frac{\mathrm{d}\varepsilon_{\text{LR}}}{\mathrm{d}t} + \varepsilon_{\text{UD}}\frac{\mathrm{d}\varepsilon_{\text{UD}}}{\mathrm{d}t}\right) \tag{7.74}$$

$$= \frac{1}{\varepsilon_{\text{tot}}}\left(\varepsilon_{\text{LR}}\frac{\partial\varepsilon_{\text{LR}}}{\partial\alpha}\frac{\partial\alpha}{\partial t} + \varepsilon_{\text{UD}}\left(\frac{\partial\varepsilon_{\text{UD}}}{\partial t} + \frac{\partial\varepsilon_{\text{UD}}}{\partial\alpha}\frac{\partial\alpha}{\partial t}\right)\right). \tag{7.75}$$

In section 7.2, a sophisticated model is presented for the decay of the in-plane polarization. However, for the measurements using the RF Wien filter, this model is not used due to its mathematical complexity. Instead, an exponential model is used introducing the only time dependence in the system of differential equations

$$\varepsilon_{\text{UD}}(t) = \varepsilon_{\text{UD},0}\exp\left(-Bt\right), \tag{7.76}$$

which consequently leads to

$$\frac{\partial\varepsilon_{\text{UD}}}{\partial t} = -\varepsilon_{\text{UD}}B. \tag{7.77}$$

The fit parameter B describes the attenuation of the in-plane polarization. Note, that the model only allows for an estimate of the Spin Coherence Time, as the data presented in Figure 7.1a and 7.1b show no direct exponential loss. The remaining derivatives can be calculated by using the following identities which can be directly derived from Figure 7.21

$$\alpha = \arctan\left(\frac{\varepsilon_{\text{LR}}}{\varepsilon_{\text{UD}}}\right), \quad \varepsilon_{\text{UD}} = \varepsilon_{\text{tot.}}\cos(\alpha), \text{ and } \varepsilon_{\text{LR}} = \varepsilon_{\text{tot.}}\sin(\alpha). \tag{7.78}$$

The derivatives that still need to be calculated are given by

$$\frac{\partial\alpha}{\partial\varepsilon_{\text{UD}}} = -\frac{\varepsilon_{\text{LR}}}{\varepsilon_{\text{tot.}}^2}, \quad \frac{\partial\varepsilon_{\text{UD}}}{\partial\alpha} = -\varepsilon_{\text{LR}}, \text{ and } \frac{\partial\varepsilon_{\text{LR}}}{\partial\alpha} = \varepsilon_{\text{UD}}. \tag{7.79}$$

The final set of differential equations can be written as

$$\frac{d\alpha}{dt} = A + B\cos(\alpha)\sin(\alpha), \tag{7.80}$$

$$\frac{d\varepsilon_{\text{tot.}}}{dt} = -B\varepsilon_{\text{tot.}}\cos^2(\alpha). \tag{7.81}$$

The first equation has no dependence on the magnitude of polarization, which means that it can be directly integrated. By inserting the solution of the first equation into the second equation, it can be integrated as well. The solution of the coupled differential equations is given by

$$\alpha(t) = \begin{cases} \arctan\left(\tan\left(\alpha_0\right) e^{B(t-t_{\mathrm{WF}})}\right) & A = 0 \\ \arctan\left(\frac{1}{2A}\left(\sqrt{4A^2-B^2}\frac{D+\tan\left(\frac{t-t_{\mathrm{WF}}}{2}\sqrt{4A^2-B^2}\right)}{1-D\tan\left(\frac{t-t_{\mathrm{WF}}}{2}\sqrt{4A^2-B^2}\right)}-B\right)\right) & 4A^2 > B^2 \\ \arctan\left(\frac{1}{2A}\left(\sqrt{B^2-4A^2}\frac{D-\tanh\left(\frac{t-t_{\mathrm{WF}}}{2}\sqrt{B^2-4A^2}\right)}{1-D\tanh\left(\frac{t-t_{\mathrm{WF}}}{2}\sqrt{B^2-4A^2}\right)}-B\right)\right) & 4A^2 < B^2 \end{cases} \tag{7.82}$$

$$\text{with } D = \frac{2A\tan(\alpha_0)+B}{\sqrt{|4A^2-B^2|}},$$

and

$$\log\left(\frac{\varepsilon(t)}{\varepsilon_0}\right) = \begin{cases} \frac{1}{2}\log\left(\frac{2A+B\sin(2\alpha_0)}{2A+B\sin(2\alpha(t))}\right) + & \\ \frac{B}{\sqrt{4A^2-B^2}}\arctan\left(\frac{\sin(\alpha_0-\alpha(t))\sqrt{4A^2-B^2}}{2A\cos(\alpha_0-\alpha(t))+B\sin(\alpha_0+\alpha(t))}\right) & 4A^2 > B^2 \\ \frac{B}{\sqrt{B^2-4A^2}}\operatorname{artanh}\left(\frac{\sin(\alpha_0-\alpha(t))\sqrt{B^2-4A^2}}{2A\cos(\alpha_0-\alpha(t))+B\sin(\alpha_0+\alpha(t))}\right) & 4A^2 < B^2. \end{cases} \tag{7.83}$$

The fit parameters are summarized in Table 7.8. The piece-wise definition is chosen to ensure non-imaginary fit functions. Both solutions are used in a combined χ^2-fit in which the correlation of α and $\epsilon_{\mathrm{tot.}}$ is neglected. An example of such a combined fit is shown in Figure 7.22. The model reproduces the shape of the data very well, which also leads to a reasonable χ^2/ndf. The decay of the in-plane polarization leads to a small nonlinearity.

Table 7.8.: Fit parameters to describe the buildup of the vertical polarization using the Initial slope method taking Spin Decoherence Effects into account.

Symbol	Description	Unit
A	Slope of the buildup	rad/s
B	Spin Coherence Time	$1/s$
t_{WF}	Fit starts when the RF Wien filter is switched on	s
α_0	α at $t = t_{\mathrm{WF}}$	rad
ε_0	Total polarization at $t = t_{\mathrm{WF}}$	

A comparison of the sophisticated model and a simple linear model for multiple cycles with different relative phases between the RF Wien filter and spin precession frequency is shown in Figure 7.23. The blue data points show the fit results of the slope (A) as a function of the relative phase using the complex model, taking the decoherence of the polarization into account, while the red data points are determined by using a pure linear model. The linear model overestimates the slope, which leads to a larger resonance strength ϵ. Also, the fit quality of the sine to the data greatly enhances using the data from the model taking the Spin Coherence Time into account. The right panel depicts the difference between the data. In general, the slope is overestimated by a factor of 20% using a linear fit.

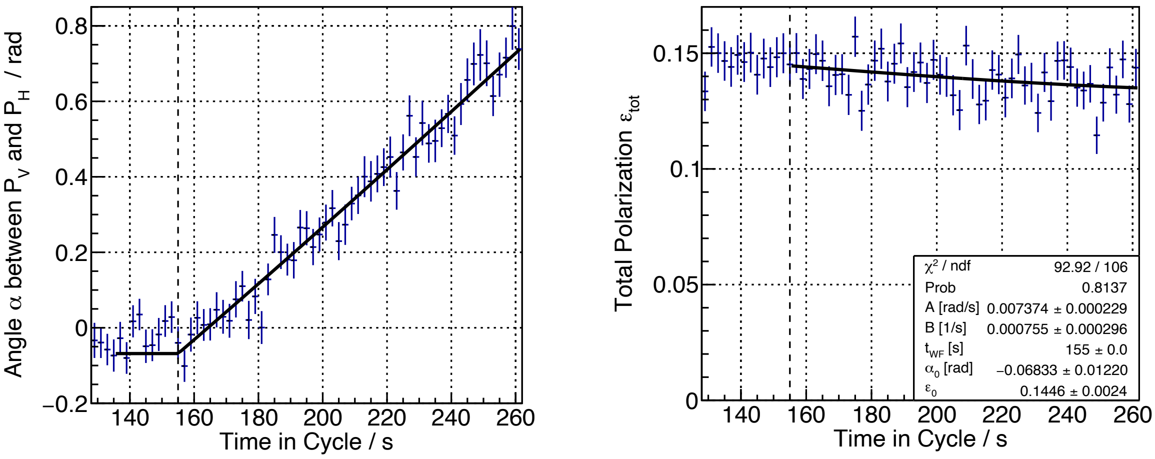

Figure 7.22.: Combined fit of the angle between the vertical and horizontal polarization α and the total polarization $\varepsilon_{\mathrm{tot}}$ according to Eq. (7.82) and (7.83) to determine the initial slope of the buildup of the polarization after the RF Wien filter is switched on at $t_{\mathrm{WF}} = 155\,\mathrm{s}$ (dashed black line).

7.6.2.2. Determination of the Invariant Spin Axis

The determination of the radial and longitudinal components of the Invariant Spin Axis at the location of the RF Wien filter using the initial slope method was used during the first Precursor experiment in 2018 for all measured maps and during the second Precursor experiment in 2021 for the first two maps. A summary of all measurements of the Invariant Spin Axis is given in Table 7.13.

The resonance strengths are measured for various settings of the RF Wien filter rotation angle and the spin kick inside the Siberian snake. An example of the slopes of the buildup of the angle between vertical and horizontal polarization for various settings of the relative phase between the Wien filter frequency and spin tune, the RF Wien filter rotation angle, and the spin kick inside the Siberian snake is shown in Figure 7.24. The resonance strengths for all maps using the initial slope method are shown in Appendix D.2.

The resonance strength squared as a function of the RF Wien filter rotation angle and the spin flip inside the Siberian snake is shown in Figure 7.25 along with a fit according to Eq. (7.57). The minimum of the map denotes the orientation of the Invariant Spin Axis in radial and longitudinal directions. The precision of setting the RF Wien filter rotation angle is given by

$$\sigma_{\phi^{\mathrm{WF}}} = 0.24\,\mathrm{mrad}. \tag{7.84}$$

The power supply of the Siberian snake has a repetition error of $\sigma_{I_{\mathrm{Snake}}} = 1 \times 10^{-3}\,\mathrm{A}$. Using Eq. (7.15) and neglecting the uncertainty of the calibration constant of the Siberian snake, the statistical uncertainty on the Spin flip angle can be calculated as

$$\sigma_{\chi_{\mathrm{Snake}}} = |I_{\mathrm{Snake}}|\sigma_{I_{\mathrm{Snake}}}. \tag{7.85}$$

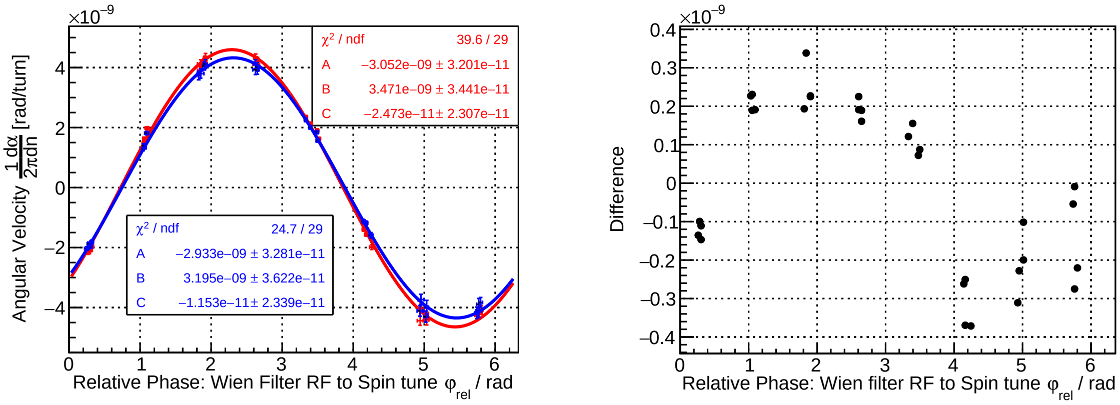

Figure 7.23.: Comparison of the initial slopes as a function of the relative phase. The red data points are determined from a standard linear fit to the data shown in Figure 7.22. The blue data points show the initial slope determined from the Spin Coherence Time corrections applied in Eq. (7.82) and (7.83). The right panel depicts the difference between both methods.

The orientation of the Invariant Spin Axis is given by

$$n_x = -4.0(1)\,\text{mrad and } n_z = -5.6(1)\,\text{mrad}. \tag{7.86}$$

The spin kick angle of the RF Wien filter is

$$\psi_0 = 2.83(1) \times 10^{-6}\,\text{rad}, \tag{7.87}$$

and the quality of the fit is given by

$$\frac{\chi^2}{\text{ndf}} = \frac{255.00}{6} = 42.50. \tag{7.88}$$

The initial spin tune, which enters the fit as a fixed parameter, is averaged over all cycles contributing to the measurement of the Invariant Spin Axis for a particular map. For the data shown in Figure 7.24, the initial spin tune histogram is shown in Figure 7.26. The averaged value is

$$\nu_s^0 = -0.160\,970\,692(1). \tag{7.89}$$

The statistical uncertainty of the averaged initial spin tune is neglected. The observed tilts of the Invariant Spin Axis are larger than expected compared to the results of the measured tilts using only the solenoids as further explained in section 7.4.3. The large χ^2/ndf is a hint towards missing systematic effects. A more detailed discussion about all results for the orientation of the Invariant Spin Axis is given in section 7.8.

7.6.3. The Pilot Bunch Method

In this section, a second method on how to extract the resonance strength is shown. Using the so-called Pilot bunch method, two bunches are rotating in COSY. The measurement scheme

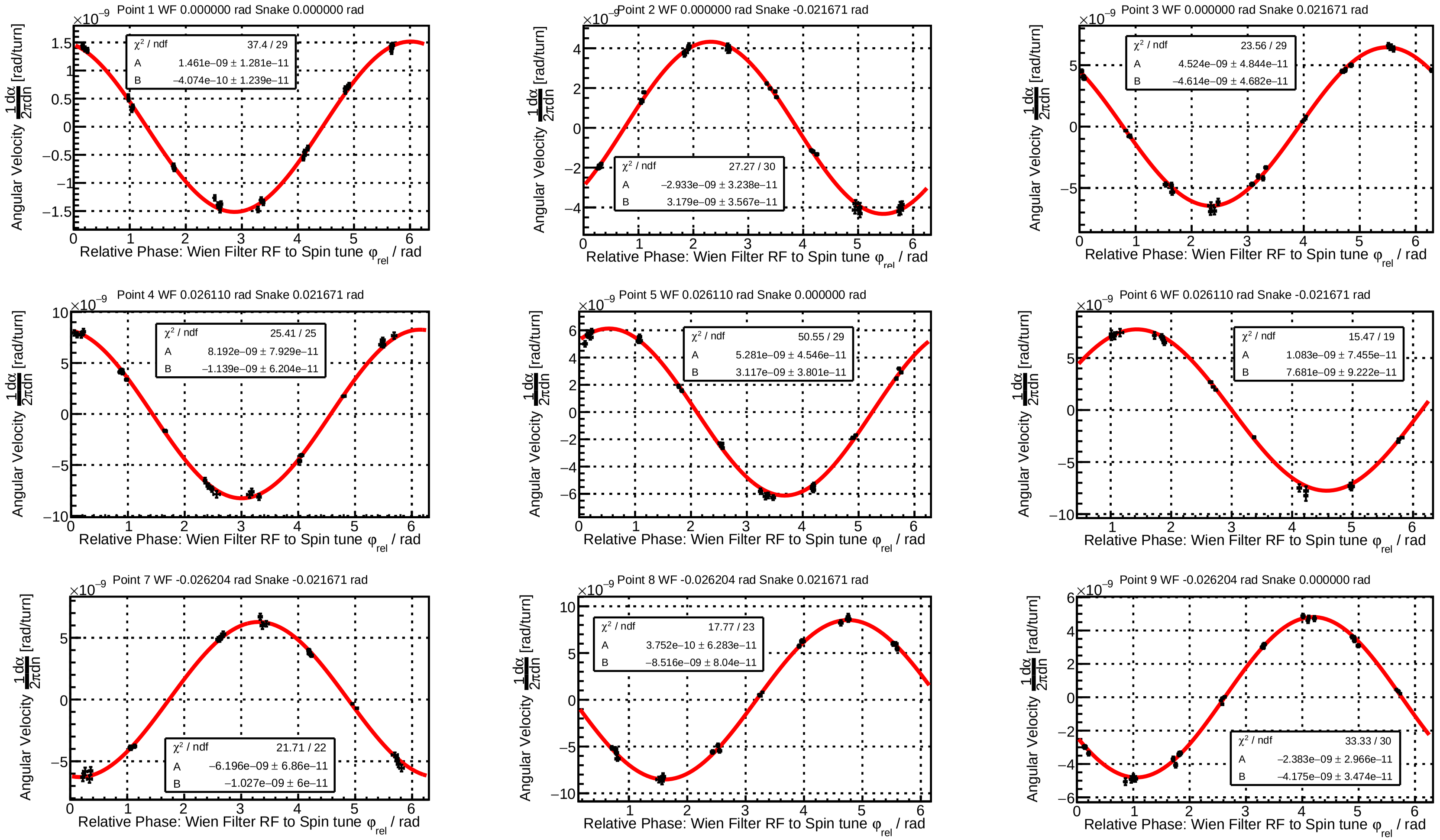

Figure 7.24.: Resonance Strengths ϵ for various settings of the Wien filter rotation angle and the spin flip inside the Siberian snake for the first Map taken during the first Precursor Run.

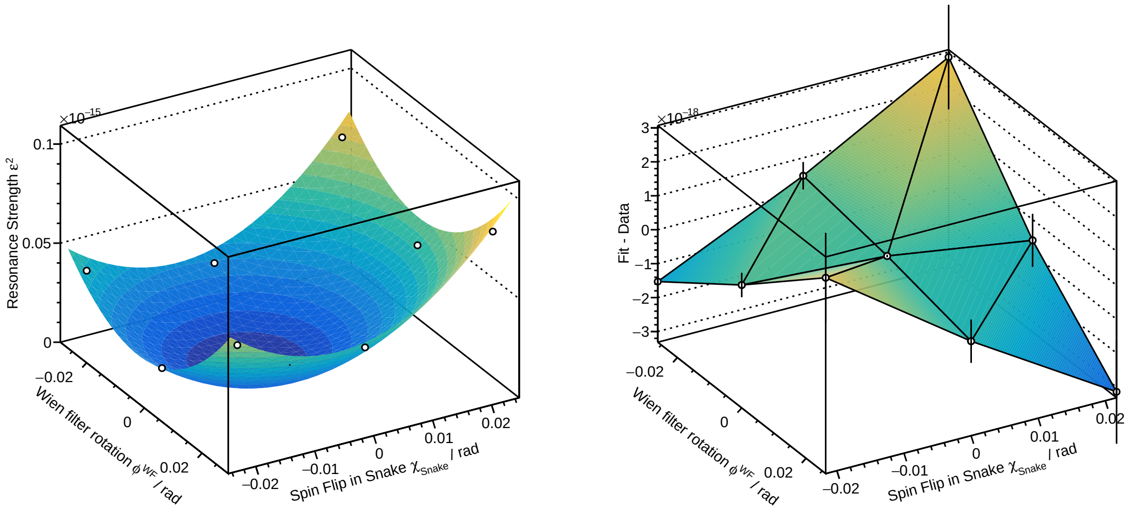

Figure 7.25.: Determination of the orientation of the Invariant Spin Axis for the second map during the first Precursor run. **Left:** The resonance strength is plotted as a function of the Wien filter rotation angle and the spin flip in the Siberian snake. The minimum of the two-dimensional paraboloid marks the orientation of the Invariant Spin Axis at the RF Wien filter. **Right:** Residuals.

described in section 7.1 remains valid. The vertically polarized beam is injected into the ring. The beam is separated into two bunches co-rotating in the ring, accelerated, and electron-cooled. Using the RF solenoid, the vertical polarization of both bunches is rotated into the accelerator plane. The Siberian snake (and the 2MV solenoid) acts as well on both bunches and rotates the Invariant Spin Axis for both bunches in the same direction while changing the spin tune. The only difference is that the RF Wien filter is gated for one of these bunches, while the other bunch remains unaffected.

The phase feedback acts on the unaffected bunch or Pilot Bunch, while the so-called Signal bunch is only affected by the RF Wien filter fields. This is depicted in Figure 7.27. Two bunches are co-rotating in COSY at the COSY revolution frequency $f_{\text{COSY}} = f_{\text{rev.}}$, and the spins are rotating at the spin precession frequency f_s. The blue bunch (Pilot bunch) is gated from the RF Wien filter, and only the red bunch (Signal bunch) is used to determine the resonance strength and consequently the Invariant Spin Axis.

In this case, the in-plane phase of the Signal bunch is not phase-locked, but can rotate according to the differential equations derived in section 7.6

$$\frac{\mathrm{d}\phi_{\text{rel.}}}{\mathrm{d}n} = 2\pi\epsilon \sin(a_{xz} - \phi_{\text{rel.}}) \tan(\alpha), \tag{7.90}$$

$$\frac{\mathrm{d}\alpha}{\mathrm{d}n} = -2\pi\epsilon \cos(a_{xz} - \phi_{\text{rel.}}). \tag{7.91}$$

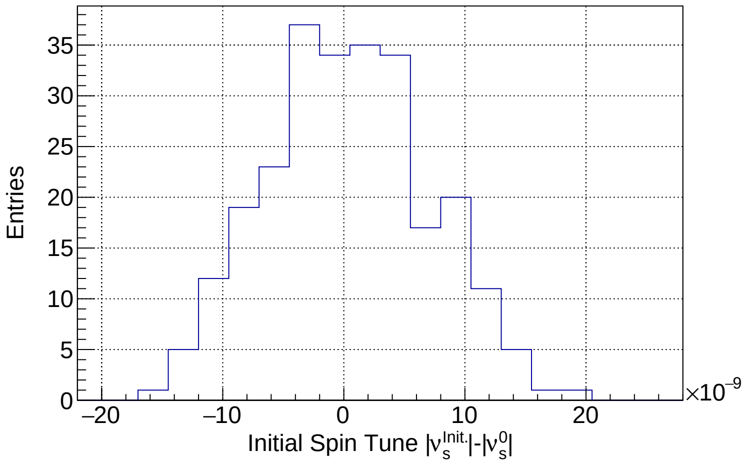

Figure 7.26.: Histogram of the initial spin tune for Precursor 1 Map 2. The averaged value is $|\nu_s^0| = 0.160\,970\,692(1)$. Note that the sign needs to be negative for the fit function as the spin tune is negative as shown in Eq. (4.37).

This set of equations can be solved by using the following substitutions

$$k = -\chi_0 \sin(a_y), \tag{7.92}$$

$$\Delta\phi = -(a_{xz} - \phi_{\text{rel.}}), \tag{7.93}$$

$$q = 0. \tag{7.94}$$

and the derivations given in Reference [100]. The parameter q describes the frequency difference between the spin tune and the RF Wien filter due to statistical fluctuations in the phase feedback and is defined as

$$q = \frac{4\pi\Delta f}{k f_{\text{COSY}}}. \tag{7.95}$$

The solution for the vertical polarization (left-right asymmetry) is given by

$$\sin\big(\alpha(n)\big) = p_y = \cos(\Delta\phi_0)\sin(2\pi\epsilon n). \tag{7.96}$$

Also, here the phase feedback gets an offset due to latencies in the signal processing, which remains constant for all cycles. Here, $\Delta\phi_0$ describes the initial ($t = t_{\text{WF}}$) phase relation between Wien filter frequency and spin tune. By using the Pilot bunch method, the resonance strength can be extracted from the oscillation of the left-right asymmetry. The oscillation amplitude depends of the choice of the initial in-plane phase set by the phase feedback using the Pilot bunch. The oscillation of the left-right asymmetry as a function of the relative in-plane phase between the Wien filter frequency and spin tune is shown in Figure 7.28. The left panel depicts the relative phase measured using the Pilot bunch. The right panel shows the oscillation of the left-right asymmetry as a function of time for three different choices of the initial in-plane phase. Note that the oscillation frequency is independent of the choice of the relative phase;

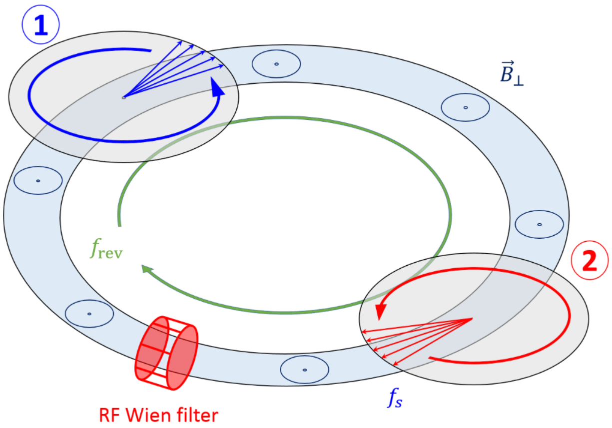

Figure 7.27.: Schematic of the Pilot bunch method. Two bunches are co-rotating in COSY. The blue bunch (Pilot Bunch) is used for the phase feedback to set the Wien filter frequency and phase and remains unaffected by the RF Wien filter. The signal bunch is affected by the RF Wien filter. The polarization of the Signal bunch behaves according to Eq. (7.96). Created by Frank Rathmann/ JEDI Collaboration.

only the amplitude changes. By performing a least-squared fit according to Eq. (7.96), the oscillation frequency and hence the resonance strength can be determined

$$2\pi\epsilon = 4.86(2) \times 10^{-2}\,\frac{1}{\mathrm{s}} \text{ for } \phi_{\mathrm{rel.}} = 5.59(1)\,\mathrm{rad} \text{ and,} \tag{7.97}$$

$$2\pi\epsilon = 4.91(2) \times 10^{-2}\,\frac{1}{\mathrm{s}} \text{ for } \phi_{\mathrm{rel.}} = 1.95(1)\,\mathrm{rad.} \tag{7.98}$$

For a relative phase of $\phi_{\mathrm{rel.}} = 4.2\,\mathrm{rad}$, the oscillation amplitude becomes zero. The measurements, shown in Figure 7.28, were taken at an RF Wien filter rotation angle of $\phi^{\mathrm{WF}} = -0.070\,\mathrm{rad}$ and spin flip angle in the Siberian snake of $\chi_{\mathrm{Snake}} = 0\,\mathrm{rad}$.

The model which describes the oscillation pattern in the right panels of Figure 7.28 is given by Eq. (7.96). However, off-resonance behaviors due to a non-ideal phase feedback as well as spin decoherence effects play a crucial role in the final determination of the resonance strengths. These correction effects are discussed in the following section.

Note, that the same procedure is applied when rotating the initially vertically polarized beam using the RF solenoid into the horizontal plane as no phase-locking of the spin precession takes place. In this case, the RF solenoid is switched off after a quarter period of the rotation period for the final polarization to be in the horizontal plane.

7.6.3.1. Spin Coherence Time and Off-Resonance Corrections

Similar to the corrections of the Spin Coherence Time for the initial slope method in section 7.6.2.1, the spin coherence also has to be corrected for the oscillations measured using the Pilot bunch

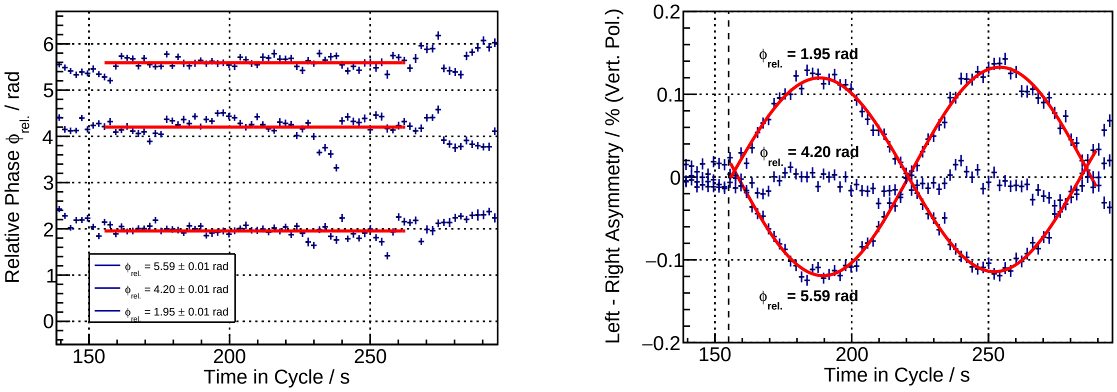

Figure 7.28.: **Left:** Relative phase measured using the Pilot bunch for three different cycles at three different chosen values for the relative phase between spin tune and Wien filter frequency. **Right:** As soon as the RF Wien filter is switched on at 155 s (dashed black line), an oscillation of the left-right asymmetry is visible for the Signal bunch. The oscillation amplitude depends on the choice of the relative phase, and, according to Eq. (7.96), the oscillation frequency is given by the resonance strength, which is independent on the choice of the relative phase.

method. In addition, off-resonance behavior due to a non-ideal phase feedback can be corrected. The analytical work is based on reference [107].

- **Off-resonance correction:** In previous measurements, a phase feedback spread of $\sigma_{\text{fb}} \approx 0.2\,\text{rad}$ was achieved in a $t_{\text{fb}} = 3\,\text{s}$ interval. The corresponding accuracy of the Wien filter frequency is approximately given by

$$\Delta f_{\text{fb}} \approx \frac{\sigma_{\text{fb}}}{2\pi t_{\text{fb}}} \approx 10\,\text{mHz}. \tag{7.99}$$

In the context of this experiment, off-resonance means that the Wien filter frequency f_{WF} does not match the spin precession frequency f_s. The off-resonance angle δ parametrizes the off-resonance behavior and is defined as

$$\delta = \frac{2\pi(f_s - f_{\text{WF}})}{f_{\text{COSY}}}. \tag{7.100}$$

In contrast to the corrections of the Spin Coherence Time, a detuned Wien filter frequency leads to a systematic shift of the measured resonance strength. The measured and detuned resonance strength is given by

$$\epsilon^2_{\text{det.}} = \epsilon^2 + \frac{\delta^2}{4\pi^2}. \tag{7.101}$$

where ϵ denotes the resonance strength as defined in Eq. (7.35). The off-resonance angle does not directly enter the fit function but appears in another parameter ρ

$$\sin(\rho) = \frac{\epsilon_0}{\epsilon_{\text{det}}} \text{ and } \cos(\rho) = \frac{2\delta}{4\pi\epsilon_{\text{det}}}. \tag{7.102}$$

Using Eq. (7.101), it can be shown that $\sin^2(\rho) + \cos^2(\rho) = 1$.

- **Spin Decoherence correction:** The Spin Coherence Time is very similarly treated for the Pilot bunch method as already described in section 7.6.2.1. While the vertical polarization remains preserved over time, an exponential decay of the in-plane polarization is assumed. The decoherence parameter Q with the Spin Coherence Time τ_{SCT} is defined as
$$Q = \frac{\Gamma}{2\pi\epsilon_{\mathrm{det}}} \text{ with } \Gamma = \frac{1}{f_{\mathrm{COSY}}\tau_{\mathrm{SCT}}}. \tag{7.103}$$

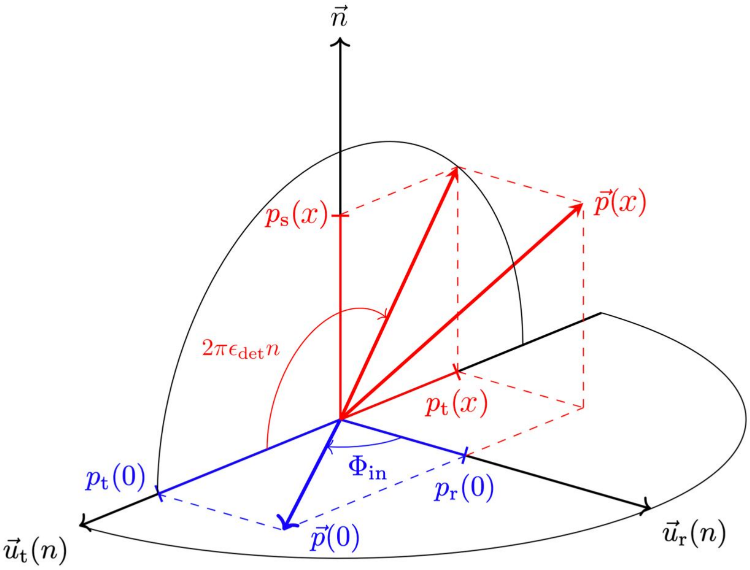

Figure 7.29.: Coordinate system with the Invariant Spin Axis, the tangential, and radial direction. At the time $x = 0$, where x is defined as $x = 2\pi\epsilon_{\mathrm{det}}(n - n_{\mathrm{WF}})$ or $x = 2\pi\epsilon_{\mathrm{det}} f_{\mathrm{COSY}}(t - t_{\mathrm{WF}})$, the polarization is rotating in the $(\vec{u}_r, \vec{u}_t)$ plane. After the RF Wien filter is switched on, the vertical polarization accumulates parallel to $\vec{n}$. Adapted from FIG. 1 in [107].

The underlying formalism describes the evolution of polarization vector $\vec{p}$ after some time $x = 2\pi\epsilon_{\mathrm{det}}(n - n_{\mathrm{WF}})$ (or $x = 2\pi\epsilon_{\mathrm{det}} f_{\mathrm{COSY}}(t - t_{\mathrm{WF}})$), where n denotes the turn number

$$\vec{p}(x) = \mathbf{E}(x) \cdot \vec{p}(x = x_{\mathrm{WF}}). \tag{7.104}$$

The polarization vector is given by $\vec{p} = (p_r, p_v, p_t)^T$ and x_{WF} denotes the time when the RF Wien filter is switched on, i.e., $x_{\mathrm{WF}} = 2\pi\epsilon_{\mathrm{det}} n_{\mathrm{WF}}$. The coordinate system is illustrated in Figure 7.29. Along the Invariant Spin Axis $\vec{n}$, the tangential component is defined in the beam direction, and the radial component points perpendicular to the Invariant Spin Axis and the tangential component. The radial component corresponds to the x axis and the tangential component corresponds to the z axis defined in Figure 7.17.

In case of decoherence and frequency mismatch between the Wien filter frequency and spin precession frequency, the polarization transfer matrix is given by

$$\mathbf{E}(x) = \begin{pmatrix} e^{-2Qx}\sin^2(\rho) + e^{-Qx}\cos^2(\rho)\cos(x) & \cos(\rho)\sin(\rho)(e^{-2Qx} - e^{-Qx}\cos(x)) & e^{-Qx}\cos(\rho)\sin(x) \\ -\cos(\rho)\sin(\rho)(e^{-2Qx} - e^{-Qx}\cos(x)) & e^{-2Qx}\cos^2(\rho) + e^{-Qx}\sin^2(\rho)\cos(x) & -e^{-Qx}\sin(\rho)\sin(x) \\ e^{-Qx}\cos(\rho)\sin(x) & e^{-Qx}\sin(\rho)\sin(x) & e^{-Qx}\cos(x) \end{pmatrix}. \tag{7.105}$$

The initial polarization condition for the experiment is given by

$$\vec{p}(x = 2\pi\epsilon_{\text{det}}n_{\text{WF}}) = \begin{pmatrix} p_{H0}\sin(\phi_{\text{rel.,0}}) \\ p_{V0} \\ p_{H0}\cos(\phi_{\text{rel.,0}}) \end{pmatrix}, \tag{7.106}$$

where p_{V0} denotes the initial vertical polarization at the time the RF Wien filter is switched on. Note that p_{V0} should be zero, as the experiment starts with the polarization of the beam in the accelerator plane. However, non-complete rotations of the RF solenoid rotating the vertically polarized beam into the horizontal plane may lead to an over- or undershoot of rotations. The initial phase relation between the Wien filter frequency and the in-plane spin precession frequency is set by the phase feedback and is denoted as $\phi_{\text{rel.,0}}$. The initial in-plane polarization is given by

$$p_{H0} = \sqrt{p_t(x_{\text{WF}})^2 + p_r(x_{\text{WF}})^2}. \tag{7.107}$$

The initial polarization vector is shown in blue in Figure 7.29. The red vector $\vec{p}(n)$ shows the polarization after turn number n. Note that not the polarization is fitted directly, but the left-right and up-down asymmetry which are directly proportional to the vertical and in-plane polarization. Therefore, p_{V0} is replaced by $\epsilon_{\text{LR},0}$ and p_{H0} is replaced by $\epsilon_{\text{UD},0}$, as the proportionality factors are the same for the asymmetries in both planes.

By multiplying the polarization transfer matrix as defined in Eq. 7.105 with the initial polarization conditions, the transversal, radial and vertical component of the polarization vector can be calculated as a function of time. The tangential component is given by

$$\begin{aligned} p_t = &- e^{-Qx}\cos(\rho)\sin(x)\cos(\phi_{\text{rel.,0}})\epsilon_{\text{UD},0} \\ &+ e^{-Qx}\sin(\rho)\sin(x)\epsilon_{\text{LR},0} + e^{-Qx}\cos(x)\sin(\phi_{\text{rel.,0}})\epsilon_{\text{UD},0}, \end{aligned} \tag{7.108}$$

the radial component is given by

$$\begin{aligned} p_r = &\left[e^{-2Qx}\sin(\rho)^2 + e^{-Qx}\cos(\rho)^2\cos(x)\right]\epsilon_{\text{UD},0}\cos(\phi_{\text{rel.,0}}) \\ &+ \epsilon_{\text{LR},0}\cos(\rho)\sin(\rho)\left(e^{-2Qx} - e^{-Qx}\cos(x)\right) \\ &+ e^{-Qx}\cos(\rho)\sin(x)\sin(\phi_{\text{rel.,0}})\epsilon_{\text{UD},0}, \end{aligned} \tag{7.109}$$

and the vertical component is given by

$$\begin{aligned} p_V = &\left[-\cos(\rho)\sin(\rho)\left(e^{-2Qx} - e^{-Qx}\cos(x)\right)\right]\epsilon_{\text{UD},0}\sin(\phi_{\text{rel.,0}}) \\ &+ \left[e^{-2Qx}\cos(\rho)^2 + e^{-Qx}\sin(\rho)^2\cos(x)\right]\epsilon_{\text{LR},0} \\ &- e^{-Qx}\sin(\rho)\sin(x)\epsilon_{\text{UD},0}\sin(\phi_{\text{rel.,0}}). \end{aligned} \tag{7.110}$$

Using the polarimeter, only the in-plane polarization (up-down asymmetry), given by

$$p_{rt} = \sqrt{p_r^2 + p_t^2}, \tag{7.111}$$

and the vertical polarization (left-right asymmetry) can be determined. An example of a combined fit of the left-right asymmetry and the up-down asymmetry is shown in Figure 7.30. Using Eq. (7.102), the unperturbed resonance strength can be calculated via

$$\epsilon^2 = \sin^2(\rho)\epsilon_{\text{det}}^2, \tag{7.112}$$

$$\sigma_{\epsilon^2} = 2\epsilon_{\text{det}}\sin(\rho)\cdot\left[\sin^2(\rho)\sigma_{\epsilon_{\text{det}}}^2 + \cos^2(\rho)\epsilon_{\text{det}}^2\sigma_\rho^2 + 2\epsilon_{\text{det}}\sin(\rho)\cos(\rho)\sigma_{\epsilon_{\text{det}}}\sigma_\rho k(\rho,\epsilon_{\text{det}})\right]^{\frac{1}{2}}, \tag{7.113}$$

where $k(\rho, \epsilon_{\text{det}})$ denotes the correlation coefficient between the detuned resonance strength and ρ. The dependency of the resonance strength is computed in section 7.6.1 for ϵ^2. For the data shown in Figure 7.30, the corrected resonance strength is given by

$$\epsilon^2 = 3.07(2)\times 10^{-17}. \tag{7.114}$$

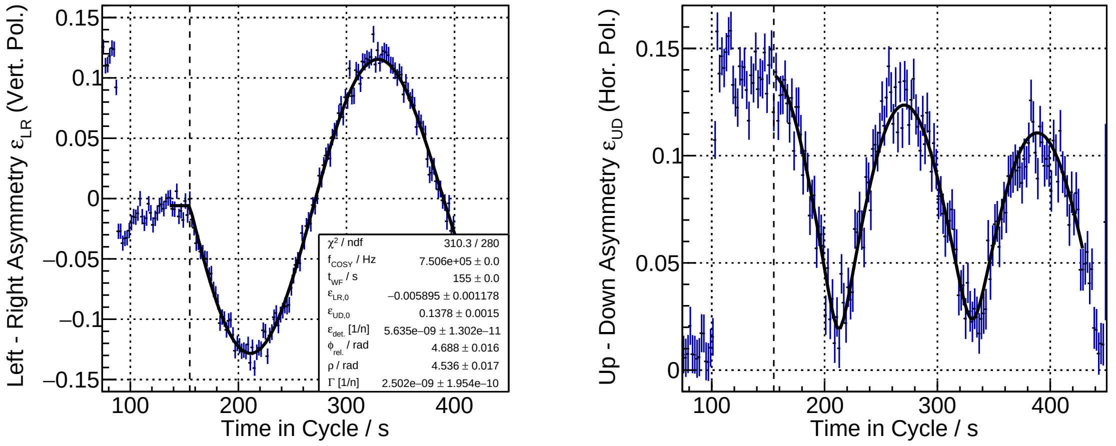

Figure 7.30.: Simultaneous fit of the left-right asymmetry (left) and the up-down asymmetry (right) for determining the detuned resonance strength using the signal bunch. The spin flip angle in the Siberian snake is given by $\chi_{\text{Snake}} = 7.9\,\text{mrad}$, the Wien filter rotation angle is given by $\phi^{\text{WF}} = 34.9\,\text{mrad}$ and the relative phase between the Wien filter frequency is set to $\phi_{\text{rel.}} = 3.4\,\text{rad}$. The dotted line marks the timestamp when the RF Wien filter is switched on ($t_{\text{WF}} = 155\,\text{s}$).

Using Eq. (7.100) and (7.102), the frequency mismatch between the Wien filter frequency and the spin precession frequency can be studied by calculating

$$\Delta f = f_s - f_{\text{WF}} = \cos(\rho) f_{\text{COSY}}\epsilon_{\text{det.}}. \tag{7.115}$$

A histogram of this mismatch for 158 cycles with different settings for the relative phase between the Wien filter frequency and spin precession frequency, Wien filter rotation angle, and spin flip in the Siberian snake is shown in Figure 7.31. The mean of the distribution is given by 6.329×10^{-5} Hz. The width of the distribution is 1.2 mHz.

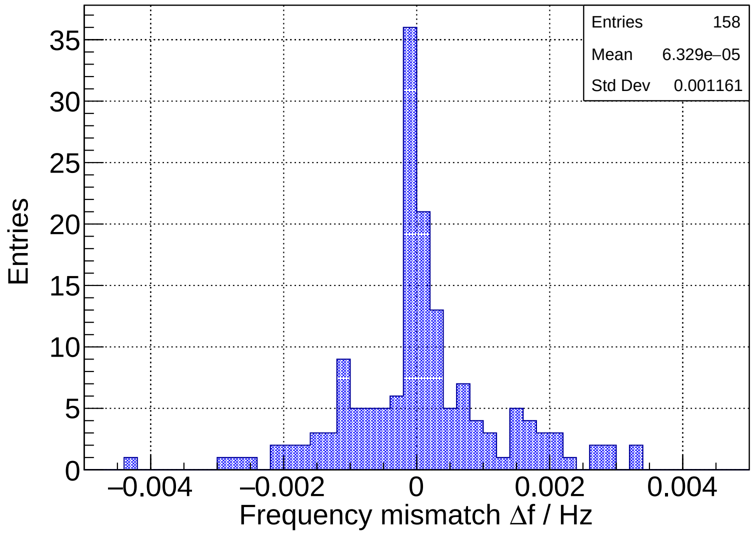

Figure 7.31.: Accuracy of the phase feedback matching the Wien filter frequency to the spin precession frequency derived from 158 cycles with different settings of the relative phase between the Wien filter frequency and spin precession frequency, RF Wien filter rotation angle, and spin flip in the Siberian snake. The width of the frequency mismatch is in the order of 1 mHz.

7.6.3.2. Monte Carlo Studies

To validate the derived formulas in the previous section on the buildup of the vertical component of the polarization among all the parameter space, Monte Carlo studies are performed. An example of a cycle with simulated data according to Eq. (7.110) and (7.111) is shown in Figure 7.32. The left-right asymmetry (left) and the up-down asymmetry (right) are shown during a time interval of 300 s. For both, the left-right asymmetry and the up-down asymmetry, a statistical uncertainty of $\sigma_{\epsilon_{\mathrm{LR}}} = \sigma_{\epsilon_{\mathrm{UD}}} = 10\,\%$(absolute) is assumed which approximately corresponds to the statistical uncertainty of both asymmetries as in the real experiment. The data is fitted using the same formula which is used to produce the data. The input data and fit results are summarized in Table 7.9. Using the input data, the fit results can reproduce the expected results.

Table 7.9.: Input parameters and fit results for the Monte Carlo data and regression shown in Figure 7.32.

	$\epsilon_{\mathrm{LR},0}$	$\epsilon_{\mathrm{UD},0}$	ϵ / $^{\mathrm{rad}}/_{\mathrm{n}}$	$\phi_{\mathrm{rel.},0}$ / rad	ρ / rad	Γ / $^{1}/_{\mathrm{n}}$	χ^2/ndf
Input	0.01	0.14	5×10^{-9}	1	4.5	2×10^{-9}	
Fit Result	0.012(1)	0.138(1)	4.99(1)	0.9996(92)	4.496(7)	$1.84(13) \times 10^{-9}$	$^{643.9}/_{594} = 1.08$

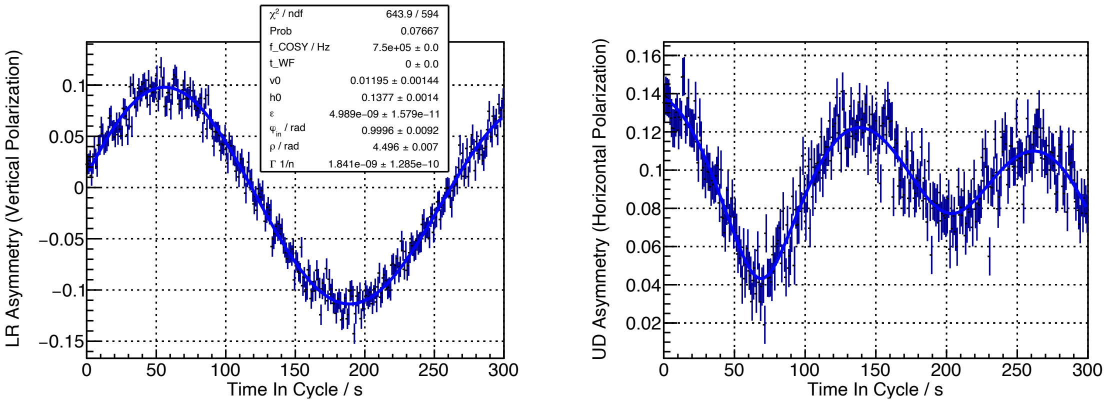

Figure 7.32.: Example of Monte Carlo data of the left-right and up-down asymmetry during a cycle of 300 s. The data is produced and fitted according to Eq. (7.110) and (7.111). The input parameters and fit results are summarized in Table 7.9 and agree well within their uncertainties.

For small resonance strengths, the fit overestimates the resonance strength. This can be intuitively explained as fitting the onset of a sine wave is more difficult than fitting a constant slope. Therefore, data points which are measured close to the map minimum are disregarded in the analysis for the determination of the orientation of the Invariant Spin Axis using real data.

In Figure 7.33 a projection of the histogram which compares the input to the outcome of the fit is shown for a constant attenuation parameter of $\Gamma = 5 \times 10^{-10}\,{}^{1}\!/\!{}_{\mathrm{n}}$. If the input of the resonance strength is smaller than $\epsilon \approx 5 \times 10^{-10}$, the resonance strength is overestimated. These data points are discarded from the analysis of the determination of the Invariant Spin Axis.

7.6.3.3. Determination of the Invariant Spin Axis

The method of measuring the orientation of the Invariant Spin Axis at the location of the RF Wien filter using the Pilot Bunch was only used during the second Precursor experiment in 2021 after the fast switches were installed in the driving circuit of the RF Wien filter, which allowed the Pilot bunch to be gated from the RF Wien filter fields. In addition to data taken with the Siberian snake alone, the 2MV solenoid was used alongside the Siberian snake at currents of 5 A and −5 A. A summary of all measured data is given in Table 7.13. However, while the current of the Siberian snake was changed, the current of the 2 MV solenoid remained constant, which means that the additional spin flip $\chi_{\text{2MV sol.}}$ enters the fit as an additional fixed parameter. According to Eq. (7.15), the currents can be converted into

$$\chi_{\text{2MV sol.}}(5\,\mathrm{A}) = 0.002\,\mathrm{rad} \quad \text{and} \quad \chi_{\text{2MV sol.}}(-5\,\mathrm{A}) = -0.002\,\mathrm{rad}. \tag{7.116}$$

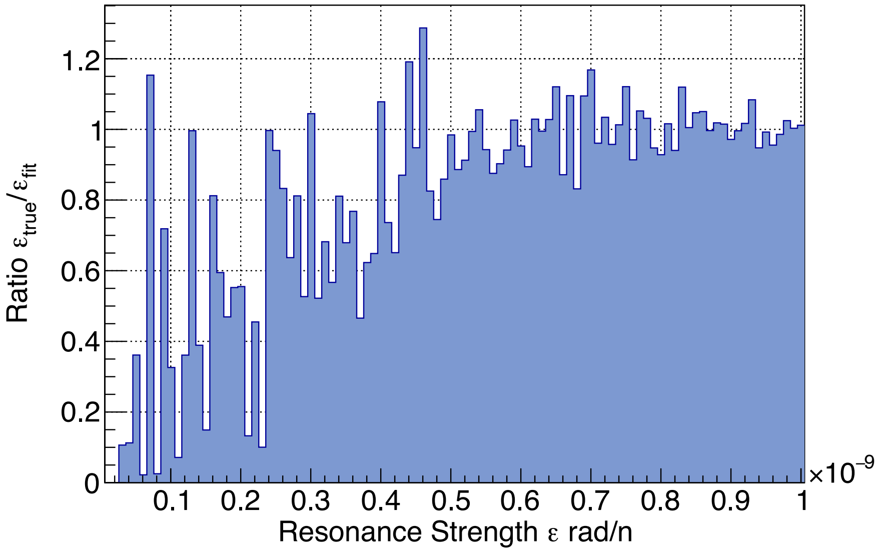

Figure 7.33.: Projection of the ratio between the input of the resonance strength versus the output of the fit for a constant in-plane polarization attenuation parameter of $\Gamma = 5 \times 10^{-10}\,{}^{1}\!/\!_{\mathrm{n}}$. For a resonance strength smaller than $\epsilon < 5 \times 10^{-10}$, the resonance strength is overestimated by the fit.

The uncertainty of $\chi_{2\mathrm{MV\ sol.}}$ can be neglected for both cases. When using the 2 MV solenoid, Eq. (7.56) needs to be used to fit the resonance strength as a function of the Siberian snake spin flip angle and the RF Wien filter rotation angle.

The main advantage of the Pilot bunch method is that no relative phase scans have to be made to find the resonance strength. Instead, the phase that yields approximately the largest oscillation amplitude is chosen. For reproducibility, the measurement of the resonance strength is repeated multiple times for the same setting of the relative phase between the Wien filter frequency and spin precession frequency, RF Wien filter rotation angle, and spin flip in the Siberian snake. An example of a repetition of a measurement of the resonance strength for the same settings is shown in Figure 7.34. The unperturbed resonance strength as defined in Eq. (7.112) is shown for multiple consecutive cycles. The settings of the Wien filter rotation angle, spin flip in the Siberian snake, and relative phase between the Wien filter frequency and spin tune are $\phi^{\mathrm{WF}} = -0.035\,\mathrm{rad}$, $\chi_{\mathrm{Snake}} = 0.016\,\mathrm{rad}$, and $\phi_{\mathrm{rel.}} = 2.94\,\mathrm{rad}$, respectively.

The results presented in this section are derived from Precursor 2 Map 4. The resonance strength as a function of the Wien filter rotation angle and the spin flip in the Siberian snake is shown in Figure 7.35. The data points are fitted according to Eqs. (7.57) and (7.56). As discussed in the previous sections, data points close to the map minimum are discarded as the resonance strength is overestimated at low oscillation frequencies. The precision of setting the RF Wien filter rotation angle is given by

$$\sigma_{\phi^{\mathrm{WF}}} = 0.000\,24\,\mathrm{rad}. \tag{7.117}$$

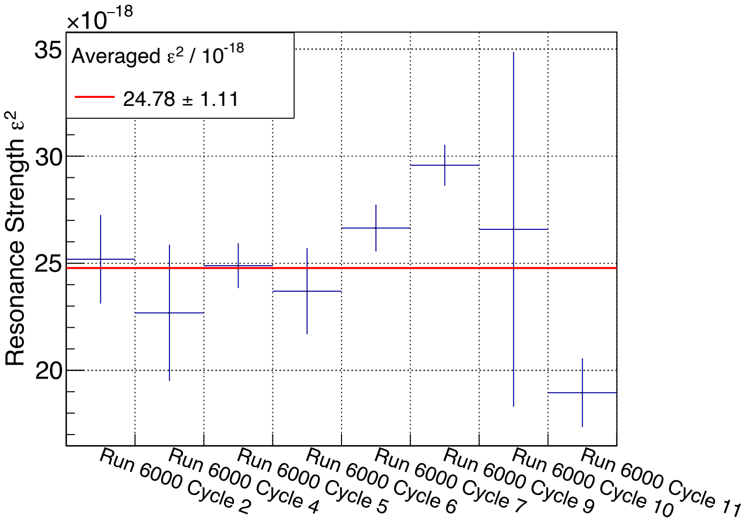

Figure 7.34.: Measurement of the resonance strength for eight consecutive cycles. The Wien filter rotation angle is $\phi^{\mathrm{WF}} = -0.035\,\mathrm{rad}$, the spin flip in the Siberian snake is $\chi_{\mathrm{Snake}} = 0.016\,\mathrm{rad}$, and the relative phase is given by $\phi_{\mathrm{rel.}} = 2.94\,\mathrm{rad}$. The averaged resonance strength is given by $\epsilon^2 = (24.78 \pm 1.11) \times 10^{-18}$. The cycles using unpolarized beam (1 and 8) do not contribute to the determination of the averaged resonance strength.

The power supply of the Siberian snake and the 2MV solenoid have a repetition error of $\sigma_{I_{\mathrm{Snake}}} = 1 \times 10^{-3}\,\mathrm{A}$ and $\sigma_{I_{\mathrm{2MV\ Sol.}}} = 5 \times 10^{-4}\,\mathrm{A}$, respectively. Using Eq. (7.15) and neglecting the uncertainty of the calibration constant of the Siberian snake and the 2 MV solenoid, the statistical uncertainty on the Spin flip angle can be calculated as

$$\sigma_{\chi_{\mathrm{Snake}}} = |I_{\mathrm{Snake}}|\sigma_{I_{\mathrm{Snake}}} \text{ and } \sigma_{\chi_{\mathrm{2MV\ Sol.}}} = |I_{\mathrm{SMV\ Sol.}}|\sigma_{I_{\mathrm{2MV\ Sol.}}}. \tag{7.118}$$

The orientation of the Invariant Spin Axis is given by

$$n_x = -2.20(9)\,\mathrm{mrad} \text{ and } n_z = 3.74(4)\,\mathrm{mrad}. \tag{7.119}$$

The spin kick angle of the RF Wien filter is

$$\psi_0 = 1.871(3) \times 10^{-6}\,\mathrm{rad}, \tag{7.120}$$

and the quality of the fit is given by

$$\frac{\chi^2}{\mathrm{ndf}} = \frac{136.92}{21} = 6.52. \tag{7.121}$$

The initial spin tune, which enters the fit as a fixed parameter, is averaged over all cycles contributing to the measurement of the Invariant Spin Axis for a particular map. For the data shown in Figure 7.35, the initial spin tune histogram is shown in Figure 7.36. The averaged value is

$$\nu_s^0 = -0.160\,973\,363(1). \tag{7.122}$$

The statistical uncertainty of the averaged initial spin tune is neglected. A detailed discussion of the results of the fits to the resonance strength is given in section 7.8.

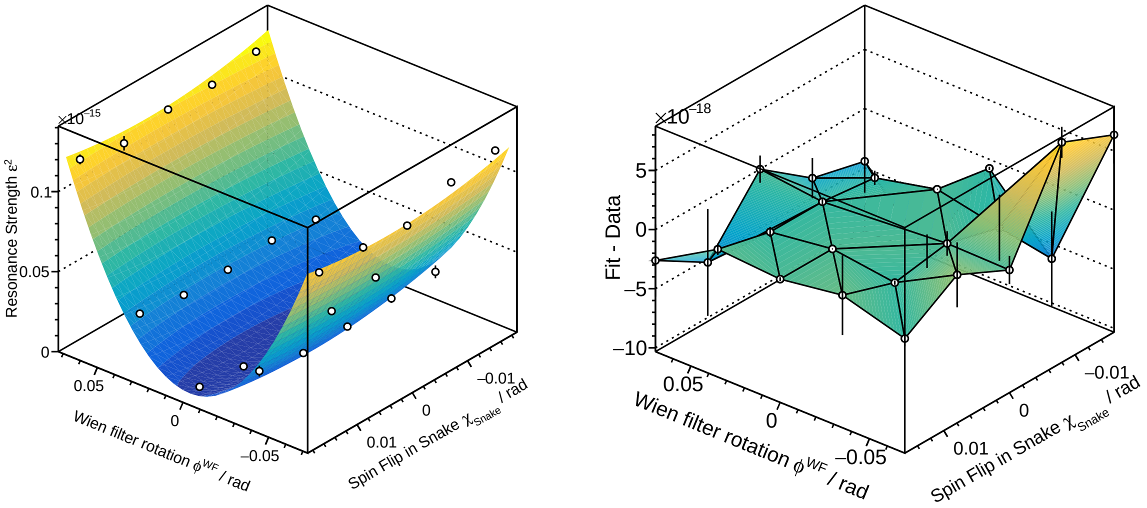

Figure 7.35.: Determination of the orientation of the Invariant Spin Axis for the fifth map during the second Precursor run. **Left:** The resonance strength is plotted as a function of the Wien filter rotation angle and the spin flip in the Siberian snake. The minimum of the two-dimensional paraboloid marks the orientation of the Invariant Spin Axis at the RF Wien filter. **Right:** Residuals.

7.6.4. Comparison of the Methods

The great advantage of the Pilot bunch method over the initial slope method is the reduced time required to measure the orientation of the Invariant Spin Axis. While relative phase scans are necessary for the initial slope method, the measurement of the resonance strength with the Pilot bunch method requires only a single phase with a large amplitude of the vertical component of the polarization. Additionally, the initial slope method limits the measurement time to the buildup of the slope. Once the vertical component of the polarization becomes too large, the spin tune is no longer measurable, and the phase feedback cannot adjust the relative phase between the spin tune and the Wien filter frequency. Consequently, the remaining measured data cannot contribute to determining the orientation of the Invariant Spin Axis. This issue is particularly problematic when measuring the resonance strength at large Wien filter rotation angles or during large spin flips in the Siberian snake.

Using the Pilot bunch method and the free oscillation of the vertical component of the polarization of the signal bunch, the entire cycle time can be utilized to fit data, provided enough particles survive until the end of the cycle. At larger angles, a better statistical uncertainty on the map minimum and consequently on the orientation of the Invariant Spin Axis can be achieved due to the larger leverage arm. This can be easily explained using Monte Carlo data. In Figure 7.37, Monte Carlo data of the resonance strength is shown for both small and large step sizes. The map minimum is set to $n_x = 1\,\text{mrad}$ and $n_z = 5\,\text{mrad}$. The results of the statis-

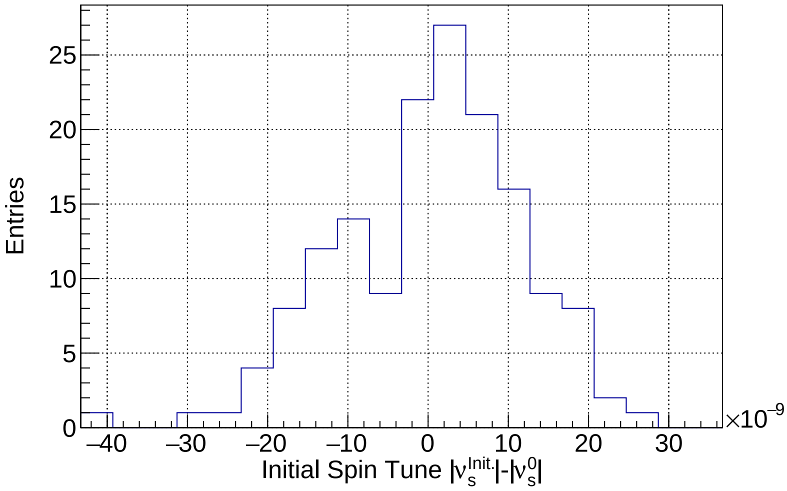

Figure 7.36.: Histogram of the initial spin tune for Precursor 2 Map 5. The averaged value is given by $|\nu_s^0| = -0.160\,973\,363(1)$. Note that the sign needs to be negative for the fit function as the spin tune is in negative as shown in Eq. (4.37).

Table 7.10.: Comparison of the statistical uncertainty of the map minimum for different step sizes.

	$d_{\text{Point}} = 0.01\,\text{rad}$	$d_{\text{Point}} = 0.04\,\text{rad}$
σ_{n_x} / mrad	3.51×10^{-5}	8.76×10^{-6}
σ_{n_z} / mrad	2.78×10^{-5}	6.97×10^{-6}

tical uncertainty of the map minimum using Monte Carlo data are summarized in Table 7.10. The larger step size shows a significant difference in statistical uncertainty compared to the smaller map size.

However, Monte Carlo studies in section 7.6.3.2 have shown that the oscillating vertical component close to the minimum cannot be easily fitted, as the buildup cannot be distinguished from a linear buildup. Close to the map minimum, the slope method can be used, as a linear buildup can be fit throughout the measurement time. Additionally, at larger fields in the solenoids, fringe field components also increase, leading to additional systematic contributions to the buildup of the polarization.

7.7. Experimental Overview

The COSY Beam Advisory Committee (CBAC) granted two measurement periods in 2018 and 2021 for the first direct determination of the deuteron Electric Dipole Moment. In the following sections, an overview of these experimental periods is presented.

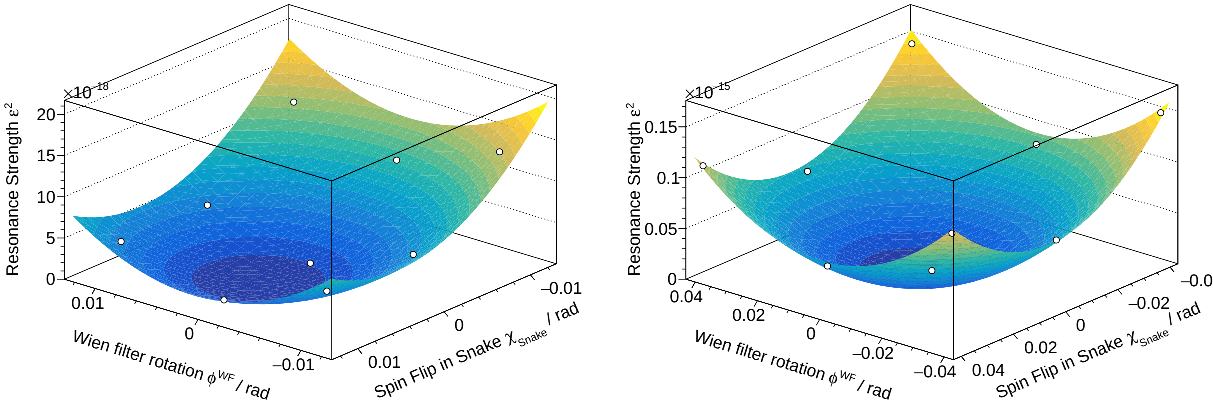

(a) $d_{\mathrm{Point}} = 0.01\,\mathrm{rad}$

(b) $d_{\mathrm{Point}} = 0.04\,\mathrm{rad}$

Figure 7.37.: Comparison of the distance between the data points of the resonance strength shows that if the distance is larger, the statistical uncertainty on the map minimum decreases.

7.7.1. Precursor I

The first Precursor run took place in November/ December 2018. The measurement period of four weeks marks the first direct measurement period of the deuteron Electric Dipole moment. The Spin Coherence Time was optimized for 2.5 weeks and the Invariant spin axis was measured in so-called maps. During the first Precursor Run, the switches gating one of the bunches in the RF Wien filter were not installed, which means than only a single bunch was circulating in the machine and only the initial slope measurement could be used to determine the orientation of the Invariant Spin Axis. A measurement of a single maps takes approximately 2.5 days. In total three maps were measured. The first map is the first reference map to determine the Invariant spin axis. The second maps is a remeasurement of the first map and the final map is a measurement closer to the minimum of the Invariant Spin Axis. All data was taken using the WASA detector. In addition, also the Siberian snake was calibrated resulting in the measurement of the longitudinal component of the Invariant Spin axis at the position of the Siberian snake. An overview of the measured maps is given in Table 7.13. The table contains the number of points per map, i.e. the number of different Siberian Snake currents and Wien filter rotations, the method to determine the resonance strength, the number of relative phase selections, the number of repetitions per relative phase (4 + 1 stands for four cycles using polarized beam and a cycle using unpolarized beam), the Wien filter power and a final remark for each measured map.

7.7.2. Technical Improvements in COSY

The first Precursor Run provided valuable input for improvements of COSY. Beam and spin tracking simulations have shown that the experiment is highly sensitive to orbit deviations. To improve the orbit, the so-called beam-based alignment method was carried out in September 2019, which is shortly discussed in section 7.7.2.1. In addition, a new method to match the RF Wien filter fields was developed (cf. section 7.7.2.3), and the switches were added to the

Wien filter resonant circuit to allow for the gating of the Pilot bunch. Additionally, the new Jedi Polarimeter, which was installed in 2019, was used for the first time for the determination of the Invariant Spin axis.

7.7.2.1. Beam-Based Alignment

Several beam and spin tracking simulation studies showed that maintaining an orbit close to the design orbit is crucial to reduce systematic contributions from unknown magnetic fields to the Invariant Spin Axis. To improve the precision of the orbit, a beam-based alignment method is applied to align the magnetic centers of the quadrupole magnets and the BPMs. This procedure requires mechanical alignment of the quadrupoles, which was achieved through a surveying process by Vermessungsbüro Stollenwerk & Burghof with a precision of 200 μm. Detailed alignment data for all quadrupoles can be found in Reference [69].

By carefully moving the beam within a quadrupole and varying the quadrupole strength, the magnetic center can be located, allowing for the identification of mechanical alignment errors of beam position monitors. Utilizing the 31 BPMs, the centers of the 56 quadrupoles were determined, and the offsets between the BPMs and quadrupoles were calculated, resulting in better offset calibration of the BPMs. The calibration data for the beam position monitors is summarized in Table A.1.

The horizontal and vertical orbits during the first and second Precursor runs are shown in Figure 7.38. For the orbit data taken during the first Precursor Run, the BPM offsets (cf. Table A.1) are subtracted to compare the results with the orbit data from Precursor 2. The beam-based alignment campaign happened between these two experimental periods. The data shown in the figure is averaged over multiple cycles, always evaluating the orbit at 200 s in the cycle and averaging the orbit data for each beam position monitor. The resulting vertical and horizontal orbit RMS values for both experimental periods are summarized in Table 7.11. In both planes, the orbit RMS values improved significantly. The orbit RMS for the horizontal and vertical plane is given by

$$\Delta x_{\mathrm{RMS}} = \sqrt{\frac{1}{n_x} \sum_{i \in \mathrm{BPMs}} x_i^2} \text{ and } \Delta y_{\mathrm{RMS}} = \sqrt{\frac{1}{n_y} \sum_{i \in \mathrm{BPMs}} y_i^2}, \tag{7.123}$$

where x_i and y_i denote the beam position in the horizontal and vertical plane, measured using the ith beam position monitor. The total number of horizontal and vertical orbit measurements is given by n_x and n_y.

During the first Precursor period, a local vertical bump is visible at 110 m. This bump is used to align the deuteron beam with the electron beam of the 100 kV electron cooler. After the cooling process, the orbit correction is applied, bringing the beam close to the design orbit. However, the steerers responsible for the local bump at the 100 kV cooler were not included in the orbit correction for technical reasons. Therefore, this bump remained even after electron cooling.

Figure 7.39 displays the applied steerer values for each vertical and horizontal steerer. While the RMS values for the horizontal steerers remain in the same order of magnitude for both experiments, the RMS for the vertical steerers improved significantly, decreasing by a factor of approximately three. Nevertheless, significant improvements in the orbit have been observed

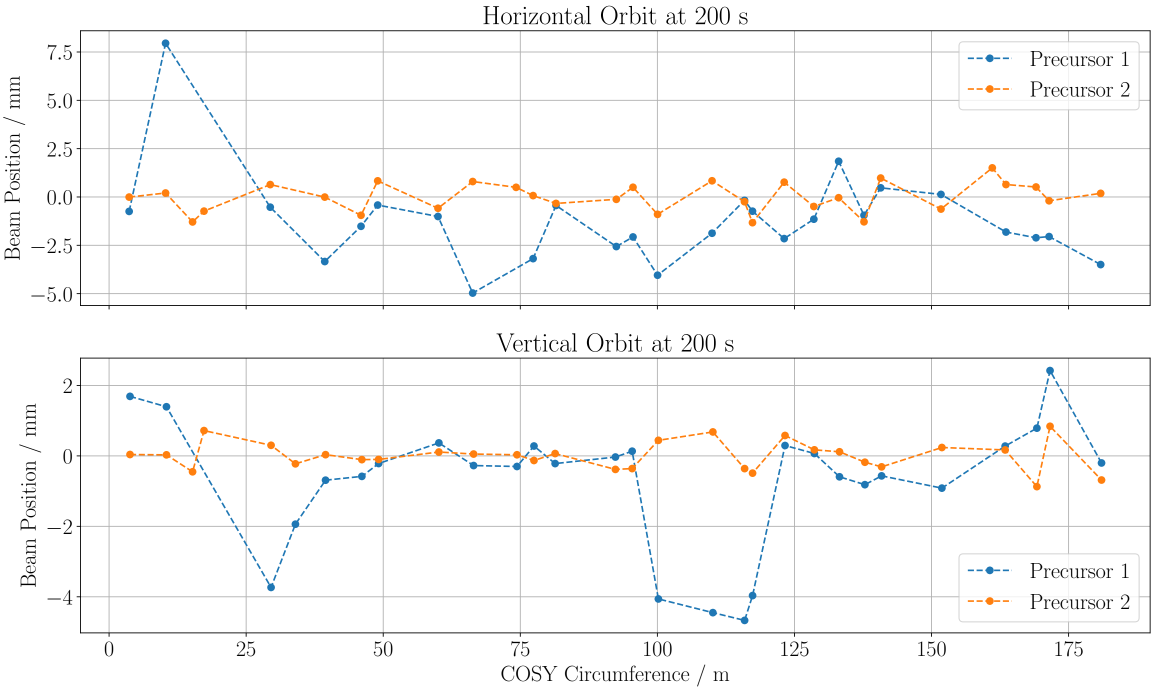

Figure 7.38.: Comparison of the vertical and horizontal orbit before and after the beam-based alignment in the cycle, along with the alignment campaign of the quadrupoles, both measured at 200 s in the cycle, reveals a significant improvement in orbit quality. This improvement is evident in the orbit RMS values listed in Table 7.11.

in both planes. Regarding the local bump at the 100 kV electron cooler, a considerable amount of vertical steering is necessary, particularly at the vertical steerers near the electron cooler.

7.7.2.2. Alignment of the Siberian Snake

During the first Precursor Run in 2018, it was noticed that the Siberian snake acted as an unwanted steerer, leading to orbit changes. The Siberian snake provides a longitudinal magnetic field that is parallel to the beam momentum. Due to this parallelism, the force should be zero on the beam. However, a slightly rotated magnetic field introduces magnetic field components not parallel to the beam momentum direction, causing this measured steering effect. Consequently, the orbit changes during the measurement itself, which also means a change of the Invariant Spin Axis according to section 3.5.

Table 7.11.: Vertical and horizontal orbit RMS values of the orbit during the first and second Precursor runs. The beam-based alignment and the alignment of quadrupoles greatly improved the orbit.

	Vertical Orbit RMS / mm	Horizontal Orbit RMS / mm
Precursor 1	1.808	2.345
Precursor 2	0.398	0.731

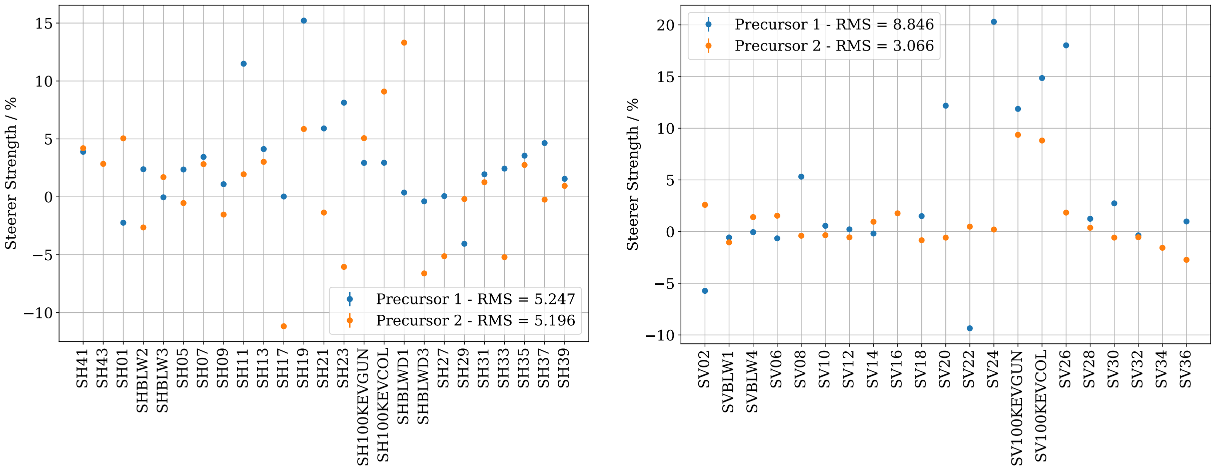

(a) Horizontal (b) Vertical

Figure 7.39.: Horizontal and vertical steerer value comparison for the two Precursor experiments. The steerer strength scales with respect to the maximum value of the power supply of the individual steerer.

The measurement of the alignment of the Siberian Snake solenoidal field was done in November 2020 and repeated in March 2021. The main part of this work was done by a previous PhD student, Tim Wagner, at IKP.

The principal idea is based on changing the path of the beam through the magnet by applying steerer kicks before and after the Siberian snake and measuring the change in orbit RMS before and after switching on the Siberian snake magnet. After a few iterations, the optimal beam path through the snake was found, and the snake was aligned accordingly. The rotation in the horizontal plane was clockwise by 0.1445°, as observed from an overhead perspective. In the vertical direction, the rotation was counter-clockwise by 0.1051°, viewed from the inside of the ring. Additionally, there was a displacement of 1.385 mm towards the outer side of the ring in the horizontal direction and a downward shift of 0.27 mm in the vertical direction. After alignment, the orbit RMS change improved by a factor of 10 when ramping the solenoid (cf. Table 7.12) [108].

Table 7.12.: The change in the root mean square (RMS) of the orbit in both the horizontal and vertical directions is observed before and after switching on the Siberian snake to 15 A. Following the alignment of the snake with the magnetic axis of COSY, the shift in orbit RMS tends to converge to a level comparable to that measured in the absence of a Siberian snake [108].

	Orbit Difference RMS	
	Horizontal	Vertical
With Siberian snake before alignment	0.351 mm	0.337 mm
With Siberian snake after alignment	0.037 mm	0.020 mm
Siberian snake off, only COSY	0.022 mm	0.009 mm

7.7.2.3. Improved Matching of the RF Wien Filter Fields

During the measurement of the in-plane polarization described in section 6.5, the event rates of the upper and lower detectors are combined to cancel out the acceptance and luminosity factors of the beam. When analyzing the count rates in the individual detectors, an interesting effect can be found. When the electromagnetic fields inside the Wien filter do not exactly cancel out the Lorentz force on the deuteron beam, the beam experiences a small kick either by the electric or magnetic field, leading to small coherent oscillations of the beam. These beam oscillations can be studied by performing a Fourier transformation of the signals measured with the electrodes of beam position monitors. To enhance the sensitivity, a beam position is chosen where the natural betatron amplitudes are large, which is in the case of COSY BPM 17. Beam oscillation amplitudes close to the quantum limit of $0.077(32)\,\mu$m have been found [109].

A different approach to quantify the matching of the RF Wien filter is by analyzing event rate changes in the polarimeter. When the unmatched RF Wien filter induces coherent beam oscillations, the number of deuterons hitting the carbon target in the polarimeter is periodically changing by the frequency the Wien filter is kicking the beam f_{WF}. The change of rate on the carbon target is simultaneously measured in the four quadrants of the detector after scattering on the carbon block. The rate of change can be mathematically expressed by adding an oscillation term to the luminosity of the beam

$$\mathcal{L}_{\mathrm{COSY}} \to \mathcal{L}_{\mathrm{COSY}} \cdot \big(1 + a\cos\left(2\pi f_{\mathrm{WF}} t\right)\big), \tag{7.124}$$

where a denotes an amplitude, scaling with the oscillation amplitude of the beam. The oscillation beam amplitude parameter a cannot be trivially translated into an amplitude in standard units as the parameter depends on beam position and vertical betatron oscillation amplitude. For the analysis, only the relative change of the parameter when the RF Wien filter is switched off and on is relevant. The oscillation frequency is given by the Wien filter frequency which is equal to the spin tune when the phase feedback is keeping the phase between the Wien filter frequency and spin tune constant, i.e., $\omega_{\mathrm{WF}} = \omega_{\mathrm{s}}$. In addition, the phase feedback ensures a constant phase relation between the Wien filter frequency and spin tune. The event rates in the individual detector quadrants are therefore given by

$$\begin{aligned}
\dot{N}_{\mathrm{Up}} &\propto \big(1 + a\cos(\omega_s n + \phi_{\mathrm{rel.}})\big) \cdot \big(1 - \varepsilon_{\mathrm{UD}}\cos(\omega_s n)\big), && (7.125)\\
\dot{N}_{\mathrm{Down}} &\propto \big(1 + a\cos(\omega_s n + \phi_{\mathrm{rel.}})\big) \cdot \big(1 + \varepsilon_{\mathrm{UD}}\cos(\omega_s n)\big), && (7.126)\\
\dot{N}_{\mathrm{Left}} &\propto \big(1 + a\cos(\omega_s n + \phi_{\mathrm{rel.}})\big) \cdot \big(1 + \varepsilon_{\mathrm{LR}}\big), && (7.127)\\
\dot{N}_{\mathrm{Right}} &\propto \big(1 + a\cos(\omega_s n + \phi_{\mathrm{rel.}})\big) \cdot \big(1 - \varepsilon_{\mathrm{LR}}\big), && (7.128)
\end{aligned}$$

with $\varepsilon_{\mathrm{LR}} = \frac{3}{2} p_V \overline{A_y}$, $\varepsilon_{\mathrm{UD}} = \frac{3}{2} p_{xz} \overline{A_y}$ and the dot denotes the time derivative, i.e. the counting rate (${}^{\mathrm{d}N}/_{\mathrm{d}t}$). The expected Fourier amplitudes at the frequency of the Wien filter and spin tune in the left and right detector quadrants can be trivially calculated as

$$A_{\rightleftarrows}(\omega = \omega_{\mathrm{WF}} = \omega_s) = a. \tag{7.129}$$

The amplitude of the Fourier spectra in the left and right detectors at the spin tune as a function of time in the cycle are shown in Figure 7.41 (left and right panel). As soon as the Wien filter is switched on at 155 s, the unmatched Wien filter starts to periodically kick the beam resulting in beam oscillations which are measured in the detectors. Note that the amplitude at low amplitudes is biased because of the fitting procedure discussed in section 6.5. The measured amplitudes in the upper and lower quadrants are more complicated as they overlap with the oscillating signal from the spin tune. The count rates in the up and down detectors are given by

$$\dot{N}_{\uparrow\downarrow} \propto \big(1 + a\cos(\omega_\mathrm{s} n + \phi_\mathrm{rel.})\big) \cdot \big(1 \mp \epsilon_\mathrm{UD}\cos(\omega_s n)\big), \tag{7.130}$$

with $\omega_s = 2\pi\nu_s$. Multiplication leads to

$$\dot{N}_{\uparrow\downarrow} \propto 1 \mp \epsilon_\mathrm{UD}\cos(\omega_s n) + a\cos(\omega_s n + \phi_\mathrm{rel.}) \mp a\epsilon_\mathrm{UD}\cos(\omega_s n)\cos(\omega_s n + \phi_\mathrm{rel.}). \tag{7.131}$$

Performing a Fourier transform leads to peaks at $\omega = 0$, $\omega = \omega_s$, and $\omega = 2 \cdot \omega_s$.[2] Relevant is the peak at the spin tune. Ignoring the other terms gives

$$\begin{aligned} \dot{N}_{\uparrow\downarrow} &\propto \mp\epsilon_\mathrm{UD}\cos(\omega_s n) + a\cos(\omega_s n + \phi_\mathrm{rel.}) \\ &= a\big(\cos(\omega_s n)\cos(\phi_\mathrm{rel.}) - \sin(\omega_s)\sin(\phi_\mathrm{rel.})\big) \mp \epsilon_\mathrm{UD}\cos(\omega_s n) \\ &= \cos(\omega_s n) \cdot (a\cos(\phi_\mathrm{rel.}) \mp \epsilon_\mathrm{UD}) - a\sin(\omega_s n)\sin(\phi_\mathrm{rel.}). \end{aligned} \tag{7.132}$$

The Fourier amplitudes at the spin tune are given by

$$\begin{aligned} A_{\uparrow\downarrow}(\omega = \omega_s) &= \sqrt{(a\cos(\phi_\mathrm{rel.}) \mp \epsilon_\mathrm{UD})^2 + a^2\sin(\phi_\mathrm{rel.})^2} \\ &= \sqrt{a^2 + \epsilon_\mathrm{UD}^2 \mp 2a\epsilon_\mathrm{UD}\cos(\phi_\mathrm{rel.})}. \end{aligned} \tag{7.133}$$

The amplitudes in the individual detectors depend on the horizontal polarization ϵ_UD, the beam oscillation amplitude a, and the phase between beam oscillations and spin tune precession $\phi_\mathrm{rel.}$. The phase $\phi_\mathrm{rel.}$ is a value that is fixed by the operators before starting the measurement and remains constant throughout the measuring time. The overlap of beam oscillation amplitude and spin tune amplitude is shown in Figure 7.40. The upper and lower panels show the amplitude of the Fourier spectra in the up and down detector at the spin tune as a function of time in the cycle are shown in Figure 7.41.

As a final consequence, signals mimicking in-plane polarization can be detected even in unpolarized cycles. The count rates in the individual detectors are given by

$$\dot{N}_\mathrm{Up} \propto 1 + a\cos\left(\omega_\mathrm{WF} n\right), \tag{7.134}$$

$$\dot{N}_\mathrm{Down} \propto 1 + a\cos\left(\omega_\mathrm{WF} n\right), \tag{7.135}$$

$$\dot{N}_\mathrm{Left} \propto 1 + a\cos\left(\omega_\mathrm{WF} n\right), \tag{7.136}$$

$$\dot{N}_\mathrm{Right} \propto 1 + a\cos\left(\omega_\mathrm{WF} n\right). \tag{7.137}$$

A Fourier transformation of Eq. (7.134) to Eq. (7.137) leads to a Fourier amplitude directly related to the beam oscillation amplitude parameter a

$$A_{\rightleftarrows}(\omega = \omega_\mathrm{WF} \overset{!}{=} \omega_s) = a, \tag{7.138}$$

$$A_{\uparrow\downarrow}(\omega = \omega_\mathrm{WF} \overset{!}{=} \omega_s) = a. \tag{7.139}$$

---

[2] $\cos(a)\cos(b) = \frac{\cos(a-b)+\cos(a+b)}{2}$.

The findings of the Fourier amplitudes in the individual detectors triggered the idea of a new tool monitoring the periodic change of luminosity while data taking. During the second Precursor run, the new tool was used for the first time to properly match the RF Wien filter fields, minimizing the beam oscillation amplitude. For the tool, not the individual detectors are relevant but the sum of the count rates in the individual detectors as polarization effects cancel out

$$\begin{aligned} \dot{N}_{\mathrm{sum}} &= \dot{N}_{\mathrm{Up}} + \dot{N}_{\mathrm{Down}} + \dot{N}_{\mathrm{Left}} + \dot{N}_{\mathrm{Right}} && (7.140) \\ &\propto 4 \cdot \big(1 + a\cos(\omega_{\mathrm{WF}} t + \varphi_{\mathrm{WF}})\big). && (7.141) \end{aligned}$$

By performing a Fourier transformation of Eq. (7.141) and scaling by the total number of events per chosen time bin, i.e., $N_{\mathrm{sum}} = N_{\mathrm{Up}} + N_{\mathrm{Down}} + N_{\mathrm{Left}} + N_{\mathrm{Right}}$, the Fourier amplitude does not depend on the polarization or feedback settings

$$A_{\mathrm{sum}}(\omega = \omega_{\mathrm{WF}} = \omega_s) = a. \tag{7.142}$$

In addition, also the highest accuracy is reached as all detector events can be used to determine the beam oscillation amplitude parameter a. The Fourier amplitude of all combined detector events as a function of time in the cycle is shown in the middle panel of Figure 7.40.

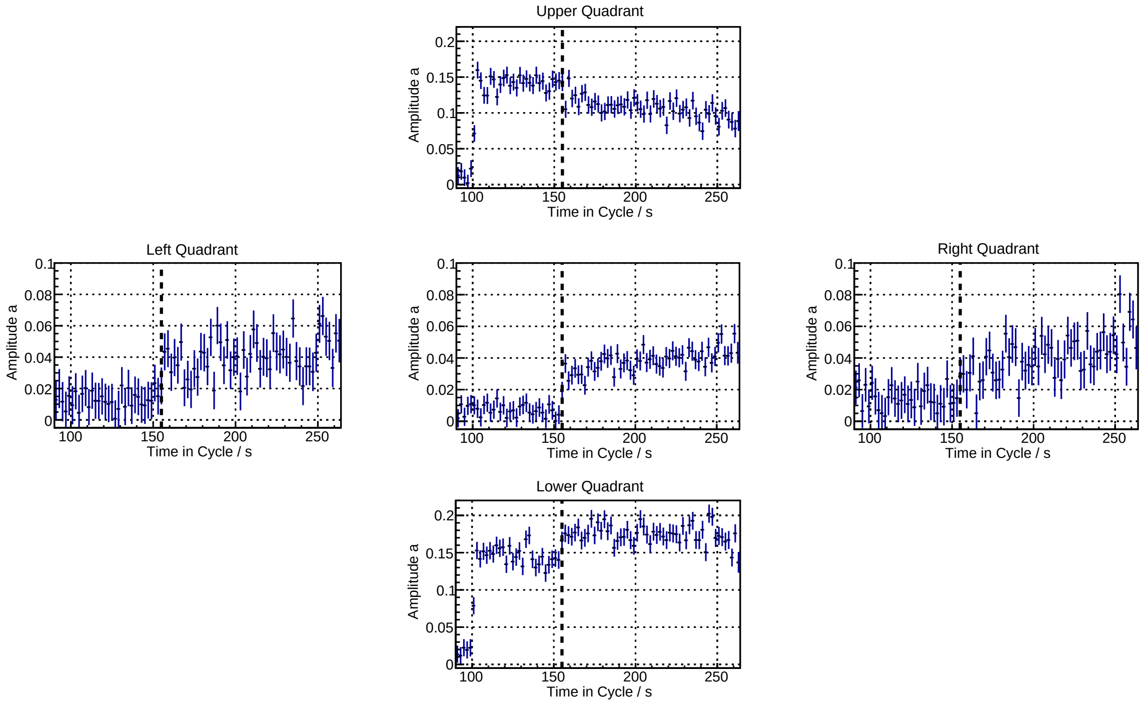

Figure 7.40.: Fourier amplitudes of the event rates measured at the RF Wien filter frequency (= spin tune) measured individually at the detector quadrants. The upper and lower quadrants measure an overlap of the horizontal polarization and the beam oscillation amplitude. The overlap becomes visible when the Wien filter is switched on at 155 s (dotted black line). The left and right detectors show a similar signal which is directly given by the beam oscillation amplitude. The panel in the middle shows a combination of all detector events.

In Figure 7.41, the beam oscillation amplitude a is shown as a function of time in the cycle. In both panels, the RF Wien filter is switched on at 155 s. The left panel depicts data taken during the first Precursor period before the new online tool was developed. A clear jump is visible at $t_{\mathrm{WF}} = 155\,\mathrm{s}$, when the RF Wien filter is switched on. The right panel shows data from the second Precursor experimental period when the Pilot bunch method is used. Both, the unaffected Pilot bunch and the Signal bunch show no effect when the RF Wien filter is switched on, which means that the Wien filter fields are matched more precisely.

In section 8.1 analytical calculations are presented which prove, that beam oscillations don't influence the buildup of the vertical spin component.

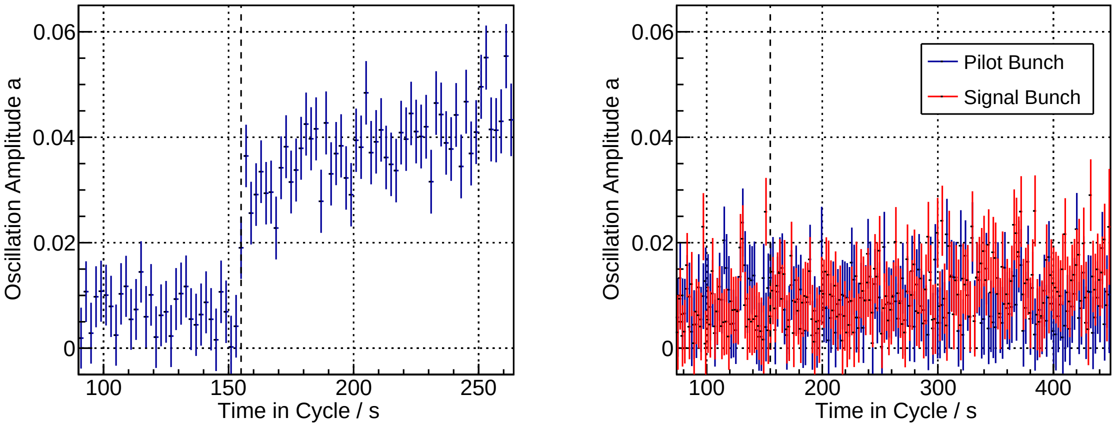

Figure 7.41.: Comparison of the beam oscillation amplitude measured at the polarimeter during the first (left) and second (right) Precursor run. The matching of the RF Wien filter fields for both bunches significantly improved for the second experimental period. The dashed black line marks the time when the RF Wien filter is switched on ($t_{\mathrm{WF}} = 155\,\mathrm{s}$).

7.7.3. Precursor II

After alignment campaigns by Stollenwerk, the Beam-based alignment calibrations of the Beam position monitors, and the installation and commissioning of the switches into the RF Wien filter for the Pilot bunch method, as well as the new Jedi Polarimeter Jepo, the second Precursor Run took place in spring 2021. For the Pilot bunch method, two polarized deuteron bunches are required, meaning that for all experiments, two bunches were circulating in COSY. The optimization of Spin Coherence Time took five days. After that, the initial slope method was used to determine the orientation of the Invariant Spin Axis in two consecutive maps, repeating the experimental method from the first experimental Precursor run. The Pilot bunch method was used for the first time during Map 3, where the relative phase was changed to observe the sinusoidal effect on the oscillation amplitude of the vertical polarization. During Map 4 and Map 5, the relative phase was kept constant to gain statistics for the experiment. In addition, two final maps were taken in which the 2MV solenoid was kept at two different constant currents to benchmark models with two static solenoids in the ring. The beam time ended with dedicated cycles to calibrate both the Siberian snake and the 2 MV solenoid. A summary of all maps is given in Table 7.13.

7.8. Results

A summary of all measurement results of the orientation of the Invariant Spin Axis is shown in Figure 7.42. The first three data points show the results of the Invariant Spin Axis measured in 2018 during the first Precursor run and the seven remaining data points were taken during the second Precursor Run in 2021. The dotted black line separates the data sets collected in 2018 and 2021. During the first Precursor Run, only the initial slope method was used. For the first two maps of the second Precursor Run, the initial slope method was used but for two bunches co-rotating in the ring in preparation for the remaining maps where the Pilot bunch method was applied. While relative phase scans were performed during the third map to prove the method of the Pilot bunch, the relative phase was kept fixed during Map 4 and Map 5 to collect statistics. During Map 6 and Map 7, the 2 MV solenoid in the first straight section of COSY after injection, which is placed 8 m in front of the RF Wien filter, was used in addition to the Siberian snake as an additional spin rotator providing a longitudinal magnetic field.

The exact meaning of the parameters summarized in Figure 7.42 is derived in section 7.6.1, Eq. (7.56). The description of the parameters is listed in Table 7.7. The upper panels in Figure 7.42 show the orientation of the Invariant Spin Axis in the radial and longitudinal directions. The predictions of the orientation of the Invariant Spin Axis are derived in section 4.2.1. According to the Thomas-BMT equation, the Electric Dipole Moment leads to a tilt of the Invariant Spin Axis in the radial (x) direction, while the longitudinal component (z) remains unaffected. Any other tilts are purely related to systematics like unwanted magnetic fields and orbit imperfections

$$n_x = \phi_{\mathrm{EDM}} + n_x^{\mathrm{sys.}} \text{ and } n_z = n_z^{\mathrm{sys.}}. \tag{7.143}$$

The averaged tilts of the Invariant Spin Axis for the first Precursor experiment are given by

$$n_{x,\mathrm{avg.}}^{\mathrm{Prec.\ 1}} = -3.6(3)\,\mathrm{mrad} \text{ and } n_{z,\mathrm{avg.}}^{\mathrm{Prec.\ 1}} = -5.5(5)\,\mathrm{mrad}, \tag{7.144}$$

and for the second Precursor experiment by

$$n_{x,\mathrm{avg.}}^{\mathrm{Prec.\ 2}} = -2.1(12)\,\mathrm{mrad} \text{ and } n_{z,\mathrm{avg.}}^{\mathrm{Prec.\ 2}} = 3.9(6)\,\mathrm{mrad}. \tag{7.145}$$

A final discussion of the tilt of the Invariant Spin Axis is given in section 7.9. The use of the Pilot bunch can be also seen in in the lower left panel in Figure 7.42. While for the measurements using the Initial slope method the spin kick angle per turn is in the order of approximately 2.8×10^{-6} rad, the spin kick angle is reduced to roundabout 1.9×10^{-6} rad. The power on the RF Wien filter was reduced during the experiment to protect the switches in the driving circuit which are gating the Pilot bunch. These switches were not in use during the initial slope method. A smaller power means also less fields and hence a smaller kick angle in the RF Wien filter according to Eq. (D.12).

The reduced chi-squared for the individual maps is shown in the lower right panel in Figure 7.42. It has to be noted that the fit quality of the maps improved drastically from the first Precursor experiment to the second, which can almost certainly be related to the improvements in the

Table 7.13.: Precursor 1 & 2: Data Overview

		# Points	Solenoid	Method	# $\phi_{\text{rel.}}$ / Point	Repetitions per $\phi_{\text{rel.}}$	WF Power / W	Remark
Prec. 1	Map 1	9	Siberian Snake	Initial Slope	8	$4+1$	1000	
	Map 2	9	Siberian Snake	Initial Slope	8	$4+1$	1000	Repetition of Map 1
	Map 3	13	Siberian Snake	Initial Slope	8	$4+1$	1000	Measurement closer to the Minimum
	Map 10		Siberian Snake	Solenoid Calibration	-	-		Spin Tune ν_s vs. solenoid currents
Prec. 2	Map 1	11	Siberian Snake	Initial Slope	7	$4+1$	1000	
	Map 2	11	Siberian Snake	Initial Slope	7	$4+1$	1000	
	Map 3	12	Siberian Snake	Pilot Bunch	7	$4+1$	470	Scanning ε as a function $\varphi_{\text{rel.}}$
	Map 4	25	Siberian Snake	Pilot Bunch	1	$8+2$	470	
	Map 5	25	Siberian Snake	Pilot Bunch	1	$8+2$	470	Repetition of Map 4
	Map 6	9	Siberian Snake & 2MV solenoid	Pilot Bunch	1	$8+2$	470	2MV solenoid constant at 5 A
	Map 7	9	Siberian Snake & 2MV solenoid	Pilot Bunch	1	$8+2$	470	2MV solenoid constant at -5 A
	Map 10		Siberian Snake & 2MV solenoid	Solenoid Calibration	-	-		Spin Tune ν_s vs. Solenoid currents

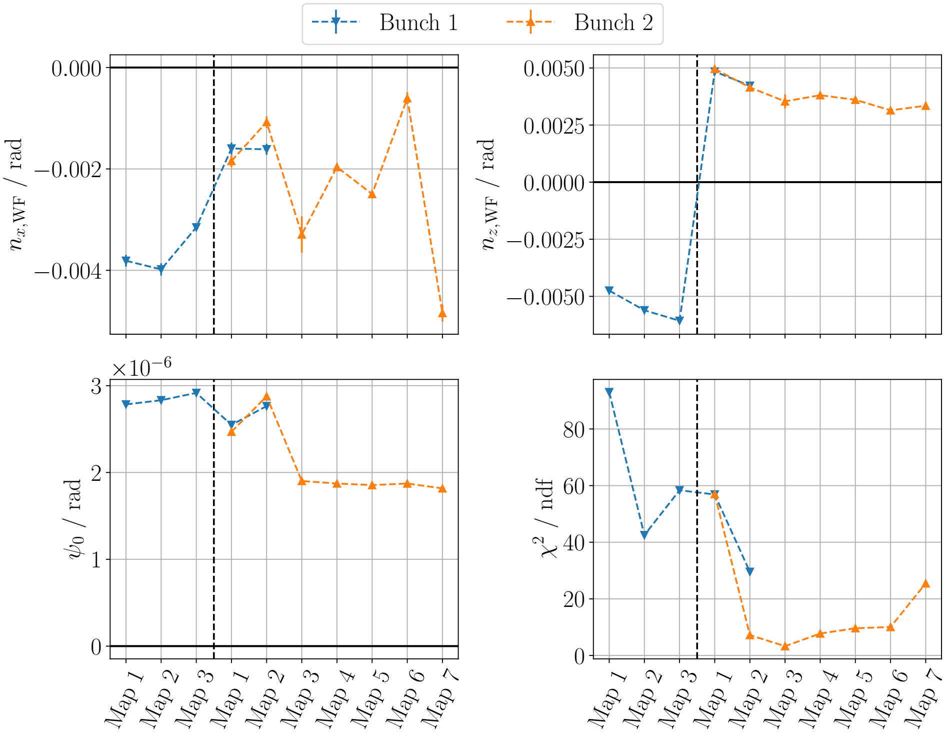

Figure 7.42.: The panels depict the fit results according to Eq. (7.56) for all measured maps listed in Table 7.13. The upper two panels show the measured orientation of the Invariant Spin Axis. The lower panel depicts the spin kick angle in the RF Wien filter per turn, and the lower right panel shows the reduced chi-squared. The dashed black line separates the dataset from 2018 from the dataset from 2021.

machine listed in section 7.7.2. However, the reduced chi-squared remains at a high level, which means that there are still systematic effects on the buildup that are not included in the analytical fitting procedure. Any larger systematic shifts of the map minimum can be excluded when looking at Figure 7.43. The data shows the slope of the buildup of the vertical polarization scaled by the revolution frequency as a function of the relative phase at a data point close to the map minimum of Precursor 1 Map 3. The settings of the Wien filter rotation angle and the spin flip in the Siberian snake are given by

$$\phi^{\mathrm{WF}} = -3.695\,\mathrm{mrad} \text{ and } \chi_{\mathrm{Snake}} = -6.175\,\mathrm{mrad}. \tag{7.146}$$

According to the fit, the map minimum is given by

$$n_x = -3.15(5)\,\mathrm{mrad} \text{ and } n_z = -6.06(3)\,\mathrm{mrad}. \tag{7.147}$$

As the oscillation amplitude at the map minimum is almost consistent with a zero amplitude, the settings of the Wien filter rotation angle and the spin flip in the Siberian snake listed in Eq. (7.146) have to align the magnetic field of the RF Wien filter with the orientation of the Invariant Spin Axis.

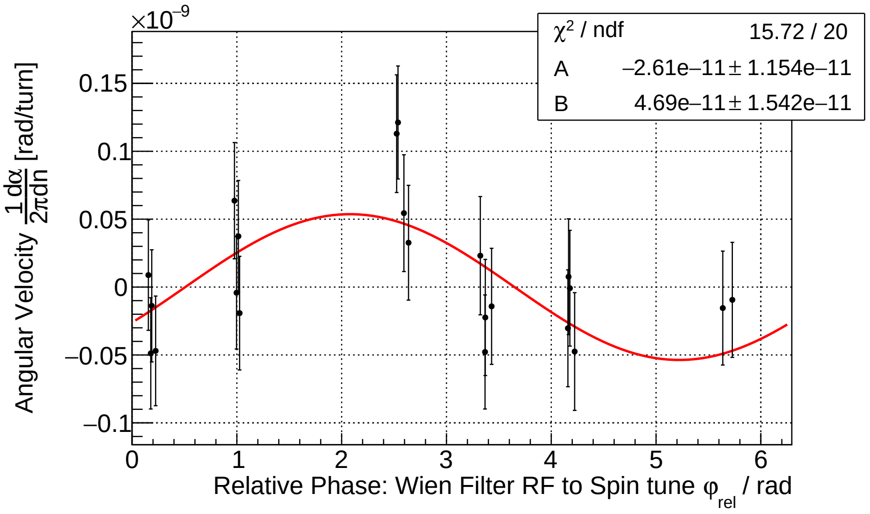

Figure 7.43.: Measurement of the resonance strength close to the map minimum. As indeed almost a zero resonance strength is measured, no large systematic shifts of the map minimum (and hence the Invariant Spin Axis) are expected from systematics in the fitting procedure.

7.8.1. Event Selection Studies

An introduction to the Event Selection Studies is given in section 6.3. After selecting data in the head and tails and the center of the distribution of the COSY phase, the resonance strength is either determined using the Pilot bunch method or the Initial slope method for both data sets independently. The results for the first Precursor experiment are shown in Figure 7.44. Regarding the orientation of the Invariant Spin Axis in radial and longitudinal directions and the reduced chi-squared, no larger effects are visible. However, the spin kick angle in the RF Wien filter per turn is significantly reduced in the head and tails of the COSY phase distribution compared to the data located in the center. The significantly smaller spin kick angle is most certainly related to a larger relative phase distribution in the bunch for larger synchrotron oscillation amplitudes. According to Eq. (7.65), the slope of the build is given for the initial slope method by

$$\dot{\alpha} = -2\pi\epsilon f_{\mathrm{COSY}} \cos(a_{xz} - \phi_{\mathrm{rel.,0}}). \tag{7.148}$$

The Event Selection Studies presented in section 7.4.4 revealed a consistent spin tune along the bunch. However, as the RF Wien filter is a stroboscopic device, the relative phase in the head and tails experience a different phase relation than the particles in the bunch center. In consequence, the relative phase is smeared out, leading to a larger width in the relative phase distribution and hence a smaller buildup of the vertical polarization. The smeared-out phase has no effect on the map minimum of the measured data.

The same finding can be also seen in the data taken in 2021 during the second Precursor experiment as shown in Figure 7.45.

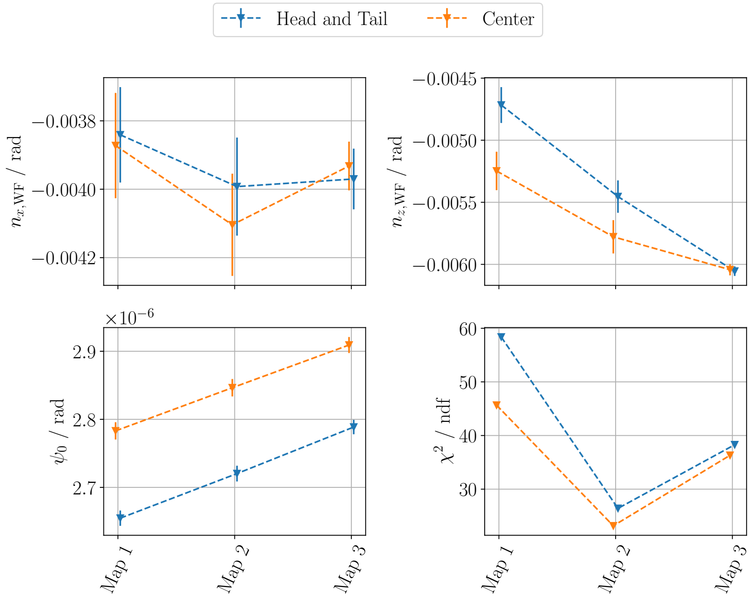

Figure 7.44.: Event Selection Studies results for the data taken during the first Precursor Run. The upper panels show the orientation of the Invariant Spin Axis in radial (left) and longitudinal (right) directions. The lower panels depict the spin filp angle in the RF Wien filter and the reduced chi-squared of the individual fits.

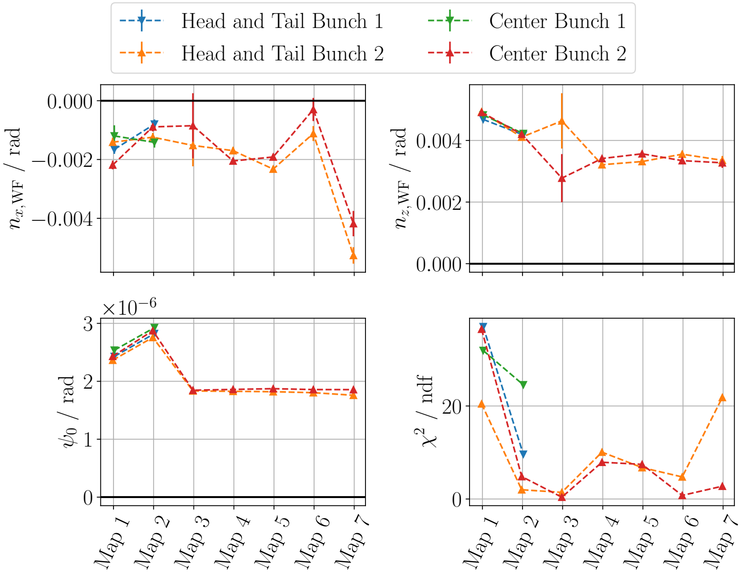

Figure 7.45.: Event Selection Studies results for the data taken during the second Precursor Run. The upper panels show the orientation of the Invariant Spin Axis in radial (left) and longitudinal (right) directions. The lower panels depict the spin filp angle in the RF Wien filter and the reduced chi-squared of the individual fits.

7.9. Summary & Discussion

In the following section, the findings of the previous sections are again summarized and discussed. The results of the orientation of the Invariant Spin Axis at the Siberian snake, the 2 MV solenoid, and the RF Wien filter are given in Figure 7.46.

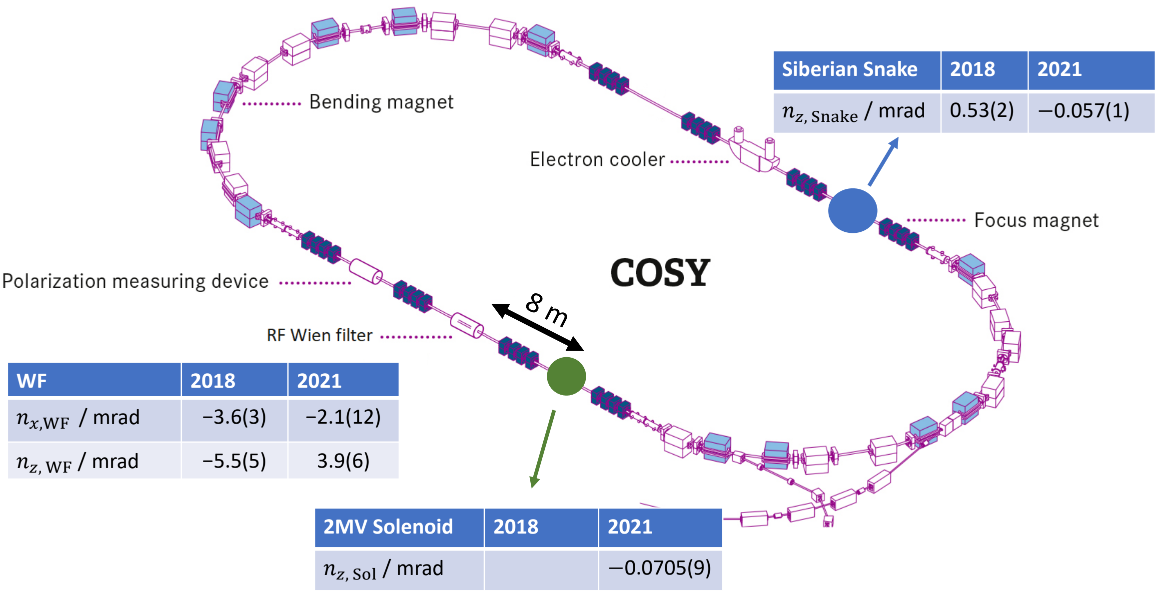

Siberian Snake	2018	2021
$n_{z,\text{Snake}}$ / mrad	0.53(2)	−0.057(1)

WF	2018	2021
$n_{x,\text{WF}}$ / mrad	−3.6(3)	−2.1(12)
$n_{z,\text{WF}}$ / mrad	−5.5(5)	3.9(6)

2MV Solenoid	2018	2021
$n_{z,\text{Sol}}$ / mrad		−0.0705(9)

Figure 7.46.: Summary of the determination of the orientation of the Invariant Spin Axis at the Siberian snake, the 2 MV solenoid and the RF Wien filter for both experimental periods. Created by Jamal Slim/ JEDI Collaboration and adapted by this author.

The findings in the previous sections can be summarized as follows:

1. Spin tune scans presented in section 7.4.3 showed an improvement of the longitudinal component of the Invariant Spin Axis from 5×10^{-4} rad (Precursor 1) to -5×10^{-5} rad (Precursor 2). Note that from the Thomas BMT equation (4.22), no tilt of the Invariant Spin Axis in longitudinal direction is expected in an idealized storage ring. A non-zero tilt is directly related to unknown systematic effects in the COSY. The improvement by an order of magnitude can be attributed to all the improvements in COSY listed in section 7.7.2 between both experimental periods. These results are consistent with beam and spin tracking simulations by Maximilian Vitz [104], which include all misalignments of magnets in COSY. The spin tune scans extracted from the RF Wien filter scans are consistent with the dedicated solenoidal calibration cycles, proving that switching on the RF Wien filter does not change the spin tune and consequently also not the orientation of the Invariant Spin Axis. Additionally, the Pilot bunch method wouldn't work if the RF Wien filter changes the spin precession frequency.
2. Mapping of the resonance strength using the RF Wien filter revealed much larger tilts in radial and longitudinal direction of the Invariant Spin Axis as expected. Furthermore, the sign of the longitudinal component of the Invariant Spin Axis switched between the data

from 2018 and 2021. The switch in sign remains unexplainable. Beam and spin tracking simulations by Maximillian Vitz that include all known sources of systematics, imperfections, and misalignments of magnetic elements can only explain tilts of the Invariant Spin Axis in the radial and longitudinal directions along the ring no larger than 1 mrad [104]. Moreover, the effects on the Invariant Spin Axis of unwanted radial or longitudinal fields would be measurable throughout COSY, including both solenoids. Local tilts in front of and after the RF Wien filter can only be generated with symmetric, canceling fields before and after, like an orbit bump. Such an orbit bump was not measured.

3. The reduced χ^2 of the individual map fits are large, which means that the unsystematic uncertainties are dominating the results. On the other side, the reduced χ^2 to determine the resonance strength for a fixed setting of the RF Wien filter rotation angle and the spin flip in the Siberian snake are reasonable as shown in Figure 7.24. Systematic shifts of the minimum due to systematic shifts of the resonance strength can still be excluded, as measurements of the resonance strength at the map minimum result in no buildup of vertical polarization, as shown in Figure 7.43. Additionally, the buildup of vertical polarization without the Siberian snake and/or the 2 MV solenoid is significant. Therefore, solenoidal imperfections cannot explain the large tilts of the measurements.
4. Event Selection Studies showed no inconsistent spin rotations along the longitudinal particle distribution in the bunch for the spin tune as well as the resonance strength maps, as shown in section 7.4.4 and 7.8.1.

As already discussed, the Invariant Spin Axis should have no component in the longitudinal direction around the ring, and a radial tilt would be the result of a permanent Electric Dipole Moment. The fact that the tilts in both directions are of the same order of magnitude is a clear hint that no Electric Dipole Moment, but unknown systematic effects, are the reason for these large tilts. Three options are valid to explain the large tilts:

- The measured tilts are real and correctly measured at the RF Wien filter. In this case, a systematic effect rotating the Invariant Spin Axis in the longitudinal direction before and after or inside the RF Wien filter needs to be identified; otherwise, the tilts wouldn't be as small as at both solenoids, also given the fact that the RF Wien filter and the 2MV solenoid are only 8 m apart. A local, vertical orbit bump, or an effect induced by the Wien filter while it is on, cannot be excluded at the moment. The orbit bump angle needed corresponds to a 5 mrad tilt of the beam. In addition, the change of sign of the longitudinal component of the Invariant Spin Axis still needs to be explained.
- Another option is that the spin tune scans with the solenoids are wrong. However, measurements at both solenoids would need to be consistently wrong. Additionally, spin tracking simulations by Maximilian Vitz [104] benchmarked the method.
- The tilts are caused by unknown systematic effects, meaning that the measured tilt of the Invariant Spin Axis does not correspond to the true orientation of the Invariant Spin Axis. Systematic effects from the fit can be excluded, as no buildup of the vertical polarization is measured at the minimum of a map. One option is the direction of the field axis in the Wien filter. If the magnetic field of the RF Wien filter is tilted, correction factors have to be applied in Eq. (7.56) and (7.57). The necessary tilt needs to be in the order of 5 mrad.

8. Systematic Studies

8.1. Systematic Calculations on the Buildup of the Vertical Polarization considering Beam and RF Wien Filter Misalignments

These calculations are based on an internal note *Analytic calculation of various tilt effects in the WF* of Volker Hejny [110].

So far, the assumption that the magnetic field and beam direction are perpendicular is used to calculate the spin rotations in the RF Wien filter. Taking this factor into account, the Magnetic Dipole Moment contribution of the T-BMT Equation to the motion of the spin is given by

$$\vec{\Omega} = -\frac{q}{m}\left[\left(G+\frac{1}{\gamma}\right)\vec{B} - \frac{\gamma G}{\gamma+1}\vec{\beta}\left(\vec{\beta}\cdot\vec{B}\right) - \left(G+\frac{1}{\gamma+1}\right)\frac{\vec{\beta}\times\vec{E}}{c}\right]. \tag{8.1}$$

Using the Wien filter condition

$$\vec{E} = -c\vec{\beta}\times\vec{B}, \tag{8.2}$$

the last term can be written as

$$\vec{\beta}\times\vec{E} = -c\vec{\beta}\times(\vec{\beta}\times\vec{B}) = -c\vec{\beta}\left(\vec{\beta}\cdot\vec{B}\right) + c\beta^2\vec{B}. \tag{8.3}$$

Using this relation, Eq. (8.1) can be written as

$$\vec{\Omega} = -\frac{qB(1+G)(1-\beta^2)}{m}\left[\vec{e}_B + (\gamma-1)\vec{e}_\beta\left(\vec{e}_\beta\cdot\vec{e}_B\right)\right]. \tag{8.4}$$

Evaluating Eq. (8.4), it can be directly seen that radial tilts of the beam (δ_1) or the RF Wien filter (δ_2) don't have an impact on the buildup of the vertical component

$$\vec{e}_\beta = \begin{pmatrix}\sin(\delta_1)\\ 0\\ \cos(\delta_1)\end{pmatrix} \text{ and } \vec{e}_B = \begin{pmatrix}\sin(\delta_2)\\ \cos(\delta_2)\\ 0\end{pmatrix} \overset{\delta_1\ll 1,\delta_2\ll 1}{\Rightarrow} \vec{e}_\beta\cdot\vec{e}_B \approx 0, \tag{8.5}$$

ignoring all terms of second order. Reasonable estimates for beam tilts and RF Wien filter tilts are in the order of 1 mrad, which justifies this approximation. In this case, Eq. (8.4) corresponds to Eq. (D.12) which leads to the calculations presented in section 7.6. However, vertical beam and RF Wien filter tilts have an impact on the buildup of the vertical polarization component.

The phase feedback adjusts the frequency and the relative phase of the oscillating Wien filter fields to the spin tune

$$B = B_0 \sin\left(\omega_s t + \phi_{\mathrm{WF}}^{\mathrm{abs.}}\right) \text{ with } \omega_s = 2\pi\nu_s f_{\mathrm{COSY}}. \tag{8.6}$$

Taking the in-plane precession as well as a vertical component of the spin into account, the spin vector can be written as

$$\vec{S} = \begin{pmatrix} \cos(\alpha)\cos(\omega_s t) \\ \sin(\alpha) \\ \cos(\alpha)\sin(\omega_s t) \end{pmatrix}, \tag{8.7}$$

where α denotes the angle between vertical and horizontal polarization. In the case of a vertical beam tilt (δ_1) and a vertical magnetic field (δ_2), the momentum vector and the magnetic field axis vector can be written as

$$\vec{e}_\beta = \begin{pmatrix} 0 \\ \sin(\delta_1) \\ \cos(\delta_1) \end{pmatrix} \approx \begin{pmatrix} 0 \\ \delta_1 \\ 1 \end{pmatrix} \text{ and } \vec{e}_B = \begin{pmatrix} 0 \\ \cos(\delta_2) \\ \sin(\delta_2) \end{pmatrix} \approx \begin{pmatrix} 0 \\ 1 \\ \delta_2 \end{pmatrix}. \tag{8.8}$$

In this case, the Magnetic Dipole Moment contribution to the spin can be written as

$$\vec{\Omega} = -\frac{qB(1+G)(1-\beta^2)}{m}\left[\vec{e}_y + \gamma\delta_1\vec{e}_z + (\gamma-1)\delta_2\vec{e}_z\right]. \tag{8.9}$$

The change of the vertical component of the spin can be calculated using the cross product of Magnetic Dipole Moment rotation and spin

$$\begin{aligned} \frac{\mathrm{d}S_y}{\mathrm{d}t} &= \left(\vec{\Omega} \times \vec{S}\right)_y (t) && (8.10) \\ &= -\frac{qB_0(1+G)(1-\beta^2)}{m}\left(\gamma\delta_1 + (\gamma-1)\delta_2\right)\cos(\alpha)\cos(\omega_s t)\sin\left(\omega_s t + \phi_{\mathrm{WF}}^{\mathrm{abs.}}\right). && (8.11) \end{aligned}$$

By averaging over a full spin precession period $T = {}^{2\pi}/_{\omega_s} = {}^{1}/_{f_s}$, the average net change of the vertical polarization component can be calculated

$$\begin{aligned} \frac{\mathrm{d}\bar{p}_y}{\mathrm{d}t} &= \frac{1}{T}\int_0^T \frac{\mathrm{d}S_y}{\mathrm{d}t}(t)\mathrm{d}t && (8.12) \\ &= \frac{\omega_s}{2\pi}\int_0^{\frac{2\pi}{\omega_s}} \frac{\mathrm{d}S_y}{\mathrm{d}t}(t)\mathrm{d}t && (8.13) \\ &= -\frac{qB_0(1+G)(1-\beta^2)}{2m}\left(\gamma\delta_1 + (\gamma-1)\delta_2\right)\cos(\alpha)\sin\left(\phi_{\mathrm{WF}}^{\mathrm{abs.}}\right). && (8.14) \end{aligned}$$

While the buildup of the vertical polarization remains unchanged for radial imperfections of the RF Wien filter or the beam, longitudinal tilts of the beam or magnetic field axis have an impact on the buildup of the vertical component of the spin vector. In this case, the measured longitudinal component of the Invariant Spin Axis does not correspond to the real longitudinal component but needs to be corrected for vertical beam tilts and longitudinal RF Wien filter misalignments

$$n_z^{\mathrm{true}} = n_z^{\mathrm{meas.}} - \left(\gamma\delta_1 + (\gamma-1)\delta_2\right). \tag{8.15}$$

Note that the impact of a misaligned beam is larger ($\gamma \approx 1.1258$) than the impact of a misaligned RF Wien filter ($\gamma - 1 \approx 0.1258$). These results are benchmarked by spin tracking simulations by Maximillian Vitz [104]. Unfortunately, there is little information available on the beam tilts at the location of the RF Wien filter and tilts of the device itself. However, reasonable estimates are in the order of 1 mrad and smaller for the beam tilt at the RF Wien filter. For larger beam tilts, the device couldn't be matched. The tilt of the device itself is expected to be even smaller. In addition, the measured tilts of the Invariant Spin Axis in the radial direction, which are not affected by tilts of the beam or the RF Wien filter, are in the same order of magnitude as the measured tilts in the longitudinal direction. Therefore, longitudinal tilts of the beam or the RF Wien filter cannot explain the measured tilts of the Invariant Spin Axis at the location of the RF Wien filter.

The formalism described in this section can also be used to study the effects of beam oscillations on the buildup. When the RF Wien filter fields are not properly matched, they induce beam oscillations as described in section 7.7.2.3. These oscillations can be described with an oscillation of the beam momentum direction. The frequency of these oscillations is given by the Wien filter frequency, which is adjusted to the spin tune

$$\delta_1(t) = \delta_0 \sin\Big(\omega_s t + \phi_{\mathrm{WF}}^{\mathrm{abs.}}\Big). \tag{8.16}$$

By inserting the oscillating beam parameter into Eq. (8.11) and integrating over a full oscillation period of the polarization, the dependence on the oscillation drops out. Therefore, these beam oscillations don't have a direct impact on the buildup of the vertical component of the spin vector.

8.2. Measurement of the Solenoidal Field Directions

A possible solution for the change of sign of the Invariant Spin Axis in the longitudinal direction (cf. section 7.8) could be the change of polarity of the power supply attached to the Siberian snake. A switch in polarity would result in an opposite field direction and thus the Invariant Spin Axis would rotate in the opposite direction. A switch in polarity could occur due to a change of power supply between the two experiments. To exclude such an effect, the magnetic field direction measured by a Hall probe, which is installed close to the Siberian snake, is analyzed. The results are shown in Figure 8.1. The first three rows show the magnetic field direction in the x, y, and z directions. The directions are defined by the orientation of the Hall probe. The last row represents the applied current in amperes to the solenoid as a function of time. The left column shows data from the first Precursor Run in 2018, and the right column shows data from the second Precursor Run in 2021. In both examples, the snake is ramped to positive values (5.44 A and 4 A). When ramping the snake, the magnetic field changes in both measurement periods in the same directions, meaning that the polarity of the power supply was not switched between the two experiments, assuming that the Hall probe was not rotated in between. Note that the absolute magnetic field does not have to be equal as the Siberian snake is ramped to two different values. In addition, the Hall probe is not calibrated against a zero magnetic field, which is not important as only relative changes are relevant for this measurement.

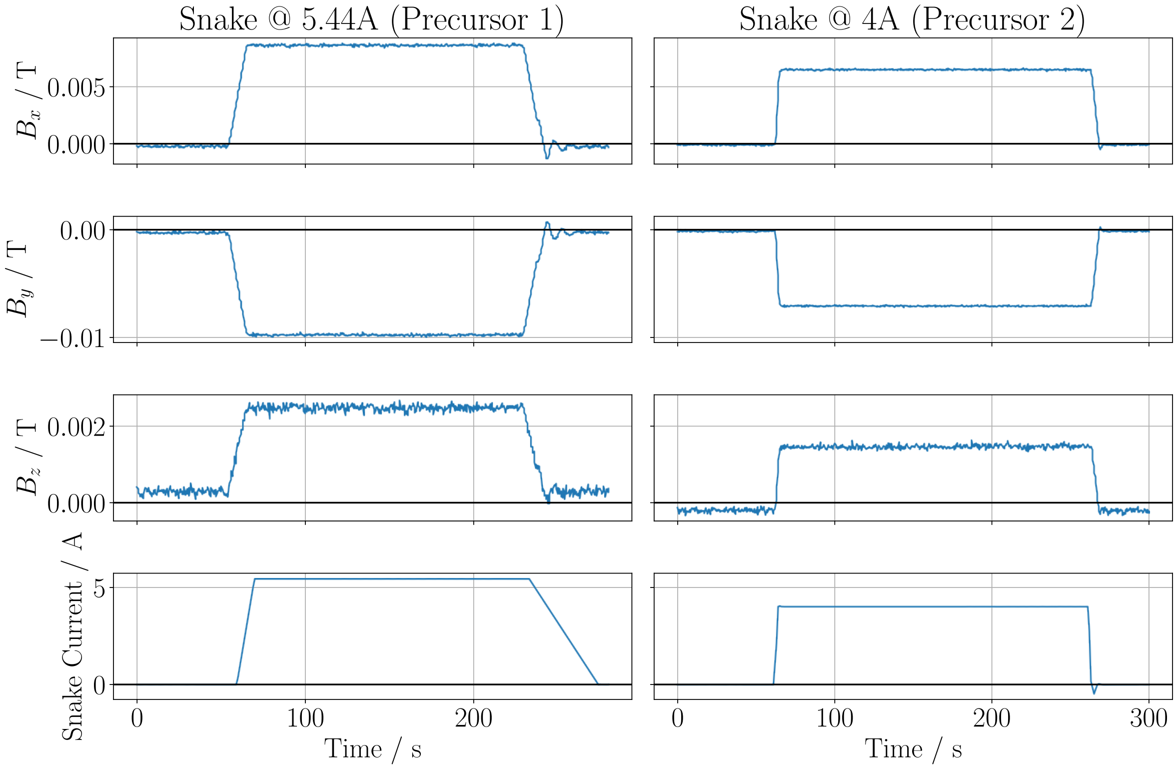

Figure 8.1.: Magnetic field measurements with a Hall probe close to the Siberian snake were conducted for two measurement periods during Precursor I and II. The Hall probe tends toward the same values for positive snake current. Assuming that the Hall probe was not rotated between the experiments, the polarity of the power supply attached to the Siberian snake was not changed.

In addition, the field directions of the Siberian snake and the 2MV solenoid are also measured with respect to the beam direction. For the measurement at the 2MV solenoid, the measurement position is outside the iron, and thus the return field direction is measured. Due to quadrupole stray fields, it was not possible to measure the field at the exit of the solenoid. For an applied current of $-20\,\mathrm{A}$, the south pole points in beam direction while the north pole points against the beam direction, and vice versa for an applied current of $20\,\mathrm{A}$. At the Siberian snake, the measurement position is directly at the beam pipe at the exit of the Siberian snake, meaning that the actual field direction is measured. For a current of $-6\,\mathrm{A}$, the north pole points in the beam direction while the south pole points against the beam direction, and vice versa for a current of $6\,\mathrm{A}$. The conclusion of these measurements is that in both solenoids, the fields point in the same direction for positive currents and vice versa. This is important for the spin rotation calculations in section 7.6.1.

8.3. RF Wien Filter Field Studies

Another reason behind the significant tilt angles observed in the Invariant Spin Axis, as summarized in section 7.8, could stem from unknown magnetic field components within the RF Wien filter. In Eq. (7.56), the buildup of the vertical vector spin component is calculated assuming precise knowledge about the orientation. However, unknown field components would lead to a correction of the fit formula.

During the Precursor runs, the direction of the Invariant Spin Axis is determined by aligning the Magnetic Dipole Moment rotation axis with the magnetic field axis of the RF Wien filter. In this setup, no spin rotation from the in-plane precession to the vertical direction is detectable. In an ideal scenario with a Wien filter, the Magnetic Dipole Moment rotation axis aligns with the magnetic field axis, pointing vertically. Typically, this axis is defined by the geometric configuration and operational parameters of the Wien filter. While simulations of the RF Wien filter fields indicate that uncertainties in field directions ($\vec{B}$ and $\vec{E}$) are below a mrad [88, 111, 112], experimental confirmation during a dedicated experiment is needed.

As the RF Wien filter was still installed in COSY during the period of this thesis, a direct field measurement was not possible. Instead, a measurement idea based on the excitation of vertical and horizontal betatron oscillations using the RF Wien filter was developed and tested, which will be further discussed in the upcoming sections.

8.3.1. Initial Idea of Measuring the Wien Filter Fields Orientation

In the actual Precursor experiments involving a polarized beam and a properly matched RF Wien filter (ensuring negligible Lorentz force), the Wien filter does not influence the orbit. However, even a slight deviation from this match would induce coherent beam oscillations at the operational frequency of the Wien filter, typically around 871 kHz, as observed in our measurements, which revealed oscillation amplitudes in the order of 1 μm [109], which is further discussed in section 7.7.2.3.

In this proposed approach, a different strategy by intentionally mismatching the Wien filter fields is used. The resulting Lorentz force reveals the orientation of the combined $\vec{B}$ and $\vec{E}$ fields by exciting the betatron frequencies. The main assumption is that the directions of the betatron oscillation planes should be mainly defined by the alignment of the quadrupoles, which is, after the beam-based alignment campaign, below 1 mrad. By running the RF Wien filter at the betatron resonance of Q_x or Q_y (depending on the orientation of the magnetic field and the Lorentz force), the betatron oscillation amplitudes are excited similar to a harmonic oscillator which is excited with a sinusoidal force, leading to beam losses due to the acceptance limit of the beam pipe of COSY. The beam excitation (and, thus, the beam loss) should be minimal when the Lorentz force is perpendicular to the corresponding betatron plane. Therefore, the vertical and horizontal betatron frequencies need to be well separated. By slowly rotating the RF Wien filter (and, thus, the Lorentz force) around the beam pipe, the beam loss rate quantity can be probed for different Lorentz force angles. In simple words, if the magnetic field points in the vertical direction, the Lorentz force acts in the horizontal plane. As the oscillation frequency is adjusted to the vertical betatron tune, the horizontal betatron remains unaffected, and no resonance occurs. By rotating the RF Wien filter, the Lorentz force gains additional vertical components which resonate with the vertical tune and excite the beam.

As the betatron oscillation amplitudes grow over time, the beam starts to hit the beam pipe, resulting in beam loss. Using this method, only a potential correction factor for the radial component of the Invariant Spin Axis can be found. The longitudinal component cannot be probed.

For probing the vertical magnetic field axis, the Wien filter frequency needs to be adjusted to a sideband frequency of the vertical betatron tune, as in Eq. (6.55)

$$B_{\mathrm{WF}} = |B|\sin\left(2\pi f_{\mathrm{WF}} + \phi_{\mathrm{WF}}^{\mathrm{abs.}}\right) \text{ with } f_{\mathrm{WF}} = f_{\mathrm{COSY}}(1 + \mathrm{frac}(Q_y)), \tag{8.17}$$

where $\mathrm{frac}(Q_y)$ denotes the fractional vertical tune. This scenario is depicted in Figure 8.2. Similarly, the horizontal betatron tune frequency can be used to probe the magnetic field direction of the RF Wien filter. By rotating the magnetic field of the RF Wien filter into the accelerator plane, the Lorentz force points in the vertical direction. By adjusting the oscillation frequency to a fractional part of the horizontal betatron tune and rotating the magnetic field, the orientation can be measured in the same way as in the vertical magnetic field case. This scenario is shown in Figure 8.3. The magnetic field is given by

$$B_{\mathrm{WF}} = |B|\sin\left(2\pi f_{\mathrm{WF}} + \phi_{\mathrm{WF}}^{\mathrm{abs.}}\right) \text{ with } f_{\mathrm{WF}} = f_{\mathrm{COSY}}(1 + \mathrm{frac}(Q_x)). \tag{8.18}$$

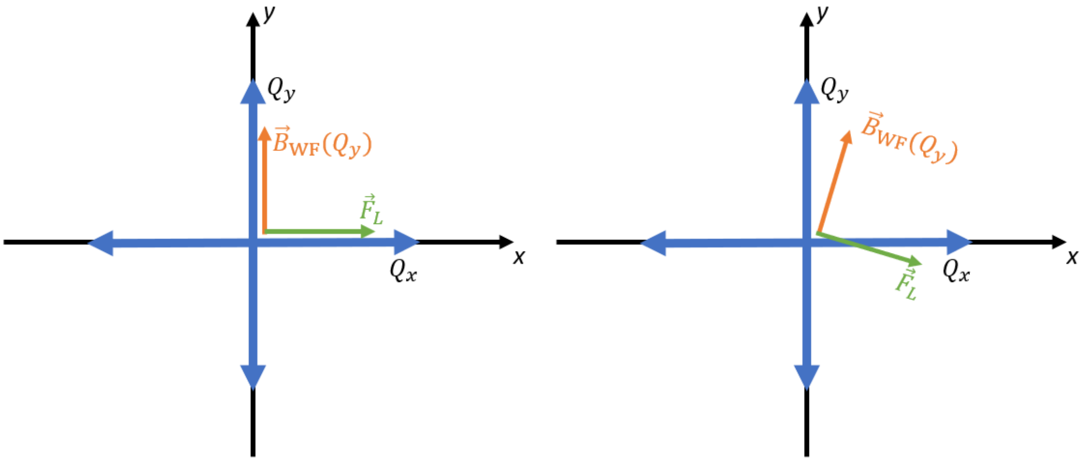

Figure 8.2.: Measuring scheme of the vertical magnetic field direction. The betatron oscillations take place in the vertical and horizontal directions. The vertical magnetic field oscillates with the same frequency as the vertical betatron tune. The Lorentz force points perpendicular to the vertical magnetic field. By rotating the Wien filter, the Lorentz force gets a vertical component which resonates with the vertical betatron tune.

For technical and cost reasons, protons are chosen to run the experiment. The plan is to maintain the operation of the RF Wien filter similar to that during the Precursor beam times with polarized deuterons. Since the RF Wien filter frequency during the Precursor beam times

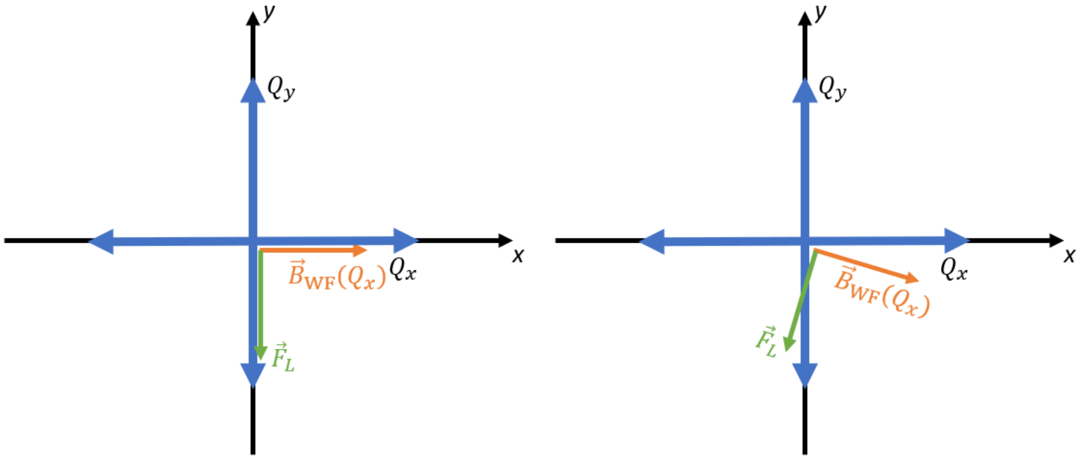

Figure 8.3.: Measuring scheme of the horizontal magnetic field direction. The betatron oscillations take place in the vertical and horizontal directions. The horizontal magnetic field oscillates with the same frequency as the horizontal betatron tune. The Lorentz force points perpendicular to the horizontal magnetic field. By rotating the Wien filter, the Lorentz force gets a horizontal component which resonates with the horizontal betatron tune.

is approximately 871 kHz, the momentum of the proton beam must be adjusted to match the betatron resonance with the RF Wien filter frequency. Assuming a tune of 0.56, the proton beam revolution frequency is 558 kHz, with a kinetic energy of 60 MeV, and the proton momentum at 341 MeV/c, with $\beta = 0.346$. At this proton energy, the corresponding electron energy for electron-cooled protons is around 34 keV for the 100 kV electron cooler. Operating at this energy automatically detunes the RF Wien filter due to different Lorentz β factors (0.346 vs. 0.459), allowing the RF Wien filter to be operated with the same parameters as in the Precursor runs. During all experiments, the RF Wien filter is powered at a power of 222 W.

8.3.2. Measurement of the Orientation of Betatron Planes

The main observable is the exponential loss of the number of particles when the RF Wien filter is switched on depending on the orientation of the magnetic field direction of the RF Wien filter with respect to the respective betatron oscillation plane. The loss of beam current is shown in Figure 8.5. The initial beam loss comes from the orbit correction and acceleration of the proton beam. At 45 s in the cycle, the RF Wien filter is switched on the resonance frequency of the betatron frequency which is supposed to be analyzed resulting in an extra loss. At 80 s in the cycle, the RF Wien filter is switched off. The beam current is saved at a rate of 10 Hz per second and for further analysis processed into bins of one second. The fit function is given by

$$N_p(t > t_{\mathrm{WF}}) = N_p(t = t_{\mathrm{WF}}) \exp(\tau t) + N_p(t = t_{\mathrm{WF\ Off}}). \tag{8.19}$$

The beam loss parameter is given by τ. To avoid a regression of an exponential model, the rebinned data is logarithmized changing the exponential fit model to

$$\begin{aligned} \ln(N_p(t > t_{\mathrm{WF}})) &= \ln\left(N_p(t = t_{\mathrm{WF}})\exp(\tau t) + N_p(t = t_{\mathrm{WF\ Off}})\right) && (8.20)\\ &= \tau t + \ln\left(N_p(t = t_{\mathrm{WF}}) \cdot N_p(t = t_{\mathrm{WF\ Off}})\right), && (8.21)\end{aligned}$$

i.e., a linear model where $\ln\left(N_p(t = t_{\mathrm{WF}}) \cdot N_p(t = t_{\mathrm{WF\ Off}})\right)$ denotes the offset and the beam loss rate τ denotes the slope. In consequence, the binned beam current data needs to be logarithmized

$$N_p \to \ln(N_p) \quad \text{and} \quad \sigma_{\ln(N_p)} = \frac{\sigma_{N_p}}{N_p}. \tag{8.22}$$

An example of the beam loss determined from logged binned beam current data is shown in Figure 8.6. To guarantee a stable fitting procedure of the beam loss, the latter method is used for data fitting.

To find the RF Wien filter frequency, the vertical and horizontal betatron tune is constantly measured at the following BPMs: 10, 20, and 22, which are marked in Figure 5.4. In Figure 8.4, an example of a tune measurement is shown at BPM 22 at 43 s in the cycle. The two panels show the frequency spectra for the horizontal and vertical tunes along with a Gaussian fit, to determine the value of the horizontal and vertical betatron tunes. The fit is performed during the measurement and saved to the COSY archiver. For a succesful measurement, the vertical and horizontal betatron tunes need to be well separated of the orientation of the RF Wien filter minimizing the beam loss rate.

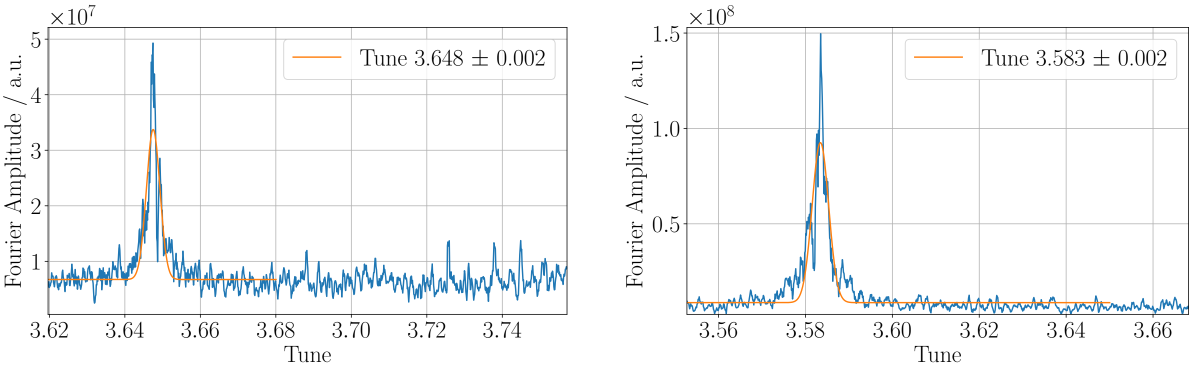

(a) Horizontal

(b) Vertical

Figure 8.4.: Example of tune measurements of the horizontal (left) and vertical (right) betatron tune at BPM 22 at 43 s in the cycle. The Fourier spectra are fitted using a Gaussian model to determine the horizontal and vertical tunes.

In Figure 8.7, the first measurement of the experimental method is shown. During this measurement, the magnetic field points in the horizontal direction, and the Wien filter frequency is adjusted to the horizontal betatron tune. The scenario corresponds to the sketch in Figure 8.3. A Wien filter rotation angle of 0 mrad as shown in Figure 8.7 points into the accelerator surface. By rotating the RF Wien filter out of the accelerator plane, the beam loss rate τ varies in a parabola. For each rotation angle of the RF Wien filter, the beam loss rate is measured three times. The data points show the average calculated from the single measurement cycles. For the measurements, the RF Wien filter direction was previously calibrated with respect to the COSY plane as described in section 7.5.. The uncertainty of the RF Wien filter rotation angle is given by $\sigma_{\phi^{\mathrm{WF}}} = 0.24\,\mathrm{mrad}$. The minimum beam loss rate is achieved at an RF Wien filter rotation angle of

$$\phi^{\mathrm{WF}}_{\mathrm{min.}} = (-5.9 \pm 0.5)\,\mathrm{mrad}, \tag{8.23}$$

for the Wien filter in MDM (=horizontal magnetic field) mode.

In Figure 8.8, the measurement with the magnetic field pointing perpendicular to the accelerator plane is shown. A Wien filter rotation angle of 0 mrad corresponds to a vertical magnetic field, which is the configuration of the RF Wien filter during the Precursor experiments. By rotating the vertical magnetic field, the beam loss rate was minimized at an angle of

$$\phi^{\mathrm{WF}}_{\mathrm{min.}} = (45.2 \pm 3.7)\,\mathrm{mrad} \tag{8.24}$$

for the Wien filter in EDM (=vertical magnetic field) mode. However, a minimum beam loss at such a large angle is nowhere close to what is expected from this measurement. Especially given, that the measurement of the Invariant Spin Axis during the Precursor runs shows no angles larger than 3 mrad is not possible. The source of this measurement result is most certainly a tilt of the betatron oscillation plane in the vertical direction, which contradicts the alignment precision which was achieved during the Beam-based alignment experiments. The results are further discussed in the following sections in which further systematic sources are studied.

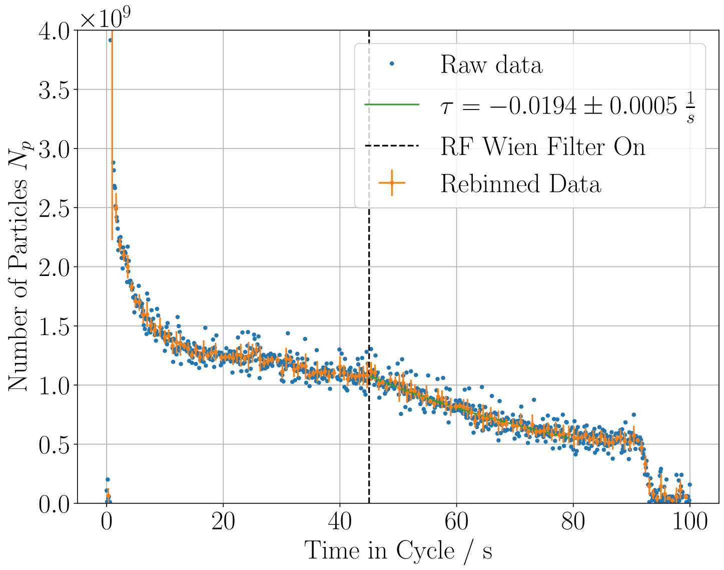

Figure 8.5.: The number of particles in the proton beam as a function of time in the cycle. The initial loss at the beginning of the cycle results from orbit correction and acceleration. At 45 seconds into the cycle, the RF Wien filter is switched on, and the exponential decrease of beam current starts. The beam loss rate depends on the magnetic field direction inside the RF Wien filter with respect to the corresponding betatron plane.

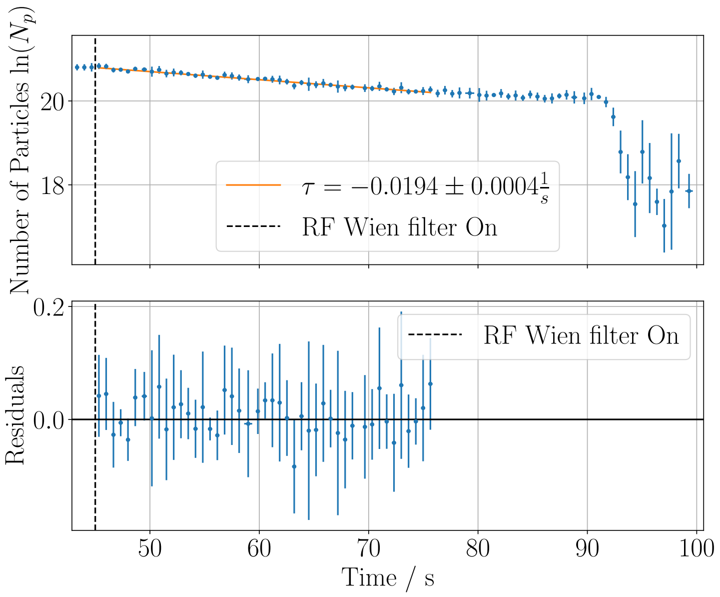

Figure 8.6.: Same as in Figure 8.5, but the beam current is logarithmized, resulting in a linear decrease of the beam current as a function of time. The lower panel shows the residuals of the linear fit as a function of time.

8.3.3. Scraper Studies

The method of exciting the betatron oscillations, which results in beam loss due to the acceptance limit of the beam pipe, relies on the geometrical acceptance of COSY. Using so-called beam scrapers, the acceptance limit of COSY is changed to rule out acceptance limit problems that might affect the result of the parabola minima seen in Figures 8.7 and 8.8. Using beam scrapers, the acceptance of COSY is reduced to ±15 mm. The result with the magnetic field of the RF Wien filter pointing in the vertical direction is shown in Figure 8.9. Due to the geometrical acceptance reduction, the beam loss rate is much higher compared to the measurements shown in the previous section. The parabola minimum is given by (42.6 ± 7.4) mrad, which matches with the previous result of (45.2 ± 3.7) mrad. Therefore, a geometrical limit of the acceptance of COSY cannot explain this large angle.

8.3.4. Measurement with Orbit Bumps in the First Arc after Injection

For further studies of the minimum beam loss rate as a function of the RF Wien filter rotation angle, the beam orbit is distorted in the first arc after injection using the following steerers: MSH9, MSH11, MSH13, and MSH17. The target of the orbit bump is the quadrupole QU4. The shift in orbit is shown in Figure 8.10. By changing the orbit, the betatron tunes are slightly changed. For a bump of -7.5 mm, the horizontal tune ($Q_x = 3.6298(14)$) matched the vertical tune ($Q_y = 3.6382(60)$), meaning that no measurement is possible as both betatron planes are excited by the RF Wien filter.

The RF Wien filter rotation angle at which the beam loss rate is minimized as a function of the orbit shifts is shown in Figure 8.11. All measurements are taken with a vertical magnetic

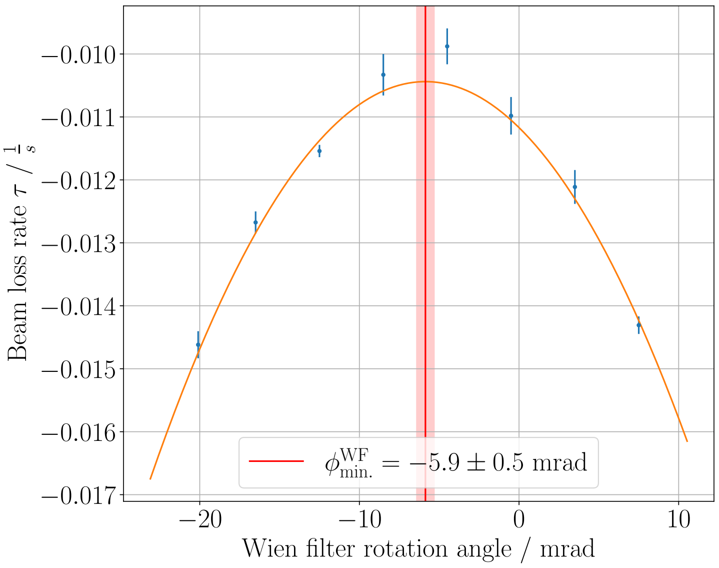

Figure 8.7.: The beam loss rate as a function of the RF Wien filter rotation angle. The magnetic field of the RF Wien filter points into the accelerator plane at an angle of 0 mrad (cf. Figure 8.3). The minimum beam loss rate occurs at an angle of (-5.9 ± 0.5) mrad.

field. A small dependence of a shift in the minimum rotation angle can be seen for large bump sizes. Further discussion is provided in the following chapter, where bumps at the location of the RF Wien filter are also presented.

8.3.5. Measurement with Orbit Bumps at the RF Wien Filter

Using the following steerers: SH43, SH01, SH05, SH07, SV02, SWBLW1, SV06, and SV08, orbit bumps are also applied at the location of the RF Wien filter. Parallel orbit bumps in the horizontal direction (cf. Figure E.1) and vertical direction (cf. Figure E.2), as well as angular bumps in the horizontal direction (cf. Figure 8.12) and vertical direction (cf. Figure E.3), are applied to study the effects in the minimum beam loss rate when rotating the magnetic field of the RF Wien filter. Since the applied orbit bumps are much smaller than the orbit bumps in the arc, the betatron tunes only change slightly. The vertical and horizontal betatron tunes are given by

$$Q_y = 3.6201(12) \text{ and } Q_x = 3.5460(09). \tag{8.25}$$

The RF Wien filter frequency is given by 870 227 Hz. All measurements are taken with a vertical magnetic field.

The RF Wien filter rotation angle for which the beam loss parameter is minimized as a function of the applied beam bumps is shown in Figure 8.13. Even though the orbit changes are relatively small, the effects on the beam loss rate minimum are drastic. The strongest dependence is seen when changing the horizontal beam tilt angle at the location of the RF Wien filter. Changes in the beam tilt angle of 2 mrad lead to a change of the minimum angle of 150 mrad. Also,

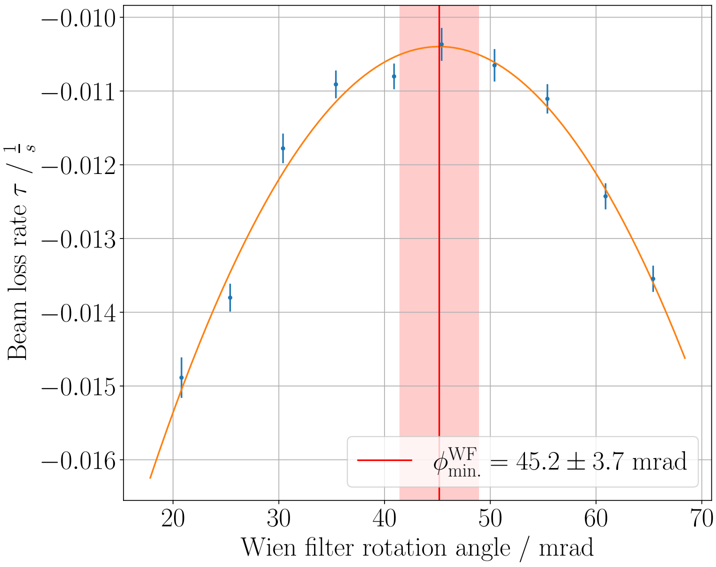

Figure 8.8.: The beam loss rate as a function of the RF Wien filter rotation angle. The magnetic field of the RF Wien filter points perpendicular to the accelerator plane at an angle of 0 mrad (cf. Figure 8.2). The minimum beam loss rate occurs at an angle of (45.2 ± 3.7) mrad.

horizontal orbit bumps lead to a change of the beam loss rate minimum Wien filter rotation angle. Vertical orbit bumps don't have an effect.

At the moment, it is not clear where the strong behavior comes from. As can be seen in the orbit change plots (cf. Figure E.1 - E.3), the orbit bumps are not clean orbit bumps at the location of the RF Wien filter but also affect the orbit before and after the RF Wien filter. On the other hand, problems with the RF Wien filter field direction cannot be excluded. Extensive beam simulations, which are not part of this work, could help resolve the problem of the strong dependence of the shifts in the minimum of the beam loss parameter as a function of the Wien filter rotation angle.

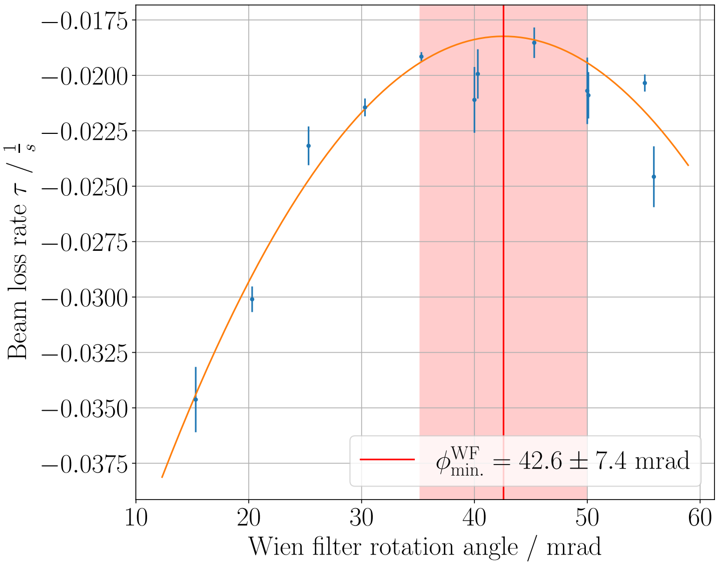

Figure 8.9.: The beam loss rate as a function of the Wien filter rotation angle is shown. The beam pipe acceptance is reduced to ±15 mm by using beam scrapers. The magnetic field of the RF Wien filter points perpendicular to the accelerator plane at an angle of 0 mrad (cf. Figure 8.2). The minimum beam loss rate occurs at an angle of (42.6 ± 7.4) mrad.

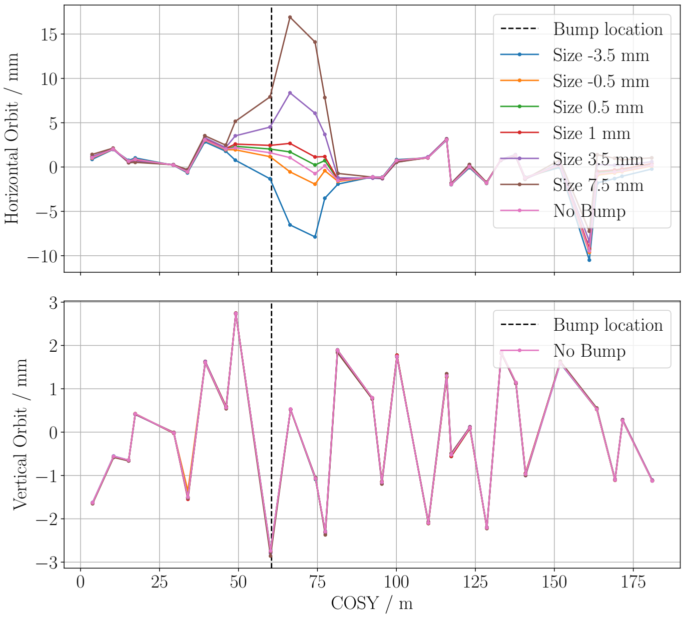

Figure 8.10.: Horizontal orbit bumps in the first arc after injection are used to systematically study the effect on the betatron plane minimum. The bump target is Quadrupole QU4, using the following steerers: MSH9, MSH11, MSH13 and MSH17.

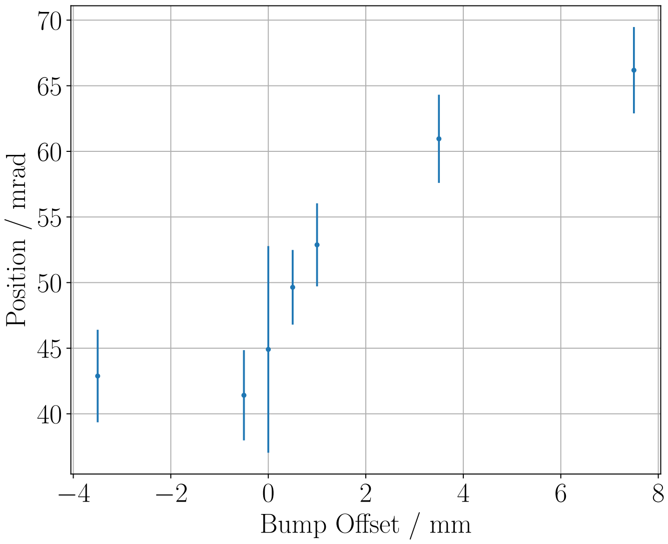

Figure 8.11.: The RF Wien filter rotation angle at which the beam loss rate is minimized as a function of the orbit bump in the first arc at the quadrupole QU4 is shown. A small dependence appears for increasing bump size.

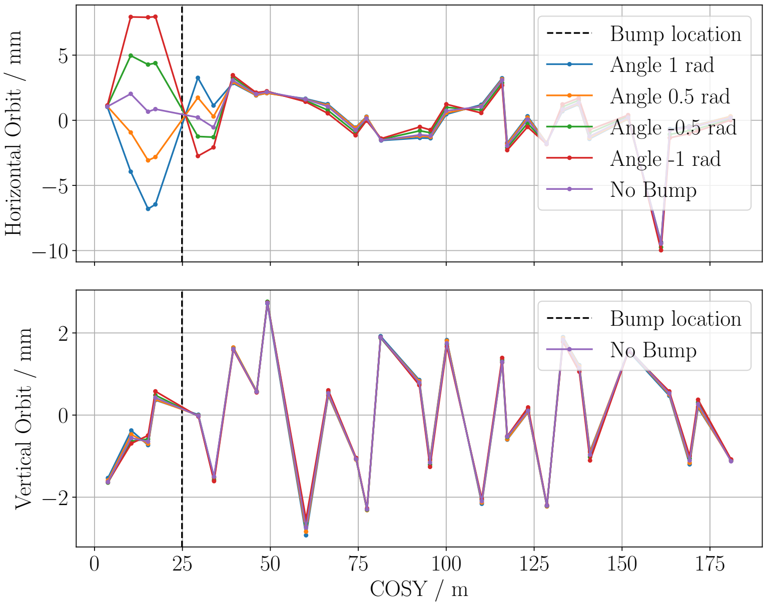

Figure 8.12.: Horizontal orbit bump angles at the RF Wien filter using the following steerers: SH43, SH01, SH05, and SH07.

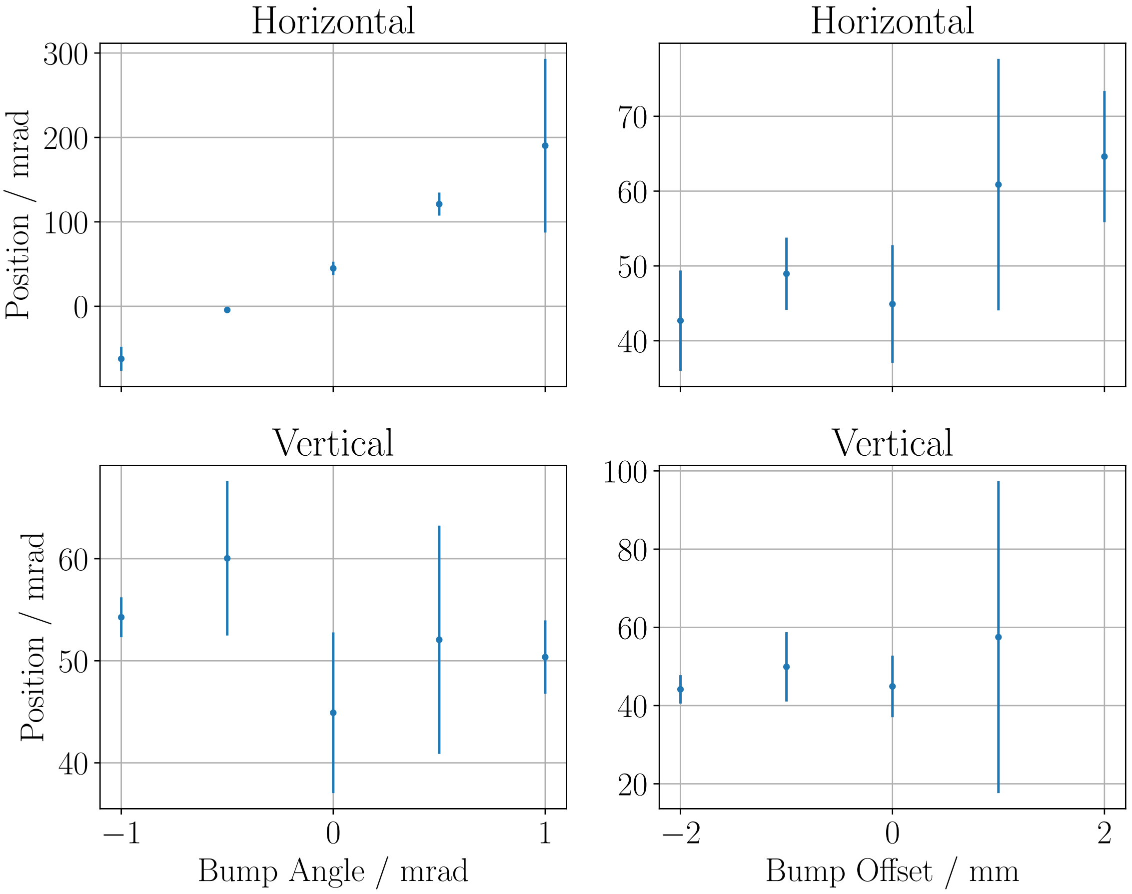

Figure 8.13.: Dependence of the minimum of the beam loss rate parameter as a function of the RF Wien filter rotation angle for different orbit bumps at the location of the RF Wien filter. The strong dependence for horizontal orbit shifts and angles remains unclear and could either come from the orbit deviations or unknown RF Wien filter field components.

9. Results

Extensive beam and spin tracking simulations, which include misalignments of magnets and the settings of all relevant devices for the experiments described in this thesis, have shown that the longitudinal and radial components of the Invariant Spin Axis in COSY cannot be larger than 1 mrad [104]. Given that the longitudinal tilt of the Invariant Spin Axis at the 2MV solenoid, located 8 m in front of the RF Wien filter, is well below a tenth of a mrad, it can be assumed that the large longitudinal tilts, which are on the order of a few mrad, are dominated by systematic errors. Consequently, this also affects the results of the radial component.

As shown in Eq. (7.46), using the RF Wien filter, the angle between the Invariant Spin Axis and the magnetic field axis of the RF Wien filter is measured. Unfortunately, no experimental data is available on the direction of the magnetic field in the RF Wien filter. Only simulations have been performed, indicating that the possible relative field errors in the perpendicular direction are in the range of 1×10^{-3} with respect to the full field integral [90]. Consequently, this relative field uncertainty corresponds to a systematic error of 1 mrad for the direction of the magnetic field in the longitudinal direction. However, these simulations correspond to the case with installed ferrites, which were not used in the actual experiment. Further simulations without the ferrite cage were not possible during the course of these studies.

Due to the shutdown of COSY in October 2023, it was not possible to perform additional studies of the RF Wien filter, such as conducting the experiment with the ferrite cage, which was initially intended to be installed at the RF Wien filter. Simulations have shown that the ferrite cage significantly impacts the homogeneity of the magnetic field in the RF Wien filter [88].

Assuming that the tilts of the Invariant Spin Axis are dominated by systematic effects of the RF Wien filter, the measured tilt can be used to determine the first direct limit of the deuteron Electric Dipole Moment. The measured tilt, and consequently the systematic uncertainty of the measured tilts in radial and longitudinal direction, is given by

$$n_{z,\text{avg.}} \mathrel{\hat{=}} \sigma_{n_{z,\text{sys.}}} \mathrel{\hat{=}} \sigma_{n_{x,\text{sys.}}} = -0.0055\,\text{rad}. \tag{9.1}$$

Using Eq. (4.41) and the values given in Table 7.1, the dimensionless η factor can be calculated as

$$\eta_{\text{EDM}} = \frac{2\phi_{\text{EDM}}G}{\beta} \Rightarrow |\eta_{\text{EDM}}| < 0.0067\ (95\,\%\ \text{C.L.}). \tag{9.2}$$

From the dimensionless η_{EDM} factor, a first limit of the deuteron Electric Dipole Moment is determined using Eq. (2.13)

$$d^d = \eta_{\text{EDM}}\frac{q\hbar}{2mc} \Rightarrow |d^d| < 2.2 \times 10^{-16}\,\text{e} \cdot \text{cm}\ (95\,\%\ \text{C.L.}). \tag{9.3}$$

Without further studies, it is not possible to reduce the systematic error ($\mathcal{O}(1\,\mathrm{mrad})$) to the same order of magnitude as the statistical uncertainty of the individual measurements ($\mathcal{O}(0.1\,\mathrm{mrad})$) by further investigating systematic uncertainties of the magnetic field direction of the RF Wien filter.

It is worth noting that the precision is still remarkable, given the fact that 30 years ago, nobody planned to do precision experiments at COSY, such as the measurement of the Electric Dipole Moment of the deuteron. Especially, when comparing these results with the latest upper limits of the muon Electric Dipole Moment measured by the g−2 collaboration [15]

$$|d^{\mu}| < 1.9 \times 10^{-19}\,\mathrm{e} \cdot \mathrm{cm}\ (95\,\%\ \mathrm{C.L.}), \tag{9.4}$$

which use a dedicated muon storage ring for precision experiments.

In addition, further systematic uncertainties can be reduced using counter and counterclockwise beams in dedicated proton and deuteron Electric Dipole Moment storage rings as described in section 10.2.

10. Outlook

The following sections describe alternative methods for measuring the Electric Dipole Moment of charged elementary particles. In section 10.1, a method based on static Wien filters is discussed, which can be applied in any magnetic ring providing polarized beams. In section 10.2, a new generation of storage rings dedicated to measurements of Electric Dipole Moments of charged elementary particles is presented. These rings are designed to minimize the influence of the Magnetic Dipole Moment on spin motion, thus being sensitive only to changes in polarization due to the Electric Dipole Moment.

10.1. Determination of the Electric Dipole Moment using Static Solenoids

The radial component of the Invariant Spin Axis can also be measured using a static Wien filter as described in section C.1. By providing a radial magnetic field, the scalar product of the Invariant Spin Axis and the magnetic field of the solenoid, as described in Eq. (7.18), gives the radial component of the Invariant Spin Axis. To avoid orbit distortions, the magnetic field needs to be compensated by an electric field to cancel out the Lorentz force. In this case, the Wien filter can be operated statically. By changing the magnetic field, the spin tune changes as a function of the magnetic field, similar to the data shown in Figure 7.12.

By providing a static magnetic field, the field components can be measured using Hall probes to determine unwanted magnetic field components. Additionally, a static Wien filter does not need to be rotated around the beam pipe to measure the radial component of the Invariant Spin Axis. The measurement period would be on the order of an hour, compared to the measurements using the RF Wien filter, which takes approximately a day. However, a downside is that only the radial component can be measured, not both the radial and longitudinal components simultaneously.

10.2. Staged Storage Ring Approach

In principle, the search for Electric Dipole Moments of charged elementary particles in storage rings can be carried out using two distinct methods. The first method described in this thesis is the resonant method using the RF Wien filter. A second method, called the frozen spin method, is based on canceling all effects from the Magnetic Dipole Moment. By setting the contributions to the spin motion of the magnetic dipole to zero, the spin motion is only sensitive to the Electric Dipole Moment. For completeness, the Thomas-BMT equation is given again, as in section 4.2, which describes the spin motion of a particle propagating in external magnetic $\vec{B}$ and electric $\vec{E}$ fields

$$\frac{\mathrm{d}\vec{S}}{\mathrm{d}t} = \vec{\Omega}_{\mathrm{MDM}} \times \vec{S} + \vec{\Omega}_{\mathrm{EDM}} \times \vec{S}, \tag{10.1}$$

$$\vec{\Omega}_{\mathrm{MDM}} = -\frac{q}{m}\left[\left(G+\frac{1}{\gamma}\right)\vec{B} - \frac{G\gamma}{\gamma+1}\left(\vec{\beta}\cdot\vec{B}\right)\vec{\beta} - \left(G+\frac{1}{\gamma+1}\right)\vec{\beta}\times\frac{\vec{E}}{c}\right], \tag{10.2}$$

$$\vec{\Omega}_{\mathrm{EDM}} = -\frac{q}{mc}\frac{\eta_{\mathrm{EDM}}}{2}\left[\vec{E} - \frac{\gamma}{\gamma+1}\left(\vec{\beta}\cdot\vec{E}\right)\vec{\beta} + c\vec{\beta}\times\vec{B}\right]. \tag{10.3}$$

In this equation, $\vec{S}$ denotes the spin vector in the particle rest frame, t denotes the time in the laboratory system, $\vec{\beta}$ denotes the velocity with respect to the speed of light, and γ denotes the Lorentz factor. The dimensionless quantities G and η are linked to the magnetic moment $\vec{\mu}$ and Electric Dipole Moment $\vec{d}$

$$\vec{\mu} = g\frac{q\hbar}{2m}\vec{S} = (1+G)\frac{q\hbar}{m}\vec{S} \quad \text{and} \quad \vec{d} = \eta_{\mathrm{EDM}}\frac{q\hbar}{2mc}\vec{S}. \tag{10.4}$$

Assuming only vertical magnetic fields and radial electric fields which are perpendicular to the beam momentum vector ($\vec{\beta}\cdot\vec{B} = \vec{\beta}\cdot\vec{E} = 0$), the Thomas-BMT equation can be further simplified to

$$\frac{\mathrm{d}\vec{S}}{\mathrm{d}t} = \left(\vec{\Omega}_{\mathrm{MDM}} + \vec{\Omega}_{\mathrm{EDM}}\right) \times \vec{S}, \tag{10.5}$$

$$\vec{\Omega}_{\mathrm{MDM}} = -\frac{q}{m}\left[\left(G+\frac{1}{\gamma}\right)\vec{B} - \left(G+\frac{1}{\gamma+1}\right)\vec{\beta}\times\frac{\vec{E}}{c}\right], \tag{10.6}$$

$$\vec{\Omega}_{\mathrm{EDM}} = -\frac{q}{mc}\frac{\eta_{\mathrm{EDM}}}{2}\left[\vec{E} + c\vec{\beta}\times\vec{B}\right]. \tag{10.7}$$

As already introduced in section 4.2.1, due to the Magnetic Dipole Moment component, the polarization of the particles oscillates in the plane of the storage ring relative to the beam path. This rotation can be suppressed by matching the contribution of the Magnetic Dipole moment to the equation of motion, Ω_{MDM}, to the cyclotron frequency

$$\vec{\Omega}_{\mathrm{rev}} = -\frac{q}{\gamma m}\left(\vec{B} - \frac{\vec{\beta}\times\vec{E}}{\beta^2 c}\right). \tag{10.8}$$

When the rotation of the polarization due to the Magnetic Dipole Moment component matches with the revolution frequency $\left(\vec{\Omega}_{\mathrm{rev}} = \vec{\Omega}_{\mathrm{MDM}}\right)$, the so-called frozen spin condition is fulfilled, which means that the polarization vector is fixed with respect to the momentum vector. The frozen spin condition can be written as

$$\vec{\Omega}_{\mathrm{MDM}} - \vec{\Omega}_{\mathrm{rev}} = -\frac{q}{m}\left[G\vec{B} - \left(G - \frac{1}{\gamma^2-1}\right)\frac{\vec{\beta}\times\vec{E}}{c}\right] \overset{!}{=} 0. \tag{10.9}$$

Note that in a pure magnetic ring ($\vec{E} = 0$), the frozen spin condition can not be reached as the magnetic fields, the anomalous gyromagnetic g-factor G and the Lorentz factor can not be zero

$$G\vec{B}\gamma \overset{!}{=} 0 \;\lightning. \tag{10.10}$$

In principle, there are two ways to reach the frozen spin condition. In an all-electric ring without any magnetic fields, the frozen spin condition can be further reduced to

$$\vec{\Omega}_{\text{MDM}} - \vec{\Omega}_{\text{rev}} = \frac{q}{m}\left(G - \frac{1}{\gamma^2 - 1}\right)\frac{\vec{\beta} \times \vec{E}}{c} \overset{!}{=} 0. \tag{10.11}$$

The frozen spin condition is fulfilled, when

$$G - \frac{1}{\gamma^2 - 1} \overset{!}{=} 0 \quad \Rightarrow \quad p_{\text{magic}} = \frac{mc}{\sqrt{G}}. \tag{10.12}$$

The particles' momentum fulfilling the frozen spin condition in an all-electric ring is called magic momentum. In the case of protons, the magic momentum is given by 0.7 GeV/c. Note that this method only works for particle species which have a positive anomalous magnetic moment G.

When studying the Electric Dipole Moment of particles with a negative anomalous magnetic moment G, a second option for the frozen spin condition can be chosen. By choosing the strength of the vertical magnetic field as

$$B = E \cdot \frac{\beta^2\gamma^2 G - 1}{c\beta\gamma^2 G}, \tag{10.13}$$

for each chosen energy, there exists a set of vertical magnetic and radial electric field strengths such that the frozen spin condition (cf. Eq. (10.9)) holds.

An additional requirement for the next generation of storage rings for an Electric Dipole Moment measurement is clockwise and counter-clockwise circulating beams. Systematic contributions resulting from imperfections in the magnetic field and misalignments of the device cause a tilt of the Invariant Spin Axis. Consequently, these factors can introduce a vertical polarization buildup unrelated to the Electric Dipole Moment. Specifically, unwanted radial magnetic fields, interacting with the Magnetic Dipole Moment, contribute to the buildup of the vertical polarization component. To solve this issue, measurements employing both clockwise and counter-clockwise beams within the same storage ring are planned. In an all-electric ring with pure electric fields, both beams would follow the same closed orbit. However, the impact of radial magnetic fields differs for clockwise and counter-clockwise beams. As a result, these fields induce a splitting of the vertical orbit for both beams, which can be detected using beam position monitors.

10.2.1. Prototype EDM Ring

Discussions within the CPEDM [113] collaboration led to the conclusion that before building the final all-electric ring dedicated to the measurement of the proton Electric Dipole Moment, a smaller ring, also called a prototype ring, shall be built. It is supposed to be a small and cost-effective ring design (circumference ≈ 100 m). The prototype Electric Dipole Moment ring would operate in two stages. In the first stage, it would run as an all-electric ring with a proton kinetic energy of $T = 30\,\mathrm{MeV}$. The main goals of this stage of the ring are gaining experience in operating a large-scale high-electric-field electrostatic storage ring and demonstrating the ability to produce and manipulate two polarized beams, each with an intensity of 10^9 particles, simultaneously countercirculating in the same ring. During the second stage, the bends encompass an additional magnetic component, and the kinetic energy is increased to 45 MeV for the frozen-spin condition. This stage allows for the proof of concept of the frozen-spin method. Note that this mode allows only one beam in the accelerator at a time. However, it is still possible to flip the magnetic field after each fill and do another cycle with a beam circulating in the opposite direction to cancel out systematic errors. In such a ring, the first direct proton Electric Dipole Moment measurement could be carried out [86]. A possible layout of the prototype ring is shown in Figure 10.1.

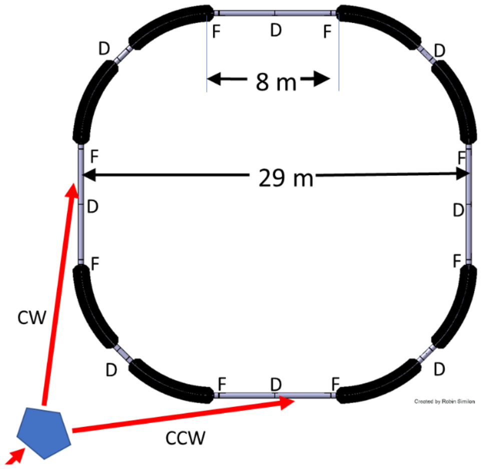

Figure 10.1.: The basic concept of the prototype ring involves eight dual superimposed bends, each incorporating both electric and magnetic elements, along with two families of quadrupoles denoted as F (focusing) and D (defocusing). The overall circumference of the prototype ring is approximately 100 m. Taken from [86].

10.2.2. Final Proton EDM Storage Ring

After gaining experience from the prototype EDM ring, the final dedicated proton Electric Dipole Moment machine is planned with a circumference of approximately 600 m. The ring accelerates protons to the magic momentum and features only electric bending elements. The anticipated sensitivity for the proton Electric Dipole Moment limit is in the order of $1 \times 10^{-29}\,\mathrm{e \cdot cm}$. Two counter-rotating beams of protons are simultaneously circulating in the ring. The most important characteristics of the prototype and all-electric Electric Dipole Moment storage rings and accelerators are summarized in Table 10.1 [86].

Table 10.1.: Parameters of the storage rings of the three staged approach of measuring EDMs of charged elementary particles.

	COSY	Prototype Ring	Final ring
mode	resonant (RF Wien filter)	frozen spin	frozen spin
particle	deuteron	proton	proton
circumference / m	184	~ 100	~ 600
bending elements	magnetic	magnetic / electric	electric
bending radius / m	7	~ 8.86	50
bending field	1.7 T	7 MV/m + 30 mT	8 MV/m
# beams	1	2 or 1	2
E / MeV	2111	30 or 45	1175
p / MeV/c	970	239 or 294	700.7 (magic)

11. Summary

The Electric Dipole Moment remains a topic of high interest in the experimental physics community, as it could help answer the unexplained matter-antimatter asymmetry and contribute to understanding the existence of our universe. Even though many scientists and various collaborations are improving their statistical and systematic sensitivities, no finite experimental signature of an Electric Dipole Moment has been measured so far.

This thesis outlines the first direct measurement of the deuteron Electric Dipole Moment. The goal of the experiment is to measure the influence of the Electric Dipole Moment on the polarization of a deuteron beam rotating in a storage ring. A measurement of the orientation of the so-called Invariant Spin Axis results in the first direct measurement of the deuteron Electric Dipole Moment.

In November 2018 and March 2021, two experimental runs, called Precursor Run 1 and Precursor Run 2, were conducted by the JEDI collaboration at the Cooler Synchrotron COSY at Forschungszentrum Jülich to measure the orientation of the Invariant Spin Axis by mapping the buildup of the vertical polarization induced by the RF Wien filter. The RF Wien filter-induced buildup is directly proportional to the cross product of the Invariant Spin Axis and the magnetic field axis of the RF Wien filter.

To probe the Invariant Spin Axis, the RF Wien filter is rotated around the beam pipe, which changes the direction of the magnetic field axis in the positive and negative radial directions. In addition, a Siberian snake is installed in the opposite straight section, which is used to change the orientation of the Invariant Spin Axis in the longitudinal direction at the location of the RF Wien filter. The rotation angle of the RF Wien filter and the rotation angle of the Invariant Spin Axis in the Siberian snake that lead to a zero buildup of the vertical polarization correspond to the orientation of the Invariant Spin Axis at the location of the RF Wien filter. The averaged tilts of the Invariant Spin Axis for the first Precursor experiment are given by

$$n_{x,\text{avg.}}^{\text{Prec. 1}} = -3.6(3)\,\text{mrad and } n_{z,\text{avg.}}^{\text{Prec. 1}} = -5.5(5)\,\text{mrad}, \tag{11.1}$$

and for the second Precursor experiment by

$$n_{x,\text{avg.}}^{\text{Prec. 2}} = -2.1(12)\,\text{mrad and } n_{z,\text{avg.}}^{\text{Prec. 2}} = 3.9(6)\,\text{mrad}. \tag{11.2}$$

During the last few years, extensive spin and beam tracking simulations have been performed to study both beam and spin dynamics in the ring. Assuming that the simulated data are still in reasonable agreement with measured observables like orbit and steerer settings from the real experiment, no larger tilts than 1 mrad in radial and longitudinal directions of the Invariant Spin Axis could be found. In most simulations, the tilts were even smaller.

Many improvements in COSY between both experiments have been performed to further reduce the systematic errors. Physical misalignments of the magnets in COSY have been measured and corrected by moving the magnets. In addition, the beam-based alignment helped to calibrate the position of beam position monitors with respect to the measured quadrupole positions. Lastly, the matching of the electromagnetic fields in the RF Wien filter has been improved by implementing a new online monitoring system. Even though this improvement led to much better experimental conditions, the apparent tilts of the Invariant Spin Axis remained in the same order of magnitude. The only striking difference is the sign change of n_z from the run in 2018 to the run in 2021, which remains unexplainable.

To determine the orientation of the Invariant Spin Axis, a least-squares fit is performed to the buildup rate of the vertical polarization. The quality of these fits is rather poor and is a strong indicator that systematic effects are not included in the fit. However, the buildup rate was also measured very close to the point where no buildup is expected, which means that the measured Invariant Spin Axis corresponds to the settings of the RF Wien filter and the Siberian snake where indeed no buildup is measured. This is a strong indicator that the method itself works.

The results of the large tilts of the Invariant Spin Axis are also contradicting measurements of the Invariant Spin Axis at other locations in COSY. Static solenoids offer the possibility to measure the longitudinal direction of the Invariant Spin Axis at the location of the solenoids. In total, two solenoids have been used to perform these measurements, namely the Siberian snake and the 2 MV solenoid. The main results are given by

$$n_z^{\text{Snake}} = 0.53(2)\,\text{mrad}, \tag{11.3}$$

for the first Precursor Run and

$$n_z^{\text{Snake}} = -0.057(1)\,\text{mrad and } n_z^{\text{2MV Sol.}} = -0.0705(9)\,\text{mrad}, \tag{11.4}$$

for the second Precursor Run. These tilts are drastically smaller than the tilts of the Invariant Spin Axis at the location of the RF Wien filter. In addition, the tilt angle is reduced by an order of magnitude, which is most likely related to the improvements of the storage ring between both experimental periods. This is a remarkable result as in an ideal machine no tilts of the Invariant Spin Axis are expected in longitudinal direction.

In principle, multiple scenarios could explain these results:

Unwanted additional longitudinal fields do not affect the orbit, as they are parallel to the beam momentum vector. However, like artificial solenoids, unwanted longitudinal fields lead to extra rotations of the Invariant Spin Axis in the longitudinal direction. These tilts would be of the same order of magnitude all around the ring and, consequently, at the position of the RF Wien filter, the Siberian snake, and the 2 MV solenoid, contradicting the measurement of the longitudinal component at those devices. There is the possibility of two counteracting and compensating longitudinal fields before and after the RF Wien filter, which lead to large tilts in the longitudinal direction. However, given the magnetic design of COSY, this scenario is highly unlikely.

It can be shown that beam tilts and tilts of the RF Wien filter have an influence on the apparent measured longitudinal component of the Invariant Spin Axis at the location of the RF Wien filter, while the radial component remains unaffected (assuming a homogeneous field). Unfortunately, there is no beam position measurement available at the location of the RF Wien filter, and a tilt angle of the device itself is also unknown. However, a large contribution of the effects on the measured Invariant Spin Axis can most certainly still be excluded, as otherwise, the tilts of the Invariant Spin Axis in both directions wouldn't be in the same order of magnitude.

A final possibility is tilts of the magnetic field axis inside the RF Wien filter itself. During the experiment, a full knowledge of the magnetic field axis of the RF Wien filter is assumed. However, there is no experimental data available to underline these assumptions, as the Wien filter field cannot be easily measured. There are simulations available which test the relative field errors with respect to geometrical misalignments of the RF Wien filter. The simulation led to a systematic uncertainty of the tilt of the magnetic field in the longitudinal direction of 1 mrad. However, initially, the RF Wien filter was planned with an additional ferrite cage around the device which further stabilizes the homogeneity of the magnetic field. These simulations were done with the ferrites, which were never used in the real experiment. To understand the measured tilts of the Invariant Spin Axis at the location of the RF wien filter, the misalignment of the magnetic field have to be in the order of several millirad.

Given these facts, the most likely scenario is that the results of the tilts of the Invariant Spin Axis at the location of the RF Wien filter are dominated by systematic errors. Therefore, these measured tilts are assumed to be purely systematic, which leads to a first limit of the permanent deuteron Electric Dipole Moment of

$$|d^d| < 2.2 \times 10^{-16}\,\mathrm{e} \cdot \mathrm{cm}\ (95\,\%\ \text{C.L.}). \tag{11.5}$$

Appendices

A. Physical Offsets of the Beam Position Monitors

Using the Beam-Based Alignment method, the physical alignment of the BPMs with respect to the magnetic center of the quadrupoles was determined between Precursor 1 & 2. To compare both orbits, the values have to be subtracted from the Precursor 1 data as shown in Figure 7.38.

Table A.1.: BPM offsets determined during the Beam-Based alignment [69].

BPM Name	**Horizontal Offset (mm)**	**Vertical Offset (mm)**
1	1.127	-0.754
2	0.690	0.736
3	0.213	3.839
4	-0.259	2.526
6	1.033	3.642
7	1.915	1.077
8	3.699	2.217
9	2.357	0.165
10	0.457	1.303
11	1.532	-0.795
12	5.764	0.337
13	1.865	1.914
14	1.662	-0.258
15	1.750	0.320
16	2.096	-1.555
17	1.254	0.837
18	4.444	1.178
19	1.551	3.570
ecolgun	2.0	-1.3
ecolcol	1.0	-0.7
20	2.470	0.016
anke2	1.233	0.175
21	0.982	1.468
22	1.907	0.540
23	-2.050	-0.477
24	0.738	0.667
25	-20.203	-
26	1.468	-0.849
27	2.170	-0.161
28	2.282	-2.622
29	3.671	-2.435

B. Constraints on the Cycle Selection for the Measurements of the Invariant Spin Axis

B.1. Steerer Setting Margins for the Deuteron EDM Precursor experiments

Stable conditions throughout the experiment are essential for accurately determining the Invariant Spin Axis. The steerers, used to correct the orbit to closely match the design orbit, are connected to power supplies that occasionally fail to ramp the steerer magnets properly. For both experiments, the range of acceptable readbacks for each steerer magnet power supply is determined by analyzing the distribution of steerer currents for each cycle. The ranges are listed in Table B.1 and B.2.

Table B.1.: Steerer Boundaries for the two experiments. The values are given in % where 100 % stands for a maximum deflection angle of 15 mrad.

	Precursor 1		Precursor 2	
Steerer Name	**Lower Bound**	**Upper Bound**	**Lower Bound**	**Upper Bound**
SV02	−5.7336	−5.7261	2.57	2.61
SVBLW1	−0.5694	−0.5668	−1.05	−1.02
SVBLW4	−0.0495	−0.0455	1.39	1.415
SV06	−0.6575	−0.6477	1.525	1.55
SV08	5.3075	5.3263	−0.405	−0.395
SV10	0.5569	0.5634	−0.37	−0.34
SV12	0.2085	0.2264	−0.565	−0.535
SV14	−0.1948	−0.1759	0.93	0.97
SV16	No Value	No Value	1.74	1.79
SV18	1.4919	1.5004	−0.85	−0.825
SV20	12.1769	12.1825	−0.59	−0.575
SV22	−9.3632	−9.3453	0.475	0.49
SV24	20.2	20.5	0.19	0.215
SV100KEVGUN	11.8676	11.8747	9.3	9.45
SV100KEVCOL	14.8500	14.8567	8.7	8.85
SV26	18.0127	18.0207	1.82	1.87
SV28	1.2385	1.2471	0.37	0.38
SV30	2.7274	2.7391	−0.6	−0.56
SV32	−0.3647	−0.3545	−0.555	−0.535
SV34	No Value	No Value	−1.6	−1.54
SV36	0.9457	1.0116	−2.9	−2.65
SV38	−3.7251	−3.7198	1.45	1.48

Table B.2.: Steerer Boundaries for the two experiments. The values are given in % where 100 % stands for a maximum deflection angle of 15 mrad.

	Precursor 1		Precursor 2	
Steerer Name	**Lower Bound**	**Upper Bound**	**Lower Bound**	**Upper Bound**
SH41	3.8765	3.8955	4.190	4.197
SH43	No Value	No Value	2.8425	2.8452
SH01	−2.2445	−2.2308	5.0	5.055
SHBLW2	2.3719	2.3847	−2.7	−2.6
SHBLW3	−0.0479	−0.0420	1.69	1.715
SH05	2.3457	2.3687	−0.55	−0.53
SH07	3.4304	3.4538	2.78	2.84
SH09	1.0801	1.0970	−1.56	−1.51
SH11	11.4863	11.4908	1.92	1.97
SH13	4.1188	4.1256	3.0	3.04
SH17	0.0088	0.0398	−11.3	−10.9
SH19	15.1994	15.2199	5.8	5.9
SH21	5.8829	5.9244	−1.4	−1.3
SH23	8.1248	8.1297	−6.18	−6.02
SH100KEVGUN	2.9204	2.9377	5.0	5.1
SH100KEVCOL	2.9340	2.9472	8.9	9.25
SHBLWD1	0.3568	0.3762	13.2	13.5
SHBLWD3	−0.4005	−0.3811	−6.65	−6.45
SH27	0.0411	0.0765	−5.2	−4.9
SH29	−4.0646	−4.0408	−0.2	−0.19
SH31	1.9332	1.9532	1.24	1.27
SH33	2.4276	2.4453	−5.25	−5.1
SH35	3.5447	3.5631	2.725	2.765
SH37	4.6282	4.6458	−0.245	−0.235
SH39	1.5454	1.5636	0.935	0.955

B.2. BPM Value Margins for the Deuteron EDM Precursor experiments

In addition to the steerer values, the orbit is continuously monitored through Beam Position Monitor readings, which are stored in the local COSY Archiver. If a BPM reading falls outside a predefined margin, the cycle is discarded. The ranges are determined by analyzing the distribution of the measured beam position for all cycles during the experiment. The accepted range for each beam position monitor in the horizontal and vertical direction is listed in Tables B.3 and B.4. If no value is available, the readings were not successfully saved to the archiver or the Beam Position Monitor didn't work.

Table B.3.: Margins of the accepted range for each Beam Position Monitor measuring the horizontal beam position are given below. All values are in mm.

	Precursor 1		Precursor 2	
BPM Name	**Lower Bound**	**Upper Bound**	**Lower Bound**	**Upper Bound**
bpmx01	−3.597	−3.397	−0.061	0.139
bpmx02	−0.105	0.095	−0.070	0.130
ecbpmx113	0.105	0.305	−0.551	−0.351
ecbpmx114	−1.391	−1.191	0.618	0.818
bpmx51	−0.833	−0.633	No Value	No Value
bpmx52	No Value	No Value	No Value	No Value
bpmx06	No Value	No Value	0.201	0.401
bpmx07	0.541	0.741	−0.325	−0.125
bpmx08	No Value	No Value	−0.065	0.135
bpmx09	−0.106	0.094	−0.206	−0.006
bpmx10	−1.048	−0.848	−0.200	0.000
bpmx11	0.734	0.934	0.010	0.210
bpmx12	−0.684	−0.484	−0.048	0.152
bpmx13	0.699	0.899	−0.068	0.132
bpmx14	0.399	0.599	−0.230	−0.030
bpmx15	−0.028	0.172	−0.034	0.166
bpmx16	−0.434	−0.234	−0.483	−0.283
bpmx17	−0.221	−0.021	−0.460	−0.260
bpmx18	0.402	0.602	0.342	0.542
bpmx19	−0.998	−0.798	0.580	0.780
becx01	0.738	0.938	−0.461	−0.261
becx02	−0.345	−0.145	−0.589	−0.389
bpmx20	−1.429	−1.229	0.479	0.679
banx01	0.666	0.866	No Value	No Value
banx02	No Value	No Value	0.072	0.272
bpmx21	−0.593	−0.393	0.017	0.217
bpmx22	−0.139	0.061	−0.280	−0.080
bpmx23	−1.384	−1.184	−0.411	−0.211
bpmx24	0.879	1.079	0.138	0.338
bpmx25	−0.725	−0.525	0.069	0.269
bpmx26	1.405	1.605	−0.972	−0.772
bpmx27	0.544	0.744	0.740	0.940
bpmx28	0.416	0.616	−0.785	−0.585

Table B.4.: Margins of the accepted range for each Beam Position Monitor measuring the vertical beam position are given below. All values are in mm.

	Precursor 1		Precursor 2	
BPM Name	**Lower Bound**	**Upper Bound**	**Lower Bound**	**Upper Bound**
bpmy01	−0.846	−0.646	1.590	1.790
bpmy02	7.852	8.052	1.295	1.495
ecbpmy113	No Value	No Value	No Value	No Value
ecbpmy114	No Value	No Value	No Value	No Value
bpmy51	No Value	No Value	No Value	No Value
bpmy52	No Value	No Value	No Value	No Value
bpmy06	−0.628	−0.428	−3.834	−3.634
bpmy07	No Value	No Value	−2.039	−1.839
bpmy08	−3.440	−3.240	−0.790	−0.590
bpmy09	−1.616	−1.416	−0.681	−0.481
bpmy10	−0.518	−0.318	−0.317	−0.117
bpmy11	−1.109	−0.909	0.269	0.469
bpmy12	−5.070	−4.870	−0.374	−0.174
bpmy13	No Value	No Value	−0.401	−0.201
bpmy14	−3.289	−3.089	0.180	0.380
bpmy15	−0.538	−0.338	−0.318	−0.118
bpmy16	−2.665	−2.465	−0.132	0.068
bpmy17	−2.168	−1.968	0.033	0.233
bpmy18	−4.147	−3.947	−4.161	−3.961
bpmy19	−1.975	−1.775	−4.550	−4.350
becy01	−0.273	−0.073	−4.770	−4.570
becy02	−0.836	−0.636	−4.066	−3.866
bpmy20	−2.254	−2.054	0.195	0.395
bany01	No Value	No Value	No Value	No Value
bany02	−1.249	−1.049	−0.032	0.168
bpmy21	1.748	1.948	−0.693	−0.493
bpmy22	−1.047	−0.847	−0.917	−0.717
bpmy23	0.373	0.573	−0.667	−0.467
bpmy24	0.033	0.233	−1.015	−0.815
bpmy26	No Value	No Value	0.178	0.378
bpmy27	−1.914	−1.714	0.688	0.888
bpmy28	−2.210	−2.010	2.322	2.522
bpmy29	−2.149	−1.949	−0.301	−0.101

C. Additional Material on the Determination of the Invariant Spin Axis using Static Solenoids

C.1. Description of the Spin Motion in a Static Solenoid Providing a Magnetic Field Pointing in Beam Direction

The analytical work from Eq. (C.4) to (C.19) is based on *Spin tune mapping as a novel tool to probe the spin dynamics in storage rings* [103].

For the derivation of the dependencies of the change of spin tune as a function of the solenoidal fields of the Siberian snake and the 2 MV cooler solenoid with respect to the longitudinal components of the Invariant Spin Axis at the two solenoids, the following identities are used.

- For $\vec{a} = a\vec{n}$ with $|\vec{n}| = 1$, the matrix exponential of the Pauli matrices can be written as

  $$e^{ia(\vec{n}\vec{\sigma})} = I\cos(a) + i\,(\vec{n}\cdot\vec{\sigma})\sin(a) \text{ or} \tag{C.1}$$

  $$e^{-ia(\vec{n}\vec{\sigma})} = I\cos(a) - i\,(\vec{n}\cdot\vec{\sigma})\sin(a), \tag{C.2}$$

  where I denotes the unity matrix. This identity can be proven by expanding the Taylor polynomial of the exponential and using $(\vec{n}\cdot\vec{\sigma})^{2p} = I$ for $p \in \mathbb{N}$.
- The relation to dot and cross product of the Pauli matrices with two arbitrary vector operators $\vec{a}$ and $\vec{b}$ is also called Dirac's relation and is given by

  $$(\vec{\sigma}\cdot\vec{a})\left(\vec{\sigma}\cdot\vec{b}\right) = \left(\vec{a}\cdot\vec{b}\right)I + i\vec{\sigma}\cdot\left(\vec{a}\times\vec{b}\right). \tag{C.3}$$

The standard spinor formalism describes the motion of the spin with one-turn spin rotation matrices. For simplicity, the calculations are given only for a single solenoid. The calculations of the change in spin tune as a function of two solenoids in COSY are only outlined. The one-turn spin rotation matrix for a magnetic ring (vertical dipole fields) is given by [114]

$$\mathbf{t}_{\text{Ring}} = e^{-i\pi\nu_s^0\vec{\sigma}\cdot\vec{n}} = \cos\left(\pi\nu_s^0\right)I - i\,(\vec{\sigma}\cdot\vec{n})\sin\left(\pi\nu_s^0\right), \tag{C.4}$$

where ν_s^0 denotes the unperturbed spin tune, $\vec{\sigma}$ denotes a vector containing the Pauli matrices

$$\vec{\sigma}^{\mathrm{T}} = [\sigma_1, \sigma_2, \sigma_3], \tag{C.5}$$

and $\vec{n}$ is the unit vector around which the spins are precessing, i.e., the Invariant Spin Axis.

By adding a solenoid into a ring, the spins experience an additional, artificial spin rotation. The spin transfer matrix of a solenoid can be written as

$$\mathbf{t}_X = e^{-i\frac{\chi_X}{2}\vec{\sigma}\cdot\vec{k}} = \cos\left(\frac{\chi_X}{2}\right) I - i\left(\vec{\sigma}\cdot\vec{k}\right)\sin\left(\frac{\chi_X}{2}\right), \tag{C.6}$$

where X represents either the Siberian snake or the 2 MV solenoid, χ represents the spin rotation angle in the solenoid, and $\vec{k}$ represents the spin rotation axis. To describe the full spin motion, the total spin transfer matrix needs to be calculated, which is the product of the contribution to the spin of the ring and the additional solenoid

$$\begin{aligned}
\mathbf{T} &= \mathbf{t}_{\text{Ring}}\mathbf{t}_X \\
&= \cos\left(\pi\nu_s^0\right)\cos\left(\frac{\chi_X}{2}\right)I - i\left(\vec{\sigma}\cdot\vec{k}\right)\sin\left(\frac{\chi_X}{2}\right)\cos\left(\pi\nu_s^0\right) \\
&\quad - i\left(\vec{\sigma}\cdot\vec{n}\right)\sin\left(\pi\nu_s^0\right)\cos\left(\frac{\chi_X}{2}\right) - \left(\vec{\sigma}\cdot\vec{n}\right)\left(\vec{\sigma}\cdot\vec{k}\right)\sin\left(\pi\nu_s^0\right)\sin\left(\frac{\chi_X}{2}\right) \\
&\overset{\text{Eq. (C.3)}}{=} \cos\left(\pi\nu_s^0\right)\cos\left(\frac{\chi_X}{2}\right)I - \left(\vec{n}\cdot\vec{k}\right)I\sin\left(\pi\nu_s^0\right)\sin\left(\frac{\chi_X}{2}\right) \\
&\quad - i\vec{\sigma}\cdot\left[\left(\vec{n}\times\vec{k}\right)\sin\left(\pi\nu_s^0\right)\sin\left(\frac{\chi_X}{2}\right) + \vec{k}\sin\left(\frac{\chi_X}{2}\right)\cos\left(\pi\nu_s^0\right) + \vec{n}\sin\left(\nu_s^0\right)\cos\left(\frac{\chi_X}{2}\right)\right] \\
&\overset{!}{=} \cos(\pi\nu_s(\chi_X))I - i\left(\vec{\sigma}\cdot\vec{n}(\chi_X)\right)\sin(\pi\nu_s(\chi_X)).
\end{aligned} \tag{C.7}$$

In the last step, the fact that the resulting matrix needs to be again a one-turn spin transfer matrix is used, with $\nu_s(\chi_X)$ describing the modified spin tune and $\vec{n}(\chi_X)$ describing the orientation of the Invariant Spin Axis as a function of the spin rotation angle of the solenoid. By comparing the real and imaginary components in Eq. (C.7), the change of the Invariant Spin Axis and spin tune can be written as

$$\begin{aligned}
\vec{n}(\chi_X) = \frac{1}{\sin(\pi\nu_s(\chi_X))}\cdot\Bigg[&\left(\vec{n}\times\vec{k}\right)\sin\left(\pi\nu_s^0\right)\sin\left(\frac{\chi_X}{2}\right) \\
&+\vec{k}\sin\left(\frac{\chi_X}{2}\right)\cos\left(\pi\nu_s^0\right) + \vec{n}\sin\left(\nu_s^0\right)\cos\left(\frac{\chi_X}{2}\right)\Bigg],
\end{aligned} \tag{C.8}$$

and

$$\cos\left(\pi\nu_s(\chi_X)\right) = \cos\left(\pi\nu_s^0\right)\cos\left(\frac{\chi_X}{2}\right) - \left(\vec{n}\cdot\vec{k}\right)\sin\left(\pi\nu_s^0\right)\sin\left(\frac{\chi_X}{2}\right). \tag{C.9}$$

A direct formula for the absolute change of spin tune $\Delta\nu_s = \nu_s(\chi_X) - \nu_s^0$ can be found by evaluating

$$\cos(\pi\nu_s(\chi_X)) - \cos\left(\pi\nu_s^0\right) = \cos\left(\pi\left(\nu_s^0 + \Delta\nu_s\right)\right) - \cos\left(\pi\nu_s^0\right) \tag{C.10}$$

$$= \cos\left(\pi\nu_s^0\right)\cos(\pi\Delta\nu_s) - \sin(\pi\nu_s)\sin(\pi\Delta\nu_s) - \cos\left(\pi\nu_s^0\right) \tag{C.11}$$

$$\overset{\Delta\nu_s\ll 1}{\approx} -\pi\Delta\nu_s\sin(\pi\nu_s). \tag{C.12}$$

The largest absolute changes of spin tune are in the order of 1×10^{-5} (cf. section 7.4.3), which justifies the approximation. Rearranging leads to

$$\begin{aligned}\Delta\nu_s &= -\frac{\cos(\pi\nu_s(\chi_X)) - \cos\left(\pi\nu_s^0\right)}{\pi\sin\left(\nu_s^0\right)} &\text{(C.13)}\\ &= -\frac{1}{\pi}\left[\cot\left(\pi\nu_s^0\right)\left(\cos\left(\frac{\chi_X}{2}\right)-1\right) - \left(\vec{n}\cdot\vec{k}\right)\sin\left(\frac{\chi_X}{2}\right)\right]. &\text{(C.14)}\end{aligned}$$

During the second Precursor run, experiments were done using two solenoids at the same time. The derivation of the spin tune change as a function of two solenoids ramping at the same time is very similar to the case using only a single solenoid but rather lengthy. Therefore the derivation is only outlined. The one-turn rotation matrix consists of two rotation matrices due to the arcs and two rotation matrixes for the solenoids

$$\mathbf{T} = \mathbf{t}_{\text{Arc 1}}\mathbf{t}_{\text{Snake}}\mathbf{t}_{\text{Arc 2}}\mathbf{t}_{\text{2MV Sol.}}. \tag{C.15}$$

The individual matrices are given by

$$\begin{aligned}\mathbf{t}_{\text{Arc 1}} = \mathbf{t}_{\text{Arc 2}} = e^{-i\frac{\pi\nu_s^0}{2}\vec{\sigma}\cdot\vec{n}} &= \cos\left(\frac{\pi\nu_s^0}{2}\right)I - i\left(\vec{\sigma}\cdot\vec{n}\right)\sin\left(\frac{\pi\nu_s^0}{2}\right), &\text{(C.16)}\\ \mathbf{t}_{\text{Snake}} = e^{-i\frac{\chi_{\text{Snake}}}{2}\vec{\sigma}\cdot\vec{k}_{\text{Snake}}} &= \cos\left(\frac{\chi_{\text{Snake}}}{2}\right)I - i\left(\vec{\sigma}\cdot\vec{k}_{\text{Snake}}\right)\sin\left(\frac{\chi_{\text{Snake}}}{2}\right), &\text{(C.17)}\\ \mathbf{t}_{\text{2MV Sol.}} = e^{-i\frac{\chi_{\text{2MV Sol.}}}{2}\vec{\sigma}\cdot\vec{k}_{\text{2MV Sol.}}} &= \cos\left(\frac{\chi_{\text{2MV Sol.}}}{2}\right)I - i\left(\vec{\sigma}\cdot\vec{k}_{\text{2MV Sol.}}\right)\sin\left(\frac{\chi_{\text{2MV Sol.}}}{2}\right). &\text{(C.18)}\end{aligned}$$

By following the same steps as in the case for a single solenoid, the change of spin tune as a function of two solenoids is given by

$$\begin{aligned}\Delta\nu_s(\chi_{\text{Snake}}, \chi_{\text{2MV Sol.}}) = &\frac{1}{-\pi\sin\left(\pi\nu_s^0\right)}\times\\ &\left[\cos\left(\pi\nu_s^0\right)\left(\cos\left(\frac{\chi_{\text{Snake}}}{2}\right)\cos\left(\frac{\chi_{\text{2MV Sol.}}}{2}\right)-1\right)\right.\\ &-\sin\left(\frac{\chi_{\text{Snake}}}{2}\right)\sin\left(\frac{\chi_{\text{2MV Sol.}}}{2}\right)\\ &-\left(\vec{n}\cdot\vec{k}_{\text{2MV Sol.}}\right)\sin\left(\pi\nu_s^0\right)\sin\left(\frac{\chi_{\text{Snake}}}{2}\right)\cos\left(\frac{\chi_{\text{2MV Sol.}}}{2}\right)\\ &\left.-\left(\vec{n}\cdot\vec{k}_{\text{Snake}}\right)\sin\left(\pi\nu_s^0\right)\sin\left(\frac{\chi_{\text{2MV Sol.}}}{2}\right)\cos\left(\frac{\chi_{\text{Snake}}}{2}\right)\right]\\ &+\Delta\nu_{s,0}.\end{aligned} \tag{C.19}$$

C.2. Event Selection Studies for the Determination of the Longitudinal Component of the Invariant Spin Axis during the First Precursor Run.

Event Selection Studies are performed to validate a coherent change of the spin tune when ramping solenoids in COSY within the bunch. At the polarimeter, the particles within the bunch scatter on a carbon target into the four quadrants. From the timing signals of the single events, a longitudinal beam profile measurement can be analyzed, which scales with the true longitudinal bunch shape, which is, to a good approximation, given by a Gaussian function, as only the particles with the largest betatron amplitude scatter with the carbon target.

The events within the bunch distribution are pre-selected from the center and the head and tail of the Gaussian and analyzed separately to determine the calibration factor for converting the current of the power supply of the Siberian snake into a spin flip angle and the longitudinal component of the Invariant Spin Axis at the Siberian snake. As shown in Figure C.1, the results within the bunch are comparable. More information about the Event Selection Studies is given in section 6.3. The methodology of fitting the events is explained in section 7.4.2.

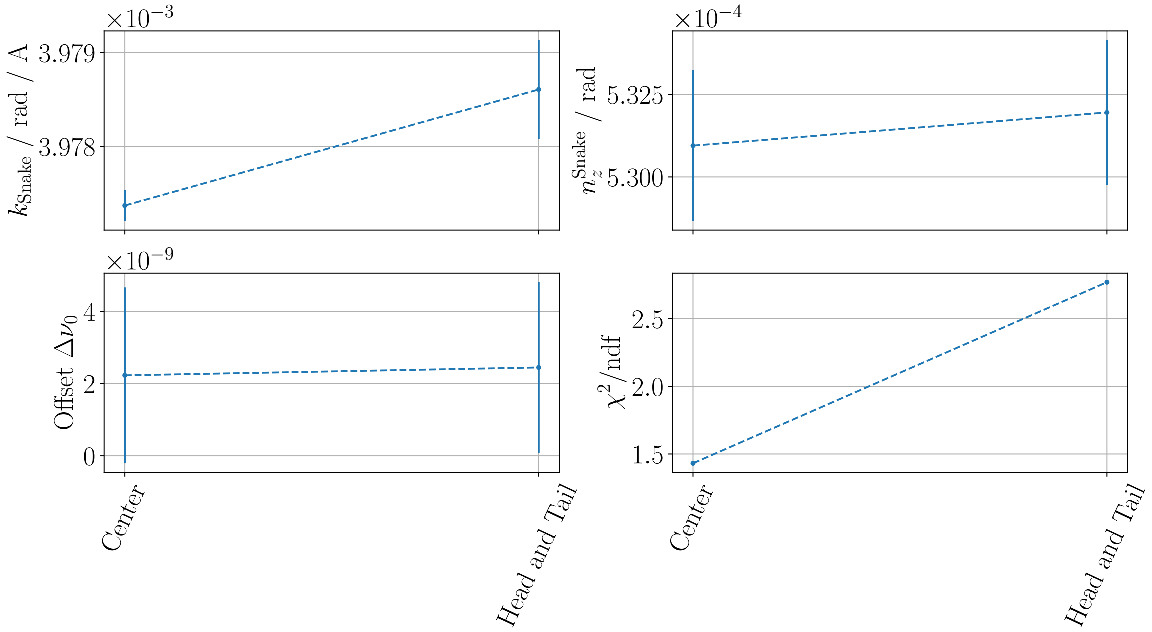

Figure C.1.: Event Selection Studies for the determination of the longitudinal component of the Invariant Spin Axis during the first Precursor run.

D. Additional Material on the Determination of the Invariant Spin Axis using the RF Wien Filter

D.1. Description of the Spin Motion in an RF Wien Filter

The following derivations of the spin dynamics in an RF Wien filter are based on the internal note *Spin motion in an rf Wien filter* by Volker Hejny [105].

The following equations are used to extract the so-called resonance strength from data and describe the relative phase between Wien filter frequency and spin tune and the opening angle between the vertical polarization and the in-plane polarization plane as a function of time (or turn number). Once the resonance strength is known, the orientation of the invariant spin axis $\vec{n}$ can be determined.

The coordinate system is chosen to be in a reference frame with respect to the Invariant Spin Axis $\vec{n}$ at the location of the RF Wien filter

$$\vec{e}_y = \vec{n},\ \vec{e}_x = \vec{n} \times \vec{\beta},\ \text{and}\ \vec{e}_z = \vec{e}_x \times \vec{e}_y. \tag{D.1}$$

The coordinate system is illustrated in Figure D.1 together with the orientation of the magnetic field of the RF Wien filter.

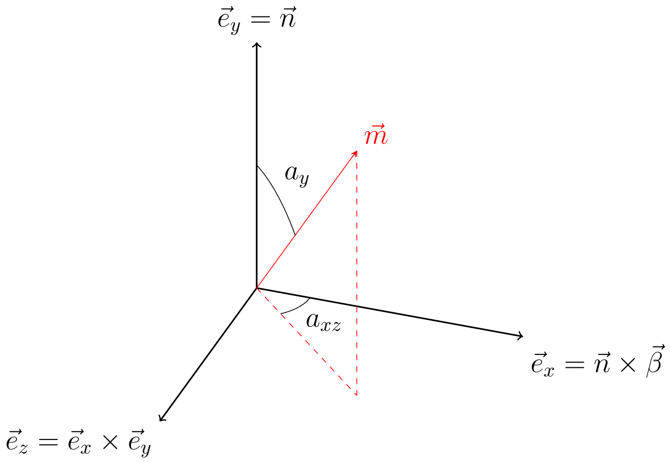

Figure D.1.: Coordinate system for the description of the magnetic field axis of the Wien filter $\vec{m}$ with respect to the coordinate system defined in Eq. (D.1).

The spin vector at the location of the RF Wien filter is defined with respect to the out-of-plane angle α (the angle between vertical and horizontal polarization plane) and the spin precession angle $\omega_s = 2\pi\nu_s f_{\mathrm{COSY}}$ in the accelerator plane $(x - z)$

$$\vec{S} = \begin{pmatrix} \cos(\alpha)\sin(\omega_s t) \\ \sin(\alpha) \\ \cos(\alpha)\cos(\omega_s t) \end{pmatrix}. \tag{D.2}$$

When the measurement time begins ($t = t_{\mathrm{WF}}$), the spin points along $\vec{e}_z$ without loss of generality. In addition, the spin might have a vertical component when the rotation of the initial vertically polarized beam is not fully rotated into the accelerator plane using the RF solenoid.

In this coordinate system, the magnetic field axis of the RF Wien filter is given by

$$\vec{m} = \begin{pmatrix} -\sin(a_y)\cos(a_{xz}) \\ \cos(a_y) \\ \sin(a_y)\sin(a_{xz}) \end{pmatrix}. \tag{D.3}$$

The parameter a_y describes the angle between the magnetic field of the RF Wien filter and the Invariant Spin Axis (cf. Figure D.1)

$$\sin(a_y) = |\vec{n} \times \vec{m}|. \tag{D.4}$$

The angle a_y is later on replaced by the resonance strength defined in Eq. (7.35). The parameter a_{xz} describes the orientation of the magnetic field of the RF Wien filter in the $x - z$ plane with respect to $\vec{e}_x$.

The spin kick angle in the RF Wien filter ψ_0 can be calculated by evaluating the Thomas BMT equation. The RF Wien filter is EDM transparent which can be shown by evaluating the precession component due to the EDM in the Thomas-BMT equation (4.22)

$$\vec{\Omega}_{\mathrm{EDM}} = -\frac{q}{mc}\frac{\eta_{\mathrm{EDM}}}{2}\left[\vec{E} - \frac{\gamma}{\gamma+1}\left(\vec{\beta}\cdot\vec{E}\right)\vec{\beta} + c\vec{\beta}\times\vec{B}\right]. \tag{D.5}$$

Using the fact, that the beam enters the RF Wien filter perpendicular to the electric field ($\vec{\beta}\cdot\vec{E} = 0$) and the Lorentz force condition

$$\vec{E} = -c\vec{\beta}\times\vec{B}, \tag{D.6}$$

the contribution due to the EDM becomes zero

$$\vec{\Omega}_{\mathrm{EDM}} = 0. \tag{D.7}$$

The only contribution is a result from the Magnetic Dipole Moment contribution

$$\vec{\Omega}_{\mathrm{MDM}} = -\frac{q}{m}\left[\left(G + \frac{1}{\gamma}\right)\vec{B} - \frac{G\gamma}{\gamma+1}\left(\vec{\beta}\cdot\vec{B}\right)\vec{\beta} - \left(G + \frac{1}{\gamma+1}\right)\vec{\beta}\times\frac{\vec{E}}{c}\right]. \tag{D.8}$$

The magnetic field axis ($\vec{m}$)

$$\vec{B} = B\vec{m} \tag{D.9}$$

describes the axis around which the spins experience an additional spin rotation. Assuming that $\vec{m} \perp \vec{\beta}$ leads to

$$\vec{\beta} \cdot \vec{B} = 0 \text{ and } \vec{\beta} \times \left(\vec{\beta} \times \vec{B}\right) = -\beta^2 B\vec{m}, \tag{D.10}$$

and, using again the Lorentz force condition, consequently to

$$\vec{\Omega}_{\text{MDM}} = -\frac{q}{m}\left[\left(G + \frac{1}{\gamma}\right) + \left(G + \frac{1}{\gamma+1}\right)\beta^2\right] B\vec{m}. \tag{D.11}$$

Using $\beta^2 = 1 - {}^1\!/_{\gamma^2}$ and integrating the magnetic field along the length of the RF Wien filter leads to

$$\vec{\Omega}_{\text{MDM}} = -\frac{q(1+G)(1-\beta^2)}{\beta m}\int B\text{d}l \cdot \vec{m} = \psi_0\vec{m}. \tag{D.12}$$

The amplitudes of the magnetic (and electric) fields in the RF Wien filter are oscillating. The oscillation frequency and phase are controlled by the phase feedback described in section 6.7 to fulfill the resonance condition

$$\omega_{\text{WF}} = 2\pi k f_{\text{COSY}} + \omega_s, k \in \mathbb{Z}. \tag{D.13}$$

The rotation angle as a function of time, can therefore be written as

$$\psi(t) = \psi_0 \cos(\omega_{\text{WF}} t - \phi_{\text{rel.}}), \tag{D.14}$$

where $\phi_{\text{rel.}}$ denotes the relative phase dependence between the Wien filter frequency and the spin precession frequency. Since the RF Wien filter is located at a distinct location in the ring and COSY is operated using a bunched beam, the spin is rotated at distinct times $t = {}^n\!/_{f_{\text{COSY}}}$, with $n \in \mathbb{N}$

$$\begin{aligned} \cos(\omega_{\text{WF}} - \phi_{\text{rel.}}) &\rightarrow \cos\left(2\pi k n + \omega_s \cdot \frac{n}{f_{\text{COSY}}} - \phi_{\text{rel.}}\right) \qquad &(\text{D.15}) \\ &= \cos\left(\omega_s \cdot \frac{n}{f_{\text{COSY}}} - \phi_{\text{rel.}}\right) = \cos(\omega_s t - \phi_{\text{rel.}}). \qquad &(\text{D.16}) \end{aligned}$$

In general, the rotation matrix around an axis $\vec{n}^{\text{T}} = (n_x, n_y, n_z)$ with $|\vec{n}| = 1$ around an angle α is given by

$$R(\vec{n}, \alpha) = \begin{pmatrix} \cos(\alpha) + n_x^2(1-\cos(\alpha)) & n_x n_y(1-\cos(\alpha)) - n_z\sin(\alpha) & n_x n_z(1-\cos(\alpha)) + n_y\sin(\alpha) \\ n_y n_x(1-\cos(\alpha)) + n_z\sin(\alpha) & \cos(\alpha) + n_y^2(1-\cos(\alpha)) & n_y n_z(1-\cos(\alpha)) - n_x\sin(\alpha) \\ n_z n_x(1-\cos(\alpha)) - n_y\sin(\alpha) & n_z n_y(1-\cos(\alpha)) + n_x\sin(\alpha) & \cos(\alpha) + n_z^2(1-\cos(\alpha)) \end{pmatrix}. \tag{D.17}$$

Assuming that the spin rotations are small $\psi(t) \ll 1$ ($\psi_0 \approx 1 \times 10^{-6}\,\text{rad}$), the one-turn spin transfer matrix for the RF Wien filter is given by

$$R\big(\vec{m}, \psi(t)\big) = \psi(t)\begin{pmatrix} 1 & \sin(a_{xz})\sin(a_y) & \cos(a_y) \\ \sin(a_{xz})\sin(a_y) & 1 & -\cos(a_{xz})\sin(a_y) \\ \cos(a_y) & \cos(a_{xz})\sin(a_y) & 1 \end{pmatrix}. \tag{D.18}$$

The one-turn spin rotation matrix allows to calculate the orientation of the spin vector based on the information of the spin vector in the previous turn

$$S_{n+1} = R\big(\vec{m}, \psi(t)\big) S_n. \tag{D.19}$$

The change of the spin vector can be calculated by evaluating

$$\begin{aligned} \Delta\vec{S} &= (R - I) \cdot \vec{S} &\text{(D.20)}\\ &= \psi_0 \cos\Big(\omega_s t - \phi^{\text{rel.}}\Big) \begin{pmatrix} \cos(\alpha)\cos(a_y)\cos(\omega_s t) + \sin(\alpha)\sin(a_{xz})\sin(a_y) \\ -\cos(\alpha)\sin(a_y)(\cos(a_{xz})\cos(\omega_s t) + \sin(a_{xz})\sin(\omega_s t)) \\ \sin(\alpha)\sin(a_y)\cos(a_{xz}) - \cos(\alpha)\cos(a_y)\sin(\omega_s t) \end{pmatrix}. &\text{(D.21)} \end{aligned}$$

The buildup of the vertical polarization along the Invariant Spin Axis is given by

$$\Delta p_y = \Delta\vec{S}_y. \tag{D.22}$$

The induced phase shift within the $x - z$ plane can be calculated using

$$\begin{aligned} \Delta\phi_{\text{rel.}} &= \frac{\Delta\vec{S}_x \cos(\omega_s t) - \Delta\vec{S}_z \sin(\omega_s t)}{\cos(\alpha)} &\text{(D.23)}\\ &= \psi_0 \cos(\omega_s t - \phi_{\text{rel.}})\big(\cos(a_y) - \sin(a_y)\sin(\omega_s t - a_{xz})\tan(\alpha)\big). &\text{(D.24)} \end{aligned}$$

By averaging over a full spin precession period $T = {}^{2\pi}/_{\omega_s} = {}^{1}/_{f_s}$, the average net change per turn of the vertical polarization component ($\Delta p_y \rightarrow {}^{\mathrm{d}p_y}/_{\mathrm{d}n}$) and the phase shift of the relative phase ($\Delta\phi_{\text{rel.}} \rightarrow {}^{\mathrm{d}\phi_{\text{rel.}}}/_{\mathrm{d}n}$) can be calculated via

$$\begin{aligned} \frac{\mathrm{d}\phi_{\text{rel.}}}{\mathrm{d}n} &= \frac{1}{T}\int_0^T \Delta\phi_{\text{rel.}}\mathrm{d}t = \frac{\omega_s}{2\pi}\int_0^{\frac{2\pi}{\omega_s}} \Delta\phi_{\text{rel.}}\mathrm{d}t = \frac{\psi_0}{2}\sin(a_y)\sin(a_{xz} - \phi_{\text{rel.}})\tan(\alpha), &\text{(D.25)}\\ \frac{\mathrm{d}p_y}{\mathrm{d}n} &= \frac{1}{T}\int_0^T \Delta p_y \mathrm{d}t = \frac{\omega_s}{2\pi}\int_0^{\frac{2\pi}{\omega_s}} \Delta p_y \mathrm{d}t = -\frac{\psi_0}{2}\sin(a_y)\cos(a_{xz} - \phi_{\text{rel.}})\cos(\alpha). &\text{(D.26)} \end{aligned}$$

Using the following geometrical identity

$$\frac{\mathrm{d}p_y}{\mathrm{d}n} = \cos(\alpha)\frac{\mathrm{d}\alpha}{\mathrm{d}n}, \tag{D.27}$$

and the relation between time, beam revolution frequency, and turn number

$$f_{\text{COSY}} \cdot t = n, \tag{D.28}$$

the final set of coupled differential is given by

$$\begin{aligned} \frac{1}{f_{\text{COSY}}}\frac{\mathrm{d}\phi_{\text{rel.}}}{\mathrm{d}t} &= \frac{\mathrm{d}\phi_{\text{rel.}}}{\mathrm{d}n} = \frac{\psi_0}{2}\sin(a_y)\sin(a_{xz} - \phi_{\text{rel.}})\tan(\alpha), &\text{(D.29)}\\ \frac{1}{f_{\text{COSY}}}\frac{\mathrm{d}\alpha}{\mathrm{d}t} &= \frac{\mathrm{d}\alpha}{\mathrm{d}n} = -\frac{\psi_0}{2}\sin(a_y)\cos(a_{xz} - \phi_{\text{rel.}}). &\text{(D.30)} \end{aligned}$$

Using the definition of the resonance strength as described in Eq. (7.35), these formulas can be written as

$$\frac{\mathrm{d}\phi_{\text{rel.}}}{\mathrm{d}n} = 2\pi\epsilon \sin(a_{xz} - \phi_{\text{rel.}}) \tan(\alpha), \tag{D.31}$$

$$\frac{\mathrm{d}\alpha}{\mathrm{d}n} = -2\pi\epsilon \cos(a_{xz} - \phi_{\text{rel.}}), \tag{D.32}$$

or

$$\boxed{\begin{aligned} \frac{\mathrm{d}\phi_{\text{rel.}}}{\mathrm{d}t} &= 2\pi\epsilon f_{\text{COSY}} \sin(a_{xz} - \phi_{\text{rel.}}) \tan(\alpha), && \text{(D.33)} \\ \frac{\mathrm{d}\alpha}{\mathrm{d}t} &= -2\pi\epsilon f_{\text{COSY}} \cos(a_{xz} - \phi_{\text{rel.}}). && \text{(D.34)} \end{aligned}}$$

D.2. Resonance Strengths for the EDM Precursor Experiments

In the following section, the resonance strength for all measurements (Precursor 1 & 2) of the orientation of the Invariant Spin Axis in longitudinal and radial directions at the location of the RF Wien filter is shown. The data for the first Precursor Run is shown in Figures 7.24, D.2, and D.3. Each panel depicts the measured slope scaled by the revolution frequency as a function of the relative phase between the spin tune and Wien filter frequency at a fixed setting for the Wien filter rotation angle and the spin flip in the Siberian snake, which is shown in the title of each panel. According to Eq. (7.67), the resonance strength is given by the amplitude of the sinusoidal dependence of the slope as a function of relative phase. The same method was used during the second Precursor Run. This data is depicted in Figures D.4 to D.7. Note that in preparation for the Pilot Bunch method, two bunches were co-circulating in COSY. The RF Wien filter acts on both bunches during the Initial Slope method, which means that both bunches are analyzed independently.

The individual Maps in which the resonance strength is plotted against the Wien filter rotation angle and the spin flip angle in the Siberian snake are shown for the first Precursor Run in Figure D.8 and for Precursor 2 in Figure D.9 for the Maps using the Initial slope method and in Figure D.10 for the Pilot bunch method. By performing a least squares fit according to Eq. (7.56), the orientation of the Invariant Spin Axis can be determined. The results for all individual Maps are summarized in Section 7.8.

The methods describing the determination of the orientation of the Invariant Spin Axis are described in Section 7.6. A summary of the measurement campaigns is given in Table 7.13.

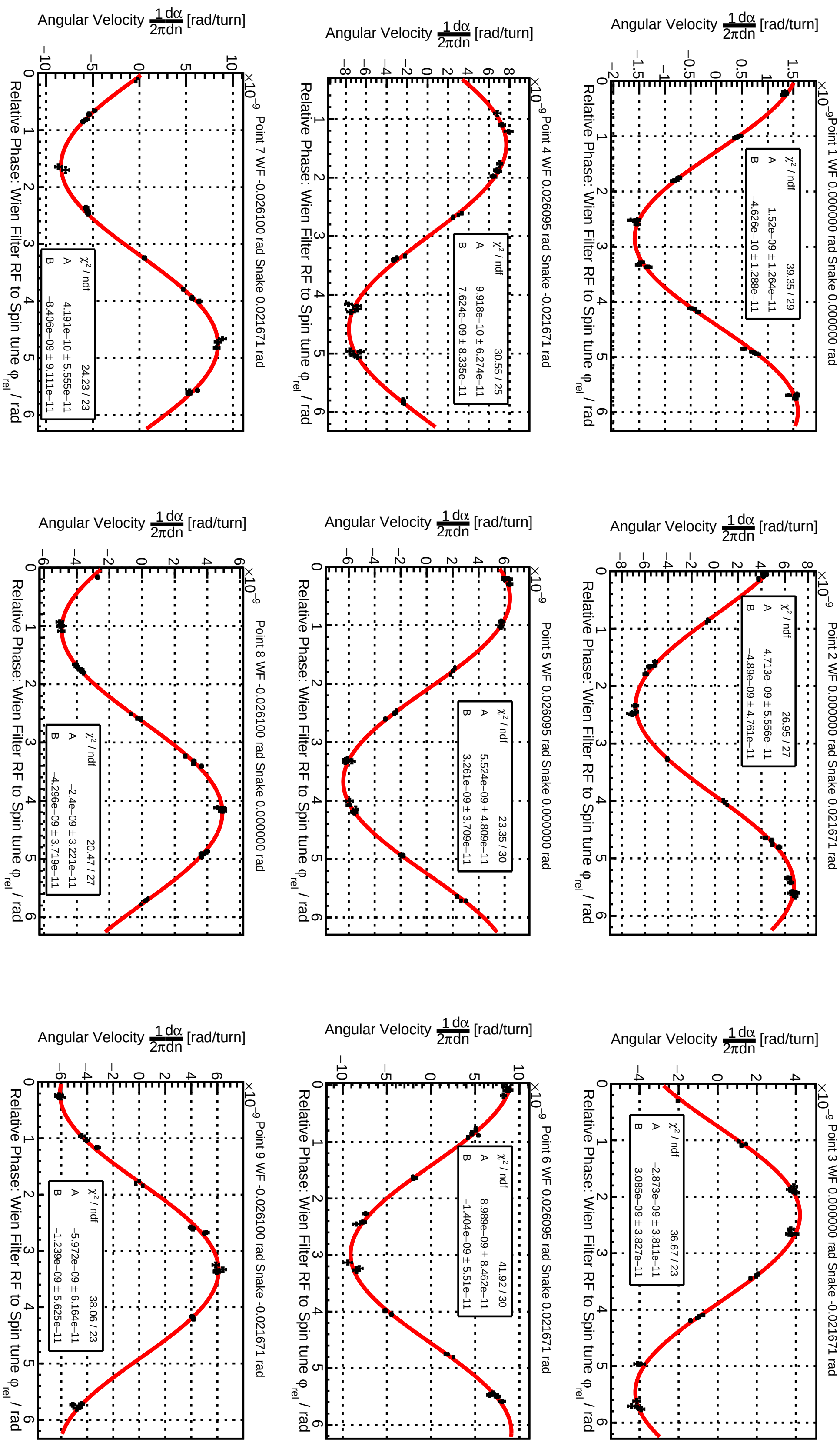

Figure D.2.: Resonance strengths for the second Map measured during the first Precursor period.

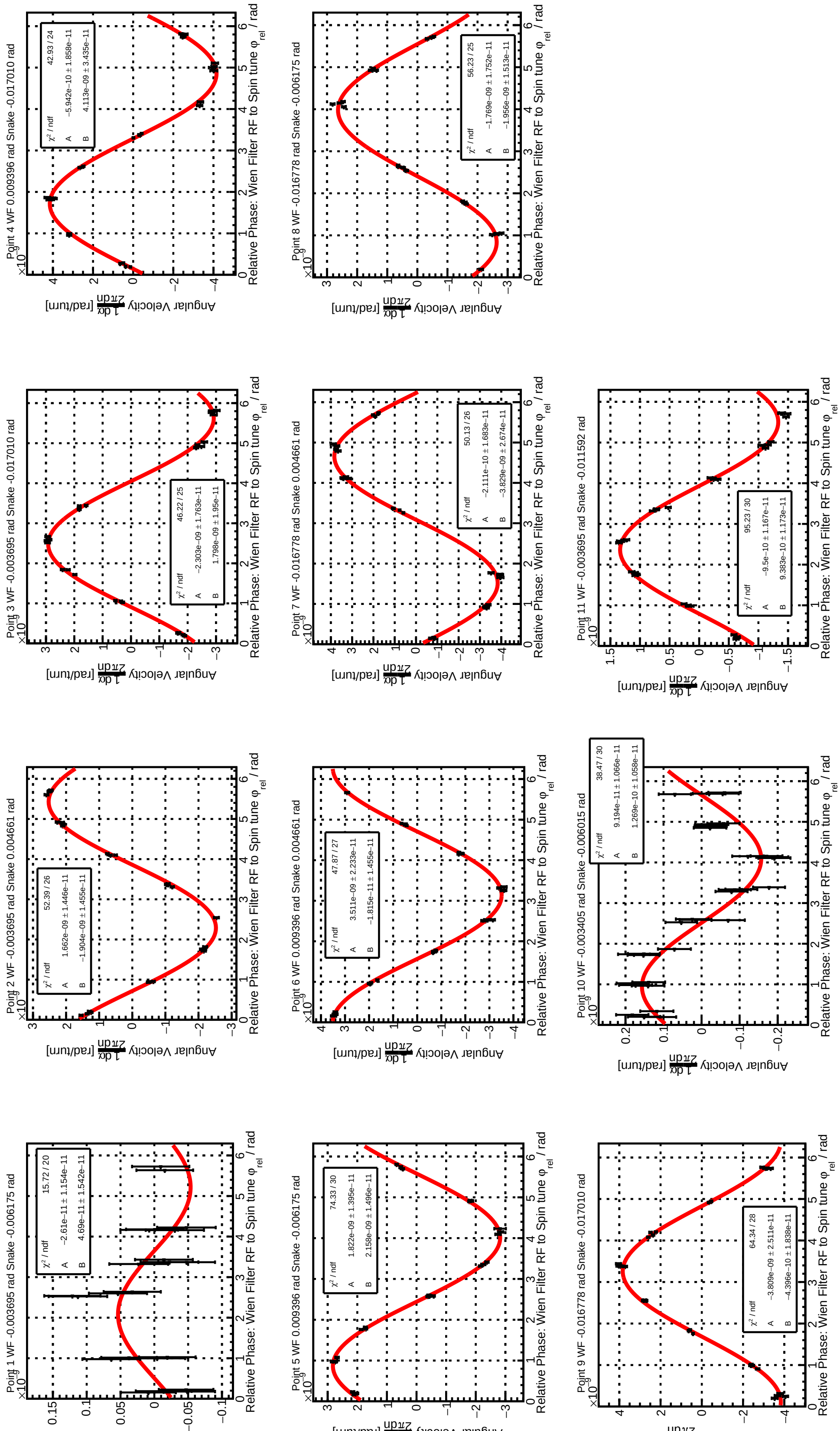

Figure D.3.: Resonance strengths for the third Map measured during the first Precursor period.

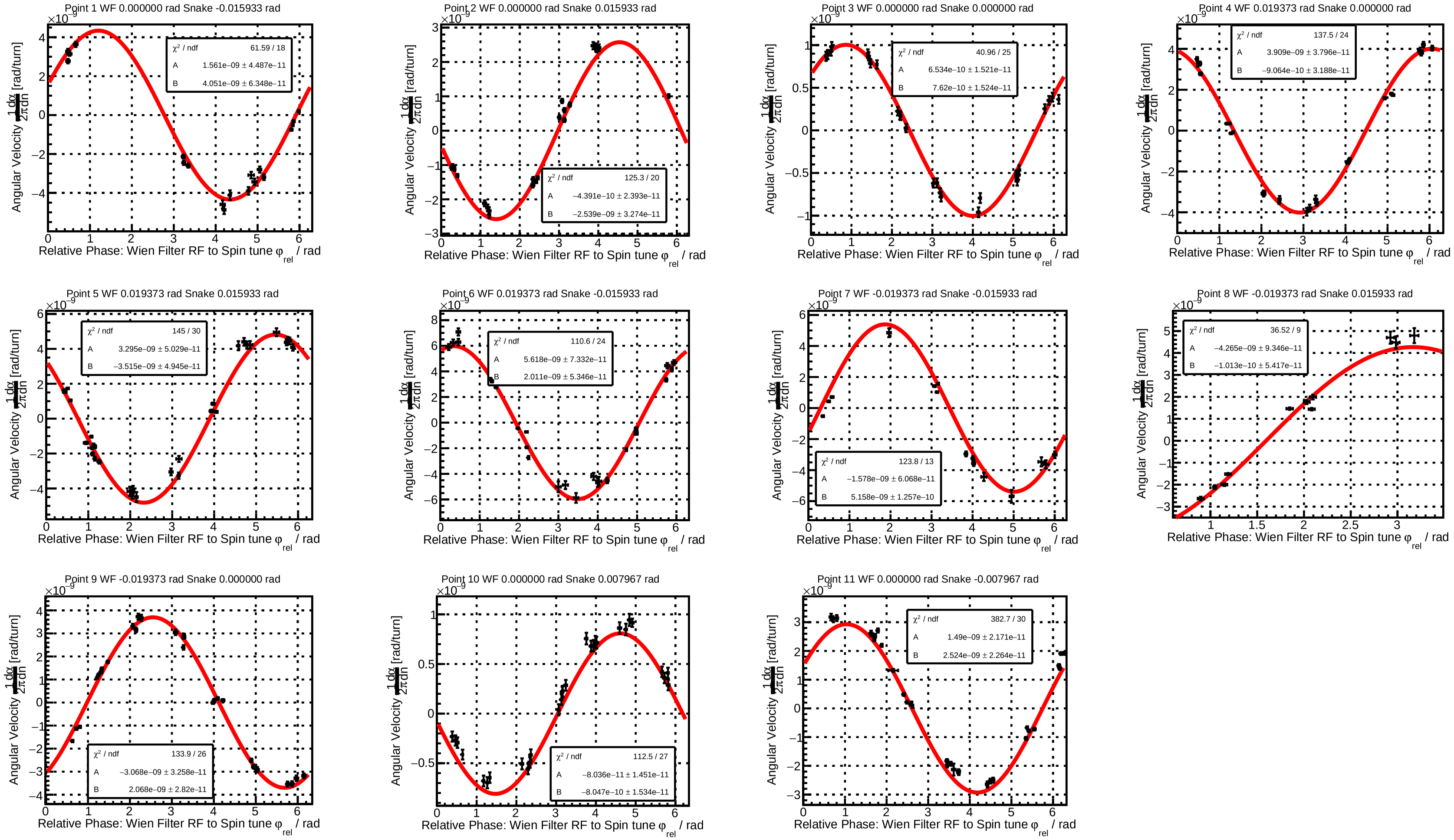

Figure D.4.: Resonance strengths for the first Map and first bunch measured during the second Precursor period.

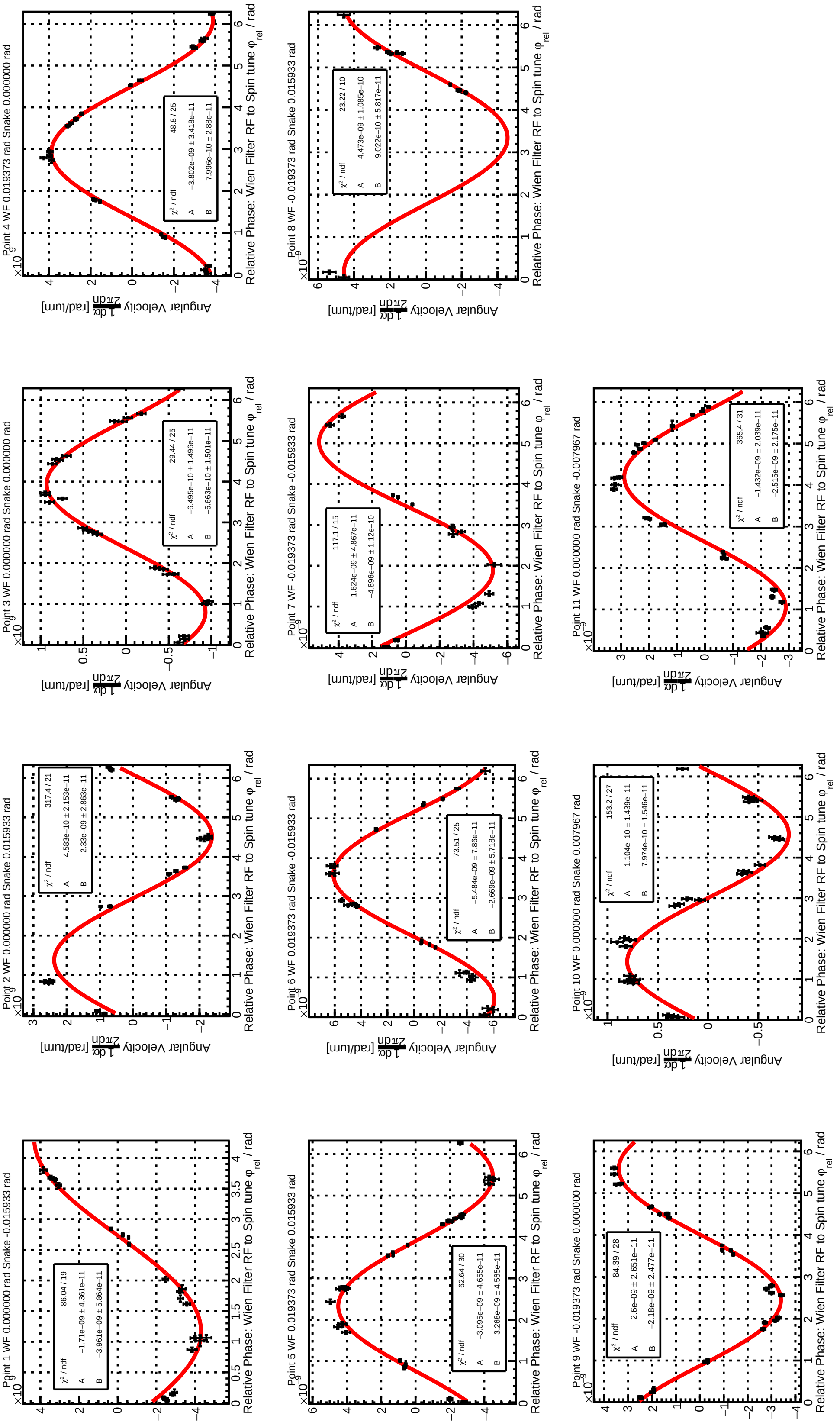

Figure D.5.: Resonance strengths for the first Map and second bunch measured during the second Precursor period.

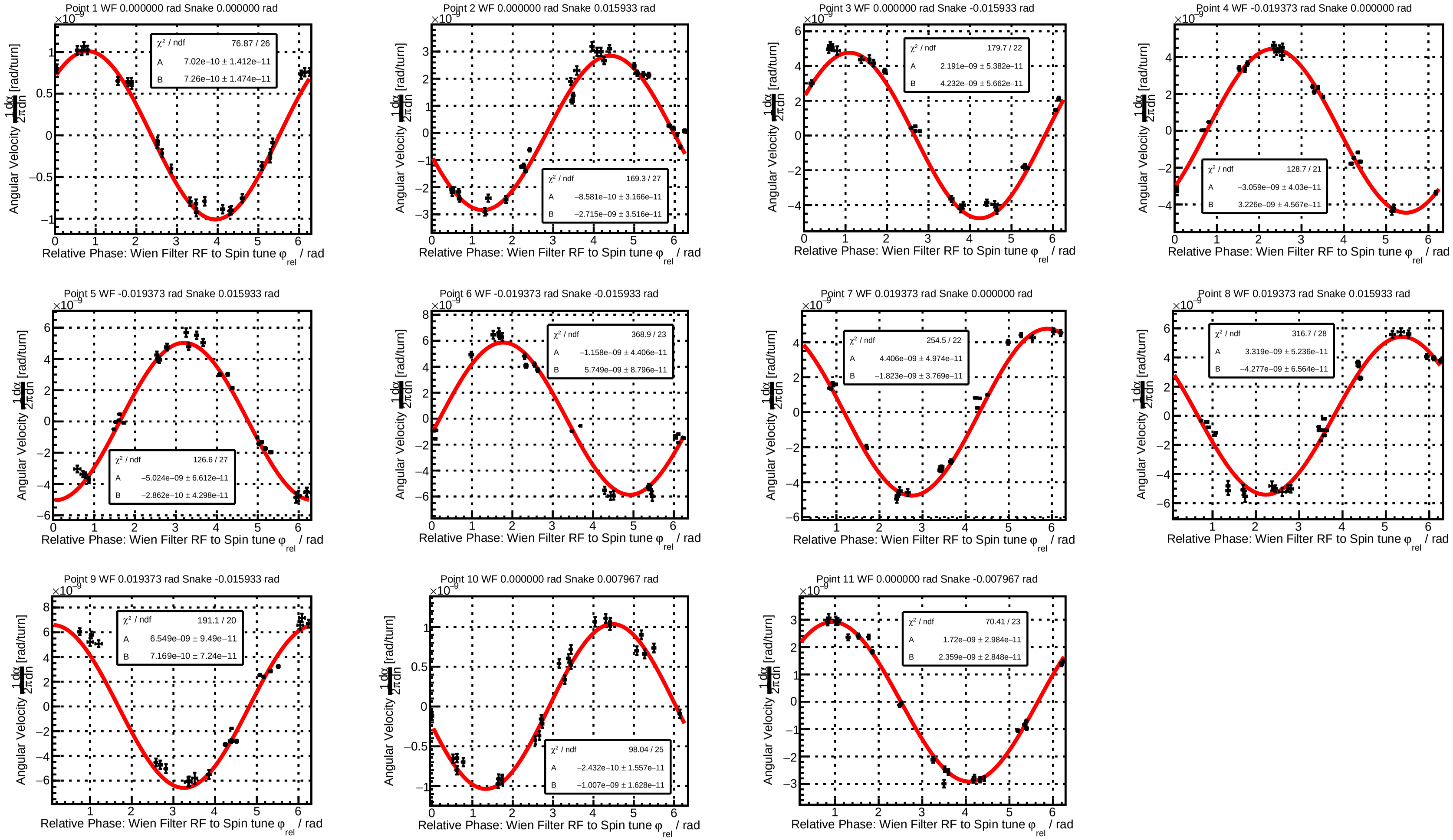

Figure D.6.: Resonance strengths for the second Map and first bunch measured during the second Precursor period.

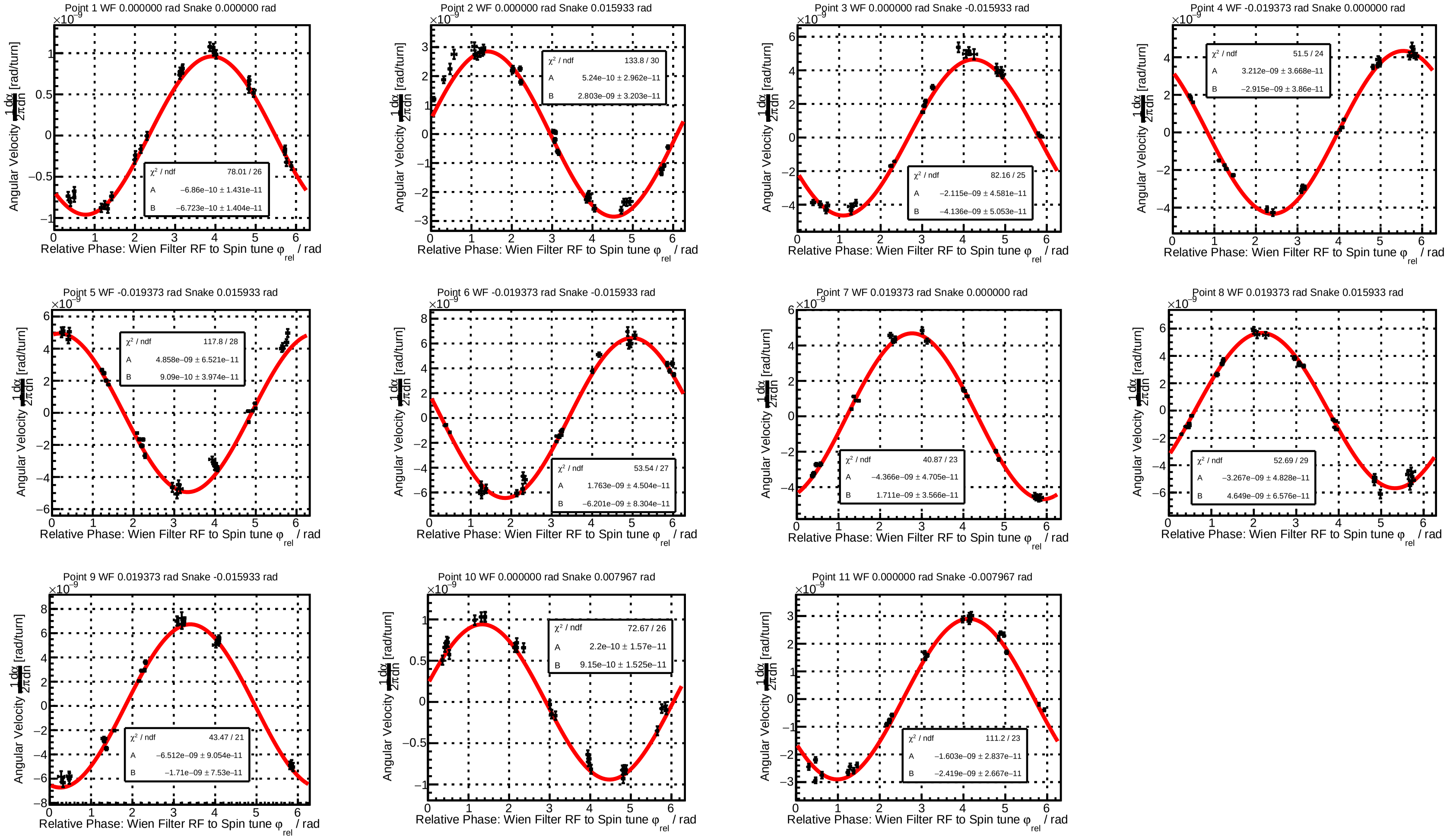

Figure D.7.: Resonance strengths for the second Map and second bunch measured during the second Precursor period.

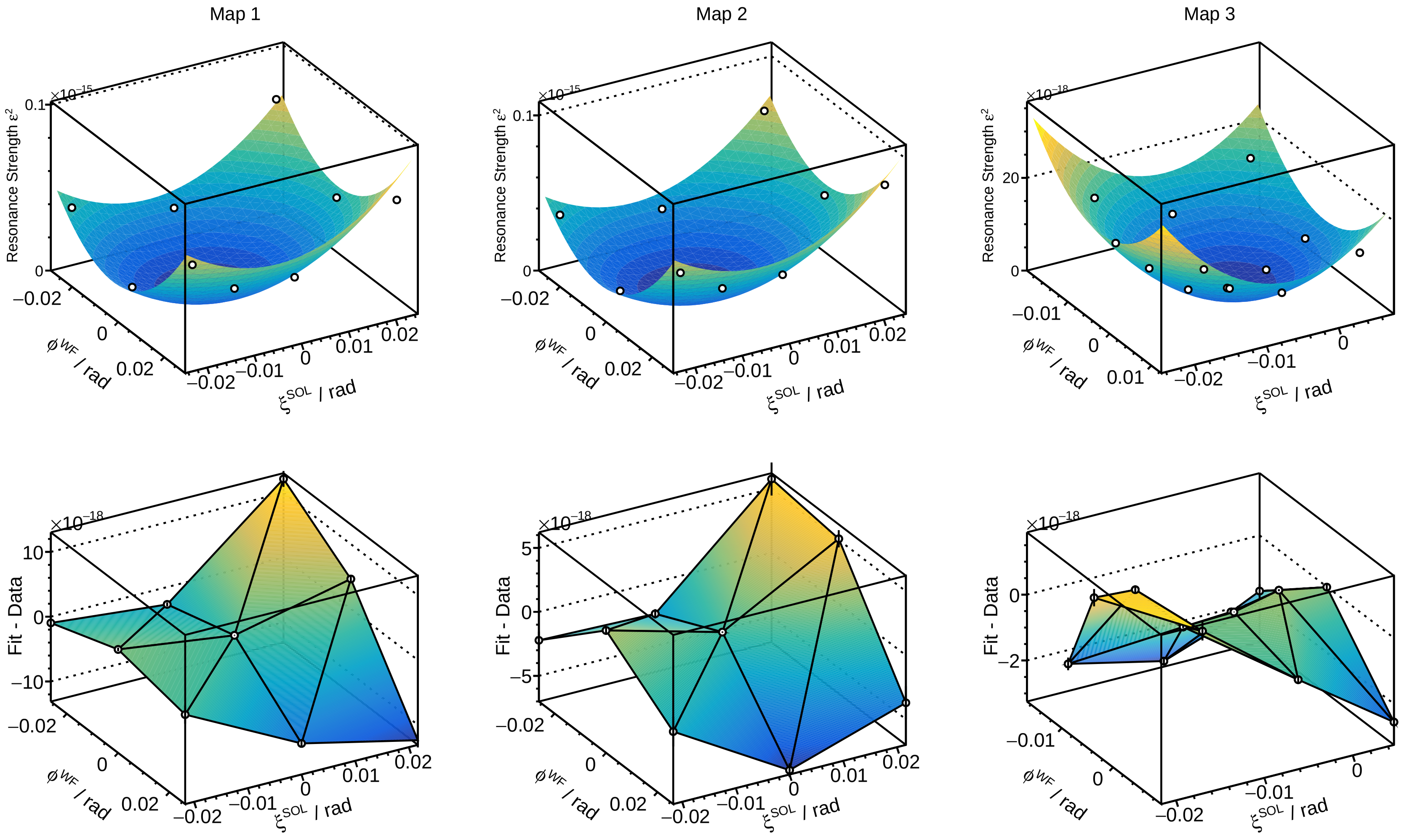

Figure D.8.: Resonance strengths for all measured Maps during Precursor 1. The plane illustrates the fit according to Eq. (7.57). The lower panel depict the residuals.

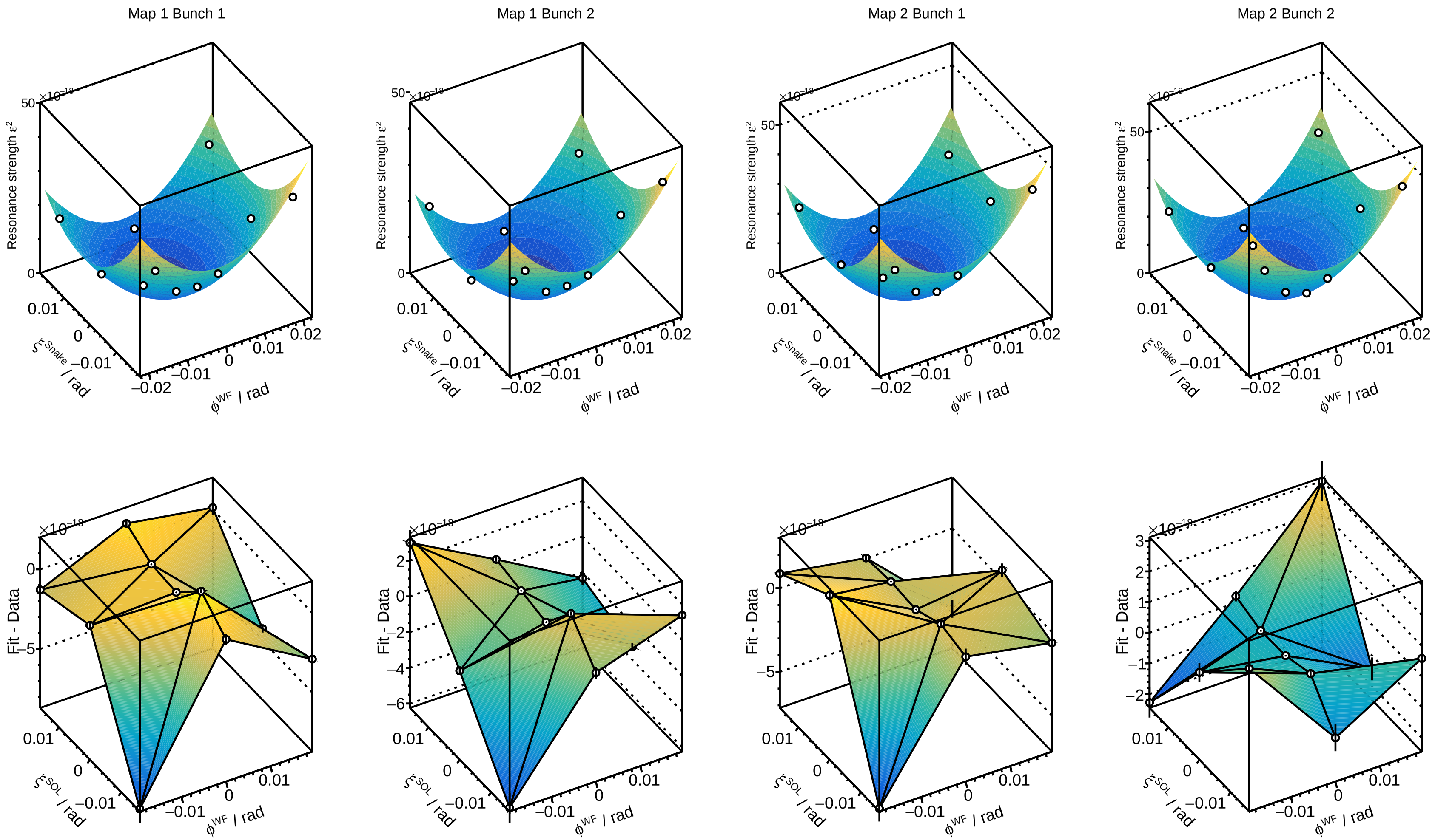

Figure D.9.: Resonance strengths for all measured Maps using the initial slope method during Precursor 2. The plane illustrates the fit according to Eq. (7.57). The lower panel depict the residuals.

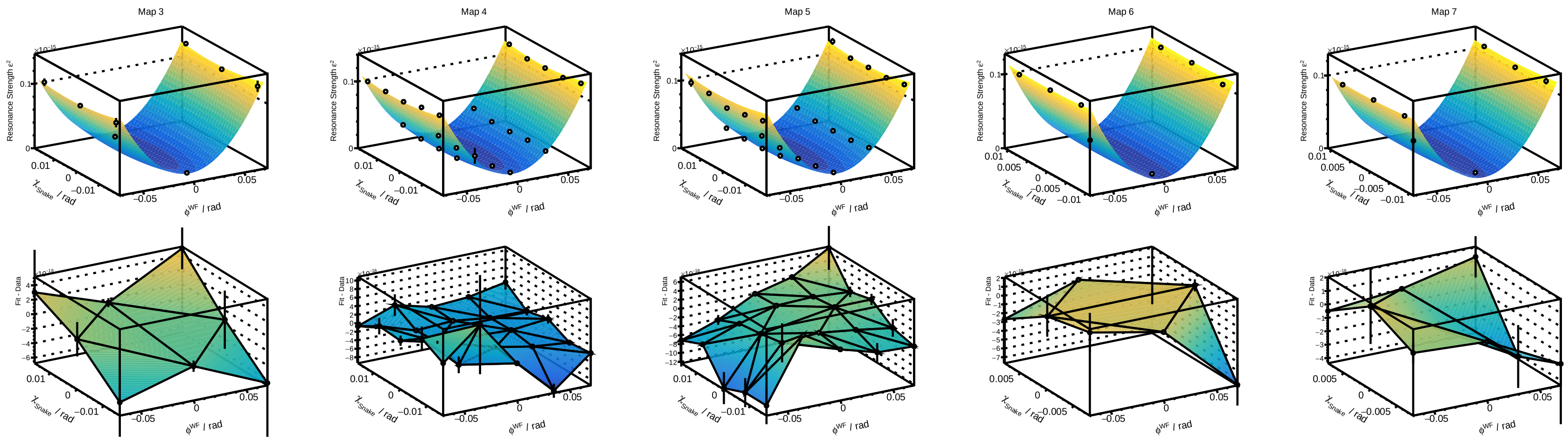

Figure D.10.: Resonance strengths for all measured Maps using the Pilot bunch method during Precursor 2. The plane illustrates the fit according to Eq. (7.57). The lower panel depict the residuals. During Map 6 & 7, the 2 MV solenoid is used in addition.

D.3. Analysis of the Off-Resonance Behaviour of the Phase Feedback

As described in Section 7.6.3.1, statistical fluctuations of the phase feedback only allow for approximate matching of the Wien filter frequency to the spin tune. These effects are accounted for in Eq. (7.110). Using Eq. (7.115), the phase matching can be studied. The results are shown in Figure D.11 for the individual maps using the Pilot Bunch.

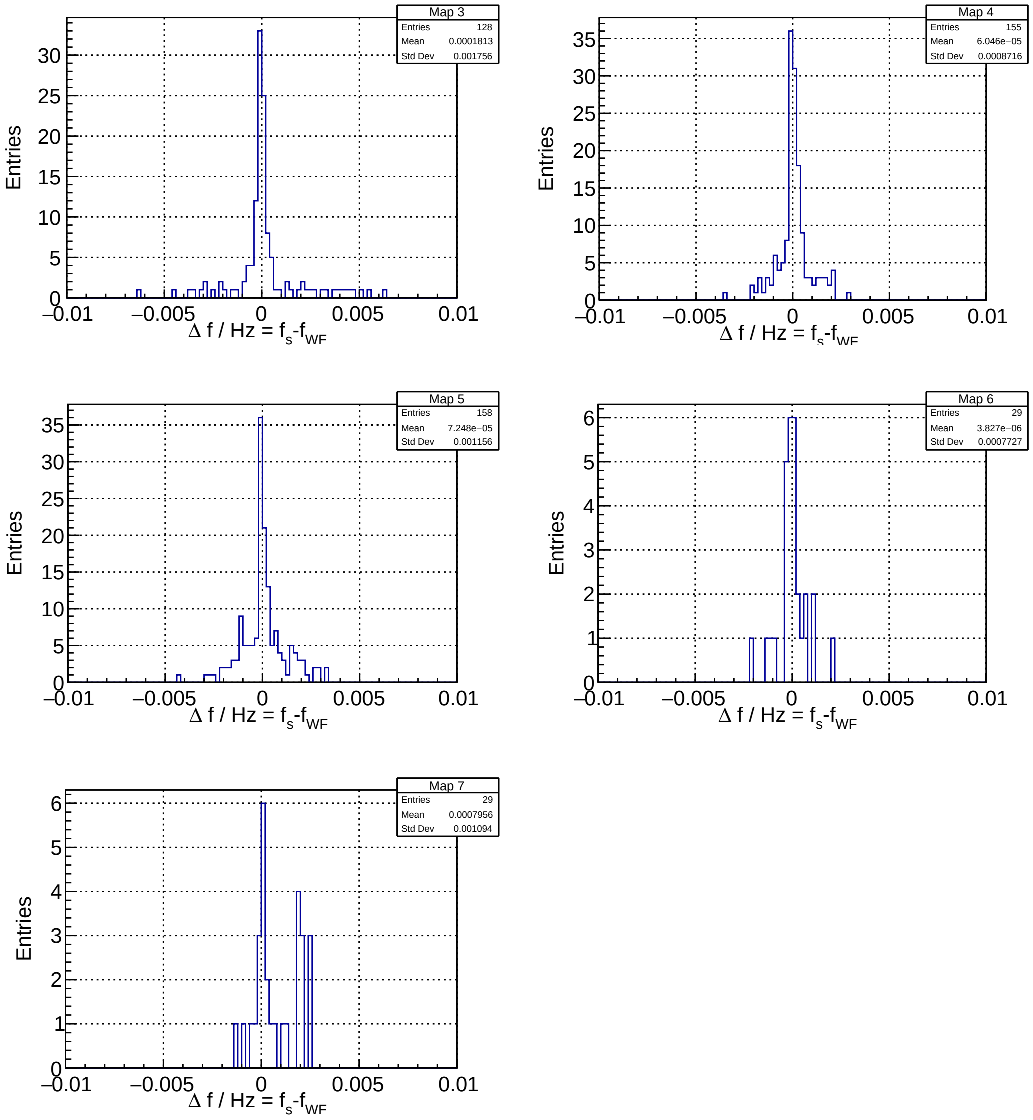

Figure D.11.: Histogram of the off-resonance parameter (Eq. 7.115) for all measured Maps using the Pilot bunch method.

E. Additional Material on the RF Wien Filter Field Studies

E.1. Measurements with Orbit Bumps at the location of the RF Wien Filter

During the systematic studies orbit variations are performed to study the effect on the beam loss minima as a function of different RF Wien filter rotation angles. The results are presented in section 8.3.5. Horizontal (cf. Figure E.1) and vertical (cf. Figure E.2) orbit bumps as well as vertical beam angles (cf. Figure E.3) at the target location of the RF Wien filter were measured.

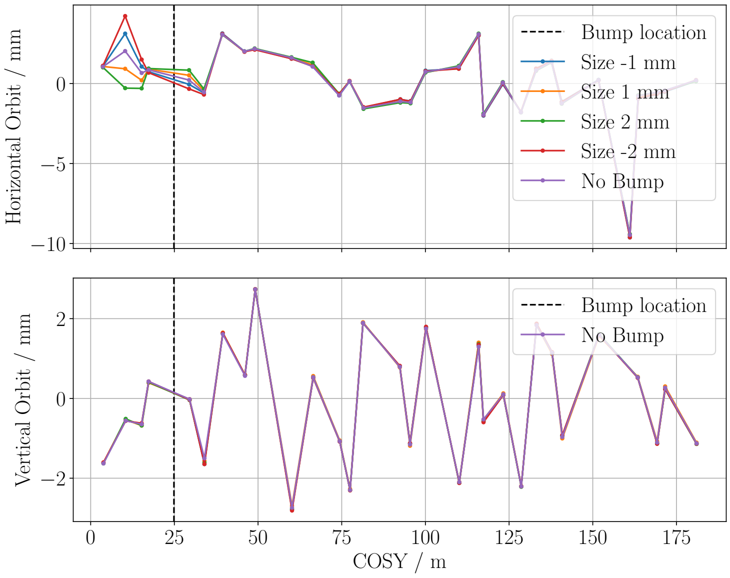

Figure E.1.: Horizontal orbit bumps at the RF Wien filter using the following steerers: SH43, SH01, SH05, and SH07.

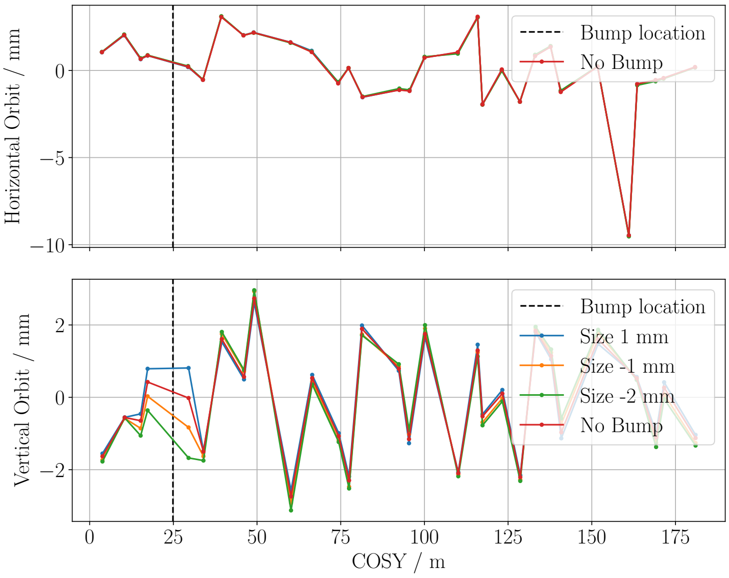

Figure E.2.: Vertical orbit bumps at the RF Wien filter using the following steerers: SV02, SWBLW1, SV06, and SV08.

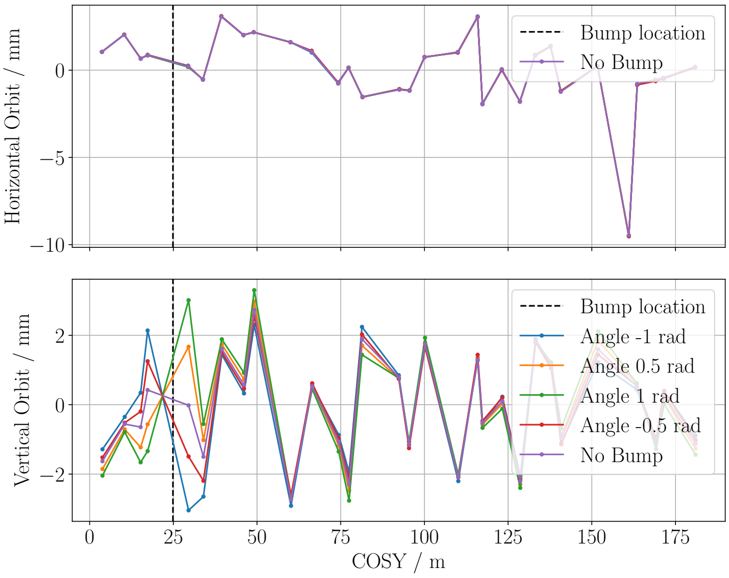

Figure E.3.: Vertical orbit bump angles at the RF Wien filter using the following steerers: SV02, SWBLW1, SV06, and SV08.

Bibliography

[1] "JEDI Homepage". `https://collaborations.fz-juelich.de/ikp/jedi/`. Accessed on January 2, 2024.

[2] L. Canetti, M. Drewes, and M. Shaposhnikov. "Matter and antimatter in the universe". *New Journal of Physics*, **14(9)**, 095012 (2012). ISSN 1367-2630. doi:10.1088/1367-2630/14/9/095012.

[3] W. Bernreuther. "CP violation and baryogenesis". *Lect. Notes Phys.*, **591**, 237 (2002).

[4] B. Borgia. "The alpha magnetic spectrometer on the International Space Station". *IEEE Transactions on Nuclear Science*, **52(6)**, 2786 (2005). doi:10.1109/TNS.2005.862781.

[5] A. D. Sakharov. "Violation of CP Invariance, C asymmetry, and baryon asymmetry of the universe". *Pisma Zh. Eksp. Teor. Fiz.*, **5**, 32 (1967). doi:10.1070/PU1991v034n05ABEH002497.

[6] E. Noether. "Invariante Variationsprobleme". *Nachrichten von der Gesellschaft der Wissenschaften zu Göttingen, Mathematisch-Physikalische Klasse*, **1918**, 235 (1918).

[7] M. Sozzi. *Discrete Symmetries and CP Violation: From Experiment to Theory.* Oxford University Press (2007). ISBN 9780199296668. doi:10.1093/acprof:oso/9780199296668.001.0001.

[8] C. S. Wu *et al.* "Experimental Test of Parity Conservation in Beta Decay". *Phys. Rev.*, **105**, 1413 (1957). doi:10.1103/PhysRev.105.1413.

[9] G. Backenstoss *et al.* "Helicity of μ^- Mesons from π-Meson Decay". *Phys. Rev. Lett.*, **6**, 415 (1961). doi:10.1103/PhysRevLett.6.415.

[10] D. J. Griffiths. *Introduction to elementary particles; 2nd rev. version.* Wiley, New York, NY (2008).

[11] J. H. Christenson *et al.* "Evidence for the 2π Decay of the K_2^0 Meson". *Phys. Rev. Lett.*, **13**, 138 (1964). doi:10.1103/PhysRevLett.13.138.

[12] M. Kobayashi and T. Maskawa. "CP Violation in the Renormalizable Theory of Weak Interaction". *Prog. Theor. Phys.*, **49**, 652 (1973). doi:10.1143/PTP.49.652.

[13] T. Gershon and V. V. Gligorov. "CP violation in the B system". *Reports on Progress in Physics*, **80(4)**, 046201 (2017). doi:10.1088/1361-6633/aa5514.

[14] J. Schwinger. "The Theory of Quantized Fields. I". *Phys. Rev.*, **82**, 914 (1951). doi:10.1103/PhysRev.82.914.

[15] G. W. Bennett *et al.* "Improved limit on the muon electric dipole moment". *Physical Review D*, **80(5)** (2009). ISSN 1550-2368. doi:10.1103/physrevd.80.052008.

[16] P. A. Zyla *et al.* "Review of Particle Physics". *Progress of Theoretical and Experimental Physics*, **2020(8)**, 083C01 (2020). ISSN 2050-3911. doi:10.1093/ptep/ptaa104.

[17] E. Tiesinga *et al.* "The 2022 CODATA Recommended Values of the Fundamental Physical Constants (Web Version 9.0)". Database developed by J. Baker, M. Douma, and S. Kotochigova. Available at `https://physics.nist.gov/constants` (2024).

[18] V. Bargmann, L. Michel, and V. L. Telegdi. "Precession of the Polarization of Particles Moving in a Homogeneous Electromagnetic Field". *Phys. Rev. Lett.*, **2**, 435 (1959). doi:10.1103/PhysRevLett.2.435.

[19] E. Commins, J. Jackson, and D. Demille. "The electric dipole moment of the electron: An Intuitive explanation for the evasion of Schiff's theorem". *American Journal of Physics - AMER J PHYS*, **75**, 532 (2007). doi:10.1119/1.2710486.

[20] G. Baym and D. H. Beck. "Elementary quantum mechanics of the neutron with an electric dipole moment". *Proceedings of the National Academy of Sciences*, **113(27)**, 7438 (2016). doi:10.1073/pnas.1607599113.

[21] M. Pospelov and A. Ritz. "Electric dipole moments as probes of new physics". *Annals of Physics*, **318(1)**, 119–169 (2005). ISSN 0003-4916. doi:10.1016/j.aop.2005.04.002.

[22] A. Czarnecki and B. Krause. "Neutron Electric Dipole Moment in the Standard Model: Complete Three-Loop Calculation of the Valence Quark Contributions". *Physical Review Letters*, **78(23)**, 4339–4342 (1997). ISSN 1079-7114. doi:10.1103/physrevlett.78.4339.

[23] W. Dekens *et al.* "Unraveling models of CP violation through electric dipole moments of light nuclei". *Journal of High Energy Physics*, **2014(7)** (2014). ISSN 1029-8479. doi:10.1007/jhep07(2014)069.

[24] F.-K. Guo and U.-G. Meißner. "Baryon electric dipole moments from strong CP violation". *Journal of High Energy Physics*, **2012(12)** (2012). ISSN 1029-8479. doi:10.1007/jhep12(2012)097.

[25] R. D. Peccei and H. R. Quinn. "CP Conservation in the Presence of Pseudoparticles". *Phys. Rev. Lett.*, **38**, 1440 (1977). doi:10.1103/PhysRevLett.38.1440.

[26] S. Karanth *et al.* "First Search for Axionlike Particles in a Storage Ring Using a Polarized Deuteron Beam". *Phys. Rev. X*, **13**, 031004 (2023). doi:10.1103/PhysRevX.13.031004.

[27] J. H. Smith, E. M. Purcell, and N. F. Ramsey. "Experimental Limit to the Electric Dipole Moment of the Neutron". *Phys. Rev.*, **108**, 120 (1957). doi:10.1103/PhysRev.108.120.

[28] C. Abel *et al.* "Measurement of the Permanent Electric Dipole Moment of the Neutron". *Phys. Rev. Lett.*, **124**, 081803 (2020). doi:10.1103/PhysRevLett.124.081803.

[29] W. B. Dress, P. D. Miller, and N. F. Ramsey. "Improved Upper Limit for the Electric Dipole Moment of the Neutron". *Phys. Rev. D*, **7**, 3147 (1973). doi:10.1103/PhysRevD.7.3147.

[30] W. B. Dress *et al.* “Search for an electric dipole moment of the neutron”. *Phys. Rev. D*, **15**, 9 (1977). doi:10.1103/PhysRevD.15.9.

[31] I. S. Altarev *et al.* “Search for an Electric Dipole Moment of the Neutron”. *JETP Lett.*, **44**, 460 (1986).

[32] K. Smith *et al.* “A search for the electric dipole moment of the neutron”. *Physics Letters B*, **234(1)**, 191 (1990). ISSN 0370-2693. doi:https://doi.org/10.1016/0370-2693(90)92027-G.

[33] I. S. Altarev *et al.* “Search for the neutron electric dipole moment”. *Phys. Atom. Nucl.*, **59**, 1152 (1996).

[34] P. G. Harris *et al.* “New Experimental Limit on the Electric Dipole Moment of the Neutron”. *Phys. Rev. Lett.*, **82**, 904 (1999). doi:10.1103/PhysRevLett.82.904.

[35] C. A. Baker *et al.* “Improved Experimental Limit on the Electric Dipole Moment of the Neutron”. *Phys. Rev. Lett.*, **97**, 131801 (2006). doi:10.1103/PhysRevLett.97.131801.

[36] I. Altarev *et al.* “New constraints on Lorentz invariance violation from the neutron electric dipole moment”. *Europhysics Letters*, **92(5)**, 51001 (2011). doi:10.1209/0295-5075/92/51001.

[37] A. P. Serebrov *et al.* “New measurements of the neutron electric dipole moment”. *JETP Letters*, **99(1)**, 4 (2014). ISSN 1090-6487. doi:10.1134/s0021364014010111.

[38] W. C. Griffith *et al.* “Improved Limit on the Permanent Electric Dipole Moment of ^{199}Hg”. *Phys. Rev. Lett.*, **102**, 101601 (2009). doi:10.1103/PhysRevLett.102.101601.

[39] B. Graner *et al.* “Reduced Limit on the Permanent Electric Dipole Moment of ^{199}Hg”. *Phys. Rev. Lett.*, **116**, 161601 (2016). doi:10.1103/PhysRevLett.116.161601.

[40] L. Pondrom *et al.* “New limit on the electric dipole moment of the Λ hyperon”. *Phys. Rev. D*, **23**, 814 (1981). doi:10.1103/PhysRevD.23.814.

[41] K. Inami and K. Hayasaka. “An improved search for the electric dipole moment of the τ lepton”. *Journal of High Energy Physics*, **2022(110)** (2022). doi:10.1007/JHEP04(2022)110.

[42] W. B. Cairncross *et al.* “Precision Measurement of the Electron’s Electric Dipole Moment Using Trapped Molecular Ions”. *Phys. Rev. Lett.*, **119**, 153001 (2017). doi:10.1103/PhysRevLett.119.153001.

[43] M. Berz, K. Makino, and W. Wan. *An Introduction to Beam Physics*. Series in high energy physics, cosmology, and gravitation. Taylor & Francis (2015). ISBN 978-1-4200-1182-1, 978-1-138-19890-6, 978-0-7503-0263-0, 978-0-429-14813-2. doi:10.1201/b12074.

[44] D. Eversmann. *High Precision Spin Tune Determination at the Cooler Synchrotron in Julich*. Ph.D. thesis, RWTH Aachen University (2017). Unpublished.

[45] H. Wiedemann. *Particle Accelerator Physics*. Graduate Texts in Physics. Springer, Berlin, Germany (2015). ISBN 978-3-319-18316-9. doi:10.1007/978-3-319-18317-6.

[46] V. Poncza. *Extensive Optimization of a Simulation Model for the Electric Dipole Moment Measurement at the Cooler Synchrotron COSY*. Ph.D. thesis, RWTH Aachen University (2021). doi:10.18154/RWTH-2021-04834.

[47] J. Buon. “Beam phase space and emittance; Rev. Version” (1994). doi:10.5170/CERN-1994-001.89.

[48] F. Hinterberger. *Physik der Teilchenbeschleuniger und Ionenoptik*. Springer Berlin, Heidelberg, 1 ed. (1997). ISBN 978-3-662-09312-2. doi:10.1007/978-3-662-09312-2.

[49] V. Schmidt. *Analysis of Closed-Orbit Deviations for a first direct Deuteron Electric Dipole Moment Measurement at the Cooler Synchrotron COSY*. Master’s thesis, RWTH Aachen University (2016).

[50] M. Rosenthal. *Experimental Benchmarking of Spin Tracking Algorithms for Electric Dipole Moment Searches at the Cooler Synchrotron COSY*. Ph.D. thesis, RWTH Aachen University (2016).

[51] D. Fick. *Einführung in die Kernphysik mit polarisierten Teilchen*. BI-Hochschultaschenbücher. Bibliogr. Inst., Mannheim u.a. (1971).

[52] F. Mueller. *Polarimeter Development for Electric Dipole Moment Measurements in Storage Rings*. Ph.D. thesis, RWTH Aachen University (2019). doi:10.18154/RWTH-2019-11439.

[53] T. Fukuyama and A. J. Silenko. “Derivation of Generalized Thomas-Bargmann-Michel-Telegdi Equation for a Particle with Electric Dipole Moment”. *Int. J. Mod. Phys. A*, **28**, 1350147 (2013). doi:10.1142/S0217751X13501479.

[54] F. Rathmann, N. Nikolaev, and J. Slim. “Spin dynamics investigations for the electric dipole moment experiment”. *Physical Review Accelerators and Beams*, **23(2)** (2020). ISSN 2469-9888. doi:10.1103/physrevaccelbeams.23.024601.

[55] S. Weinberg. “A New Light Boson?” *Phys. Rev. Lett.*, **40**, 223 (1978). doi:10.1103/PhysRevLett.40.223.

[56] F. Wilczek. “Problem of Strong P and T Invariance in the Presence of Instantons”. *Phys. Rev. Lett.*, **40**, 279 (1978). doi:10.1103/PhysRevLett.40.279.

[57] R. L. Workman *et al.* “Review of Particle Physics”. *Progress of Theoretical and Experimental Physics*, **2022(8)**, 083C01 (2022). ISSN 2050-3911. doi:10.1093/ptep/ptac097.

[58] P. W. Graham and S. Rajendran. “Axion dark matter detection with cold molecules”. *Phys. Rev. D*, **84**, 055013 (2011). doi:10.1103/PhysRevD.84.055013.

[59] P. W. Graham and S. Rajendran. “New observables for direct detection of axion dark matter”. *Phys. Rev. D*, **88**, 035023 (2013). doi:10.1103/PhysRevD.88.035023.

[60] G. G. Ohlsen and P. Keaton. “Techniques for measurement of spin-1/2 and spin-1 polarization analyzing tensors”. *Nuclear Instruments and Methods*, **109(1)**, 41 (1973). ISSN 0029-554X. doi:https://doi.org/10.1016/0029-554X(73)90450-3.

[61] B. v. Przewoski *et al.* “Analyzing powers and spin correlation coefficients for $p + d$ elastic scattering at 135 and 200 MeV”. *Phys. Rev. C*, **74**, 064003 (2006). doi:10.1103/PhysRevC.74.064003.

[62] F. Müller *et al.* “Measurement of deuteron carbon vector analyzing powers in the kinetic energy range 170-380 MeV”. *Eur. Phys. J. A*, **56**, 211 (2020). doi:10.1140/epja/s10050-020-00215-8.

[63] R. Maier. “Cooler synchrotron COSY — Performance and perspectives”. *Nuclear Instruments and Methods in Physics Research Section A: Accelerators, Spectrometers, Detectors and Associated Equipment*, **390(1)**, 1 (1997). ISSN 0168-9002. doi:https://doi.org/10.1016/S0168-9002(97)00324-0.

[64] O. Felden *et al.* “Negative ion source development at the cooler synchrotron COSY/Jülich”. *AIP Conference Proceedings*, **1515(1)**, 321 (2013). ISSN 0094-243X. doi:10.1063/1.4792800.

[65] R. Weidmann *et al.* “The polarized ion source for COSY”. *Review of Scientific Instruments*, **67(3)**, 1357 (1996). ISSN 0034-6748. doi:10.1063/1.1146665.

[66] W. Haeberli. “Sources of Polarized Ions”. *Annu. Rev. Nucl. Sci., 17: 373-426(1967).* (1967). doi:10.1146/annurev.ns.17.120167.002105.

[67] D. Chiladze *et al.* “Determination of deuteron beam polarizations at COSY”. *Phys. Rev. ST Accel. Beams*, **9**, 050101 (2006). doi:10.1103/PhysRevSTAB.9.050101.

[68] K. Strijckmans. “The isochronous cyclotron: principles and recent developments”. *Computerized Medical Imaging and Graphics*, **25(2)**, 69 (2001). ISSN 0895-6111. doi:https://doi.org/10.1016/S0895-6111(00)00056-2.

[69] T. Wagner *et al.* “Beam-based alignment at the Cooler Synchrotron COSY as a prerequisite for an electric dipole moment measurement”. *Journal of Instrumentation*, **16(02)**, T02001–T02001 (2021). ISSN 1748-0221. doi:10.1088/1748-0221/16/02/t02001.

[70] G. Guidoboni *et al.* “How to Reach a Thousand-Second in-Plane Polarization Lifetime with $0.97-\mathrm{GeV}/c$ Deuterons in a Storage Ring”. *Phys. Rev. Lett.*, **117**, 054801 (2016). doi:10.1103/PhysRevLett.117.054801.

[71] R. Maier *et al.* “Invited Paper: Commissioning of the Cooler Synchrotron COSY”. In *Proc. Cyclotrons’95*, pp. 338–344. JACoW Publishing, Geneva, Switzerland.

[72] S. Barsov *et al.* “ANKE, a new facility for medium energy hadron physics at COSY-Jülich”. *Nuclear Instruments and Methods in Physics Research Section A: Accelerators, Spectrometers, Detectors and Associated Equipment*, **462**, 364 (2001). doi:10.1016/S0168-9002(00)01147-5.

[73] B. Hoistad and J. Ritman. “Proposal for the Wide Angle Shower Apparatus (WASA) at COSY-Juelich - ”WASA at COSY”” (2004). doi:10.48550/arXiv.nucl-ex/0411038.

[74] Z. Bagdasarian *et al.* “Measuring the polarization of a rapidly precessing deuteron beam”. *Phys. Rev. ST Accel. Beams*, **17**, 052803 (2014). doi:10.1103/PhysRevSTAB.17.052803.

[75] G. Ciullo. "Polarization of stored beam by spin-filtering at COSY". *Physics of Particles and Nuclei*, **45** (2014). doi:10.1134/S1063779614010201.

[76] V. V. Parkhomchuk and A. N. Skrinsky. "Electron cooling: physics and prospective applications". *Reports on Progress in Physics*, **54(7)**, 919 (1991). doi:10.1088/0034-4885/54/7/001.

[77] H. J. Stein *et al.* "Present Performance of Electron Cooling at Cosy-Jülich". In *18th Conference on Charged Particle Accelerators* (2011).

[78] V. Kamerdzhiev. *Untersuchung und Verbesserung des Stabilitätsverhaltens eines intensiven elektronengekühlten Teilchenstrahles in COSY*. Ph.D. thesis, Universität Dortmund (2004). doi:http://dx.doi.org/10.17877/DE290R-238.

[79] D. Prasuhn *et al.* "Electron and stochastic cooling at COSY". *Nuclear Instruments and Methods in Physics Research Section A: Accelerators, Spectrometers, Detectors and Associated Equipment*, **441**, 167 (2000). doi:10.1016/S0168-9002(99)01128-6.

[80] R. Maier *et al.* "Non-beam disturbing diagnostics at COSY-Julich". *Conf. Proc. C*, **900612**, 800 (1990).

[81] C. Böhme *et al.* "Studies for a BPM Upgrade at COSY". In *4th International Beam Instrumentation Conference*, p. TUPB017 (2016). doi:10.18429/JACoW-IBIC2015-TUPB017.

[82] F. Hinder *et al.* "Development of New Beam Position Monitors at COSY". In *4th International Beam Instrumentation Conference*, p. TUPB015 (2016). doi:10.18429/JACoW-IBIC2015-TUPB015.

[83] C. Boehme *et al.* "Gas scintillation beam profile monitor at cosy jülich". *2010 Beam Instrumentation Workshop, BIW 2010 - Proceedings*, pp. 98–100 (2010).

[84] P. Forck. "Minimal Invasive Beam Profile Monitors for High Intense Hadron Beams". *Conf. Proc. C*, **100523**, TUZMH01 (2010).

[85] V. S. Morozov *et al.* "Experimental Verification of Predicted Beam-Polarization Oscillations near a Spin Resonance". *Phys. Rev. Lett.*, **100**, 054801 (2008). doi:10.1103/PhysRevLett.100.054801.

[86] CERN Yellow Reports: Monographs. "CERN Yellow Reports: Monographs, Vol. 3 (2021): Storage ring to search for electric dipole moments of charged particles: Feasibility study" (2021). doi:10.23731/CYRM-2021-003.

[87] M. Froissart and R. Stora. "Dépolarisation d'un faisceau de protons polarisés dans un synchrotron". *Nuclear Instruments and Methods*, **7(3)**, 297 (1960). doi:10.1016/0029-554X(60)90033-1.

[88] J. Slim. *A novel waveguide RF Wien filter for electric dipole moment measurements of deuterons and protons at the COoler SYnchrotron (COSY)/Jülich*. Dissertation, Rheinisch-Westfälische Technische Hochschule Aachen, Aachen (2018). doi:10.18154/RWTH-2018-229484. Veröffentlicht auf dem Publikationsserver der RWTH

Aachen University. - Ausgezeichnet mit der Borchers-Plakette und dem Friedrich-Wilhelm-Preis 2019.; Dissertation, Rheinisch-Westfälische Technische Hochschule Aachen, 2018.

[89] J. Slim *et al.* "Pilot bunch and co-magnetometry of polarized particles stored in a ring". *ArXiv preprint arXiv:2309.06561* (2023).

[90] J. Slim *et al.* "Polynomial Chaos Expansion method as a tool to evaluate and quantify field homogeneities of a novel waveguide RF Wien filter". *Nuclear Instruments and Methods in Physics Research Section A: Accelerators, Spectrometers, Detectors and Associated Equipment*, **859**, 52 (2017). ISSN 0168-9002. doi:https://doi.org/10.1016/j.nima.2017.03.040.

[91] V. Kamerdzhiev *et al.* "Commissioning of the 2MeV Electron Cooler for COSY / HESR". In *IPAC2012 - Proceedings*, p. 379. New Orleans, Louisiana, USA (2012).

[92] "WASA-at-COSY". `https://collaborations.fz-juelich.de/ikp/wasa/`. Accessed on May 21, 2024.

[93] T. Saito *et al.* "The WASA-FRS project at GSI and its perspective". *Nuclear Instruments and Methods in Physics Research Section B: Beam Interactions with Materials and Atoms*, **542**, 22 (2023). ISSN 0168-583X. doi:https://doi.org/10.1016/j.nimb.2023.05.042.

[94] F. Müller *et al.* "A new beam polarimeter at COSY to search for electric dipole moments of charged particles". *Journal of Instrumentation*, **15(12)**, P12005–P12005 (2020). ISSN 1748-0221. doi:10.1088/1748-0221/15/12/p12005.

[95] R. Brun and F. Rademakers. "ROOT — An object oriented data analysis framework". *Nuclear Instruments and Methods in Physics Research Section A: Accelerators, Spectrometers, Detectors and Associated Equipment*, **389(1)**, 81 (1997). ISSN 0168-9002. doi:https://doi.org/10.1016/S0168-9002(97)00048-X. New Computing Techniques in Physics Research V.

[96] "EPICS Homepage". `https://epics-controls.org/`. Accessed on October 29, 2023.

[97] "atan2". `http://en.cppreference.com/mwiki/index.php?title=cpp/numeric/math/atan2&oldid=79630`. Online, accessed January 9, 2024.

[98] D. Eversmann, J. Pretz, and M. Rosenthal. "Amplitude estimation of a sine function based on confidence intervals and Bayes' theorem". *Journal of Instrumentation*, **11(05)**, P05003 (2016). doi:10.1088/1748-0221/11/05/P05003.

[99] N. Hempelmann *et al.* "Phase Locking the Spin Precession in a Storage Ring". *Phys. Rev. Lett.*, **119**, 014801 (2017). doi:10.1103/PhysRevLett.119.014801.

[100] N. Hempelmann *et al.* "Phase measurement for driven spin oscillations in a storage ring". *Phys. Rev. Accel. Beams*, **21**, 042002 (2018). doi:10.1103/PhysRevAccelBeams.21.042002.

[101] S. Karanth *et al.* "Influence of electron cooling on the polarization lifetime of a horizontally polarized storage ring beam". *Nuclear Instruments and Methods in Physics Research Section A: Accelerators, Spectrometers, Detectors and Associated Equipment*, **987**, 164797 (2021). ISSN 0168-9002. doi:https://doi.org/10.1016/j.nima.2020.164797.

[102] M. Beyss. *Detection and Analysis of Recombination Rates during Electron Cooling at COSY*. Master's thesis, RWTH Aachen University (2019).

[103] A. Saleev *et al.* "Spin tune mapping as a novel tool to probe the spin dynamics in storage rings". *Phys. Rev. Accel. Beams*, **20**, 072801 (2017). doi:10.1103/PhysRevAccelBeams.20.072801.

[104] M. Vitz. *Investigation of Systematic Effects and Uncertainties involved in the Determination of the Invariant Spin Axis in a storage ring for an EDM Measurement*. Ph.D. thesis, RWTH Aachen University (2024). Unpublished.

[105] V. Hejny. "Spin motion in an rf Wien filter" (2019). Internal document, JEDI collaboration.

[106] N. Hempelmann. *Polarization Measurement and Manipulation for Electric Dipole Moment Measurements in Storage Rings*. Ph.D. thesis, RWTH Aachen University (2018). doi:10.18154/RWTH-2018-221496.

[107] N. N. Nikolaev *et al.* "Spin decoherence and off-resonance behavior of radiofrequency-driven spin rotations in storage rings". *arXiv preprint arXiv:2309.05080* (2023).

[108] T. Wagner. *Beam-based alignment at the Cooler Synchrotron COSY for an Electric Dipole Moment measurement of charged particles*. Ph.D. thesis, RWTH Aachen University (2021). doi:10.18154/RWTH-2021-08453.

[109] J. Slim *et al.* "First detection of collective oscillations of a stored deuteron beam with an amplitude close to the quantum limit". *Phys. Rev. Accel. Beams*, **24**, 124601 (2021). doi:10.1103/PhysRevAccelBeams.24.124601.

[110] V. Hejny. "Analytic calculation of various tilt effects in the WF" (2024). Internal document, JEDI collaboration.

[111] J. Slim *et al.* "Electromagnetic Simulation and Design of a Novel Waveguide RF Wien Filter for Electric Dipole Moment Measurements of Protons and Deuterons". *Nuclear Instruments and Methods in Physics Research Section A: Accelerators, Spectrometers, Detectors and Associated Equipment*, **828**, 116 (2016). ISSN 0168-9002. doi:https://doi.org/10.1016/j.nima.2016.05.012.

[112] J. Slim *et al.* "The driving circuit of the waveguide RF Wien filter for the deuteron EDM precursor experiment at COSY". *Journal of Instrumentation*, **15(03)**, P03021 (2020). doi:10.1088/1748-0221/15/03/P03021.

[113] A. Lehrach, S. Martin, and R. Talman. "Design of a Prototype EDM Storage Ring". *PoS*, **SPIN2018**, 144 (2019). doi:10.22323/1.346.0144.

[114] V. H. Ranjbar *et al.* "Spin coupling resonance and suppression in the AGS". *Phys. Rev. ST Accel. Beams*, **7**, 051001 (2004). doi:10.1103/PhysRevSTAB.7.051001.

List of Figures

List of Tables

Acknowledgments

To conclude this thesis, I want to thank everyone who contributed. I am deeply grateful to Prof. Dr. Jörg Pretz for offering me the possibility of joining the JEDI collaboration. His guidance and patience contributed mainly to the success of this thesis. Within the JEDI collaboration, he creates a pleasant, creative, and productive working atmosphere, not only as a band leader of the Christmas band but also as a supervisor for many adolescent scientists. Many thanks also go to Dr. Ralf Gebel for supporting the scientific work of JEDI at COSY and my work. I also want to thank Prof. Dr. Achim Stahl for agreeing to be my second supervisor.

A big thank you goes to all members of the JEDI collaboration. Organizing, planning, and executing two beam times during difficult times like COVID and understaffed was certainly a challenge with little sleep. Especially, I want to thank Dr. Alexander Nass, Dr. Frank Rathmann, Dr. Jamal Slim, Dr. Volker Hejny, Dr. Vera Shmakova, and Dr. Tim Wagner and the rest of the collaboration for helping during beam times at impossible times during the day and night. I also want to thank the COSY staff for preparing the polarized deuteron beam and unpolarized proton beam and providing fantastic beam conditions.

As part of a small collaboration, I was trusted with a lot of responsibility. In addition, being able to participate in international conferences all over the world is an experience I will never forget and for which I am always grateful.

A special thank you goes to Dr. Volker Hejny, head of the analysis group. Without his vast knowledge and his ability to explain the unexplainable, this thesis would have never been possible.

Dr. Alexander Nass organizes guided tours around COSY for professionals and non-professionals. He trusted me many times in helping him with these tours which I truly enjoyed as a welcome distraction from my daily PhD work.

I can't forget to mention my coworkers, namely, Dr. Vera Poncza, Dr. Tim Wagner, Dr. Jan Hetzel, Awal Awal, Daoning Gu, Maximilian Vitz, Valentin Tempel, Michael Margos, Saad Siddique, and Rahul Shankar. In recent years, I have convinced myself that PhDs are indeed stressful. You have made this time less stressful for me during many coffee and cake breaks. I wish all of you—from the bottom of my heart—only the very best for your professional and personal future.

During this PhD, I was able to live in Vancouver and work at TRIUMF as part of a three-month-long internship, which was, without doubt, the most intense and beautiful time of my life so far. Living abroad and the experiences in Canada have shaped me positively in many ways for which I'll be forever grateful. I owe my deepest gratitude to Prof. Dr. Jörg Pretz, Dr. Ralf Gebel, Prof. Dr. Oliver Kester, and Dr. Wojciech Fedorko for making this experience possible. During this time, I met the most sincere people. I'll be always thankful to Aurora, David, Krystell, and Wen for being part of this journey, inspiring conversations, and fantastic encounters.

It's no secret that studying physics is not always the easiest thing to do. I want to thank Max, Niklas, and Yannic for making even the hard times enjoyable. Because of you, my Curve Fever skills are outstanding.

Zuletzt möchte ich meinen Eltern, Marliese und Kurt Andres, meinen tief empfundenen Dank für ihre uneingeschränkte Unterstützung und ihren unermüdlichen Einsatz in den letzten Jahren aussprechen. Sie haben es mir ermöglicht, meine Ziele zu verfolgen, ohne mich um etwas anderes als mein Physikstudium kümmern zu müssen. Nichts davon wäre ohne ihre finanzielle und emotionale Unterstützung möglich gewesen. Ich weiß, dass dies nicht selbstverständlich ist und dass ich mich in einer sehr privilegierten Position befinde.

Eidesstaatliche Erklärung

Ich, Achim Andres, erkläre hiermit, dass diese Dissertation und die darin dargelegten Inhalte die eigenen sind und selbstständig, als Ergebnis der eigenen originären Forschung, generiert wurden.

Hiermit erkläre ich an Eides statt

1. Diese Arbeit wurde vollständig oder größtenteils in der Phase als Doktorand dieser Fakultät und Universität angefertigt.

2. Sofern irgendein Bestandteil dieser Dissertation zuvor für einen akademischen Abschluss oder eine andere Qualifikation an dieser oder einer anderen Institution verwendet wurde, wurde dies klar angezeigt.

3. Wenn immer andere eigene- oder Veröffentlichungen Dritter herangezogen wurden, wurden diese klar benannt.

4. Wenn aus anderen eigenen- oder Veröffentlichungen Dritter zitiert wurde, wurde stets die Quelle hierfür angegeben. Diese Dissertation ist vollständig meine eigene Arbeit, mit der Ausnahme solcher Zitate.

5. Alle wesentlichen Quellen von Unterstützung wurden benannt.

6. Wenn immer ein Teil dieser Dissertation auf der Zusammenarbeit mit anderen basiert, wurde von mir klar gezeichnet, was von anderen und was von mir selbst erarbeitet wurde.

7. Teile dieser Arbeit wurden zuvor veröffentlicht und zwar in:
   - A. Andres on behalf of the JEDI collaboration, ”The Search for Electric Dipole Moments of Charged Particles in Storage Rings”, In *20th Conference on Flavor Physics and CP Violation (2022).* DOI: `https://doi.org/10.48550/arXiv.2207.02083`
   - A. Andres, ”Progress towards a direct measurement of the deuteron Electric Dipole Moment at COSY”, In: *Annual Report 2023, Berichte des Forschungszentrum Jülich*, p. 65, 2023. DOI: `10.34734/FZJ-2024-01973`
   - A. Andres, ”Progress towards a direct measurement of the deuteron Electric Dipole Moment at COSY”, In: *Annual Report 2022, Berichte des Forschungszentrum Jülich*, p. 97, 2022. DOI: `10.34734/FZJ-2024-01948`

- A. Andres, "Progress towards a direct measurement of the deuteron Electric Dipole Moment at COSY", In: *Annual Report 2021, Berichte des Forschungszentrum Jülich*, p. 76, 2021. https://juser.fz-juelich.de/record/1005535
- A. Andres, "Progress towards a direct measurement of the deuteron Electric Dipole Moment at COSY", In: *Annual Report 2020, Berichte des Forschungszentrum Jülich*, p. 82, 2020. https://juser.fz-juelich.de/record/901921

Ort, Datum

Achim Andres